

# **Investigation of Complex Multiphase Flows by Advanced Optical Methods at the Example of the Flotation Process of Fluorite**

## **Dissertation**

zur Erlangung des akademischen Grades eines  
Doktors der Naturwissenschaften  
– Dr. rer. nat. –

vorgelegt von

**Björn Lewandowski, M. Eng.**

geboren in Marl

am Lehrstuhl für Technische Chemie II  
der  
Universität Duisburg-Essen

Essen, 2019

# DuEPublico

Duisburg-Essen Publications online

UNIVERSITÄT  
DUISBURG  
ESSEN

*Offen im Denken*

ub | universitäts  
bibliothek

Diese Dissertation wird über DuEPublico, dem Dokumenten- und Publikationsserver der Universität Duisburg-Essen, zur Verfügung gestellt und liegt auch als Print-Version vor.

**DOI:** 10.17185/duepublico/70564

**URN:** urn:nbn:de:hbz:464-20190925-113423-1

Alle Rechte vorbehalten.

Die vorliegende Arbeit wurde im Zeitraum von Juli 2016 bis Juni 2019 im Arbeitskreis von Prof. Dr. Georg Krekel an der Hochschule Niederrhein in Krefeld durchgeführt. Die Arbeit entstand in Kooperation mit dem Lehrstuhl für Technische Chemie II der Fakultät Chemie an der Universität Duisburg-Essen unter Anleitung von Prof. Dr. Mathias Ulbricht.

Tag der Disputation: 12. September 2019

Gutachter: Prof. Dr. Mathias Ulbricht  
Prof. Dr. Georg Krekel  
Prof. Dr.-Ing. Olaf Wünsch  
Vorsitzender: Prof. Dr. Malte Behrens

---

Ich versichere hiermit an Eides statt, dass ich die vorgelegte Dissertation mit dem Titel

„Investigation of Complex Multiphase Flows by Advanced Optical Methods at the Example of the Flotation Process of Fluorite“

selbstständig, ohne fremde Hilfe und ohne die Benutzung anderer als die in der Arbeit angegebenen Hilfsmittel angefertigt habe.

Alle Stellen die wörtlich oder sinngemäß aus veröffentlichten und nicht veröffentlichten Quellen entnommen wurden, sind als solche in der Arbeit kenntlich gemacht.

Die vorliegende Arbeit hat in dieser oder ähnlicher Form oder auch auszugsweise im Rahmen einer anderen Prüfung noch nicht vorgelegen.

Essen, den 10. April 2019

---

Ort, Datum



---

Unterschrift (Björn Lewandowski)



*Monika und Klaus*



## **Acknowledgements – Danksagung**

Die vorliegende Dissertation entstand in einer Kooperation zwischen des Fachbereichs Chemie der Hochschule Niederrhein und dem Lehrstuhl für Technische Chemie II der Fakultät Chemie der Universität Duisburg-Essen im Zeitraum von Juli 2016 bis Juni 2019. Im Folgenden möchte ich den zahlreichen Beteiligten dieses Unterfanges meinen Dank aussprechen.

Zunächst möchte ich mich herzlichst bei Herrn Prof. Dr. Mathias Ulbricht für die freundliche Aufnahme in seinen Arbeitskreis an der Universität Duisburg-Essen bedanken. Durch sein Vertrauen in das ausgearbeitete Konzept dieser Arbeit war diese Promotion überhaupt erst möglich. Obwohl das Thema sicherlich nicht zu seinem Kernforschungsgebiet zählt, zeigte er sich dennoch jederzeit äußerst interessiert an den Ergebnissen und dem Fortschritt des Projektes und konnte durch viele Ideen neue Impulse für die Arbeit setzen. Für sein entgegengebrachtes Vertrauen, den stets fachlich fruchttragenden Diskussionen sowie für sein konstruktives Feedback während der gesamten Zeit danke ich herzlichst.

Meinem Betreuer von Seiten der Hochschule Niederrhein, Herrn Prof. Dr. Georg Krekel, möchte ich an dieser Stelle ganz besonderen Dank aussprechen. Seit meinem dritten Semester im Bachelorstudium stand er mir schon als Mentor zur Seite, der mein Potential früh erkannte und unablässig in allen Belangen förderte, zum Beispiel in Form von Empfehlungsschreiben für diverse Stipendien. Als Betreuer in meiner Bachelor- und Masterarbeit sowie in anderweitig durchgeführten Projekten und auch Lehrveranstaltungen überzeugte er mich immer mit seinem breit aufgestellten Fachwissen und seiner gleichzeitig zurückhaltenden Art. Er hat mir während der Arbeit stets den nötigen Freiraum gewährt, aber auch immer darauf geachtet, dass ich das eigentliche Ziel nie aus den Augen verliere. In unseren zahlreichen wissenschaftlichen Diskussion hinterfragte er die Sachverhalte aufgrund seines breit gefächerten Wissens immer kritisch, sodass er mich dadurch selber zur kritischen Reflektion anregte. Er trieb mich so stets zu Höchstleistungen an, was die Gesamtqualität der Arbeit und auch die der im Rahmen dieser Promotion hervorgegangenen Veröffentlichungen signifikant verbessert hat.

Der Sachtleben Bergbau GmbH danke ich für die Bereitstellung des industriellen Fluorit-Mineral systems. Zusätzlich danke ich Herrn Georg Jehle für die freundliche Unterstützung bei der Validierung der neu entwickelten Methode zur Quantifizierung von Calciumfluorid in dem Mineralsystem mittels FT Raman-Spektroskopie.

Der Sigmund Linder AG möchte ich für die Bereitstellung der Präzisionsglaskugeln für die Validierung der automatischen Bildauswertung herzlich danken.

Den Kolleginnen und Kollegen der Hochschule Niederrhein danke ich für ein sehr angenehmes und hilfsbereites Arbeitsklima. Bei Fragen und Problemen konnte ich mich stets an die Kolleginnen und Kollegen der anderen Schwerpunkte wenden und wurde dort immer freundlich unterstützt. Dabei möchte ich Herrn Robin Legner besonders für seine aufopfernde Unterstützung in der komplexen Welt der instrumentellen Analytik danken. Herrn Dr. Lukas Weger danke ich für die Hilfe bei der Aufnahme der Fluoreszenzspektren des fluoreszierenden Flussspat-Minerals.

Ein sehr großer Dank gilt meinen Kolleginnen und Kollegen der technischen Chemie, dabei insbesondere Herrn Dr. Bartholomäus Luczak, Herrn Dr. Alexander Stefan, Herrn Marc Labusch, Herrn Joscha Prießen sowie Herrn Florian Filarsky. Die anregenden Diskussionen untereinander waren für mich stets noch einmal ein Prüfstand für die Qualität meiner Arbeit und auch jedes Mal ein erneuter Ansporn, mich noch weiter zu verbessern. Zudem trug der Austausch über die eigenen Arbeitsthemen untereinander zu einer Erweiterung meines wissenschaftlichen Horizonts bei.

Den Kolleginnen und Kollegen der Arbeitsgruppe an der Universität Duisburg-Essen danke ich herzlich für die freundliche Aufnahme und den kollegialen Umgang. Während meiner Zeit in der Arbeitsgruppe wurde ich in allen Belangen unterstützt, vor allem während meiner Zeit als Praktikumsbetreuer vor Ort.

Meinen zahlreichen fleißigen Studierenden danke ich für die tolle Unterstützung und die interessante Zeit, während der ich ihre Projekt- und Abschlussarbeiten betreuen durfte. Ohne ihren bedingungslosen Einsatz und akribisches Arbeiten wäre der experimentelle Umfang der vorliegenden Arbeit in diesem Maße sicherlich nicht möglich gewesen.

Zuletzt möchte ich an dieser Stelle meinen Freunden und ganz besonders meiner Familie danken. Herrn Joel Schmidt, Herrn Florian Filarsky und meinem Bruder Herrn Dirk Lewandowski danke ich für die stete Hilfsbereitschaft abseits der Arbeit in allen Belangen. Sie hatten immer ein offenes Ohr, sprachen mir in schwierigen Zeiten den nötigen Mut zu und sorgten für genügend Ablenkung, um auch mal den Kopf auszuschalten.

Meinen Eltern Monika und Klaus Lewandowski danke ich für ihr bedingungsloses Vertrauen in meine Fähigkeiten. Auf meinem bisherigen Lebensweg standen sie mir immer positiv zur Seite, haben nie an mir gezweifelt und sich immer für mich stark gemacht. So eine Art von bedingungslosem Rückhalt ist nicht selbstverständlich, weshalb ich mich äußerst glücklich schätze, so eine Unterstützung erfahren zu haben.

## Abstract

The flotation process is the most important process for the enrichment of valuable minerals. Although the process is now known for approximately 160 years, the amount of investigations on the micro processes is up to now still small. Technological developments in the recent years made optical measurement techniques such as Particle Image Velocimetry (PIV) and Shadowgraphy (SH) available for scientific research. Most of the investigations in the last decades had, however, a practical orientation aiming for an optimisation of process parameters in order to increase the economics. The number of investigations applying these optical methods to the flotation process is surprisingly low. Reasons for this are the high solids and bubble concentrations as well as the high turbulence during the flotation process.

The aim of the present work is the investigation of the complex flow structures during the flotation process via PIV and SH. To facilitate the application of the optical methods, a reduced flotation system with lower bubble and solids concentrations is set up. For this purpose, a novel flotation column made from transparent poly(methyl methacrylate) is designed, which allows the formation of single bubble-particle heterocoagulates and simultaneously facilitates a full optical accessibility. Investigations are carried out both in the two-phase as well as the three-phase system. Investigations in the two-phase system focus on the analysis of the bubble behaviour in deionized water and in presence of surface active agents at various concentrations. The aim is to develop a relationship between the bubble characteristics and the induced liquid velocity around the rising bubble. A model three-phase system consisting of glass particles is the starting point for flotation related investigations. The influence of flotation process parameters, e.g. volumetric gas flow rate and particle size, on the flotation outcome in form of maximum recoveries  $R_{\max}$  and flotation kinetics with respect to order  $n$  of kinetics as well as flotation rate constant  $k$  is investigated. Furthermore, the hydrodynamic structure of the rising single bubble-particle heterocoagulates is revealed via PIV measurements. Afterwards, an industrial fluorite flotation system is investigated using a design of experiment in order to find the optimal process parameters to maximise  $R_{\max}$ ,  $k$ , as well as the grade of the concentrate with respect to the calcium fluoride weight fraction  $w(\text{CaF}_2)$ . Lastly, a fluorescent fluorite mineral is tested for application in optical analysis. The aim is to distinguish valuable fluorescent fluorite mineral particles from gangue particles such as silicon dioxide and barite.

The results show that both PIV and SH are applicable for the investigation of multiphase flows. The designed apparatus facilitates both, optical accessibility into the reduced flotation system as well as the possibility to determine important flotation parameters. An automated analysis procedure with a high accuracy has been developed to allow a fast analysis of the obtained

image sequences. The reproducibility of consecutive bubbles has been found to be excellent, thus allowing a statistical investigation of different operational parameters on the process performance. The measurements in deionized water have shown a strong relationship between the volumetric gas flow rate and the induced liquid velocity. The surfactants changed the bubble characteristics significantly with increasing concentration towards a spherical form. Furthermore, the rising velocities decreased until a threshold has been reached. Although the rising velocities decreased, an increase in the induced liquid velocity as well as in the induced kinetic energy has been observed. Analysis of the bubble trajectories revealed an oscillating behaviour in horizontal  $x$  direction. With increasing surfactant concentration this oscillation frequency increases. Thus, the oscillation has been found to be responsible for this controversial relation.

The investigation of the model flotation system has shown the influence of the different operational parameters on both maximum recovery and flotation kinetics. While the order of flotation is best described by the zeroth order model at a high initial solids concentration  $c_{p,0}$ , a shift to first order kinetics has been found for lower  $c_{p,0}$ . Optical investigations showed large differences in the bubble-particle heterocoagulate rising behaviour for particles with different wettability. The poor flotation performance of hydrophilic particles could be related to a high mobility of the particles on the bubble surface, meaning a poor attachment efficiency. Hydrophobic particles have been found to form larger bubble-particle clusters. The hydrodynamic characterization of bubble-particle heterocoagulates showed an increase of the mean liquid velocity compared to unloaded bubbles. A relation to the particle size has, however, not been found.

To investigate the industrial fluorite flotation system with respect to  $w(\text{CaF}_2)$  in the concentrate, a novel quantification method via Fourier Transform (FT) Raman spectroscopy has been developed and cross-validated. This method was then applied in the design of experiment. The optimum process parameters for maximisation of  $R_{\max}$ ,  $k$ , and  $w(\text{CaF}_2)$  have successfully been determined and correlated to further process characteristics, e.g. Zeta potential. It has been found that the pH value should be slightly alkaline, while both collector concentration and stirrer speed should be high. The volumetric gas flow rate has been found to be insignificant in the investigated parameter range.

Lastly, the applicability of the fluorescent fluorite in optical investigations has been proven. A distinction between the fluorescence and reflections at the silicon dioxide surface has been presented under static conditions. Furthermore, first single bubble-particle heterocoagulates have been shown with fluorescent fluorite particles attached to the bubble surface. Thus, further optical investigations are promising.

---

## Table of contents

<b>1</b>	<b>Introduction .....</b>	<b>1</b>
1.1	Motivation .....	1
1.2	Objective and concept .....	2
<b>2</b>	<b>Theoretical background.....</b>	<b>4</b>
2.1	Flotation.....	4
2.1.1	History of flotation .....	4
2.1.2	Flotation mechanism .....	5
2.1.2.1	Flotation process .....	5
2.1.2.2	Flotation agents .....	8
2.1.3	Flotation modelling .....	9
2.1.3.1	Flotation kinetics .....	9
2.1.3.2	Heterocoagulate formation.....	16
2.1.3.2.1	Collision process.....	16
2.1.3.2.2	Attachment process.....	17
2.1.3.2.3	Stability of bubble-particle heterocoagulates .....	19
2.1.4	Fluorite flotation.....	20
2.1.4.1	Fluorite properties .....	20
2.1.4.2	Flotation process for fluorite .....	21
2.2	Surface and interface characteristics .....	23
2.2.1	Contact angle .....	23
2.2.1.1	Contact angle measurements on flat surfaces .....	24
2.2.1.2	Contact angle measurements on particulate systems .....	25
2.2.2	Adsorption of surfactants at the gas-liquid interface.....	27
2.2.2.1	Theoretical aspects of adsorption at the gas-liquid interface .....	27
2.2.2.2	Measurement of surface tension.....	29
2.3	Bubbles .....	31
2.3.1	Characteristics of bubbles in water .....	31
2.3.1.1	Periodic bubble formation.....	31

---

2.3.1.2	Shapes of bubbles in motion.....	32
2.3.1.3	Terminal velocity of bubbles.....	36
2.3.1.4	Motion of and flow around single bubbles.....	37
2.3.2	Influence of surfactants on rising bubbles.....	38
2.3.3	Bubble sizing methods.....	40
2.3.3.1	Overview.....	40
2.3.3.2	Shadowgraphy.....	41
2.4	Fluid mechanics.....	43
2.4.1	Particle Image Velocimetry.....	43
2.4.2	Particle Tracking Velocimetry.....	46
2.5	Surface modification of glass.....	47
<b>3</b>	<b>Materials and methods.....</b>	<b>49</b>
3.1	Experimental setups.....	49
3.1.1	Single bubble apparatuses.....	49
3.1.1.1	Single bubble flotation column.....	49
3.1.1.1.1	Dispersion cell.....	51
3.1.1.1.2	Deflection cell.....	51
3.1.1.1.3	Calming cell.....	52
3.1.1.1.4	Observation cells.....	52
3.1.1.1.5	Solids deposition cell.....	53
3.1.1.2	Alternative experimental setup for simplified measurements.....	54
3.1.2	Bubble swarm investigations.....	55
3.2	Analysis methods.....	56
3.2.1	Automatic image analysis for Shadowgraphy measurements.....	56
3.2.1.1	Analysing procedure for single bubbles.....	56
3.2.1.2	Image analysis validation.....	59
3.2.2	Analysis procedure for Particle Image Velocimetry image sequences.....	63
3.2.3	Fourier Transform Raman spectroscopy.....	67
3.2.3.1	Methodology.....	67

---

3.2.3.2	Method validation .....	70
<b>4</b>	<b>Investigations in two-phase systems.....</b>	<b>72</b>
4.1	Experiments in deionized water .....	72
4.1.1	Feasibility test.....	72
4.1.2	Influence of gas flow rate on induced liquid velocity .....	75
4.2	Experiments in surfactant solutions .....	79
4.2.1	Experimental procedure .....	79
4.2.2	Results and discussion.....	80
4.2.2.1	Surface tension measurements .....	80
4.2.2.2	Bubble characteristics .....	81
4.2.2.3	Hydrodynamic characterisation.....	88
<b>5</b>	<b>Investigation of a model three-phase system.....</b>	<b>101</b>
5.1	Surface modification of glass .....	101
5.1.1	Modification of glass slides.....	101
5.1.2	Modification of glass beads.....	104
5.2	Establishment of a collector-frother system.....	108
5.2.1	Preliminary tests .....	108
5.2.2	Optimisation of the collector-frother system.....	110
5.3	Single bubble flotation experiments.....	113
5.3.1	Determination of flotation kinetics and maximum recovery.....	113
5.3.1.1	Experimental procedure .....	113
5.3.1.1.1	Preparation of the apparatus .....	113
5.3.1.1.2	Flotation experiments .....	115
5.3.1.2	Flotation results .....	118
5.3.1.3	Influence of initial solids concentration in the flotation pulp .....	124
5.3.2	Optical investigations .....	127
5.3.2.1	Bubble-particle interaction during the bubble formation process.....	127
5.3.2.2	Shadowgraphy measurements of rising single bubble heterocoagulates ..	129
5.3.2.3	Hydrodynamic characterisation of rising heterocoagulates .....	132

---

5.3.2.3.1	Experimental procedure .....	132
5.3.2.3.2	Results .....	133
<b>6</b>	<b>Flotation experiments with fluorite minerals .....</b>	<b>137</b>
6.1	Industrial fluorite mineral from Clara mine.....	137
6.1.1	Experimental procedure .....	137
6.1.2	Results and discussion .....	139
6.1.2.1	Analysis of flotation kinetics .....	139
6.1.2.2	Statistical analysis of the design of experiment.....	143
6.1.2.3	Optical investigations .....	154
6.2	Fluorescent mineral.....	157
<b>7</b>	<b>Summary and outlook .....</b>	<b>160</b>
7.1	Main results from the two-phase system investigations .....	160
7.2	Main results from the three-phase system investigations .....	161
7.3	Outlook .....	164
<b>8</b>	<b>References .....</b>	<b>166</b>
<b>9</b>	<b>Appendix .....</b>	<b>191</b>
9.1	Supporting information.....	191
9.1.1	Materials, chemicals, and software.....	191
9.1.2	Supporting information for two-phase investigations.....	195
9.1.3	Supporting information for single bubble flotation experiments.....	199
9.1.3.1	Liquid surface tension of ethanol-water solutions.....	199
9.1.3.2	Calculation of the circulating pump frequencies .....	199
9.1.4	Supporting information for fluorescent fluorite mineral .....	201
9.2	List of publications .....	202
9.3	Curriculum Vitae .....	204

## List of abbreviations

### Mathematical variables

Symbol	Meaning	SI unit
a	Activity	1
A	Area, magnitude	m <sup>2</sup> , 1
a <sup>(n)</sup>	Coefficient in Eq. (3-13)	1
$\hat{A}$	Amplitude in Eq. (4-5)	m
c	Concentration	mol m <sup>-3</sup>
C	Constant defining a mean level in Eq. (4-5)	m
c <sub>B</sub>	Bubble concentration	kg L <sup>-1</sup>
c <sub>D</sub>	Drag coefficient	1
c <sub>p</sub>	Particle mass concentration	kg L <sup>-1</sup>
C(x,y)	Centroid	(1,1)
d <sub>32</sub>	Sauter diameter	m
d <sub>50,3*</sub>	Median particle diameter	m
d <sub>B</sub>	Bubble diameter	m
d <sub>p</sub>	Particle diameter	m
d <sub>R</sub>	Stirrer diameter	m
f	Frequency	s <sup>-1</sup>
f <sub>e</sub>	Elongation	1
f*	Correction factor in Eq. (2-40)	1
F	Force	kg m s <sup>-2</sup>
g	Acceleration due to gravity	m s <sup>-2</sup>
G	Free energy	kg m <sup>2</sup> s <sup>-2</sup>
k	Flotation rate constant	L <sup>n-1</sup> mol <sup>1-n</sup> s <sup>-1</sup>
k <sub>TKE</sub>	Proportionality constant to the TKE	m <sup>2</sup> s <sup>-2</sup>
k*	Area correction factor in Eq. (3-20)	1
l	Length	m
m	Mass, order of kinetics in Eq. (2-1)	kg, 1
n	Stirrer speed, amount of substance, order of kinetics in Eq. (2-1)	s <sup>-1</sup> , mol, 1
N	Number	1
N <sub>A</sub>	Avogadro's number	mol <sup>-1</sup>
p	Exponent of Gamma distribution in Eq. (2-15)	1

Symbol	Meaning	SI unit
P	Probability	1
q <sub>0</sub>	Frequency distribution	1
Q <sub>3</sub> *	Cumulative weight distribution	1
$\bar{r}$	Average diameter	m
R	Recovery, universal gas constant	1, kg m <sup>2</sup> s <sup>-2</sup> mol <sup>-1</sup> K <sup>-1</sup>
s	Saturation	1
t	Time	s
T	Absolute temperature	K
t <sub>i</sub>	Induction time	s
t <sub>R</sub>	Reaction time	s
$\dot{V}$	Volumetric liquid flow rate	m <sup>3</sup> s <sup>-1</sup>
$\dot{V}_g$	Volumetric gas flow rate	m <sup>3</sup> s <sup>-1</sup>
w	Liquid velocity, weight fraction	m s <sup>-1</sup> , 1
w <sub>B</sub>	Bubble rising velocity	m s <sup>-1</sup>
w <sub>dl</sub>	Detection limit	1
w <sub>il</sub>	Identification limit	1
w <sub>ql</sub>	Quantification limit	1
w <sub>s</sub>	Settling velocity	m s <sup>-1</sup>
$\bar{w}$	Mean liquid velocity	m s <sup>-1</sup>
$\bar{w}^*$	Mean liquid flow velocity around rising bubbles	m s <sup>-1</sup>
x	Horizontal direction	1
y	Vertical direction	1
z	Out-of-plane direction	1

**Greek symbols**

Symbol	Meaning	SI unit
$\alpha$	Significance level	1
$\gamma$	Activity coefficient	1
$\bar{\gamma}_c$	Critical surface tension of wettability of particles	$\text{kg s}^{-2}$
$\Gamma$	Surface excess concentration	$\text{mol m}^{-2}$
$\varepsilon$	Local energy dissipation	$\text{m}^2 \text{s}^{-3}$
$\eta$	Dynamic viscosity	$\text{kg m}^{-1} \text{s}^{-1}$
$\theta$	Contact angle	$^\circ$
$\kappa$	Electrolytic conductivity	$\text{S m}^{-1}$
$\lambda$	Wave length	m
$\mu$	Chemical potential	$\text{kg m}^2 \text{s}^{-2} \text{mol}^{-1}$
$\nu$	Kinematic viscosity	$\text{m}^2 \text{s}^{-1}$
$\tilde{\nu}$	Raman shift	$\text{m}^{-1}$
$\rho$	Density	$\text{kg m}^{-3}$
$\sigma$	Surface tension of flat surfaces	$\text{kg s}^{-2}$
$\varphi$	Fraction of slow floating particles in Eq. (2-16), POD eigenfunctions in Eq. (3-13)	1, 1
$\phi$	Phase in Eq. (4-5)	1
$\omega$	(Oscillation) Frequency	$\text{s}^{-1}$
$\omega_z$	Vorticity, rotation around the out-of-plane z axis	$\text{s}^{-1}$

**Indices**

Index	Meaning	Index	Meaning
0	Initial	l	Liquid
$\infty$	Infinite	m	Monolayer
a	Attachment	max	Maximum
b	Buoyancy	r	Resistance
c	Collision, critical, capillary	s	Slow, stability, solid
f	Fast, floatability, formation	wav	Weighted average
g	Gaseous	$\eta$	Drag
i	Inertia	$\sigma$	Surface tension

**Dimensionless numbers**


---

Particle Archimedes number	$Ar_p = \frac{g \cdot (\rho_p - \rho_l)}{v^2 \cdot \rho_l} \cdot d_p^3$
Bubble Eötvös number (Bond number)	$Eo_B = Bo = \frac{We_B}{Fr_B} = \frac{g \cdot \Delta \rho \cdot d_B^2}{\sigma}$
Bubble Froude number	$Fr_B = \frac{w_B^2}{g \cdot d_B}$
Modified Bubble Froude number	$Fr_B^* = \frac{w_B^2}{g \cdot d_B} \cdot \frac{\rho_l}{\Delta \rho}$
Stirrer Froude number	$Fr_R = \frac{n^2 \cdot d_R}{g}$
Morton number	$M = \frac{We^3}{Re^4 \cdot Fr} = \frac{g \cdot \eta_l^4 \cdot \Delta \rho}{\rho_l^2 \cdot \sigma^3}$
Power number	$Ne = \frac{P}{n^3 \cdot d_R^5 \cdot \rho_l}$
Air flow number	$Q = \frac{\dot{V}_g}{n \cdot d_R^3}$
Bubble Reynolds number	$Re_B = \frac{d_B \cdot w_B \cdot \rho_l}{\eta_l}$
Capillary Reynolds number	$Re_c = \frac{4 \cdot \dot{V}_g \cdot \rho_g}{\pi \cdot \eta_g \cdot d_c}$
Particle Reynolds number	$Re_p = \frac{d_p \cdot w_s \cdot \rho_l}{\eta_l}$
Stirrer Reynolds number	$Re_R = \frac{n \cdot d_R^2}{\nu_l}$
Bubble Strouhal number	$Sr_B = \frac{d_B \cdot \omega}{w_B}$
Stokes number	$St = \frac{\rho_p \cdot d_p^2 \cdot w}{18 \cdot \eta_l \cdot d_{\text{vortex}}}$
Bubble Weber number	$We_B = \frac{w_B^2 \cdot d_B \cdot \rho_l}{\sigma}$
Capillary Weber number	$We_c = \frac{16 \cdot \rho_g \cdot \dot{V}_g^2}{\pi^2 \cdot d_c^3 \cdot \sigma}$

---

**Abbreviations of used compounds**

BaSO <sub>4</sub>	Barium sulphate, barite
CaF <sub>2</sub>	Calcium fluoride, fluorite, fluorspar
CaO	Calcium oxide
DS	n-Dodecyltriethoxysilane
DW	Deionized water
ES	Ethyltriethoxysilane
EtOH	Ethanol
F <sub>2</sub>	Fluorine
FS	1H,1H,2H,2H-Perfluorooctyltriethoxysilane
H <sub>2</sub> O <sub>2</sub>	Hydrogen peroxide
H <sub>2</sub> SO <sub>4</sub>	Sulphuric acid
HDA	Hexadecylamine
HF	Hydrofluoric acid
MgO	Magnesium oxide
MIBC	Methyl isobutyl carbinol
Na <sub>2</sub> O	Sodium oxide
NaOl	Sodium oleate
OH <sup>-</sup>	Hydroxide ion
OA	Oleic acid
OS	n-Octyltriethoxysilane
PEEK	Polyether ether ketone
PMMA	Poly(methyl methacrylate), Plexiglas <sup>®</sup>
SiO <sub>2</sub>	Silicon dioxide, glass, quartz

**Further used abbreviations**

BTV	Bubble Tracking Velocimetry
CCC	Critical coalescence concentration
CMC	Critical micelle concentration
CME	Concentration at minimum elongation
CMV	Concentration at minimum velocity
DoE	Design of experiment
FFT	Fast Fourier Transform
fps	Frames per second, camera frame rate
FT	Fourier Transform
IEP	Isoelectric point
KNIME	Konstanz Information Miner
LED	Light-emitting diode
MIP	Maximum intensity projection
P&ID	Piping and instrumentation diagram
PIV	Particle Image Velocimetry
POD	Proper Orthogonal Decomposition
PSD	Particle size distribution
PTV	Particle Tracking Velocimetry
RGB	Colour model based on the colours red, green, and blue
RMS	Root-mean-square
SEM	Scanning electron microscopy
SH	Shadowgraphy
TKE	Turbulent kinetic energy
UV	Ultraviolet
VBA	Visual Basic Application
XRF	X-ray fluorescence spectroscopy

# 1 Introduction

The motivation, objective, and concept of the present work are presented in this chapter.

## 1.1 Motivation

The flotation process is one of the most important processes for mineral concentration and recovery operations. Currently, about two billion tonnes of crude ore per year are floated ([1], p. 34). The flotation process is already well-established and has its origins back in 1860, where Haynes investigated the bulk-oil process via flotation ([2], p. xii; [3], p. 6).

The flotation process has been already investigated in several works. Nevertheless, the process has not been fully understood yet, which is due to the poor modelling of metallurgical processes in general, since these cannot be derived completely from first principles [4]. A lot of publications dealing with flotation can be found in literature, but most of these deal with empirical optimisation of the flotation parameters regarding the used chemicals or the hydrodynamics. The goal is often to maximise the separation efficiency with respect to economics. This is mainly achieved with an empirical approach.

In the last two decades, optical methods for the analysis of dynamic processes in single- and multi-phase systems have been developed. These include the Particle Image Velocimetry (PIV), the Particle Tracking Velocimetry (PTV), and the Shadowgraphy (SH). Surprisingly, the number of publications in which flotation processes are investigated with these modern optical methods is low. Reasons for this may be the fact that flotation flows are difficult to penetrate by light and that complex three-phase flows are present. However, since the flotation process is decisively influenced by dynamic processes, the investigation by optical methods is an attractive research area to the understanding of the basic operation.

An interesting substance system for visualisation of the mentioned dynamic processes is the flotation of fluorite, also called fluorspar ( $\text{CaF}_2$ ). Fluorite is up to now the only naturally occurring fluorine containing mineral and therefore of great economic importance. A supply risk of fluorite is, however, expected by the EU Raw Materials Initiative [5]. Thus, gaining a detailed understanding on the purification process and evaluation of optimisation strategies is of great interest.

Additionally, fluorite is in sense of optical investigations an interesting mineral system, as some naturally occurring fluorite minerals are fluorescent under ultraviolet (UV) radiation, due to rare earth element impurities, e.g. europium, in the crystal structure.

## 1.2 Objective and concept

The objective of this work is the investigation of complex multi-phase flows by application of optical methods, like PIV and SH, in the flotation process. General influence parameters on the process are to be investigated with respect to recoveries and kinetics. In addition, optical methods are applied to analyse and understand underlying mechanisms, which can be linked to the experimental results.

The flotation process is a complex multi-phase process with three phases present: solid particles, gaseous bubbles, and the surrounding liquid. The overall process is dominated by the interaction of the solid particles with bubbles under the formation of so-called heterocoagulates in presence of flotation agents, which manipulate the surface characteristics of the solids and bubbles. Typically, the bubble-particle interaction is divided into three micro processes [6–11]:

1. collision of a particle with a bubble,
2. attachment of a particle to a bubble,
3. and detachment of a particle from a bubble or stability of the formed heterocoagulate.

In a common flotation apparatus these micro processes take place in the same process area at high solid and high bubble concentrations in presence of turbulences induced by, e.g., an agitator. Thus, optical investigations under these conditions are infeasible. Therefore, the system is simplified by reduction of the solids and gas concentrations in order to facilitate an optical investigation.

For this purpose, a suitable apparatus for single bubble flotation experiments is designed in the first step. In this apparatus the described micro processes of collision and attachment of particles and bubbles are separated from the detachment micro process. Thus, an optical investigation of freely rising single bubble heterocoagulates is facilitated (chapter 3).

The flotation process is divided and reduced into sub-systems to simplify the investigations. Linking the results from each of the sub-systems gives then an understanding of the overall process. The concept and methodology of this work is presented in Fig. 1-1.

First experiments are conducted in the reduced two-phase system gas-liquid. In this system, optical investigations with respect to bubble characteristics as well as induced liquid hydrodynamics are carried out in absence and presence of surface active agents for single bubbles (chapter 4).

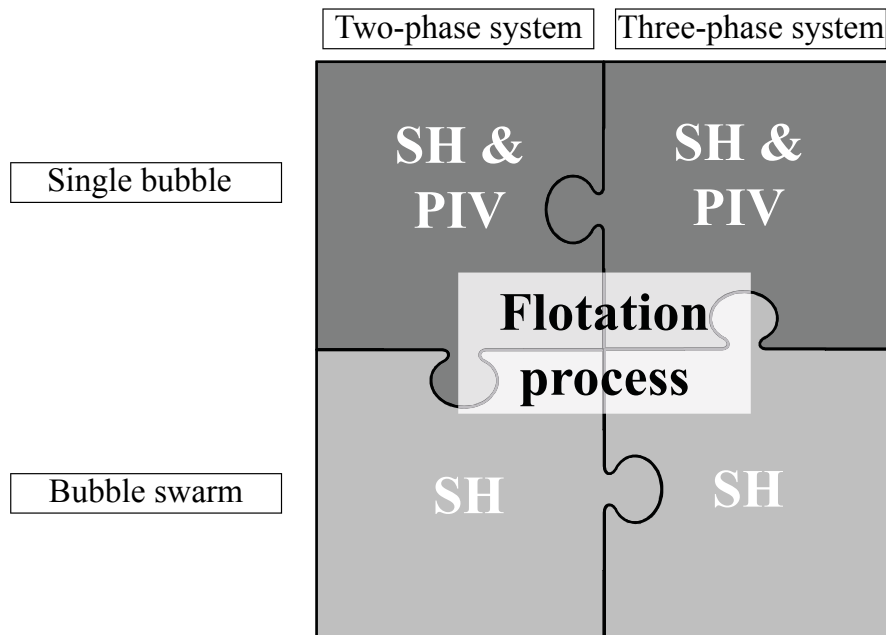


**Fig. 1-1.** Scheme of the methodology of the present work.

Various influence parameters on the flotation process are investigated using a model system consisting of glass particles. These influence parameters are the particle diameter, the gas flow rate, the flotation medium, the wettability of the particles, and the initial particle concentration. Single bubble flotation experiments are carried out in form of a design of experiments (DoE). The time-resolved determined recoveries of the particles are used to model the flotation kinetics. Optical measurements using SH and PIV are carried out to characterise the heterocoagulates formed at the varying experimental conditions (chapter 5).

Afterwards, a fluorite mineral system from an industrial production site is rigorously investigated. A DoE is used to analyse the influence of pH value, collector concentration, stirrer speed, and volumetric gas flow rate on the flotation process. The flotation kinetics are modelled for each experimental condition based on the determined recoveries. Furthermore, the grade of the product is analysed with a newly developed method via Fourier Transform (FT) Raman spectroscopy. Thus, the influence parameters are investigated not only with respect to total amount of product and rate of the process, but also with respect to the quality of the product. Finally, optical investigations with a fluorescent fluorite mineral are conducted to prove the feasibility of using optical methods in this system (chapter 6).

From these different experimental approaches, a summarising overview of different influence parameters in the two-phase as well as the three-phase system and their contribution to the flotation process is given in chapter 7.

## 2 Theoretical background

### 2.1 Flotation

Flotation is a separation process based on the different wettability of solids. Its advantages in contrast to other separation methods are its applicability to small particle sizes, it can be manipulated using chemical agents to make the separation selective for some solids over others, the purity of the froth product is higher than in other separation operations and the relative space (volume) efficiency of flotation cells is higher than, e.g., in gravity separators ([12], p. 248).

#### 2.1.1 History of flotation

Flotation is a well-established physicochemical separation process, which has a broad range of applications. With about two billion tonnes of floated crude ore per year it is one of the most important processes for mineral concentration and recovery operations ([1], p. 34). Further applications include removal of particles and bacteria in water and wastewater treatment, recovery of ink in paper recycling, and recovery of bitumen from oil sands ([12], p. 332; [13], p. 1). The origin of flotation is dated back to 1860 ([2], p. xi). The introduction of this technology has led to a significant increase in the world's natural mineral resources as billions of tonnes of rock became ore. Over the years, countless investigations, improvements, and contributions have been made to this topic. A short overview is given in Tab. 2-1.

**Tab. 2-1.** Important contributions to early flotation technology ([14], p. xii).

Year	Contributor	Contribution
1860	Haynes	Bulk-oil process
1877	Bessel	Boiling process for graphite
1885	Bessel	Chemical-generation gas process for graphite
1886	Everson	Acidulated pulps desirable
1902	Froment, Potter and Delprat	Gas as a buoyant medium for sulphide ores
1905	Schwarz	Sodium sulphide to recover oxidized base metal minerals
1906	Sulman, Pickard and Ballot	Reduced amount of oil; introduction of gas by violent agitation
1913	Bradford	Sulphur dioxide to depress sphalerite
1913	Bradford	Copper sulphate as activator for sphalerite
1921	Perkins and Sayre	Specific organic collectors
1921	-	Alkaline circuits
1922	Sheridan, Griswold	Cyanides to depress sphalerite and pyrite

Tab. 2-1. cont'd

1924	Sulman and Edser	Soaps for flotation of oxides
1925	Keller	Xanthates as collectors
1929	Gaudin	pH control
1929	Jeanprost	Flotation of highly soluble salines
1933	Nessler	Flotation separation of water-soluble chemical salt mixtures
1934	Chapman and Littleford	Agglomeration
1934	-	Alkyl sulphates as collectors
1935	-	Cationic collectors

### 2.1.2 Flotation mechanism

In the following chapters the underlying mechanisms of flotation regarding the macroscopic effects as well as process equipment and flotation agents are explained.

#### 2.1.2.1 Flotation process

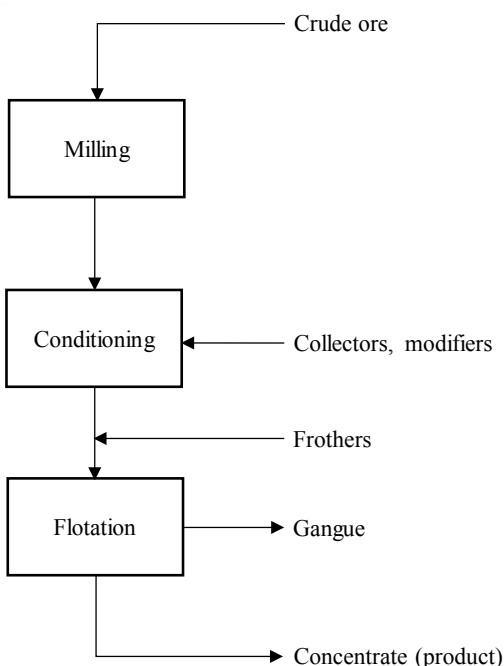
As stated in chapter 2.1, the underlying mechanism for the separation via flotation is the difference in the wettability of different materials. The aim of the process is to separate the desired particle classes (valuables) from unwanted particles classes (gangues). For this purpose, the mineral particles are suspended in an aqueous solution forming the so-called flotation pulp. Typically air is introduced into the flotation pulp in form of small bubbles with a diameter  $< 2$  mm ([15], p. 134). In the presence of turbulence due to, e.g., stirring of the suspension, the air bubbles will collide with the particles. Hydrophobic particles are able to attach to air bubbles, forming so-called heterocoagulates (cf. Fig. 2-1). The density of these heterocoagulates is lower than the density of the pulp so that the heterocoagulates will rise to the surface of the flotation cell. There they form a stable froth, which is skimmed to separate the hydrophobic particles from the hydrophilic particles, which are not floated.



Fig. 2-1. Forms of bubble-particle heterocoagulates ([16], p. 249).

Typically, the process is setup in a way that the valuable particles are obtained as the froth product, while the gangue particles are remaining in the pulp. In some systems, however, it may be the other way around, which is why these processes are called *reverse* flotation ([17], p. 266). Most of the naturally occurring mineral particles show a hydrophilic character. Therefore, flotation agents, which are called collectors, are added to the pulp in order to selectively make the valuable mineral particles hydrophobic. Additional flotation agents like frothers are used to stabilize the produced froth and, thus improve the overall process. The functionality of different flotation agents is explained in chapter 2.1.2.2.

The schematic procedure of the flotation process is shown in Fig. 2-2. In a first step, the crude ore is comminuted via milling. The approximate particle size in which a separation via flotation can be carried out ranges between 1  $\mu\text{m}$  and 0.5 mm ([18], p. 256). For flotation of metal ores, both laboratory testing and plant practice have identified approx. 200  $\mu\text{m}$  as an upper particle size limit ([3], p. 23). The comminution to small particle sizes ensures that the intergrown mineral particles are almost completely liberated. In a conditioning step, flotation agents such as collectors and modifiers (cf. chapter 2.1.2.2) are added. After the addition of frothers, the flotation process is started by introducing air in form of bubbles into the flotation pulp. Gangue particles, which are hydrophilic, remain as bottoms product in the pulp while the desired product is enriched in the froth. The product containing the valuable mineral particles is called concentrate. Typically, more than one flotation stage is operated in series, which is necessary in order to obtain a pure concentrate ([15], p. 132).



**Fig. 2-2.** Schematic overview of a flotation process (adapted from [19], p. 3).

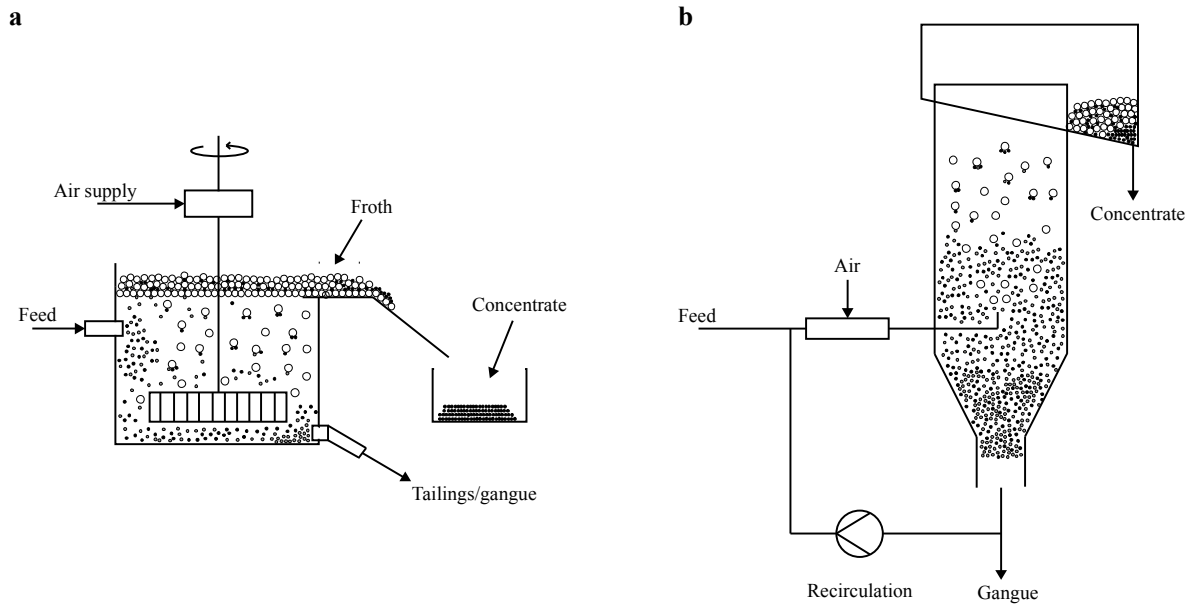


**Fig. 2-3.** Flotation machines: agitation-type flotation cell (a) and flotation column (b).

Flotation machines may be divided into two main classes:

- agitation-type flotation cells
- and flotation columns.

A schematic drawing of these types is given in Fig. 2-3. The main difference between both is the generation of turbulence. In agitation-type flotation cells, a stirrer is used for the suspension of particles. The air is introduced either at the tip of the stirrer via a hollow shaft or via a pipe at the bottom of the apparatus close to the agitator. The produced bubbles are directly comminuted due to the high shear rate at the stirrer tip. In contrast to this, the turbulence in a flotation column is induced by a pump. The air is introduced parallel to the feed and the air bubbles are comminuted due to shear at the pressure side of the pump.

Dimensionless numbers can be used to compare different processes with each other, as they incorporate geometrical changes from one system to the other. The magnitude of the main important dimensionless numbers in a flotation cell is shown in Tab. 2-2. The stated range of the stirrer Reynolds number  $Re_R$  indicates that flotation processes are typically operated in the fully turbulent region of flow ([20], p. 22).

**Tab. 2-2.** Magnitude of the main dimensionless numbers in a flotation cell ([3], p. 57).

Dimensionless number		Range
Power number	$Ne$	0.5-5
Stirrer Reynolds number	$Re_R$	$5 \cdot 10^4$ - $5 \cdot 10^6$
Air flow number	$Q$	0.001-5
Stirrer Froude number	$Fr_R$	0.1-5

### 2.1.2.2 Flotation agents

Only by using flotation agents a sorting via flotation and a selective process control is possible.

Flotation agents are typically divided into ([19], p. 36; [21], p. 1–3):

- collectors,
- frothers,
- and modifying agents / regulators.

The function of collectors is to form selectively a hydrophobic layer on a mineral surface in the flotation pulp. The attachment between bubbles and particles is therefore improved and, thus the recovery of these particles in the froth product is enhanced.

Frothers lower the surface tension of water and additionally adsorb on the bubble-water interface. They increase the film strength of the bubbles, which provides a better attachment of hydrophobic particles to the bubbles. In addition, frothers have a direct effect on the size and form of air bubbles. A strict classification into collectors and frothers is, however, not feasible, as collectors will always exhibit frothing properties and vice versa [22,23].

Modifying agents, also called regulators, can be subdivided into activators, depressants, and pH regulators. Regulators affect the selectivity of the collectors and, thus the overall flotation process. In the presence of regulators, collectors adsorb mainly on mineral particles targeted for recovery. If the regulator reacts directly with the mineral surface, e.g. copper sulphate as regulator with sphalerite as mineral surface, it is called activator. This facilitates an increased collector adsorption on the mineral surface, making the valuable minerals selectively hydrophobic. Regulators, which either reduce conditions for hydrophobisation of a particular mineral with the collector or make the mineral surface hydrophilic are called depressants. The aim of depressant addition to the flotation pulp is therefore to reduce the floatability of gangue material. To regulate the ionic composition of the flotation pulp pH regulators are used. They change the concentration of the protons in the pulp. On the one hand, pH regulators affect the electric charge of the particle surfaces, while they facilitate the ionisation of collector molecules on the other hand. Hence, an improvement of the interaction of the selected mineral with the collector is achieved. There is a certain pH range for each collector, where it is most effectively due to the appropriate electric charge ([12], p. 249). It should be noted that the classification of regulators is arbitrary, because the same regulator may act under different conditions as depressant or activator for example.

### 2.1.3 Flotation modelling

Possibilities to model the flotation process are presented in this chapter. On the one hand, kinetic equations, which rely on the determined recoveries, are introduced and on the other hand the modelling of the micro processes of flotation involving the heterocoagulate formation are presented.

#### 2.1.3.1 Flotation kinetics

The formulation of suitable rate models for the flotation process is not straightforward, as flotation systems are complex multiphase systems with many influence factors. Therefore, many different models have been presented in literature, which can be generally divided into three main classes ([3], p. 745): empirical, analytical, and analogous.

Empirical models are based on fitting a mathematical model to experimental data using the inputs and outputs as variables, e.g. ore and reagent concentration as input and recovery and tailings as output. These models are simple but not universal. Furthermore, they only offer little predictive capability outside the model boundaries.

Analytical models are developed on the basis of bubble-particle interactions as well as other sub-processes, which occur in flotation systems. These models are the most valuable ones, because of the detailed insight they give into the physics and chemistry of the process. However, their development is difficult due to many variables involved in the process as aforementioned. Analogous models are determined by the analogy with a similar process. Usually, this analogy is drawn from chemical kinetics ([3], p. 746; [24,25]). The chemical reaction kinetics are based on the collision theory, where collision of the reactants leads to formation of the product, if the relative kinetic energy of the molecules exceeds a threshold value known as activation energy ([26], p. 881). Similarly, the flotation process can be described as a “reaction” between solid particles and bubbles to form the product, which is called heterocoagulate ([3], p. 746). The rate of flotation will depend on a number of factors, e.g. concentration of particles and bubbles, frequency of collisions, efficiency of particle attachment, and stability of the formed heterocoagulate ([17], p. 297).

Equation (2-1) shows the general description of a batch-flotation process in analogy with chemical kinetics ([27], p. 704; [28]):

$$-\frac{dc_p}{dt} = k \cdot c_p^n \cdot c_B^m \quad (2-1)$$

In Eq. (2-1),  $c_p$  is the concentration of solid particles remaining in the flotation cell,  $t$  is the time,  $k$  is the flotation rate constant,  $c_B$  is the concentration of the bubbles in the flotation cell, and  $n$  and  $m$  are respective kinetic orders. If the aeration during the flotation is constant, the bubble

concentration can be assumed constant. Thus, Eq. (2-1) reduces to the general differential equation:

$$-\frac{dc_p}{dt} = k \cdot c_p^n \quad (2-2)$$

Equation (2-2) has first been used by García-Zuñiga in 1935 [29] to describe the flotation process as a rate process, which is why this equation is also referred to as “García-Zuñiga equation” ([30], p. 757; [31], p. 178; [32], p. 306).

For  $n=1$ , integration of Eq. (2-2) yields:

$$c_p(t) = c_{p,0} \cdot e^{-k \cdot t} \quad (2-3)$$

In Eq. (2-3),  $c_p(t)$  is the concentration of particles leaving the cell at a time  $t$  and  $c_{p,0}$  is the initial particle concentration at  $t=0$ . This equation predicts that after infinite time all particles have been floated. Thus, the concentration in the flotation cell after infinite time is zero:

$$\lim_{t \rightarrow \infty} c_p(t) = c_{p,0} \cdot \lim_{t \rightarrow \infty} e^{-k \cdot t} = 0 \quad (2-4)$$

In practice, however, some floatable particles may still remain unfloated in the flotation cell, even if the experiment is prolonged ([3], p. 747; [33]). Therefore, the concentration of the solid particles remaining in the flotation cell after infinite time  $c_{p,\infty}$  is taken into account in Eq. (2-2), leading to the following expression:

$$-\frac{dc_p}{dt} = k \cdot (c_p - c_{p,\infty})^n \quad (2-5)$$

In flotation processes, the recovery  $R$  is more commonly used as a measure instead of the concentration. The recovery  $R$  at a time  $t$  in terms of the flotation pulp is defined as:

$$R(t) = \frac{c_{p,0} - c_p(t)}{c_{p,0}} \quad (2-6)$$

If  $t$  is now prolonged to infinite time, the so-called ultimate recovery  $R_\infty$  is obtained:

$$\lim_{t \rightarrow \infty} R(t) \equiv R_\infty = \frac{c_{p,0} - \lim_{t \rightarrow \infty} c_p(t)}{c_{p,0}} = \frac{c_{p,0} - c_{p,\infty}}{c_{p,0}} \quad (2-7)$$

Substitution of  $c_{p,0}$  and  $c_{p,\infty}$  in Eq. (2-5) using Eqs. (2-6) and (2-7) yields:

$$\frac{dR}{dt} = k \cdot c_{p,0}^{n-1} \cdot [R_\infty - R(t)]^n \quad (2-8)$$

Equation (2-8) is the general expression for flotation kinetics in terms of the recovery. Solving this equation of specific values of  $n$  gives the expression for a specified flotation order. If for example  $n=0$ , the flotation kinetics follow 0<sup>th</sup> order. Integration of Eq. (2-8) gives:

$$R(t) = k \cdot c_{p,0}^{-1} \cdot t \quad (2-9)$$

A plot of  $R(t) \cdot c_{p,0}$  versus  $t$  leads to a straight line through the origin, if the data follows a 0<sup>th</sup> order. The flotation rate constant  $k$  is determined from the slope.

For the 1<sup>st</sup> order,  $n=1$  and integration of Eq. (2-8) yields:

$$R(t) = R_{\infty} \cdot (1 - e^{-kt}) \quad (2-10)$$

A plot of  $-\ln\left(1 - \frac{R(t)}{R_{\infty}}\right)$  versus  $t$  will result in a straight line through the origin, if the data follows first-order. The flotation rate constant  $k$  can then be obtained from the slope.

For second-order flotation kinetics ( $n=2$ ), integration of Eq. (2-8) gives:

$$R(t) = \frac{k \cdot c_{p,0} \cdot t \cdot R_{\infty}^2}{1 + k \cdot c_{p,0} \cdot t \cdot R_{\infty}} \quad (2-11)$$

Thus, if the data follows second-order kinetics, plotting  $\frac{R(t)}{c_{p,0} \cdot [R_{\infty}^2 - R_{\infty} \cdot R(t)]}$  against  $t$  yields a straight line through the origin with  $k$  as slope.

Exemplary plots of  $R(t)$  as a function of  $t$  for 0<sup>th</sup> order, 1<sup>st</sup> order, and 2<sup>nd</sup> order are presented in Fig. 2-4a. The corresponding graphs for the linearisation of the kinetic equations (2-9), (2-10), and (2-11) as stated above are shown in Fig. 2-4b. The 0<sup>th</sup> order graph exhibits a linear relationship between  $R(t)$  and  $t$ , while both 1<sup>st</sup> order and 2<sup>nd</sup> order graphs show a sharp increase in  $R(t)$  for small  $t$  with an asymptotic behaviour for large  $t$  (Fig. 2-4a). The convergence of 1<sup>st</sup> order and 2<sup>nd</sup> order is strongly dependent on the flotation rate constant  $k$ , so that 2<sup>nd</sup> order must not necessarily converge faster to  $R_{\infty}$  than 1<sup>st</sup> order. A discrimination between 1<sup>st</sup> order and 2<sup>nd</sup> order from an  $R(t)$  vs.  $t$  graph is therefore not trivial.

In the graphs of the linearised kinetic equations (Fig. 2-4b) the data will only follow a straight line, if the specified kinetic expression fits to the experimental data. Otherwise curvatures and deviations from a linear form will be observed.

There is, however, no necessary reason why the order of flotation kinetics has to be an integer. An analysis with respect to fractional order is feasible by linearisation of Eq. (2-8):

$$\ln\left(\frac{dR}{dt}\right) \approx \underbrace{\ln\left(\frac{\Delta R}{\Delta t}\right)}_y = \underbrace{n \cdot [\ln(c_{p,0}) + \ln\{R_{\infty} - R(t)\}]}_x + \underbrace{\ln(k) - \ln(c_{p,0})}_b \quad (2-12)$$

As only discrete data is available from experiments,  $\frac{dR}{dt}$  in Eq. (2-8) must be replaced by  $\frac{\Delta R}{\Delta t}$  in Eq. (2-12). The flotation kinetic order can be determined from the slope of the line given by a graph of  $\ln\left(\frac{\Delta R}{\Delta t}\right)$  against  $[\ln(c_{p,0}) + \ln(R_{\infty} - R(t))]$ . The value of the flotation rate constant  $k$  is determined from the intersection with the  $y$  axis.

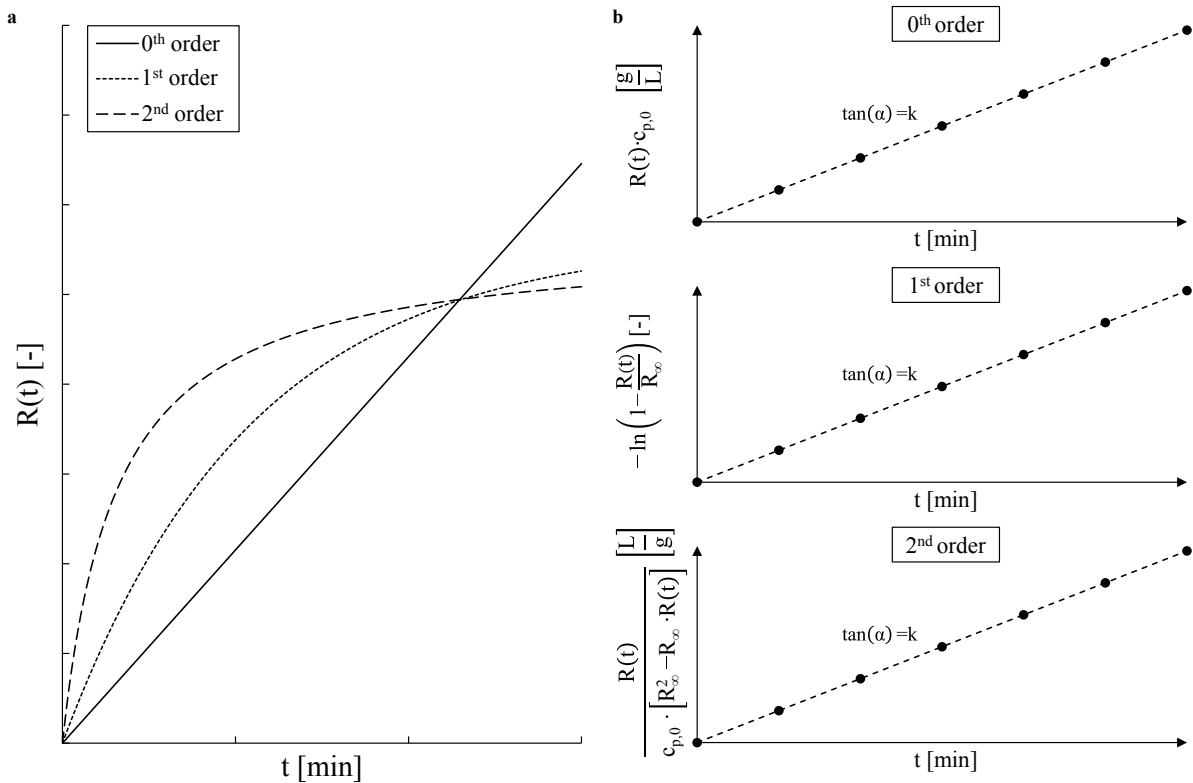


**Fig. 2-4.** Recovery  $R(t)$  as a function of time (a) and linearisation of kinetic equations (b) according to 0<sup>th</sup> order (a), 1<sup>st</sup> order (b), and 2<sup>nd</sup> order (c).

Determination of flotation kinetics is a controversial topic, as a variety of reports with differing results is present in literature [25,34]. In most applications,  $n$  in Eq. (2-8) is said to be 1 ([17], p. 297), which is why kinetic investigations published in literature mainly consider 1<sup>st</sup> order kinetics [35–39]. Nguyen and Schulze state that the order of flotation kinetics should be most frequently 1, less frequently 2 and seldom 3 or more. For flotation of single minerals or diluted pulps, the order should be 1<sup>st</sup> order, while it will be 2<sup>nd</sup> order for low grade ores or more concentrated pulps ([3], p. 749; [27], p. 710). However, Bogdanov et al. have reported orders varying from one to six [25]. Tomlinson and Fleming found the order of flotation kinetics to be in the range from zero to one, where 0<sup>th</sup> order was obtained for a high solids concentration in the flotation pulp and 1<sup>st</sup> order for small concentrations. They termed the 0<sup>th</sup> order kinetics as *inhibited flotation* and the 1<sup>st</sup> order kinetics *free flotation*. During an inhibited flotation, the bubbles rising through the pulp are fully loaded so that at no time free area is present on the bubble surface for attachment of additional particles. In contrast to this, bubbles are only sparsely covered with solid particles during the free flotation which is why there will always be enough free surface area for attachment of further particles [25,28,40]. According to, e.g., Tomlinson and Fleming, the flotation process of minerals starts with inhibited flotation (0<sup>th</sup> order). After some flotation time, a shift in the flotation kinetics towards free flotation (1<sup>st</sup> order) is observed [40]. In many cases, e.g. the flotation of lean grade sulphide ores of lead,

zinc or copper, the inhibited flotation persists only a few seconds. The overall flotation kinetics may still be determined to be of 1<sup>st</sup> order, depending on which operating mechanism and factors, which influence the order of flotation kinetics, are predominant during the flotation process. Some authors argue that the flotation rate constant  $k$  changes with time so that it will be a variable function [28]. The change of  $k$  with time is typically incorporated using a distribution model  $f(k)$ . Equation (2-8) is then rewritten to [33]:

$$\frac{dR}{dt} = f(k) \cdot c_{p,0}^{n-1} \cdot [R_{\infty} - R(t)]^n \quad (2-13)$$

There are a variety of distribution functions present in literature, e.g. gamma distribution [41] or rectangular distribution [42]. An example model incorporating a rectangular distribution of the flotation rate constant is the Klimpel model, which assumes first-order kinetics [43]:

$$R(t) = R_{\infty} \cdot \left[ 1 - \frac{1}{k \cdot t} \cdot (1 - e^{-k \cdot t}) \right] \quad (2-14)$$

A gamma distribution model based on first-order kinetics has been proposed by Loveday [44] as well as Inoue and Imaizumi ([27], p. 712):

$$R(t) = R_{\infty} \cdot \left[ 1 - \left( \frac{k}{k+t} \right)^p \right] \quad (2-15)$$

The parameter  $p$  is a dimensionless exponent, which influences the shape of the gamma distribution. An extended review of distribution models may be found in [33,36,45,46].

By grouping the flotation components into slow and fast floating fractions, Kelsall extended the classical first-order kinetic model [47]:

$$R(t) = \varphi \cdot (1 - e^{k_s \cdot t}) + (1 - \varphi) \cdot (1 - e^{-k_f \cdot t}) \quad (2-16)$$

In Eq. (2-16),  $\varphi$  is the fraction of slow floating particles and  $k_s$  and  $k_f$  are the flotation rate constants of the slow and fast floating fractions, respectively. The Kelsall model assumes an ultimate recovery of 100 % ( $R_{\infty}=1$ ), which is why this parameter is not included in the model. A modified version of the Kelsall model has been proposed by Jowett, adding the ultimate recovery as an influence parameter to increase the flexibility of the model [48]:

$$R(t) = R_{\infty} \cdot [\varphi \cdot (1 - e^{k_s \cdot t}) + (1 - \varphi) \cdot (1 - e^{-k_f \cdot t})] \quad (2-17)$$

Further classification in more than two floating fractions, e.g. three fractions categorized as slow, medium, and fast floating materials, have also been proposed in literature [48]. The general approach for dividing the components into fractions with different floatabilities can be summarized as [33]:

$$R(t) = R_{\infty} \cdot \sum_{i=1}^j [\varphi_i \cdot (1 - e^{-k_i \cdot t})] \quad (2-18)$$

**Tab. 2-3.** Overview of kinetic models investigated in the present work.

Model	Equation	
0 <sup>th</sup> order chemical analogous	$R(t)=k \cdot c_{p,0}^{-1} \cdot t$	(2-9)
1 <sup>st</sup> order chemical analogous	$R(t)=R_{\max} \cdot (1-e^{-k \cdot t})$	(2-10)
2 <sup>nd</sup> order chemical analogous	$R(t)=\frac{k \cdot c_{p,0} \cdot t \cdot R_{\max}^2}{1+k \cdot c_{p,0} \cdot t \cdot R_{\max}}$	(2-11)
Classical first-order model	$R(t)=R_{\infty} \cdot (1-e^{-k \cdot t})$	(2-10)
Klimpel model [43]	$R(t)=R_{\infty} \cdot \left[1 - \frac{1}{k \cdot t} \cdot (1-e^{-k \cdot t})\right]$	(2-14)
Kelsall model [47]	$R(t)=\varphi \cdot (1-e^{k_s \cdot t}) + (1-\varphi) \cdot (1-e^{-k_r \cdot t})$	(2-16)
Modified Kelsall model [48]	$R(t)=R_{\infty} \cdot [\varphi \cdot (1-e^{k_s \cdot t}) + (1-\varphi) \cdot (1-e^{-k_r \cdot t})]$	(2-17)
Gamma model	$R(t)=R_{\infty} \cdot \left[1 - \left(\frac{k}{k+t}\right)^p\right]$	(2-15)
Fully mixed model	$R(t)=R_{\infty} \cdot \left[1 - \left(\frac{1}{1+\frac{t}{k}}\right)\right]$	(2-19)

The subscript *i* in Eq. (2-18) describes the floatability fraction for each respective rate constant and *j* is the number of classified fractions.

A model analogous to the time-concentration relationship of a series of fully mixed reactors, assuming the number of reactors to be one, has also been found to give a good fit to experimental data ([27], p. 712; [33]; [46]):

$$R(t)=R_{\infty} \cdot \left[1 - \left(\frac{1}{1+\frac{t}{k}}\right)\right] \quad (2-19)$$

The described extensions to the classical chemical analogous kinetic models in Eqs. (2-13) to (2-19) provide more flexibility due to an increase in fitting parameters.

For the analysis of flotation kinetics in the present work, nine models are investigated. A summary of these models is given in Tab. 2-3. It should be noted that the first three models, which are referred to as chemical analogous models, use the experimentally observed maximum recovery  $R_{\max}$  instead of the ultimate recovery  $R_{\infty}$  as parameter. In addition to the models listed in Tab. 2-3, the fractional order model presented in Eq. (2-12) is applied whenever all other kinetic models are unable to describe the process accurately.

In general, the order of flotation kinetics *n*, the ultimate recovery  $R_{\infty}$  as well as the value of the flotation rate constant *k* are very sensitive towards a change in process parameters. The ultimate recovery  $R_{\infty}$  changes for example with chemical variables, e.g. the collector dosage, while *k* is reported to change with physical variables, e.g. gas flow rate. Therefore, the product  $k \cdot R_{\infty}$  is a

useful parameter to compare the influence of process parameters on the flotation kinetics ([3], p. 749; [49]). Furthermore, if  $R_{\infty}$  is plotted against  $k$ , so-called limits kinetic curves are obtained [50]. An exemplary graph is shown in Fig. 2-5. Four different regions may be arbitrarily classified in this diagram: slow-powerful, fast-powerful, slow-powerless, and fast-powerless. The flotation process will be optimal, if the observed data for  $k \cdot R_{\infty}$  is in the fast-powerful regime, because the flotation process would be fast and the recovery would be high. This type of diagram allows therefore a graphical comparison of different obtained experimental data sets, as long as the order of kinetics is equal for the data sets. Otherwise, the data cannot be compared, because the dimensions of the flotation rate constants are different.

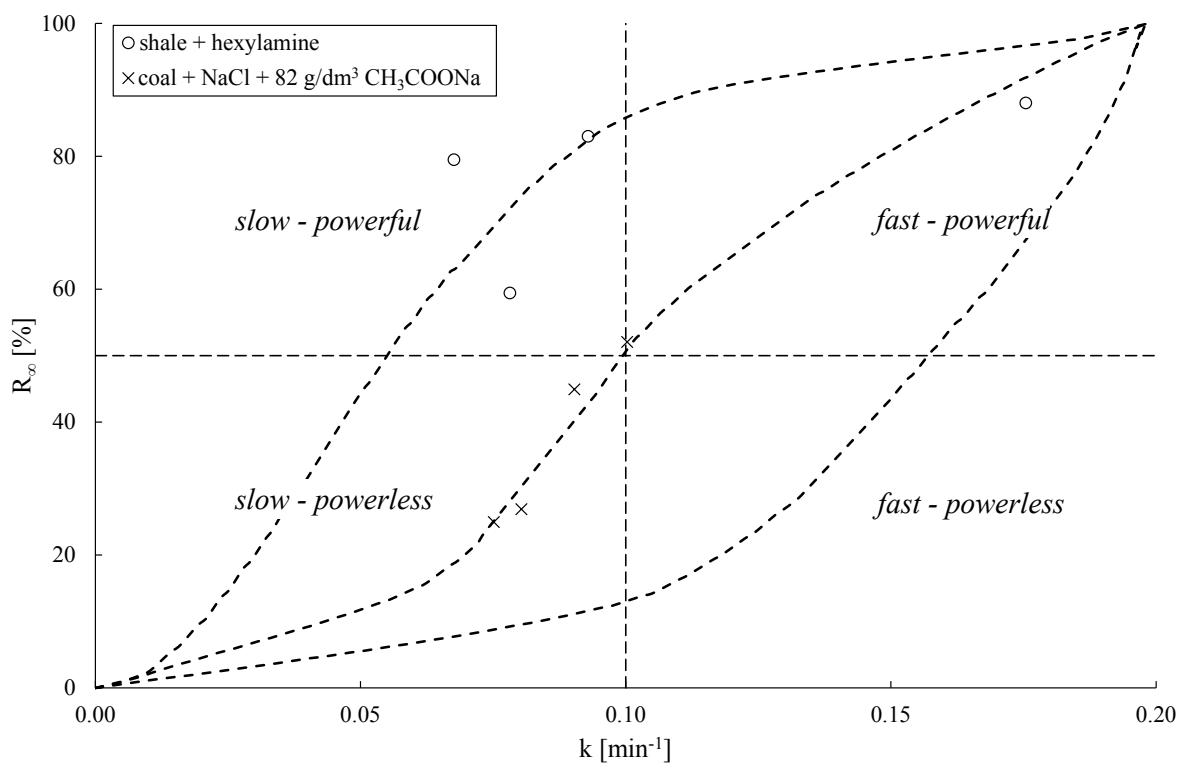


**Fig. 2-5.** Exemplary limits kinetic curve for a separation process of 1<sup>st</sup> order (adapted from [50]).

### 2.1.3.2 Heterocoagulate formation

The flotation process is based on the successful formation of bubble-particle heterocoagulates. As already stated in chapter 1.2, the process of heterocoagulate formation can be divided into three micro processes [6–11]:

1. bubble-particle collision,
2. bubble-particle attachment,
3. and bubble-particle heterocoagulate stability.

The stability of the formed bubble-particle heterocoagulate is more commonly used instead of the detachment process of particles from bubbles, which is the reverse process.

The overall flotation process in terms of particle floatability can be treated as a probability  $P_f$ , which is composed of the probabilities of each of these three micro processes ([16], p. 249):

$$P_f = P_c \cdot P_a \cdot P_s \quad (2-20)$$

In Eq. (2-20), the indices c, a, and s refer to the above stated micro processes of collision, attachment, and stability, respectively. Many experimental reports are presented in literature, where these micro processes have been investigated. The aim of these studies is always to establish equations for calculation of the probabilities of the micro processes.

#### 2.1.3.2.1 Collision process

The first step in heterocoagulate formation is the collision of bubbles with particles. The process is mainly determined by the flotation cell hydrodynamics. The collision probability  $P_c$  is generally improved with increasing turbulence in the pulp and using microsized bubbles [11].

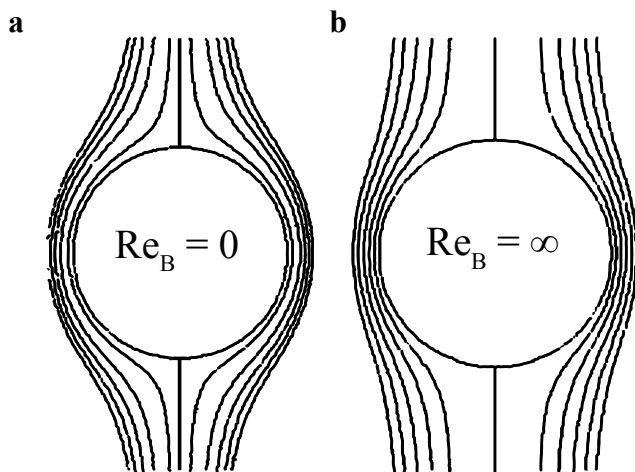


**Fig. 2-6.** Water streamlines around a bubble for Stokes flow with  $Re=0$  (a) and potential flow with  $Re=\infty$  (b) (adapted from [51], p. 360).

**Tab. 2-4.** Values for A and n of Equation (2-23) for different flow conditions [52,53].

Flow conditions	A	n
Stokes	1.5	2
Intermediate	$1.5 \cdot \left[ 1 + \frac{3/16 \cdot \text{Re}_B}{1 + 0.249 \cdot \text{Re}_B^{0.56}} \right]$	2
Potential	3	1

Sutherland was the first to derive an expression for the  $P_c$  from a stream function based on the particle diameter  $d_p$  and the bubble diameter  $d_B$  [54]:

$$P_c = 3 \cdot \frac{d_p}{d_B} \quad (2-21)$$

Equation (2-21) assumes potential flow (cf. Fig. 2-6b), which is why this equation is only valid for bubbles that are much larger than those used in flotation practice [52]. Using the stream function for the Stokes flow condition (cf. Fig. 2-6a), Gaudin derived the following equation for  $P_c$  [52]:

$$P_c = 1.5 \cdot \left( \frac{d_p}{d_B} \right)^2 \quad (2-22)$$

Equation (2-22) is, however, only applicable for small bubbles. Many more equations have been derived and presented in literature, e.g. by Weber [55] and Weber and Paddock [56]. A generalized form of all these models is given in Eq. (2-23) [52,57]:

$$P_c = A \cdot \left( \frac{d_p}{d_B} \right)^n \quad (2-23)$$

The factors A and n for different flow conditions are given in Tab. 2-4. Generally, Gaudin's model tends to underestimate  $P_c$ , while the Sutherland model overestimates  $P_c$  [53]. The probability of collision is therefore said to range between these two extrema. More detailed information on collision models are given, amongst others, in [58,59].

### 2.1.3.2.2 Attachment process

The attachment process is a stochastic process, which is mainly dependent upon the particle surface chemistry [60]. The attachment procedure is schematically depicted in Fig. 2-7. When a particle collides successfully with a bubble, it slides along the bubble surface due to the streamlines of the liquid around the bubble (cf. Fig. 2-6) and gravitational effects. The intervening liquid film between bubble and particle is thinning with time until a critical thickness  $h_{cr}$  is reached (see Fig. 2-7). Then, the liquid film ruptures so that a three-phase contact angle between solid particle, gaseous bubble, and surrounding liquid is formed.

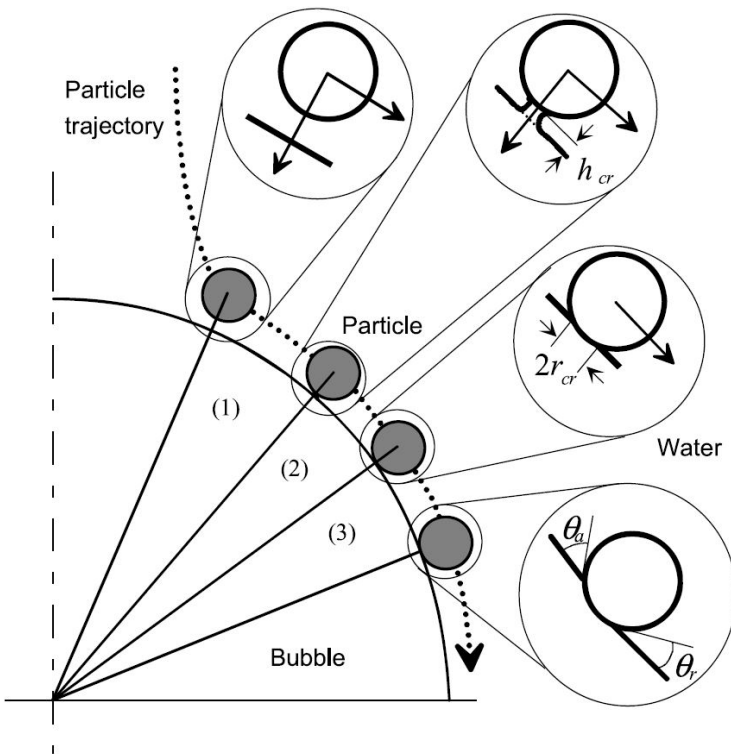


**Fig. 2-7.** Steps in bubble-particle attachment: thinning of the intervening liquid film to a critical thickness  $h_{cr}$  (1), rupture of the intervening liquid film and formation of the three-phase contact nucleus with radius  $r_{cr}$  (2), and spreading of the three-phase contact line with advancing and receding contact angle  $\theta_a$  and  $\theta_r$ , respectively (3) ([51], p. 365).

The minimum time, which is necessary for thinning and rupture of the liquid film between particle and bubble (cf. Fig. 2-7) and formation of a stable bubble-particle aggregate is defined as induction time  $t_i$  [11,61]. The induction time has to be determined experimentally as presented for example in [8,61–66]. An empirical model based on a variety of experimental investigations has been derived in order to calculate  $t_i$  [62,63,67]:

$$t_i = A \cdot d_p^B \quad (2-24)$$

In Eq. (2-24),  $A$  and  $B$  are variable parameters. The parameter  $B$  has found to be almost independent of particle contact angle, bubble size, and ionic strength. Typically,  $B$  is said to be 0.6 [62,68]. The parameter  $A$  is inversely proportional to the particle contact angle  $\theta$  [63,67]:

$$A = \frac{75}{\theta} \quad (2-25)$$

If the sliding time of the particle is lower than the induction time or if the contact angle  $\theta$  is zero, the particle will not be able to attach to the bubble surface (see also chapter 2.2.1). After successful attachment of the particle on the bubble surface, the particle is swept to the bubble rear due to the upwards directed motion of the bubble and gravitational effects.

For the attachment micro process, Yoon and Luttrell developed the following model to calculate the attachment probability  $P_a$  [52,57]:

$$P_a = \sin^2 \left[ 2 \cdot \tan^{-1} \cdot \exp \left( \frac{-(45 + 8 \cdot \text{Re}_B^{0.72} \cdot w_B \cdot t_i)}{15 \cdot d_B \cdot \left( \frac{d_B}{d_p} + 1 \right)} \right) \right] \quad (2-26)$$

In Eq. (2-26),  $\text{Re}_B$  is the bubble Reynolds number (cf. chapter 2.3.1.2) and  $w_B$  is the bubble rising velocity. Equations (2-24) to (2-26) show that  $P_a$  generally increases with increasing contact angle as well as decreasing particle size. Furthermore, smaller bubbles have a higher  $P_a$  compared to larger bubbles, if particle size and contact angle are constant.

### 2.1.3.2.3 Stability of bubble-particle heterocoagulates

The stability of the bubble-particle aggregates is mainly influenced by the particle surface characteristics and the hydrodynamics in the flotation cell [11]. Schulze proposed an equation for calculation of the probability of stability of a bubble-particle heterocoagulate  $P_s$  ([69], p. 495):

$$P_s = 1 - \exp \left[ 1 - \frac{1}{\text{Bo}^*} \right] \quad (2-27)$$

In Eq. (2-27),  $\text{Bo}^*$  is the modified Bond number defined as the ratio of detachment to attachment forces:

$$\text{Bo}^* = \frac{d_p^2 \cdot \left[ \Delta \rho \cdot g + 1.9 \cdot \rho_p \cdot \varepsilon^{2/3} \cdot \left( \frac{d_p}{2} + \frac{d_B}{2} \right)^{-1/3} \right] + 1.5 \cdot d_p \cdot \left( \frac{4 \cdot \sigma}{d_B} - d_B \cdot \rho_l \cdot g \right) \cdot \sin^2 \left( \pi - \frac{\theta}{2} \right)}{\left| 6 \cdot \sigma \cdot \sin \left( \pi - \frac{\theta}{2} \right) \cdot \sin \left( \pi + \frac{\theta}{2} \right) \right|} \quad (2-28)$$

In Eq. (2-28),  $\varepsilon$  is the local energy dissipation in a given volume of the apparatus,  $\sigma$  is the surface tension of the liquid, and  $\Delta \rho$  is the density difference between particle and fluid. Further models for calculation of the probability of stability or inversely the probability of detachment are presented in literature [70–72].

## 2.1.4 Fluorite flotation

In this chapter, an overview of the properties of fluorite minerals is given and a literature review on the flotation process of fluorite minerals is presented.

### 2.1.4.1 Fluorite properties

Fluorite, also referred to as fluorspar, is until today the only fluorine-containing raw material to be used as a starting material for the production of hydrofluoric acid (HF), an important basic chemical ([18], p. 406). HF is further used for the production of fluorine (F<sub>2</sub>), which is used for, e.g. the production of inorganic and organic fluorine compounds. Other uses of CaF<sub>2</sub> involve the iron- and steelmaking industry, where it is used as a flux to lower the melting point and to increase the fluidity of the slag, the aluminium production, and the production of opaque glass, enamels or high-quality optics for high energy laser systems ([18], p. 408–409; [73]; [74], p. 104). Since 2008, fluorite has been one of the most critical raw materials and, since 2014, it is one of the 20 most critical materials indexed in the EU Raw Materials Initiative [5]. Amongst other raw materials like silicon metal, cobalt or natural graphite, fluorite is of great economic importance, while a supply risk is expected (cf. Fig. 2-8).

Fluorite exhibits a variety of colours like purple, lilac, golden-yellow or green. It is a relatively soft mineral with a hardness of four on Mohs scale of mineral hardness. Its specific gravity is normally between 3175 and 3184 kg/cm<sup>3</sup> with a melting point of 1360 °C ([18], p. 406; [73]).

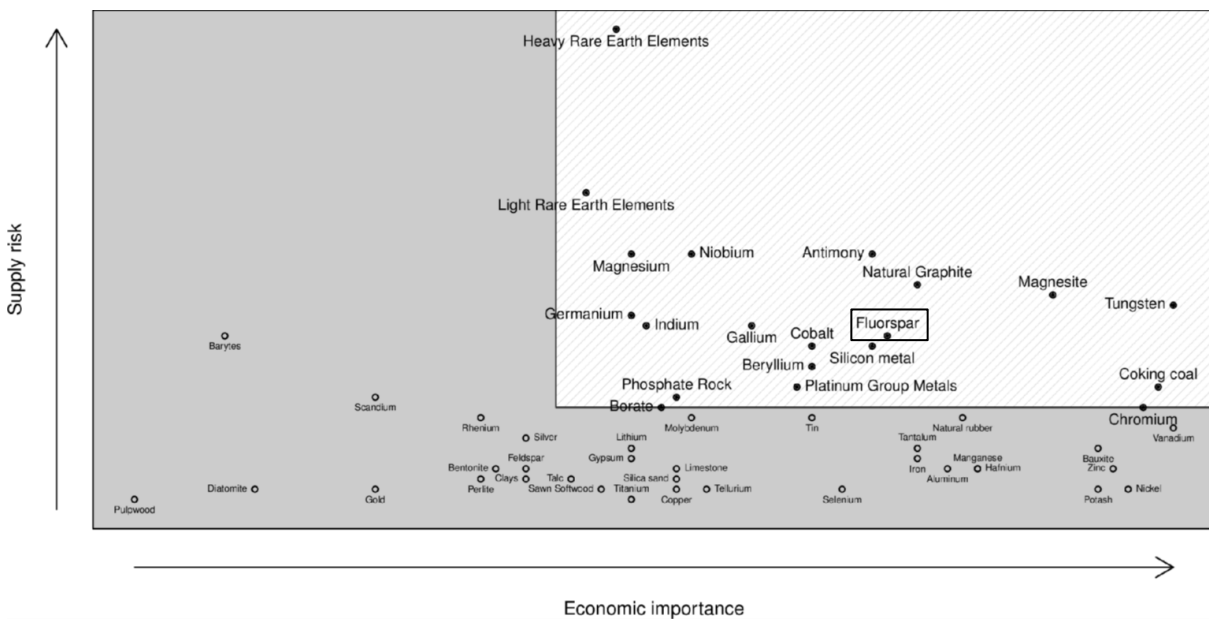


**Fig. 2-8.** Critical raw materials based on the European commission [5]. Top right rectangle marks area of identified critical materials in the initiative. Position of fluorspar is marked with a smaller rectangle for better visibility.

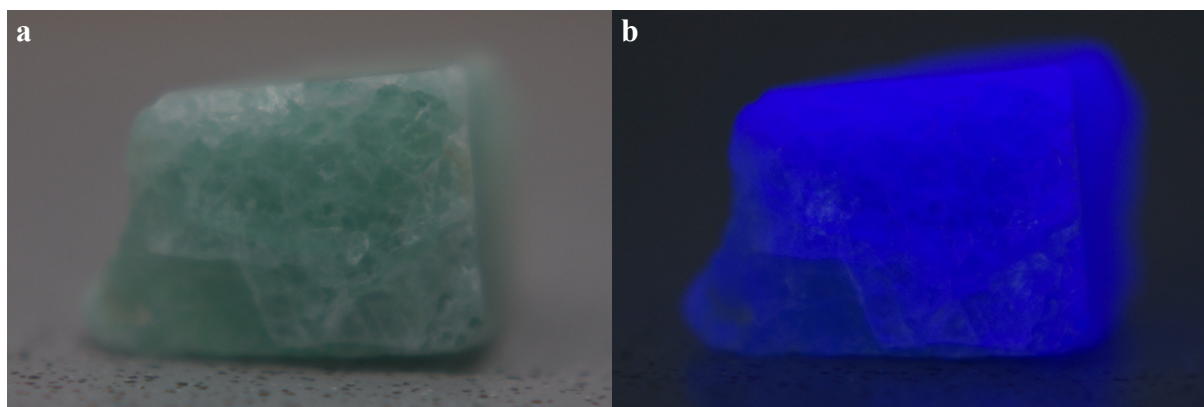


**Fig. 2-9.** Green fluorite mineral at daylight (a) and fluorescence of the mineral under UV radiation at a wavelength of 365 nm (b).

Some of the naturally occurring fluorite minerals are fluorescent under UV radiation. This is mainly influenced by impurities of rare earth elements inside the crystal structure. Europium impurities inside the calcium fluoride crystal structure for example are known to have a blue response under long wave UV radiation ([75], p. 106; [76]), which can be seen in Fig. 2-9b.

Commercially extracted fluorite contains typically 30-80 % calcium fluoride, with gangue materials attached and intergrown with the mineral. Most commonly, quartz ( $\text{SiO}_2$ ) or barite ( $\text{BaSO}_4$ ) are found alongside fluorite. These gangue materials have to be separated from the fluorite mineral to increase the  $\text{CaF}_2$  purity ([18], p. 407; [73]; [74], p. 103–104). This is most commonly carried out via flotation.

The purity of fluorite is specified in three different grades: acid grade, metallurgical grade, and ceramic grade [73]. Acid grade classifies the purest fluorite product with a  $\text{CaF}_2$  content of at least 97 %. This fluorite product is used predominantly in the production of HF. Both metallurgical grade and ceramic grade require a minimum  $\text{CaF}_2$  of 80 %. In contrast to the ceramic grade, which allows a maximum  $\text{SiO}_2$  content of only 3 %, metallurgical grade allows 15 %  $\text{SiO}_2$  in the product.

#### **2.1.4.2 Flotation process for fluorite**

Fluorite is separated from its gangue particles by means of flotation. The flotation process of fluorite is a well-known process, which is described extensively in literature. Generally, 5-10 mechanical cells per bank are used in the process, meaning five to ten flotation cells in series ([77], p. 1209).

As stated in chapter 2.1.4.1, fluorite occurs in nature with intergrowths of other minerals like quartz and barite. For a selective enrichment of fluorite in the flotation froth, collector agents based on fatty acids, e.g. oleic acid or linoleic acid, are widely used ([78], p. 34). The amount

of used collector is dependent on the amount and species of gangue particles, but ranges from 0.25 to 1.2 kg per tonne feed material ([79]; [80], p. 315ff.; [81], p. 7ff.). A problem well-known in the use of fatty acids as collector in the fluorite flotation is the concurrent adsorption on both barite and fluorite [82]. Therefore, depressants are added, which improve the wettability of the gangue particles, in order to increase the selectivity of the process towards fluorite. A common depressant for barite is starch, while water glass is used to depress quartz. The amount of starch added to the flotation pulp varies from 0.14-0.5 kg/t crude ore ([80], p. 315ff.). The pH value of the flotation pulp is adjusted alkaline using a sodium hydroxide solution. Usually, Flotol<sup>®</sup>, which is basically a mixture of  $\alpha$ -terpineol, is used for improved froth formation and stability ([80], p. 315ff.).

Elevated temperatures near the boiling point of water at approx. 75-85 °C caused by bubbling steam into the flotation apparatus has been found to improve the enrichment of fluorite in the separation from silica and calcite ([78], p. 34). Brunner investigated the influence of foreign ions on the flotation process of fluoite. He showed that the flotation works best in deionized water and that foreign ions hinder the flotation significantly ([83], p. 62). This was also presented by Hiçyılmaz and Ghaemi on the 6<sup>th</sup> international symposium for mineral processing [84]. For the analysis of the concentrate and the gangue regarding the fluorine content, different methods are feasible, for example potentiometric method after distillation [85], complexometric titration [86] or X-ray fluorescence spectroscopy (XRF) [87,88].

## 2.2 Surface and interface characteristics

Surface and interface characteristics play an important part in the flotation process, as has been described in chapter 2.1. In the following, the theoretical background on surfaces and interfaces is presented regarding the general definition of the contact angle as well as experimental techniques for measurement of contact angles on both flat surfaces and particulate systems.

### 2.2.1 Contact angle

When a liquid is in contact with a solid surface, three surface tensions have to be considered (see Fig. 2-10):  $\sigma_{lg}$  as surface tension between liquid and gaseous phase,  $\sigma_{sg}$  as surface tension between solid and gaseous phase, and  $\sigma_{sl}$  as surface tension between solid and liquid phase. At equilibrium conditions the following equation, known as Young's equation, must be fulfilled ([26], p. 686; [89], p. 419):

$$\sigma_{lg} \cdot \cos(\theta) = \sigma_{sg} - \sigma_{sl} \quad (2-29)$$

In Eq. (2-29),  $\theta$  is defined as contact angle. The hydrophobicity of a surface increases with increasing contact angle. A fully hydrophobic surface exhibits a contact angle of  $180^\circ$ , while a fully hydrophilic surface has a contact angle of  $0^\circ$ .

When a gas bubble attaches to a solid, the change in the free energy  $\Delta G$  per unit area is given by Dupre's equation ([90], p. 369ff.; [91]):

$$\Delta G = \sigma_{sg} - (\sigma_{sl} + \sigma_{lg}) \quad (2-30)$$

Combination of Eqs. (2-29) and (2-30) yields:

$$\Delta G = \sigma_{lg} \cdot [\cos(\theta) - 1] \quad (2-31)$$

The change in the free energy is therefore only dependent on the surface tension  $\sigma_{lg}$  and the contact angle  $\theta$ . Equation (2-31) is known as criteria for the possibility of a bubble-particle attachment in liquid [11]. Attachment can only occur for  $\Delta G < 0$ , thus  $\theta > 0^\circ$ .

Drelich and Marmur proposed the following classifications for flotation of particles in dependency of  $\theta$  [92]:

- $<10^\circ$  Not floatable particles
- $10-25^\circ$  Poorly floatable
- $25-50^\circ$  Low-rate floatable
- $50-70^\circ$  High-rate floatable
- $>70^\circ$  Spontaneously agglomerating and floating

They state, however, that this classification has to be studied in more depth with respect of different particle dimensions since the particle diameter and the surface landscape will have a significant influence on the flotation behaviour.

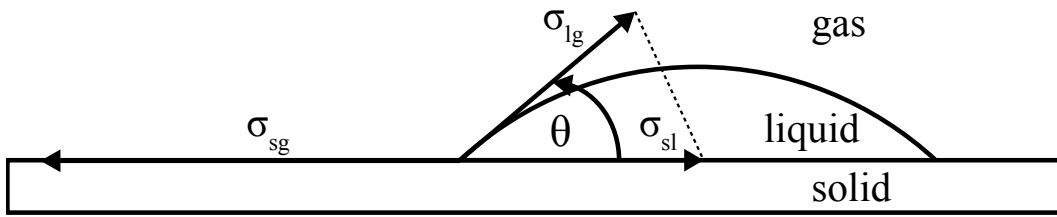


**Fig. 2-10.** Contact angle  $\theta$  and surface tensions  $\sigma$  between solid and gaseous phase (index sg), solid and liquid phase (index sl), and liquid and gaseous phase (index lg).

### 2.2.1.1 Contact angle measurements on flat surfaces

The contact angle on flat surfaces is usually measured with a telescope-goniometer. The method is referred to as sessile-drop technique, which was first mentioned by Bigelow et al. [93]. With this method the tangents left and right at the three-phase contact point of a liquid drop on the flat surface are measured (cf. Fig. 2-10). The setup consists of a horizontal plate for mounting the sample, a syringe to produce a liquid drop, a camera with a zoom lens and a backlight illumination. The syringe is usually motor-driven so that the liquid volume can be controlled precisely. The tangents at the three-phase contact points are determined semi-automatically by fitting a drop profile to the contour of the drop. This fit can either be a spherical or non-spherical. The spherical fit will result in equal contact angles left and right of the three-phase contact point due to axial symmetry, while the non-spherical fit may result in unequal contact angles, depending on the surface properties and drop deformation. Contact angles should be measured at multiple spots if the substrate is relatively large. The accuracy of this method is generally given with approximately  $\pm 2^\circ$  ([94], p. 32). One of the main limitations of this method is that contact angles below  $20^\circ$  cannot be measured accurately ([95], p. 8).

In order to compare the wettability of different solid surfaces with each other, Zisman proposed a method to determine the critical surface tension of wetting  $\sigma_c$  [96]. In this method, contact angle measurements are conducted on the surface using liquids with varying surface tensions. The cosines of the determined contact angles are then plotted against the corresponding liquid surface tensions. As a result, a linear relationship will be present. By extrapolation to  $\cos(90^\circ)=1$ , meaning a complete wetting of the surface, the critical surface tension of wetting  $\sigma_c$  is determined (cf. Fig. 2-11). A second method commonly used for determination of contact angles on flat surfaces is the so-called captive bubble method, which was introduced by Taggart et al. [97]. Instead of measuring a formed liquid drop above the solid substrate, the substrate is immersed in the testing liquid and an air bubble is produced beneath the substrate. The formed contact angle of the bubble can also be directly measured using the optical method described above. Further methods for contact angle measurement on flat surfaces are reported in literature, e.g., tilting plate method and Wilhelmy balance method [94,95,98].

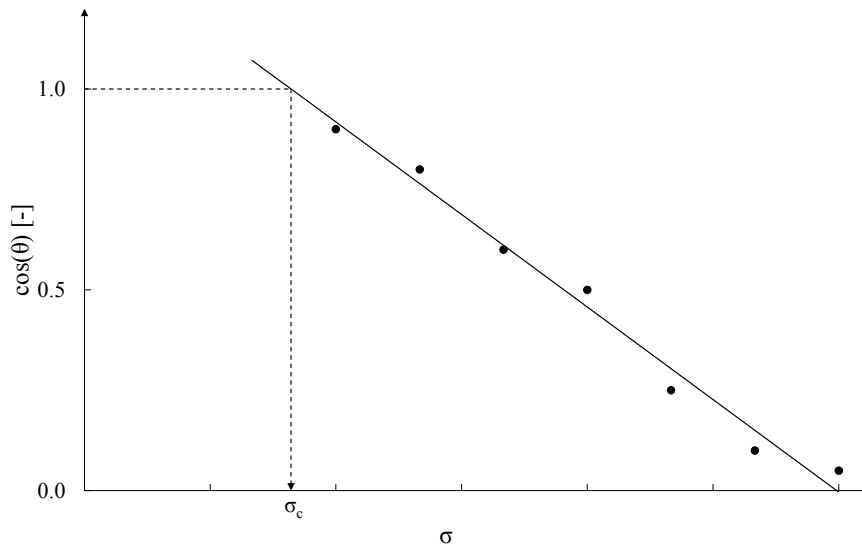


**Fig. 2-11.** Determination of the critical surface tension of wetting  $\sigma_c$  on flat surfaces according to Zisman by plotting the cosine of the measured contact angle  $\cos(\theta)$  against the surface tension of the test liquid  $\sigma$ .

### 2.2.1.2 Contact angle measurements on particulate systems

In contrast to contact angle measurements on flat surfaces, the determination of contact angles on particulate systems is far more complicated. An overview of methods is given in ([94], p. 70ff.; [99]). For large particles, the contact angle may be measured directly on the particle surface similar to the sessile drop technique. The determination of the tangents will be, however, more complex and special mathematical models as, e.g., proposed in [100] have to be applied.

Fuerstenau and Williams [101–103] as well as Marmur et al. [104] proposed independently from each other a technique for the characterization of particle wettability in terms of surface energy. This technique is often referred to as film flotation. In this method, a test solution with known surface tension is placed inside a small conical vessel. Usually, methanol-water or ethanol-water mixtures are used for this purpose. A sufficient amount of particles is then placed carefully on the liquid surface. Depending on the particle surface properties, some of the particles may sink while others may float on the given liquid. The sinking and floating fractions are then weighed. By changing the composition of the mixture, the experiment is repeated at various liquid surface tensions. A sigmoidal curve as presented in Fig. 2-12 results from a plot of the weight fraction of floating particles against the surface tension of the test liquid. From this graph three critical surface tensions of wettability  $\gamma_c$  for particles can be derived:

- all particles sink at  $\gamma_c^{\min}$ ,
- 50 % of the particles sink/float at  $\bar{\gamma}_c$ ,
- all particles float at  $\gamma_c^{\max}$ .

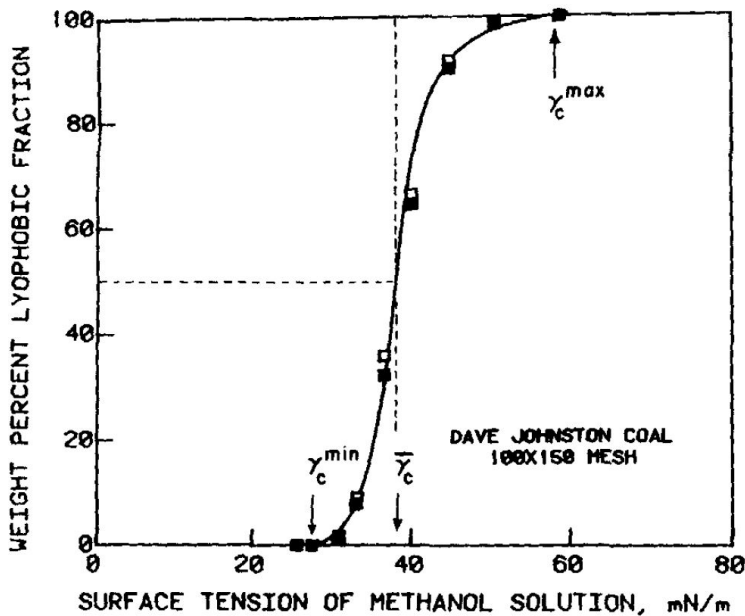


Fig. 2-12. Typical resulting plot of a film flotation experiment [101].

For completely homogeneous particle surfaces, the graph shown in Fig. 2-12 would be a step function. Hence, this method also provides an information on the degree of heterogeneity of the particle surfaces. The point at which 50 % of the particles sink/float is usually interpreted as critical surface tension of wetting  $\bar{\gamma}_c$  for the investigated particulate system ([99], p. 27; [101]). Marmur et al. as well as Fuerstenau et al. found that this critical surface tension is in good agreement with the critical surface tension of wetting determined via the Zisman method for identically flat surfaces [103,104].

Fuerstenau et al. investigated different effects on the results of the film flotation experiments [101]. In a first step, they showed that although one might be concerned with adsorption effects when analysing wetting behaviour of solids in aqueous solutions of polar organic molecules, this effect is not present. Therefore, results of the film flotation experiments are unaffected by the test solution. Additionally, they showed that particle size has no effect either. All of the investigated particle sizes in a range from 53 to 425  $\mu\text{m}$  resulted in the same curve. Furthermore, neither particle density, tested in a range of specific gravities of 2.2 to 5.0, nor particle shape had a significant effect on the experimental results.

In their theoretical derivation they showed that immersional wetting and spreading wetting, which are the critical steps in the process for a particle to sink, are spontaneous processes depending on the contact angle. This was also proven with experiments of solids in varying testing liquids over different times ranging from 1.5 to 50 minutes. Thus, time has also no significant influence on the experimental results.

## 2.2.2 Adsorption of surfactants at the gas-liquid interface

In this chapter the theoretical aspects dealing with the adsorption of surfactants at the gas-liquid interface as well as measurement techniques are presented.

### 2.2.2.1 Theoretical aspects of adsorption at the gas-liquid interface

Surface active agents, or in short surfactants, are organic compounds generally consisting of at least one *lyophilic* (solvent loving) and one *lyophobic* (solvent fearing) group. In the special case of water as solvent, the terms are named *hydrophilic* and *hydrophobic*, respectively. It is well known that addition of surfactants decreases the surface tension of water ([105], p. 35).

If a surfactant is added to an aqueous medium, the surfactant molecules will migrate to the gas-liquid interface. The molecules will orientate in order to minimize the contact between their hydrophobic groups and water. This process is called adsorption (see Fig. 2-13a). With increasing surfactant concentration, surfactant molecules will move from the gas-liquid interface into the bulk phase (see Fig. 2-13b), where aggregation of surfactant molecules will occur. If the concentration of the surfactant exceeds a critical concentration, which is known as critical micelle concentration (CMC), the process of micellisation starts. In the micelles, the surfactant molecules orientate in such a way that the hydrophilic parts are orientated towards the liquid, while the hydrophobic parts are orientated inwards (see Fig. 2-13c). Any further addition of surfactant after the CMC will have no impact on the liquid surface tension ([106], p. 270). The formation of micelles has a negative effect on the selectivity of the flotation process. Although micelles readily adsorb on solids, this adsorption is unspecific and mainly fine particles, which are present as slime, are affected ([19], p. 43).

Different models have been proposed in literature to describe the adsorption process of surfactants at the gas-liquid interface. The most famous and commonly used is the Gibbs adsorption isotherm. The model of Gibbs relates the surface tension with the excess interfacial concentrations. At a constant temperature, the Gibbs adsorption isotherm is given as ([105], p. 36; [107], p. 67; [108], p. 29; [109], p. 75):

$$d\sigma = - \sum_i \frac{n_i}{A} d\mu_i = - \sum_i \Gamma_i d\mu_i \quad (2-32)$$

In Eq. (2-32),  $d\sigma$  is the change in surface tension of the solution,  $n$  is the amount of solute  $i$ ,  $A$  is the surface area,  $d\mu_i$  is the change in chemical potential of the solute in the solution and  $\Gamma_i$  is the surface excess concentration of solute per unit area of surface.

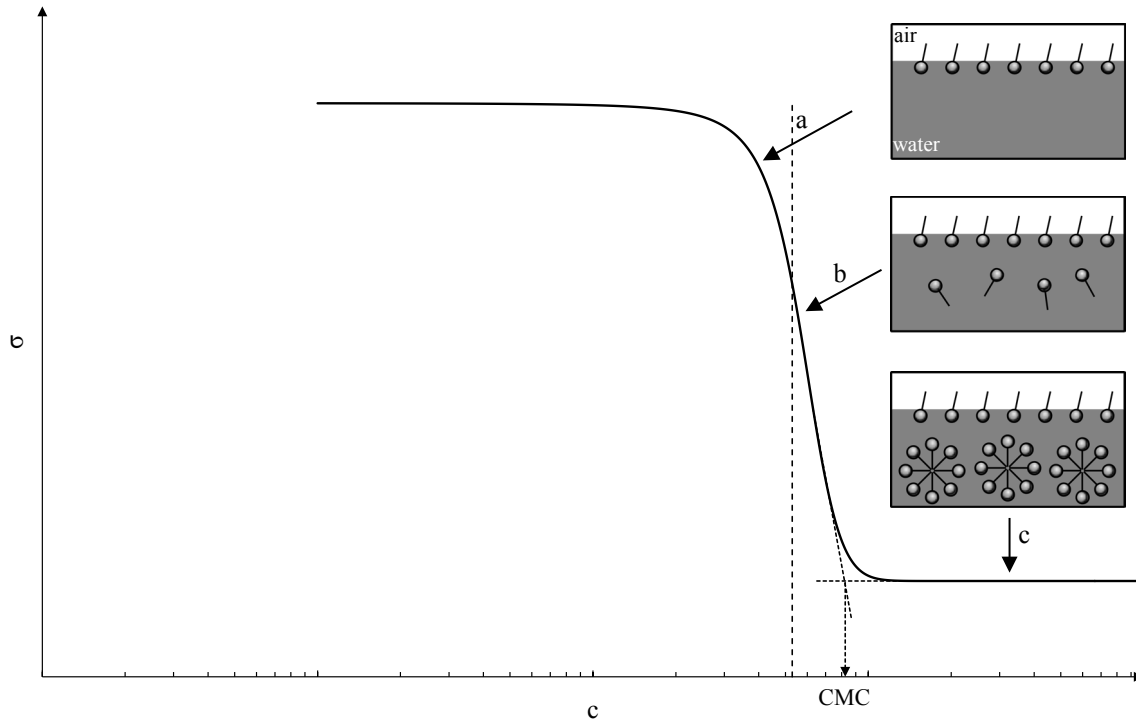


**Fig. 2-13.** Surface tension  $\sigma$  as a function of surfactant concentration  $c$  (adapted from [110], p. 680): adsorption of surfactant molecules at the air-water interface (a), transfer of surfactant molecules from the gas-liquid interface to the bulk phase (b), and formation of micelles (c).

Equation (2-32) is rewritten for a two-component system, e.g., using index 1 for the solvent and index 2 for the solute to:

$$d\sigma = -\Gamma_1 d\mu_1 - \Gamma_2 d\mu_2 \quad (2-33)$$

The surface excess concentration can be considered to be equal to the actual surface concentration without significant error, thus:

$$d\mu_i = R \cdot T \cdot d \ln(a_i) = R \cdot T \cdot d \ln(c_i \cdot \gamma_i) \quad (2-34)$$

In Eq. (2-34),  $R$  is the universal gas constant,  $T$  is the absolute temperature,  $a_i$  is the activity of solute  $i$  in the solution,  $c_i$  is the concentration of the solute  $i$  in the solution and  $\gamma_i$  is the activity coefficient of the component  $i$  in the bulk phase. The surface excess concentration  $\Gamma$  for a dilute solution of surfactant is calculated via Eq. (2-35) assuming an ideal interface ([107], p. 69f.; [111–113]; [114], p. 246):

$$\Gamma = -\frac{1}{z \cdot 2.303 \cdot R \cdot T} \cdot \left( \frac{\partial \sigma}{\partial \log c} \right)_T \quad (2-35)$$

In Eq. (2-35),  $\left( \frac{\partial \sigma}{\partial \log c} \right)_T$  is the slope of the linear part of the  $\sigma$ - $\log c$  plot (cf. Fig. 2-13) and  $z$  is a constant, which depends on the properties of the surfactant. For non-ionic surfactants and univalent ionic surfactants in the presence of excess electrolyte,  $z=1$  [111–113].

The area  $A$  occupied by a surfactant molecule at the surface or interface in square angstrom can be obtained with Eq. (2-36):

$$A = \frac{10^{16}}{N_A \cdot \Gamma} \quad (2-36)$$

In this equation,  $N_A$  is Avogadro's number ([107], p. 70). The efficiency of surfactant adsorption can be evaluated using the Frumkin equation [115]:

$$\sigma_0 - \sigma = \Delta\sigma = -2.303 \cdot R \cdot T \cdot \Gamma_m \cdot \log\left(1 - \frac{\Gamma}{\Gamma_m}\right) \quad (2-37)$$

In Eq. (2-37),  $\sigma_0$  is the surface tension of the pure solvent,  $\sigma$  is the measured surface tension, and  $\Gamma_m$  is the surface concentration of the surfactant at monolayer adsorption. Rearrangement of Eq. (2-37) gives the saturation  $s$ :

$$\frac{\Gamma}{\Gamma_m} = s = \left(1 - 10^{-\frac{\Delta\sigma}{2.303 \cdot R \cdot T \cdot \Gamma_m}}\right) \quad (2-38)$$

It is found that when  $\Delta\sigma \approx 20$  mN/m, the excess concentration of the surfactant is close to its saturation value. For example for typical excess concentrations stated in literature ranging from  $1-4.4 \cdot 10^{-10}$  mol/cm<sup>2</sup> the Frumkin equation yields saturations of  $s=84-99.9\%$  ([107], p. 100; [108], p. 39; [116], p. 60).

### 2.2.2.2 Measurement of surface tension

A variety of experimental methods using so-called tensiometers to determine the surface tension of liquids are available, e.g. Wilhelmy balance method or Du Noüy ring method ([117]; [118], p. 25ff.). In the following, the Du Noüy ring method, which was proposed in 1925 by Pierre Lecomte du Noüy [119], is described in detail.

A schematic overview of the experimental setup of the measurement method, which is standardized in the ISO 304:1985 [120], is presented in Fig. 2-14. The method is based on the measurement of a force  $F$ , which is required to raise a ring from the liquid's surface. This force is then related to the surface tension  $\sigma$  via Eq. (2-39):

$$F = F_{\text{ring}} + 4 \cdot \pi \cdot \bar{r} \cdot \sigma \quad (2-39)$$

In Eq. (2-39),  $F_{\text{ring}}$  is the weight force of the ring corrected by the buoyant force due to the part of the ring below the liquid surface and  $\bar{r}$  is the average diameter of the inner and outer radius of the ring. The ring used for the measurements is typically a wire made from a platinum-iridium alloy, which ensures a complete wetting of the liquid ([117], p. 31).

The measurement procedure for the Du Noüy ring method is as follows: in the first step, the sample is placed in the sample holder. The sample holder has to be very clean, as small impurities already have a strong influence on the measurement result.

Next, the ring is cleaned by heating it to glow in the oxidizing portion of a Bunsen burner flame. Afterwards, the ring is attached to the hook at the end of the lever arm of the tensiometer. A zero reading of the ring is carried out before the sample holder is raised until the ring is immersed, just so that the ring is completely wetted. Afterwards, the ring is lifted from the liquid. Due to the complete wetting of the ring, lamella will be formed as a result of the liquid surface tension (cf. Fig. 2-14b). When the upwards directed force  $F$  is greater than the liquid surface tension, the lamella will tear off and a sharp drop of  $F$  will be noticed. The surface tension of the liquid is determined from the measured maximum force.

Performed surface tension measurements using the Du Noüy ring method showed, however, large discrepancies between different researchers. Several authors noted therefore that Eq. (2-39) is inaccurate and measurement errors of up to  $\pm 30\%$  may be caused [121]. A problem of Eq. (2-39) is that for example the radius of the wire forming the ring is not incorporated, although this will have a significant effect on the measured liquid surface tension. Therefore, empirical models have been developed, which incorporate effects of the radius of the wire forming the ring, the height of the ring above the liquid level, and the volume of the raised liquid. Harkins and Jordan proposed such an improved model based on Eq. (2-39) by adding a correction factor  $f^*$ , which has to be determined experimentally:

$$F = F_{\text{ring}} + 4 \cdot \pi \cdot R \cdot \sigma \cdot f^* \quad (2-40)$$

In modern Du Noüy ring tensiometers, values for  $f^*$  are directly implemented, as the measurement systems are standardized.

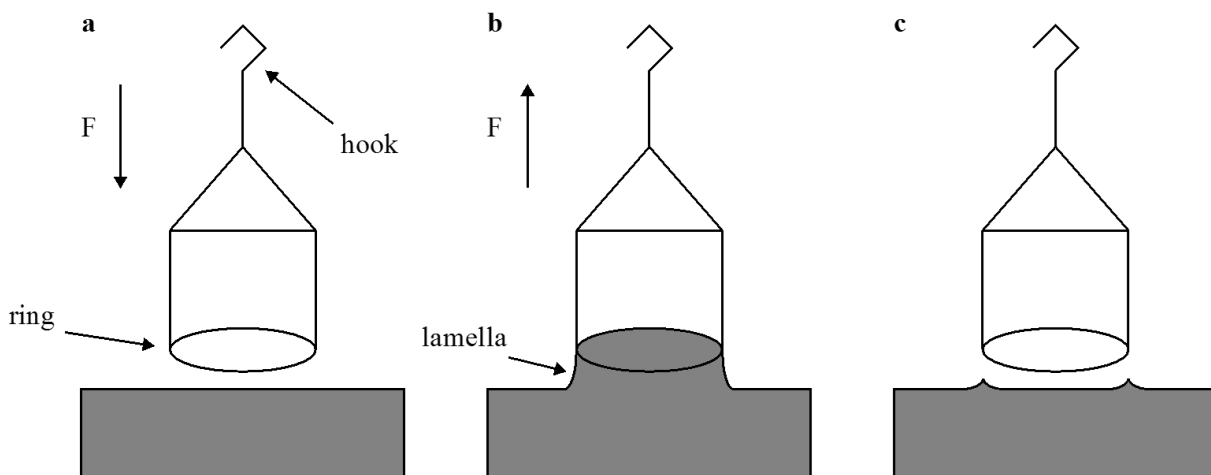


**Fig. 2-14.** Schematic experimental procedure of a Du Noüy ring tensiometer for measurement of liquid surface tensions: ring above measured liquid for zeroing procedure (a), ring lifted after immersion in the liquid (b), and tearing off of the lamella attached to the ring (c).

## 2.3 Bubbles

In this chapter, the theoretical background dealing with bubbles and their characteristics is presented. A differentiation between bubble characteristics in water and in presence of surface active agents is made. Furthermore, bubble sizing methods are presented.

### 2.3.1 Characteristics of bubbles in water

The characteristics of bubbles in water with respect to the formation process, the various bubble shapes as well as the motion of bubbles are presented. Dimensionless numbers, helpful diagrams as well as equations presented in literature for characterisation of bubbles are introduced.

#### 2.3.1.1 Periodic bubble formation

As stated in chapter 1.2, the aim of this work is the investigation and analysis of mainly single bubbles. Thus, a force balance for the production process of a bubble can be considered. Periodic bubble formation leads to a small bubble size distribution where the bubble diameter  $d_B$  increases with increasing volumetric gas flow rate  $\dot{V}_g$ . A periodic bubble formation takes place for Weber numbers  $We$  smaller than approximately two. At Weber numbers higher than two, jet gassing occurs during the formation of bubble swarms ([122], p. 1240; [123]).

The force balance during the bubble production is schematically shown in Fig. 2-15. The diameter of the generated bubble is determined by the equilibrium of the forces ([122], p. 1240):

$$F_b - F_\sigma - F_\eta - F_i = 0 \quad (2-41)$$

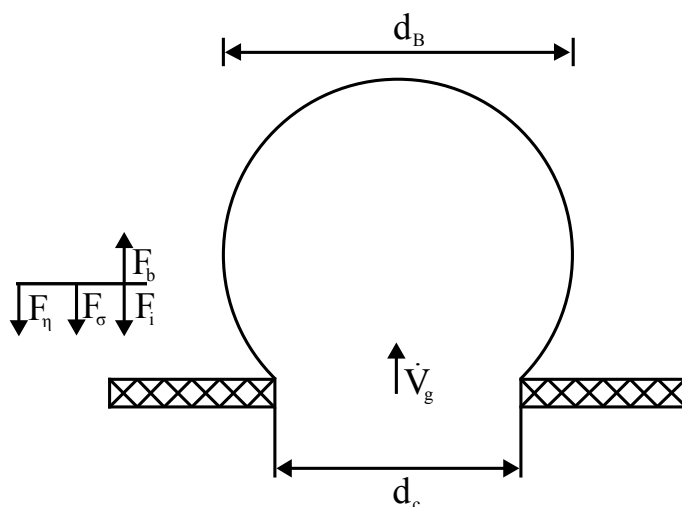


Fig. 2-15. Equilibrium of forces for quasistatic formation of a bubble at an orifice (adapted from [122], p. 1240).

In Eq. (2-41),  $F_b$  is the buoyancy force,  $F_\sigma$  is the surface tension force,  $F_\eta$  is the drag force, and  $F_i$  is the inertia force. The forces are described by Eqs. (2-42)-(2-45):

$$F_b = \frac{\pi}{6} \cdot \Delta \rho \cdot g \cdot d_B^3 \quad (2-42)$$

$$F_\sigma = \pi \cdot d_c \cdot \sigma_{lg} \quad (2-43)$$

$$F_\eta = 15 \cdot \eta_l \cdot \frac{\dot{V}_g}{d_B} \quad (2-44)$$

$$F_i = 1.3 \cdot \rho_l \cdot \left( \frac{\dot{V}_g}{d_B} \right)^2 \quad (2-45)$$

In these equations,  $\Delta \rho$  is the density difference between gaseous and liquid phase,  $g$  is the acceleration due to gravity,  $d_B$  is the bubble diameter,  $d_c$  is the capillary diameter,  $\sigma_{lg}$  is the interfacial tension between liquid and gaseous phase,  $\eta_l$  is the dynamic viscosity of the liquid,  $\dot{V}_g$  is the volumetric gas flow rate, and  $\rho_l$  is the density of the liquid. The constant values of 15 and 1.3 in Eqs. (2-44) and (2-45) are adapted to values published by different researchers [123]. Using equations (2-42) to (2-45) in equation (2-41) gives the bubble diameter  $d_B$  as:

$$d_B = \left[ \left( \frac{F_\eta + F_i + F_\gamma}{\Delta \rho \cdot g} \right) \cdot \frac{6}{\pi} \right]^{1/3} \quad (2-46)$$

### 2.3.1.2 Shapes of bubbles in motion

When no other forces or constraints act on a bubble, the action of surface tension on bubbles preserves their spherical shape. Their movement in fluids, however, creates shear stresses, which deform their spherical symmetry ([124], p. 48). The eight most commonly observed shapes of rising bubbles in liquids are depicted schematically in Fig. 2-16.

A spherical shape (s) is only possible in inviscid fluids. Shear induced by flow distorts the shapes of bubbles to ellipsoidal. When the difference between the lengths of the two principal axes is within 10 %, the bubbles may be approximated as spherical ([125], p. 23).

In contrast to oblate ellipsoidal (oe), oblate ellipsoidal disks (oed) exhibit high elongations and wobble visibly. In liquids with low viscosity, e.g. water, intermediate-size bubbles have a very irregular shape and oscillate unsteadily ([126], p. 18).

Bubbles in the form of spherical caps (scc), spherical caps with open, unsteady wakes (sco), skirted bubbles (sks), and skirted bubbles with a wavy, unsteady skirt (skw) are mainly observed in liquids with high viscosity, e.g. mineral oil ([125], p. 25).

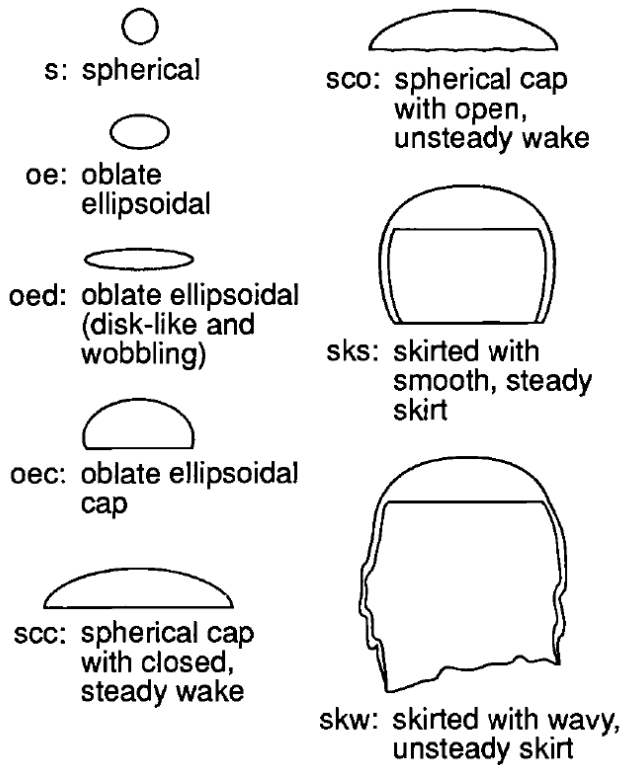


Fig. 2-16. Different bubble shapes as observed in experiments ([126], p. 18).

The bubble shape cannot be completely predicted unless all the physical variables pertinent to the bubble rise phenomenon are taken into consideration. The main variables, which determine the shape of bubbles when freely rising in a column of water under action of gravity/buoyancy, are ([126], p. 19; [124], p. 49; [127]):

- terminal velocity  $w_B$ ,
- characteristic length, which is usually the equivalent bubble diameter  $d_B$ ,
- density of the continuous phase  $\rho_l$ ,
- dynamic viscosity of the continuous phase  $\eta_l$ ,
- surface tension  $\sigma_{lg}$ ,
- gravitational acceleration  $g$ ,
- density of dispersed phase (gas inside the bubble)  $\rho_g$ ,
- and dynamic viscosity of the dispersed phase (gas inside the bubble)  $\eta_g$ .

In most cases, both density and dynamic viscosity of the continuous phase is much greater than the density of the dispersed phase ( $\rho_l \gg \rho_g$  and  $\eta_l \gg \eta_g$ ). Therefore, in a first approach the two latter parameters can be neglected. A dimensional analysis of the remaining six variables yields three independent dimensionless groups ([124], p. 49; [125], p. 26; [128], p. 7).

The bubble Reynolds number  $Re_B$  describes the ratio of inertial force and frictional force:

$$Re_B = \frac{d_B \cdot w_B \cdot \rho_l}{\eta_l} \quad (2-47)$$

The velocity  $w_B$  of a bubble in Eq. (2-47) with a diameter  $d_B$  is the relative velocity between the bubble and the surrounding liquid with the density  $\rho_l$  and dynamic viscosity  $\eta_l$ . In quiescent flows this velocity is equal to the rising velocity of the bubble. Usually, three ranges of  $Re_B$  numbers are distinguished: small  $Re_B$  numbers with  $Re_B < 1$ , intermediate  $Re_B$  numbers with  $1 < Re_B < 200$ , and large  $Re_B$  numbers with  $Re_B > 200$  ([129], p. 374).

The bubble Weber number  $We_B$  describes the ratio of inertial forces and surface forces:

$$We_B = \frac{w_B^2 \cdot d_B \cdot \rho_l}{\sigma_{lg}} \quad (2-48)$$

It is a useful dimensionless number to analyse fluid flows with an interface present between two different fluids, e.g. bubbles.

The bubble Froude number  $Fr_B$  describes the ratio between inertial forces and weight force:

$$Fr_B = \frac{w_B^2}{g \cdot d_B} \quad (2-49)$$

If the inertial forces dominate, gravity effects may be neglected. In these cases,  $Fr_B$  is very high ([130], p. 262). Incorporating the density difference of liquid density and gas density  $\Delta\rho = \rho_l - \rho_g$  as additional variable parameter, the modified bubble Froude number  $Fr_B^*$  is obtained via linear combination:

$$Fr_B^* = \frac{w_B^2}{g \cdot d_B} \cdot \frac{\rho_l}{\Delta\rho} \quad (2-50)$$

Based on combinations of the  $Re_B$ ,  $We_B$ , and  $Fr_B^*$ , other dimensionless numbers can be derived. For the investigation of multiphase flows, e.g. the Morton number  $M$  and the Eötvös number  $Eo$  are widely used ([125], p. 26; [126], p. 19; [131], p. 374).

The Morton number  $M$  is a combination of the bubble Weber number, the bubble Reynolds number as well as the modified bubble Froude number:

$$M = \frac{We_B^3}{Re_B^4 \cdot Fr_B^*} = \frac{g \cdot \eta_l^4 \cdot \Delta\rho}{\rho_l^2 \cdot \sigma_{lg}^3} \quad (2-51)$$

It is with exception of the gravitational acceleration  $g$  only depended on the physical properties of the fluids and, thus describes the physical properties of the fluid. For water at a temperature of 20 °C,  $M = 3 \cdot 10^{-11}$ .

The Eötvös number  $Eo$ , also referred to as Bond number  $Bo$ , is a combination of bubble Weber number and modified bubble Froude number. Therefore, it describes the ratio of surface tension to weight force:

$$Eo=Bo=\frac{We_B}{Fr_B^*}=\frac{g\cdot\Delta\rho\cdot d_B^2}{\sigma_{lg}} \quad (2-52)$$

For bubbles rising freely in infinite media, it is possible to prepare a generalized graphical correlation in terms of the dimensionless numbers  $Re_B$ ,  $Eo$ , and  $M$ . The so-called shape-regime map indicates bubble shapes depending on situational variables. An example of such a shape-regime map is given in Fig. 2-17. The graph is based on experimental data and, thus the boundaries for different shape forms may be arbitrary ([125], p. 28).

The gravitational acceleration is almost constant. This reduces the list of important variables for bubble characteristics listed above to five. Thus, only two of the three derived dimensional groups are necessary for the creation of a shape-regime map in order to classify bubble shapes. A combination of all three dimensionless groups is possible:  $Re_B$  and  $Eo$ ,  $Re_B$  and  $M$ , as well as  $Eo$  and  $M$ . From Fig. 2-17 some general observations can be concluded:

1. Bubbles are spherical at low  $Re_B$  and low  $Eo$ .
2. Ellipsoidal shapes appear at high  $Re_B$  and intermediate  $Eo$ .
3. Bubbles assume the shape of a spherical cap at high  $Eo$  and high  $Re_B$ .

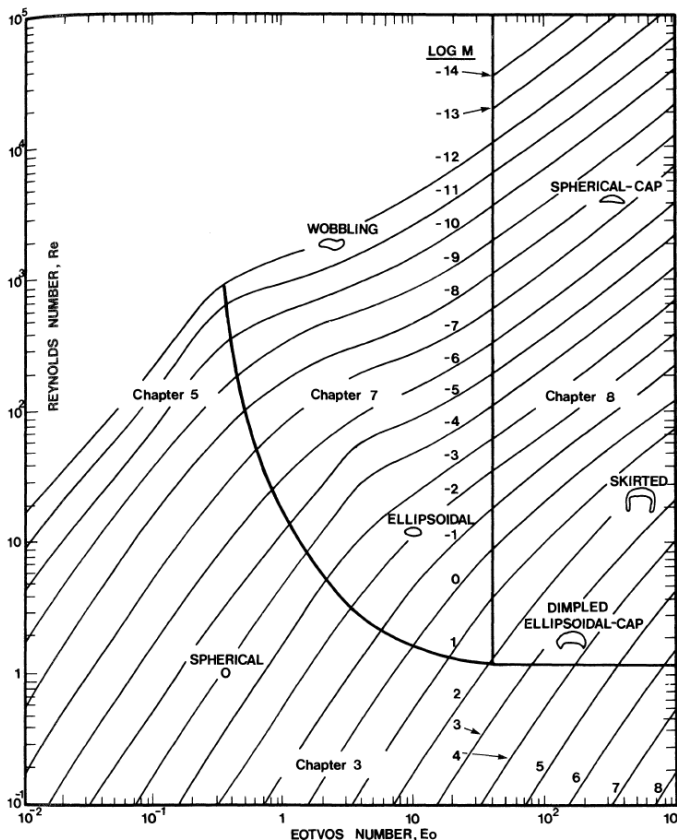


Fig. 2-17. Shape-regime map for bubbles in un hindered gravitational motion through liquids ([125], p. 27).

### 2.3.1.3 Terminal velocity of bubbles

Experimentally determined terminal velocities of rising air bubbles in water at 20 °C are shown in Fig. 2-18. The bubble drag as well as the terminal velocity of bubbles are very sensitive to the presence of surface active agents and impurities ([125], p. 171). The given curves are based on experimental data for pure deionized water and in presence of surface active agents. The terminal velocities differ significantly, if pure water or contaminated water is considered (cf. Fig. 2-18). Both curves converge for small bubbles, which have typically a spherical shape. This is due to the circumstance that even deionized water contains small amounts of surfactants, which prevent inner circulation and, thus lead to smaller rising velocities. A second convergence of both curves is present at higher equivalent diameters, because in this range surface tension forces cease to be dominant. Thus, surface active agents affect the rising velocity most strongly in the ellipsoidal range.

A freely rising bubble is only depended on the forces of buoyancy (see Eq. (2-42)) and resistance acting on it. The resistance force  $F_r$  is given by:

$$F_r = \frac{1}{2} \cdot c_D(Re_B) \cdot A \cdot \rho_l \cdot w_B^2 \quad (2-53)$$

Equalizing Eq. (2-42) and Eq. (2-53) yields with  $q_l \gg q_g$ :

$$w_B = \sqrt{\frac{4 \cdot g \cdot d_B}{3 \cdot c_D}} \quad (2-54)$$

Spherical bubbles with bubble Reynolds numbers greater than 300 can be modelled with Eq. (2-54) with  $c_D \approx 0.5$  ([131], p. 373).

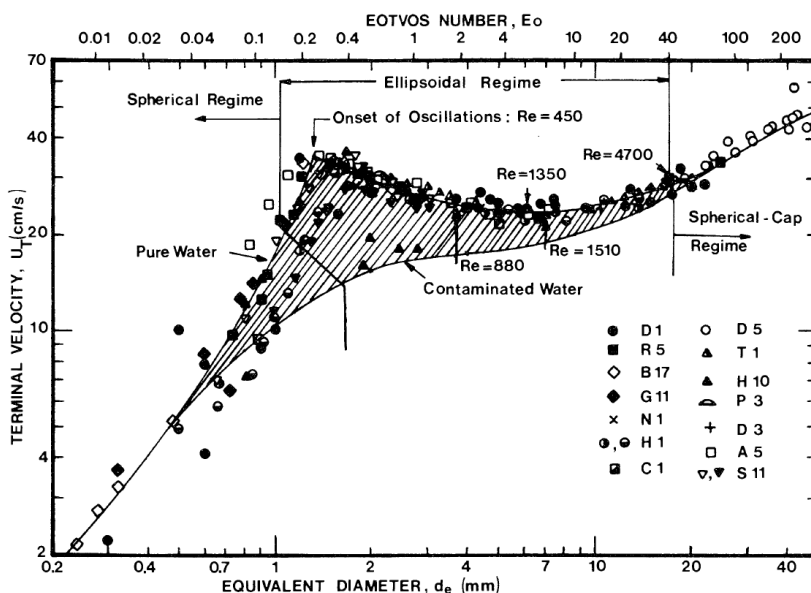


Fig. 2-18. Terminal velocity of air bubbles in water at 20 °C as a function of equivalent bubble diameter  $d_B$  ([125], p. 172).

### 2.3.1.4 Motion of and flow around single bubbles

Studies dealing with the investigation of rising bubbles have been reported extensively in literature. The rising path and the change in orientation of the bubbles are mainly related to the bubble shape ([126], p. 53). Different types of motion have been experimentally observed depending on bubble size and maximum instantaneous velocity. An overview of determined bubble rising paths in relation to bubble diameter  $d_B$ , bubble Reynolds number  $Re_B$ , and aspect ratio is given in Tab. 2-5. The classifications vary for different reports, which may be related to different experimental setups as well as different water qualities, especially with regard to impurities and surface active agents (cf. chapter 2.3.2). Other observations and classifications of bubble rising paths may be found, amongst others, in [126], p. 53ff and [132].

**Tab. 2-5.** Motion of intermediate sized air bubbles through water at 28.5 °C ([125], p. 172; [126], p. 54–55).

$d_B$ [mm]	$Re_B$ [-]	Aspect ratio [-]	Path
< 1.3	< 565	> 0.8	rectilinear
1.3 to 2.0	565 to 880	0.8 to 0.5	helical
2.0 to 3.6	880 to 1350	0.5 to 0.36	plane (zigzag) then helical
3.6 to 4.2	1350 to 1510	0.36 to 0.28	plane (zigzag)
4.2 to 17	1510 to 4700	0.28 to 0.23	rectilinear but with rocking

### 2.3.2 Influence of surfactants on rising bubbles

The bubble characteristics presented in chapter 2.3.1 change significantly in the presence of surfactants. The theoretical background of the adsorption of surfactants at the liquid-gaseous interface has been already presented in chapter 2.2.2. Air bubbles rising through a liquid exhibit also a liquid-gaseous interface, where adsorption of surfactants is possible.

The adsorption process at the interface of a rising single bubble is schematically shown in Fig. 2-19c. Adsorbing surfactant molecules are swept off the front part of the bubble due to the upwards directed motion and accumulate at the bubble rear. Thus, a surface tension gradient is induced along the bubble surface. The accumulated surfactant molecules at the bubble rear immobilise the interface and induce a tangential stress. This phenomenon is known as Marangoni effect [133–135]. The shear stress increases the bubble drag resulting in a decreasing rising velocity. With increasing surfactant concentration, the immobilisation of the bubble interface increases and, thus the rising velocity of the bubble decreases. The drag increases until a threshold is reached, which corresponds to the drag of a rigid sphere.

The adsorption of surfactants on the bubble surface takes place due to convective mass transport. However, during the formation process of a bubble, e.g. as depicted in Fig. 2-15 in chapter 2.3.1.1, diffusive mass transport will already be present, which will lead to an initial concentration of surfactants on the bubble surface. Pesci et al. stated that this initial concentration prior to bubble detachment is relatively small with usually less than 10 % of the maximum surface concentration on the bubble surface [136].

According to Sam et al. three characteristic stages can be observed for the velocity of rising bubbles in dilute surfactant solutions: acceleration, deceleration after passing a maximum, and reaching a constant rising velocity [136–138]. Tan et al. showed that the terminal velocity of rising bubbles is independent of surfactant concentration [139]. At lower concentrations more time, corresponding to a longer rising distance, is required to reach terminal velocity.

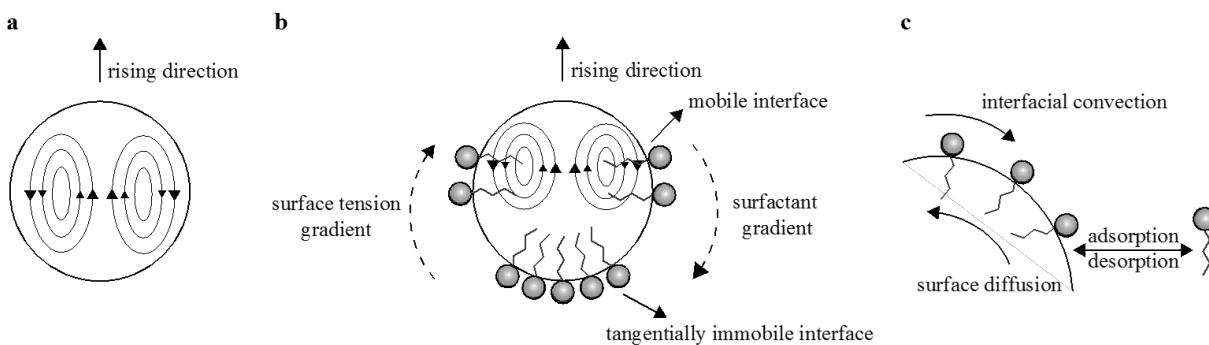


**Fig. 2-19.** Internal circulation inside a gas bubble rising in a surfactant-free liquid (a) and Marangoni effect on the bubble interface (b&c) (adapted from [140], p. 371).

The adsorption rate increases, however, with increasing concentration of the surfactant in the bulk phase so that the terminal rising velocity is reached earlier ([140], p. 424). Thus, Tan et al. applied two criteria to define the rising velocity as terminal: 1) when velocity at a given concentration reaches minimum with distance; 2) when velocity at a given distance reaches minimum with concentration.

Apart from the influence on the rising velocity, the surfactant adsorption at the bubble interface has also a significant effect on other bubble parameters. The bubble morphology changes with increasing surfactant concentration towards spherical bubbles due to the decreasing surface tension of the liquid. Furthermore, the bubble diameter is influenced by surfactant adsorption. For single bubbles this effect is rather small [141,142], while the Sauter mean bubble diameter  $d_{32}$  decreases significantly in bubble swarms from, e.g., 4 mm to 1 mm with increasing surfactant concentration [139,142–144]. Studies of Laskowski et al. [142] show that this is related to the prevented coalescence of bubbles, thus preserving the initial bubble diameter at bubble creation and after comminution due to high shear rates, e.g., induced by stirring. The  $d_{32}$  decreases with increasing surfactant concentration until a threshold is reached. A parameter called critical coalescence concentration (CCC) was proposed by Cho and Laskowski [142], representing the concentration at which the minimum  $d_{32}$  of a bubble swarm is reached. The graphical determination of the CCC is analogous to the procedure for determination of the CMC presented in chapter 2.2.2.1.

Another parameter defined as concentration at the minimum bubble velocity (CMV) proposed by Tan et al. [139,145,146] is also stated in literature. CMV is determined similarly to CCC as the concentration at which the terminal bubble velocity is reached [147]. In contrast to CCC, CMV is mainly determined for single bubbles [145–148].

### 2.3.3 Bubble sizing methods

In this chapter, a brief summary of available methods for bubble sizing is presented, including the so-called Shadowgraphy, which is mainly used in the present work.

#### 2.3.3.1 Overview

Bubble sizing methods have gained a lot of interest in recent years due to technological development. There are several bubble sizing techniques described in literature, e.g. electroresistivity [149], ultrasound [150,151] and optical methods ([152], p. 42ff.). The latter are divided into different methods, such as using optical fibres [153,154], isokinetic collection [155] or imaging techniques ([152], p. 46ff.).

Measurements carried out with optical fibres depend on the different refraction of gaseous and liquid phase. Depending on the present phase at the tip of the probe, light from the tip is reflected or refracted. This method is limited to transparent systems and low gas holdups. Additionally, the measurement accuracy is highly dependent on the bubble size ([152], p. 42). The isokinetic collection probe assumes a sampling of bubbles at uniform velocity regardless of their size. The bubbles are collected in a capillary tube, whose end is funnel shaped (see Fig. 2-20). In this capillary, bubbles are converted into cylinders (cf. Fig. 2-20 at  $t_2$ ). With known diameter of the capillary  $d_c$  and the measured length of the cylinder  $l$ , the bubble volume can be calculated. Typically, the measurement of the length is carried out automatically using a narrow light beam, which is directed through the capillary glass wall. The intensity of the detected light varies between gas and liquid phase, so that the time between the detection of the two ends of a bubble can be inferred from the signal. One example of these techniques is the so-called University of Cape Town (UCT) bubble size analyser [156].

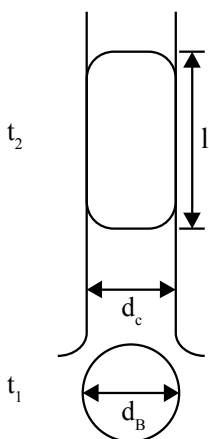


**Fig. 2-20.** Conversion of a bubble with diameter  $d_B$  into a cylinder with the length  $l$  inside a capillary with the diameter  $d_c$  during an isokinetic collection (adapted from [157]).

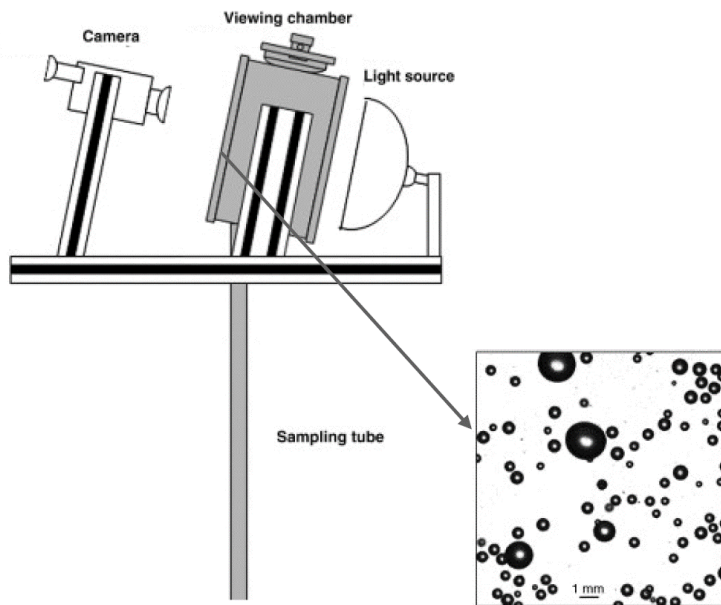


**Fig. 2-21.** Schematic sketch of the McGill bubble size analyser and a resulting image of the measurement technique (adapted from [152], p. 49 and [158,159]).

Due to their easy implementation, imaging techniques are widely used and favoured by researchers. High-speed cameras are used to capture image sequences of the rising bubbles. The image sequences are afterwards analysed, either manually or automatically. For investigations of bubble size distributions in flotation cells, different approaches and apparatuses have been proposed in literature, e.g. the McGill bubble size analyser [160], the Helsinki University of Technology (HUT) bubble size sampler [157], the LTM-BSizer [161,162] or the USM bubble size sampler [163]. The commonality of all these samplers and analysers is the use of a high-speed camera for filming bubble sequences in combination with a backlight illumination unit positioned opposite of the camera in order to illuminate the flow. This method is generally termed Shadowgraphy, because the bubble outline is presented as shadow, while the background of the image is brightly illuminated (cf. Fig. 2-21).

### 2.3.3.2 Shadowgraphy

The Shadowgraphy (SH) is an optical measurement method for the investigation of gaseous, liquid and multiphase flows. It is a non-invasive method, which means that no further objects have to be placed inside the flow, which could manipulate the flow structure. A schematic overview of a typical SH setup is given in Fig. 2-22a. The setup consists of a light source for the illumination of the background and a camera, which is placed opposite of the light source ([164]; [165], p. 1391f.). For backlight illumination, both lasers and LEDs can be used [166,167].

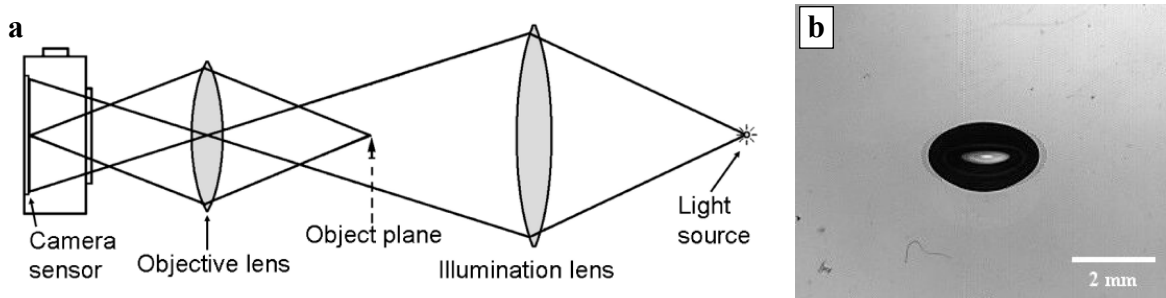


**Fig. 2-22.** Schematic overview of a typical Shadowgraphy setup [168] (a) and exemplary Shadowgraphy image of a rising single air bubble in deionized water (b).

SH uses the difference of refraction of different phases at the interface. Light, which is not refracted at an interface, passes the viewing area unhindered and, thus, yields in a white spot on the image. At phase boundaries the light is absorbed, refracted or reflected. Therefore, the image is black at spots, where an absorption, a reflection or a refraction appears. A typical SH image of a rising single bubble is presented in Fig. 2-22b.

## 2.4 Fluid mechanics

Fluid mechanics is a branch of physics concerned with the mechanics of fluids like liquids or gases as well as the forces on them ([169], p. 11). It can be divided into fluid dynamics and fluid statics, depending on whether a flow is present or not.

Fluid dynamics is a subdiscipline of fluid mechanics, which deals with the description of the flow of fluids. It can again be divided into several subdisciplines, such as aerodynamics, which deals with the analysis of air and gas flows, and hydrodynamics for the investigation of liquid motion. Experimental analysis of fluid dynamics is feasible with help of optical methods, such as Particle Image Velocimetry (PIV) and Particle Tracking Velocimetry (PTV), which will be explained in the following chapters.

### 2.4.1 Particle Image Velocimetry

The Particle Image Velocimetry (PIV) is a non-invasive optical measurement method for the visualisation of flows. It is used to obtain information about the velocity and related properties of the flow, e.g. turbulence. A typical experimental setup for PIV measurements is shown in Fig. 2-23. A PIV setup consists of the following four necessary elements:

- a laser,
- tracer particles,
- a camera,
- and a flow for investigation.

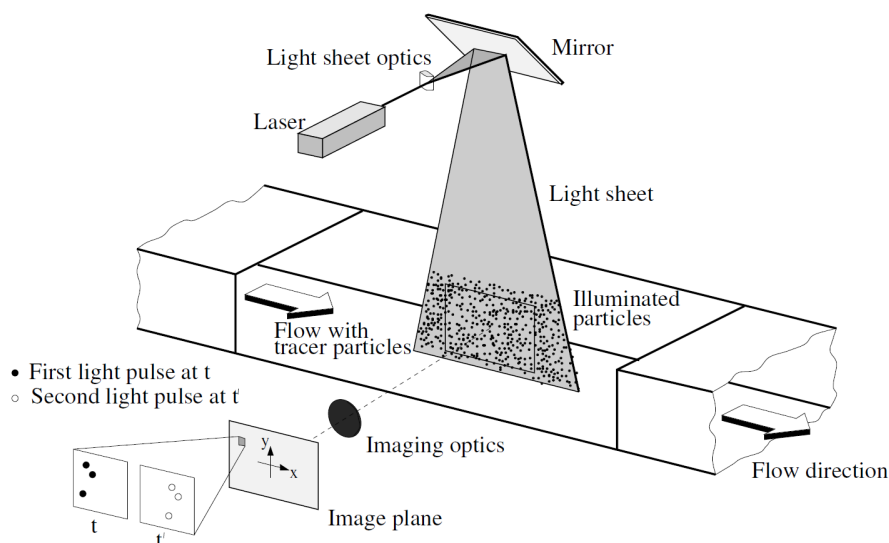


**Fig. 2-23.** Experimental arrangement for a Particle Image Velocimetry measurement in a wind tunnel ([170], p. 4).

The laser is used for the illumination of a plane of the flow, which can be either liquid or gaseous. The width of the light sheet is manipulated by light sheet optics. The tracer particles are illuminated by the laser and scatter the light, which is recorded by the camera. In most cases a pulsed laser is used. The flow is illuminated twice by the laser within a very short time at  $t$  and  $t'$ . The camera records these two images either on a single frame or on two separate frames. The tracer particles have to follow the flow as far as possible without the influence of inertia. Therefore, the particles should be small and the density should be similar to the fluid. The interaction of particles with vortices is shown in Fig. 2-24. An indicator for the movement of the particles is the dimensionless Stokes number  $St$ , which is defined as ([171], p. 831):

$$St = \frac{\rho_p \cdot d_p^2 \cdot w}{18 \cdot \eta_l \cdot d_{\text{vortex}}} \quad (2-55)$$

In Eq. (2-55),  $\rho_p$  is the density of the tracer particles,  $d_p$  is the diameter of the tracer particles,  $w$  is the liquid velocity,  $\eta_l$  is the dynamic viscosity of the liquid, and  $d_{\text{vortex}}$  is the vortex diameter as characteristic length. Large particles with a Stokes number greater than one will be unaffected by the vortex due to their large inertia. Small particles with a Stokes number less than one, however, will be in dynamic equilibrium with the fluid and, thus will follow the streamlines of the vertical flow. Particles of intermediate size with a Stokes number of one will be centrifuged from the vortex cores and accumulate at the edge of the vortices. This would lead to highly inhomogeneous particle concentrations, which will affect the resulting PIV analysis significantly ([171], p. 830; [172], p. 68). Thus, tracer particles should be as small as possible to neglect an influence of inertia. However, the smaller the particles, the worse the light scattering. Hence, a compromise between flow properties and scattering properties has to be made ([170], p. 33ff.). In aqueous systems, solid particles with a median diameter of 10 to 500  $\mu\text{m}$  made from, e.g., polyamide or hollow glass spheres are commonly used as tracer particles ([170], p. 49).

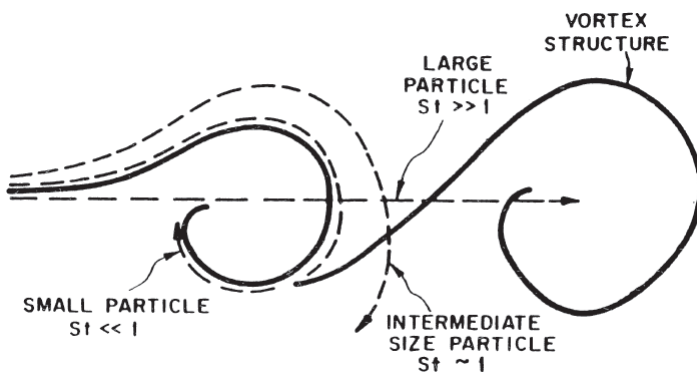
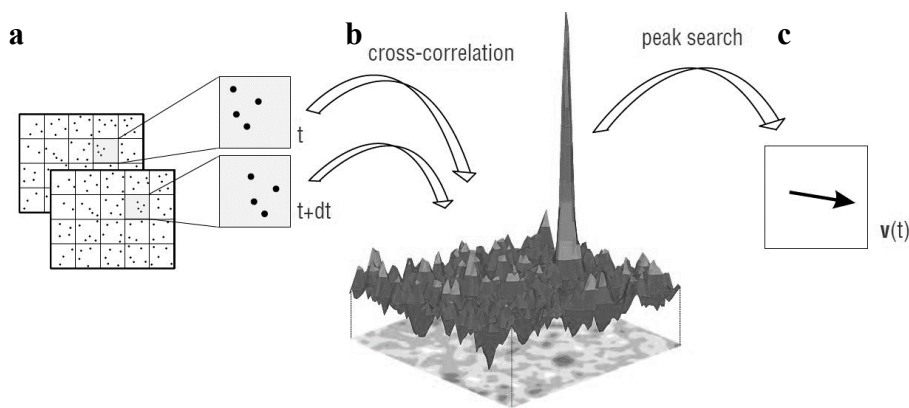


Fig. 2-24. Particle interaction with a vortex depending on the dimensionless Stokes number  $St$  ([171], p. 830).

In order to analyse the PIV measurements, each obtained image is divided into small subareas, so-called interrogation areas ([170], p. 129). The images are then analysed using statistical methods, for example the cross-correlation method ([170], p. 136ff.). A schematic representation of the cross-correlation algorithm for analysis of a PIV data set is shown in Fig. 2-25. The interrogation areas are overlapped to a certain degree and the movement of a particle collective at the two times  $t$  and  $t+dt$  is compared for each interrogation area (Fig. 2-25a). As a result, a probability function of the particle movement is produced (Fig. 2-25b). The highest peak in the correlation plane indicates the most probable mean displacement of the particles in an interrogation area. Thus, a vector giving information on, e.g., the direction of the flow or the velocity is produced (Fig. 2-25c).

Regarding the tracer particles special care has to be taken in order to establish a decent particle concentration so that an analysis with standard statistical PIV evaluation techniques is feasible. Generally, three different types of particle concentrations can be qualitatively distinguished ([170], p. 6f.). When the seeding concentration is too low, the images of individual particles can be detected and, thus tracking methods for evaluation have to be applied. Therefore, only a particle tracking is possible (see also chapter 2.4.2). If the seeding concentration is too high, the flow structure is influenced by the particles. Additionally, standard statistical PIV evaluation techniques fail in the evaluation procedure due to the formation of speckles when the images are overlapped. Thus, this case is also referred to as Laser Speckle Velocimetry ([170], p. 10f.). Typical seeding concentrations for PIV applications using standard statistical methods for the data analysis are given in literature. The stated values vary, however, between different authors in a range of 4-5 particles per interrogation area up to a range of 8-10 particles per interrogation area ([173]; [174], p. 24; [175]).



**Fig. 2-25.** Schematic representation of the cross-correlation algorithm for analysis of PIV data [176]: overlapping of captured images at  $t$  and  $t+dt$  and comparison of each interrogation area (a), establishment of a probability function (b), and resulting vector from peak search (c).

### 2.4.2 Particle Tracking Velocimetry

The Particle Tracking Velocimetry (PTV) is like PIV and SH also a non-invasive optical measurement technique to evaluate flow conditions, e.g., flow velocities and directions as already stated in chapter 2.4.1. In contrast to PIV, PTV analyses the behaviour of a single particle instead of a particle cluster. The measurement procedure is similar to PIV: tracer particles are added to the flow and a laser illuminates the particles. A camera records two consecutive images, which are then analysed. Instead of statistical methods as described in chapter 2.4.1, PTV tries to recognize and rediscover each individual particle at the time  $t$  and  $t+dt$  [177]. Thus, the particle concentration has to be low in order to facilitate a tracking of the particles.

The general technique of PTV can also be modified and applied to rising bubbles, relating to a Bubble Tracking Velocimetry (BTV). The bubbles are then considered to be large particles. Typically, the centroid of the bubbles is tracked in order to calculate rising velocities. Furthermore, bubble trajectories can be reproduced using this information.

An exemplary BTV is presented in Fig. 2-26 for a rising single bubble in deionized water. The image sequence is shown as an overlay of 20 images. Using the tracked bubble centroids from Fig. 2-26a, the rising velocity  $w_B$  can be calculated for each time  $t$ . Further bubble parameters, e.g. the bubble diameter  $d_B$ , can also be derived with respect to time from such an analysis. Thus, a deeper insight into the behaviour of rising bubbles is facilitated.

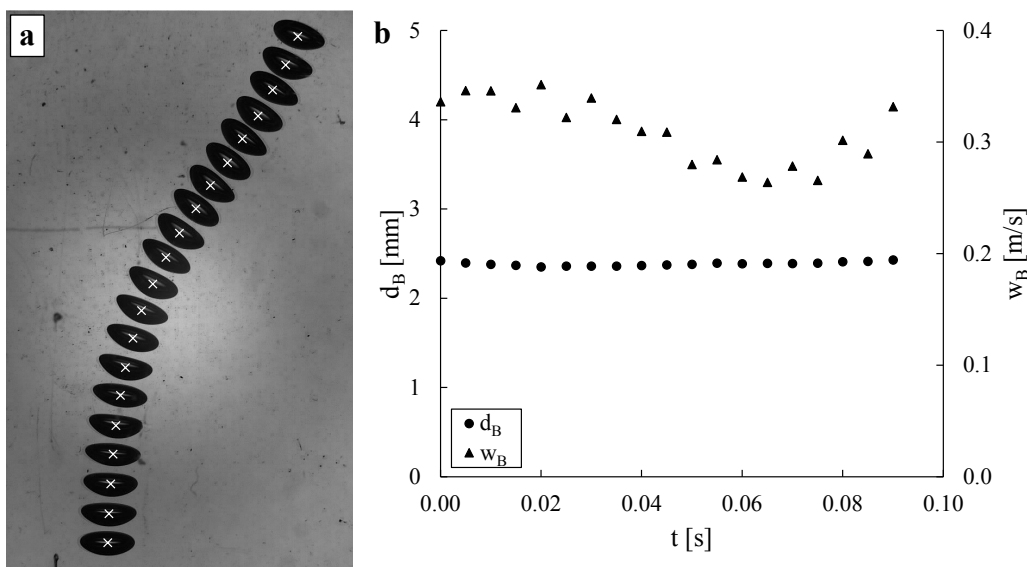


**Fig. 2-26.** Image sequence of a single bubble rising in deionized water shown as an overlay image with marked positions of bubble centroids as white “x” (a) and results of time-resolved bubble diameter  $d_B$  (circles) as well as rising velocity  $w_B$  (triangles) (b).

## 2.5 Surface modification of glass

One of the most common types of glass is soda lime glass. Its chemical composition is given by  $\text{Na}_2\text{O}\cdot\text{CaO}\cdot\text{SiO}_2$  with approx. 12.9 wt%  $\text{Na}_2\text{O}$ , 11.6 wt%  $\text{CaO}$  and 75.5 wt%  $\text{SiO}_2$  ([178], p. 976). The glass surface consists mainly of Si-O-Si bonds with a small amount of Si-OH bonds. Typically, water and hydrocarbons from the surrounding air are adsorbed at the glass surface ([179], p. 5). An activation with strong acids removes the adsorbed species and additionally results in the formation of new hydroxyl groups on the glass surface that can be used for reactions with chemicals.

For modification of glass surfaces, silanes are widely used. There are many different types of silanes available like silanols, chlorosilanes, or alkoxy silanes. The reactivity decreases from alkoxy silanes over silanols to chlorosilanes ([180], p. 23f.).

The reaction mechanism for trialkoxysilanes with a glass surface is given in Fig. 2-27. The mechanism consists of four main steps: hydrolysis of the silane, adsorption of the silane on the glass surface, oligomerisation of the silane, and covalent bonding of the silane on the surface. In the first step, the alkoxy groups of the silanes are eliminated in the presence of water (1). Hydroxyl groups remain at the silicon atom, which can adsorb on glass surfaces via hydrogen bonds (2). In this stage the silanes are still mobile on the glass surface. After adsorption of more silane molecules via hydrogen bonds, condensation reactions between silane molecules take place, which lead to the formation of oligomers (3). Finally, with elimination of water these oligomers are bound to the glass surface via covalent bonds (4). Although these reactions are presented sequentially, they can occur simultaneously after the initial hydrolysis step ([181], p. 6).

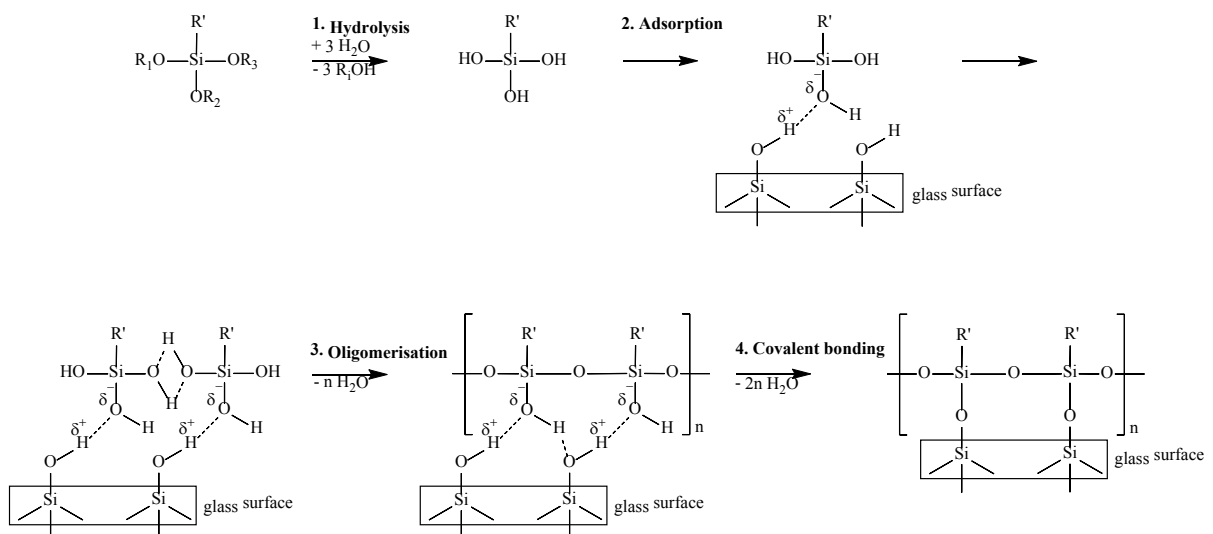


**Fig. 2-27.** Reaction mechanism of trialkoxysilanes with glass surfaces (adapted from [179], p. 8–9; [180], p. 24).

$\text{R}'$  represents a hydrophobic rest and  $\text{R}_i$  are short alkyl chains, e.g. ethyl.

The development of the silane layers starts with formation of islands which may grow together to a connected layer. The reaction rate is fast until a coverage of approx. 75 %, while it takes very long to form a complete monolayer [182]. The layers are stable against water, organic solvents, surfactant solutions and diluted acids, while they are removed in presence of diluted bases ([180], p. 25).

For a good adsorption of the silane molecules on the glass surface, the latter has to be clean and should furthermore possess a large amount of hydroxyl groups. The average density of silanol groups found at the surface of glass slides is approx. 2.5 OH groups per nm<sup>2</sup> [183,184]. Treatment of the glass surfaces by using strong acids, e.g. peroxymonosulfuric acid, also called Caro's acid or piranha acid, is often the first step described in literature for preparation of the glass surfaces in order to carry out silanisation reactions [185–188]. Caro's acid is a mixture of about three parts concentrated sulphuric acid and one part hydrogen peroxide. Amongst above mentioned contaminations due to adsorbed water and hydrocarbons from the surrounding air, soda lime glass typically exhibits contaminations of, e.g., sodium ions ([187], p. 16). Hydrogen ions can substitute these sodium ions to form hydroxyl groups, which activate the glass surface (cf. Fig. 2-28). Besides cleaning, Caro's acid additionally hydroxylates the glass surface. The density of silanol groups is found to be increased to about 4.9 OH groups per nm<sup>2</sup> for a completely hydroxylated surface [183,189].

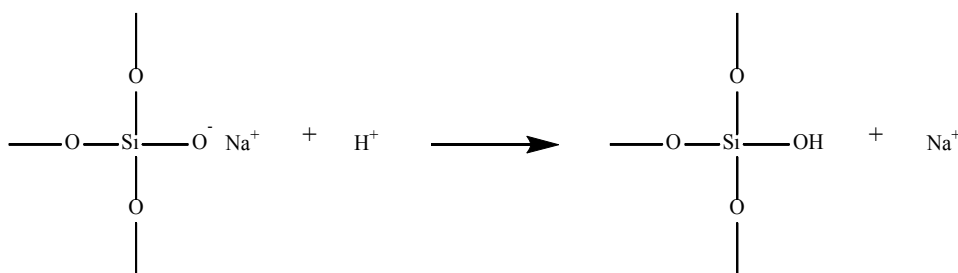


**Fig. 2-28.** Reaction of sodium ions on glass surfaces with strong acids (adapted from [187], p. 16).

### **3 Materials and methods**

In this chapter, all necessary experimental setups as well as methods for the experiments are presented. A complete list of used materials, chemicals, and software can be found in Appendix 9.1.1.

#### **3.1 Experimental setups**

For the experiments, which are presented in chapters 4 to 6, different experimental setups are used. A short description of each experimental setup is presented in this chapter.

##### **3.1.1 Single bubble apparatuses**

The main focus of the present work is the investigation of single bubble heterocoagulates (cf. chapter 1.2). For this purpose, a single bubble flotation column is designed. Furthermore, an alternative experimental setup for single bubble experiments is presented, which is used for measurements under simplified conditions.

###### **3.1.1.1 Single bubble flotation column**

For optical investigations in a system with reduced amount of bubbles and particles, a single bubble flotation column is designed. As stated in chapter 2.3.3, several experimental setups have been already proposed in literature. Most of these, however, do not allow an unhindered investigation of rising bubbles and bubble-particle heterocoagulates. Additionally, the main purpose of these setups is to work as samplers by allowing only a small amount of the complete stream to pass into the measurement area. The investigation of single bubbles and single bubble-particle heterocoagulates is, thus, not feasible with these proposed methods, which is why a novel apparatus is designed. The designed apparatus combines different aspects of experimental setups proposed in literature. A sketch of the single bubble flotation column is given in Fig. 3-1. The apparatus is designed modularly so that each part can be easily exchanged if the experimental parameters are changed.

The apparatus is made of three millimetre thick poly(methyl methacrylate) (PMMA) for a complete optical accessibility of the apparatus. A special type of PMMA (Plexiglas<sup>®</sup> GS 2458), which is UV-permeable, is used allowing an optical investigation of, e.g. fluorescent calcium fluoride ores (see chapter 2.1.4.1 and 6.2). The transmission spectrum of the PMMA is given in Appendix 9.1.1. The different modules are connected via six millimetre thick PMMA flange joints.

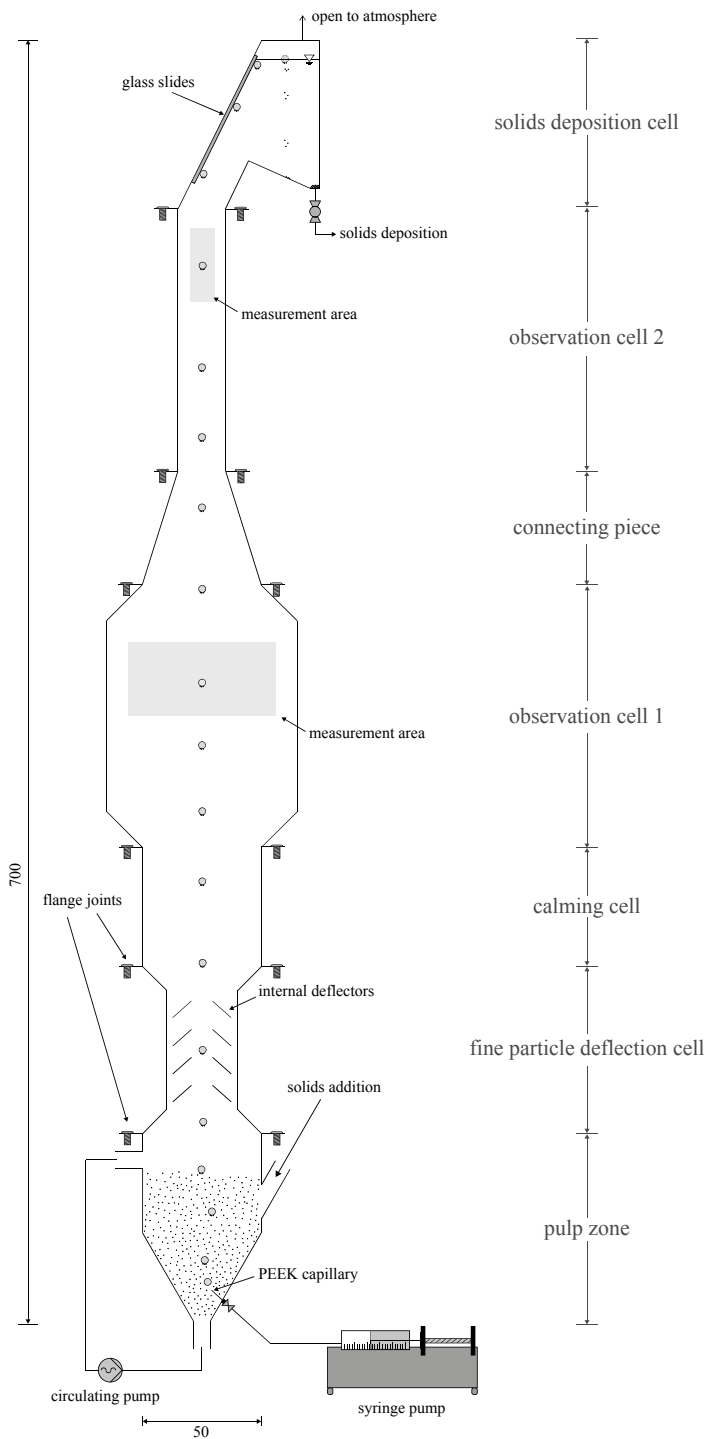


**Fig. 3-1.** Sketch of the designed single bubble flotation column (all dimensions in millimetres).

Between each flange joint a rubber sealing is placed to prevent leakage. Screws are used for a tight connection of the flange joints. The apparatus is divided into five main parts:

1. dispersion cell,
2. deflection cell,
3. calming cell,
4. observation cells,
5. and solids deposition cell.

The function of each part is described in the following sections. The different parts are designed in Adobe Illustrator and afterwards cut out using a carbon dioxide laser. The parts are agglutinated using Acrifix<sup>®</sup> 1R 192, which is a one component polymerisation adhesive based on an acrylic resin in methyl methacrylate, which is the monomer of PMMA. Under the influence of light the adhesive polymerises and, thus a tight connection between the parts is achieved.

#### **3.1.1.1.1 Dispersion cell**

The dispersion cell is the bottom part of the apparatus. As can be seen in Fig. 3-1, the cell has connections for circulation of the solution using a pump, one at the bottom of the apparatus and one on the left-hand side. For flotation experiments, solid particles are introduced into the apparatus via the connection on the right-hand of the apparatus. The circulating stream enters at the bottom of the apparatus. Particles inside the apparatus, which tend to settle, are drawn upwards in flow direction. Ideally, all of the circulating flow is kept inside the dispersion cell so that the rest of the apparatus is not influenced by the pump. This facilitates the investigation of freely rising single bubbles and single bubble-particle heterocoagulates.

A polyether ether ketone (PEEK) capillary is introduced at the bottom of the apparatus via a valve. The capillary is connected to a gastight syringe and a high-precision syringe pump. The syringe pump can be controlled to adjust the volumetric gas flow rate. In the present work, PEEK capillaries with internal diameters of 130  $\mu\text{m}$ , 250  $\mu\text{m}$ , and 500  $\mu\text{m}$  are used.

#### **3.1.1.1.2 Deflection cell**

The deflection cell is directly above the dispersion cell (see Fig. 3-1). The width changes in this section from 50 mm to 30 mm. Furthermore, deflectors made from 3 mm thick PMMA plates are installed in this cell at an angle of approx. 40°. The purpose of the deflection cell is on the one hand to centre the rising bubbles, which simplifies the optical analysis in the observation cells. On the other hand, entrained fine particles, which could rise in the wake of rising bubbles and/or heterocoagulates during flotation experiments without being actually attached to the bubble surface, should be deflected so that they settle back into the dispersion cell. This process is depicted schematically in Fig. 3-2. In this way, measurement errors are prevented, when mass balances are applied to determine flotation recoveries and kinetics. Furthermore, fine particles would quickly pollute the observation cells, which would complicate or even prevent optical investigations of the rising bubbles and heterocoagulates.

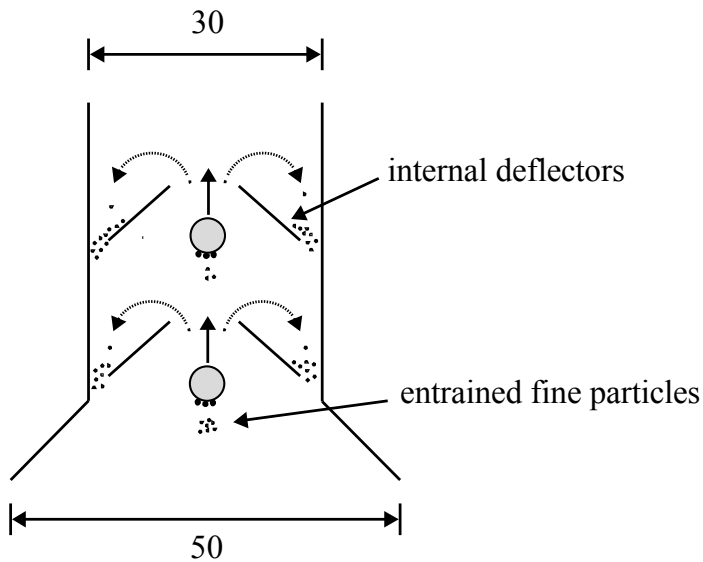


**Fig. 3-2.** Schematic representation of fine particle deflection in the deflection cell, when fine particles rise in the wake of bubble-particle heterocoagulates. Bold arrows indicate heterocoagulate rising path and dashed arrows resemble fine particle trajectories due to deflection (all dimensions in millimetres).

#### 3.1.1.1.3 Calming cell

The calming cell is on top of the deflection cell. In this part of the flotation column the width expands from 30 mm back to 50 mm. This part of the apparatus should ensure that rising bubbles and heterocoagulates have reached their terminal velocity again, before entering the areas above for optical measurements. Furthermore, this cell works as additional buffer in case very fine particles, which were not affected by the deflectors, may have been entrained.

#### 3.1.1.1.4 Observation cells

After the calming cell two observation cells are installed, which are aligned perpendicularly. A connecting piece between the two cells enables a 90° rotation, which prevents interference between the two applied optical methods Shadowgraphy (SH) and Particle Image Velocimetry (PIV). The width of the observation cells is increased from 50 mm to 80 mm in order to allow a larger viewing space. In the lower observation cell, SH measurements are typically conducted. For this purpose, a high-speed camera is placed opposite to an LED illumination. The theoretical aspects of the SH method have been presented in chapter 2.3.3.2. The second observation cell is used for the hydrodynamic characterisation via PIV, which has been explained in chapter 2.4.1. For PIV measurements, a continuous wave laser is placed perpendicularly to a high-speed camera.

### 3.1.1.1.5 Solids deposition cell

The solids deposition cell is the top part of the designed single bubble flotation column. This cell is open to the atmosphere so that a free surface is present. As can be seen in Fig. 3-1, bubbles and heterocoagulates entering the deposition cell are guided towards the free surface by an inclined surface. Glass slides are mounted on the inclined surface to prevent attachment of bubbles and heterocoagulates on the PMMA surface, which would falsify mass balance and kinetic measurements. Since only single bubbles are present in this experimental setup, no foam or froth formation occurs. The bubbles and heterocoagulates burst at the free surface. In case of heterocoagulates, the floated particles will then settle to the bottom of this cell, where the collected particles can be removed via two installed ball valves. The function of the solids deposition cell is schematically depicted in Fig. 3-3.

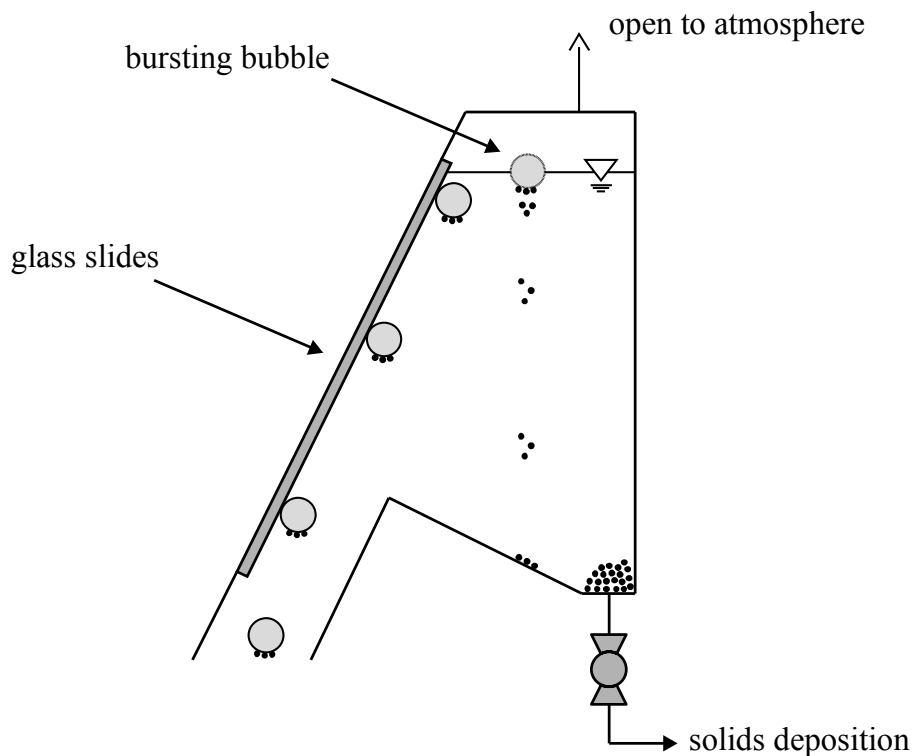


**Fig. 3-3.** Schematic representation of the solids deposition cell with a rising heterocoagulate bursting at free surface and settling particles.

### 3.1.1.2 Alternative experimental setup for simplified measurements

For simplified experiments, an additional measurement cell is designed. A schematic representation of the experimental setup is given in Fig. 3-4. The alternative measurement cell provides two valves for introduction of a capillary into the cell, one at an angle of approx.  $45^\circ$  (right-hand side) and one at an angle of  $90^\circ$  introduced directly at the bottom of the apparatus. The width of the apparatus is similarly to the observation cells of the single bubble flotation column (cf. chapter 3.1.1.1.4) increasing from 50 mm to 80 mm in order to allow a larger viewing area. The volume of the apparatus is approx. 120 mL. For the investigation of rising single bubbles the measurement area is arbitrarily positioned approximately 35 mm above the capillary outlet. This measurement cell has the advantage of a higher compactness in contrast to the single bubble flotation column presented in chapter 3.1.1.1.

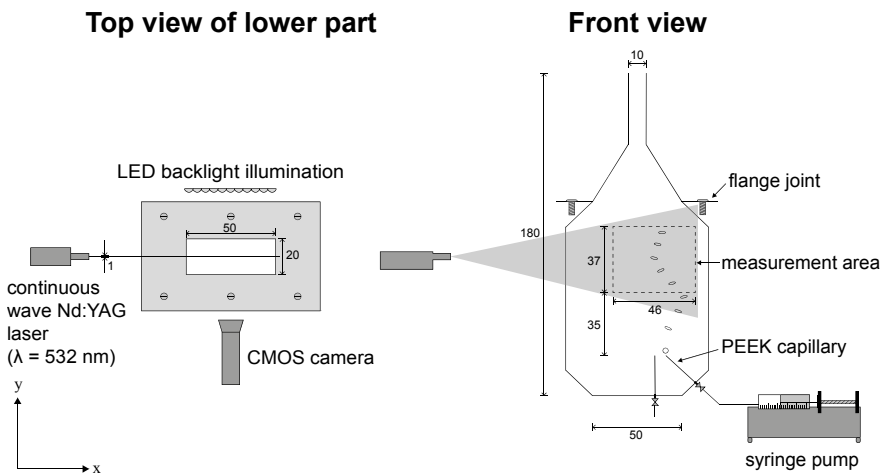


**Fig. 3-4.** Schematic representation of the experimental setup for Shadowgraphy and PIV experiments used for simplified single bubble experiments (all dimensions in millimetres). Upper part above flange joint is used for fixation of the setup. All measurements are conducted in the lower part below the flange joint.

### 3.1.2 Bubble swarm investigations

The results obtained for single bubble behaviour should be used to determine underlying mechanisms in bubble swarms (cf. chapter 1.2). In order to perform batch-flotation tests with development of a froth, an apparatus which produces bubble swarms has to be used. For this purpose, a flotation cell in laboratory scale ( $V=2$  L) is used. A schematic drawing of the experimental setup is given in Fig. 3-5. Ambient air is compressed by a screw compressor. A downstream filter separates oil droplets from the air. The length of the pipeline is sufficiently long to ensure that the air is oil-free when it reaches the outlet valve in the laboratory at a pressure of approx. 5 bar. A variable area flowmeter is used to adjust the volumetric gas flow rate. The air is introduced into the apparatus via a porous frit to form small bubbles directly beneath the stirrer. The apparatus is made of transparent PMMA providing an optical accessibility. A Rushton turbine is used to suspend the solid particles as well as to disperse and comminute the air bubbles. Small baffles made from PMMA are installed close to the stirrer in order to prevent an unwanted vortex formation. The apparatus is divided into two sections by a vertical plate. On the left-hand side, high turbulence is induced by agitation and the bubbly flow. On the right-hand side, the flow is calmed, supporting a stable froth formation. Furthermore, entrained particles can settle back into pulp zone. This mechanism is supported by an inclined wall on the right-hand side of the apparatus. The froth is skimmed manually at the top right side of the apparatus with a wiper and collected in glass beakers. Further treatment includes filtration and washing of the particles with, e.g., deionized water. A pH sensor can be included in the experimental setup to monitor the pH value during the experiments.

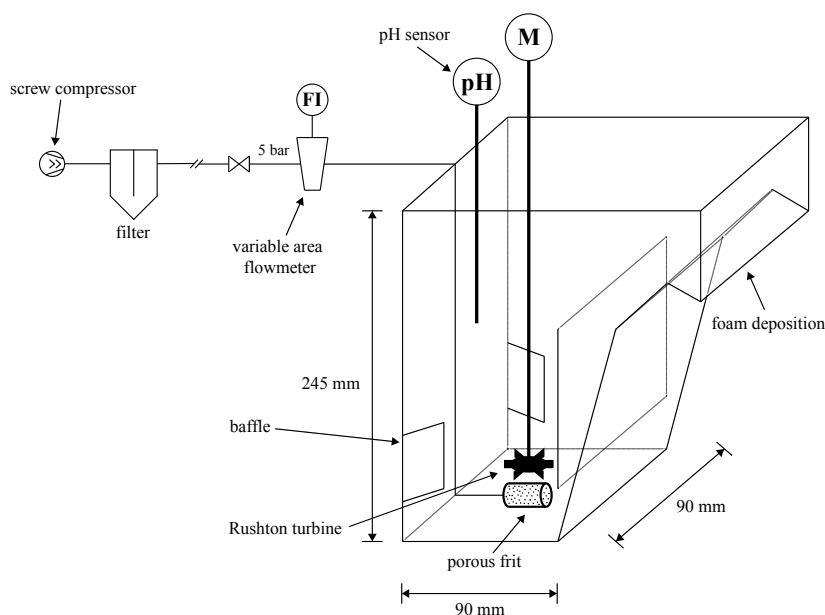


**Fig. 3-5.** Schematic experimental setup for froth flotation experiments.

## 3.2 Analysis methods

In this chapter, the methods used for analysis of the Shadowgraphy (SH) and Particle Image Velocimetry (PIV) image sequences are introduced. Furthermore, a newly developed quantification method for calcium fluoride ( $\text{CaF}_2$ ) in fluorite samples via Fourier Transform (FT) Raman spectroscopy is presented.

### 3.2.1 Automatic image analysis for Shadowgraphy measurements

Parts of this chapter have been published in [190]. The images sequences of rising single bubbles in the present study obtained via Shadowgraphy should be analysed time-resolved and with high accuracy. Due to the large amount of data, an automated analysis routine is developed. For this purpose the open source software KNIME<sup>®</sup> is chosen, which is a graphical program for analysing data. The workflow is based on so-called “nodes”, where typical analysing routines from different libraries, e.g. ImageJ, are already implemented. Due to its highly modular basis, it is possible to implement an automatic analysing routine. Key parameters for the analysis of the image sequences are the equivalent bubble diameter, the tracking of the bubble centroids for representation of bubble trajectories as well as calculation of the rising velocity, and the elongation as a morphological parameter for a quantitative description of the bubble shape. The data can be easily exported to Excel for further analysis.

#### 3.2.1.1 Analysing procedure for single bubbles

The developed analysing routine is shown in Fig. 3-6. The basic steps of the image analysis procedure are:

1. image import,
2. projection of the maximum intensity,
3. median filtering,
4. background subtraction,
5. determination of bubbles in the image,
6. removal of images with bubbles touching the image border,
7. extraction of bubbles as bitmasks from images,
8. bubble analysis,
9. and data export to Excel.

The image sequences are imported in .jpg format using the Image Reader node (1). The Projector node projects the dimensions of the images into one single dimension, which is in the present case the channel (2).

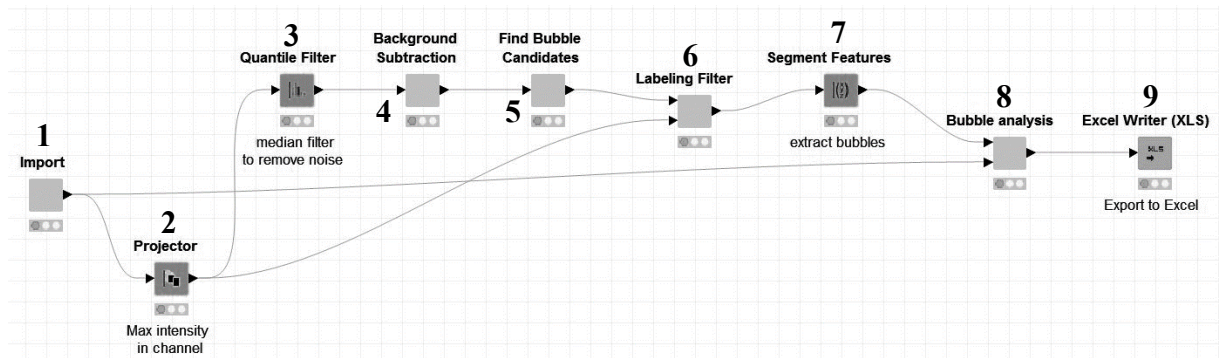


**Fig. 3-6.** Implemented analysing routine in KNIME<sup>®</sup> (summarized flow sheet for a better overview).

The projection operation is the maximum intensity, which chooses the pixels with the highest intensity from every channel and projects it to the new channel. An application of this procedure to an RGB image containing three colour channels would produce an image containing only one channel with all three colours. Afterwards, a median filter is applied using the Quantile Filter node with a value of 50 (3). This node approximates a generalized median filter using the algorithm from Perreault and Hebert [191]. In the next step, a background subtraction is carried out (4). This step is necessary to remove unwanted disturbances from the images, e.g. uneven illumination and scratches. The background subtraction is based on two steps:

1. creation of a maximum intensity projection (MIP). This creates an output image each of whose pixels contains the maximum value over all images which are in the workflow at the particular pixel location;
2. subtraction of the MIP from every single other image.

Afterwards, a subroutine for finding bubbles in the images is applied (5). This subroutine can be divided into three steps:

1. inversion of the image;
2. application of a global threshold with the Global Thresholder node. In the present case, the Otsu method as thresholding method is used [192]. Its basic idea is to find the threshold, which minimises the weighted within-class variance. It operates directly on the grey level histogram, which is why computation time is fast once the histogram is generated. This method can only be accurately applied to uniform illuminated images. This premise is fulfilled due to the application of the median filter in step (3). Grau showed in his work a successful application of the Otsu method to automatically determine bubble parameters and to improve automation [193].
3. The Connected Component Analysis node is used to identify connected components in the images, in the present case bubbles. It is an algorithm which applies graph theory. Subsets

of connected components are uniquely labelled based on a given heuristic. In the present procedure, a two-pass algorithm is implemented, meaning that the algorithm iterates through two-dimensional binary data. Thereby, the algorithm makes two passes over the image: in the first pass, labels are assigned temporarily and equivalences are recorded; in the second pass, each temporary label is replaced by the smallest label of its equivalence class. Afterwards, connectivity checks are carried out. Neighbouring elements with the same label are identified as one object.

In the next step, a filter is applied to remove images, where bubbles are touching the image borders (6). This ensures that only bubbles which are fully visible in the images are analysed. Afterwards, the detected bubbles are extracted as bitmaps from the images (7). These bitmaps are then analysed using the Feature Calculator node with respect to the aforementioned bubble characteristics (see chapter 3.2.1). The equivalent bubble diameter is determined from the longest and shortest diameters,  $d_{\text{major}}$  and  $d_{\text{minor}}$ , respectively, of an ellipse fitted to the object (see Fig. 3-7). The fitted ellipse will have the same area, orientation, and centroid as the object [194]. The equivalent diameter is calculated according to Eq. (3-1) assuming rotational symmetry around the y axis:

$$d_B = (d_{\text{minor}} \cdot d_{\text{major}}^2)^{1/3} \quad (3-1)$$

With the determined diameters, the elongation  $f_e$  as shape descriptor is calculated. It is defined as:

$$f_e = 1 - \frac{d_{\text{minor}}}{d_{\text{major}}} \quad (3-2)$$

The domain for the elongation is between 0 and 1, with 0 for a perfect circle and 1 for an infinite stretched ellipse (= a line). Therefore, the elongation is an indicator for the sphericity of the bubbles.

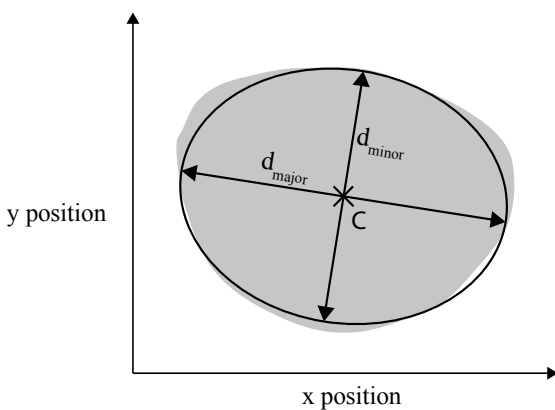


**Fig. 3-7.** Geometric shape parameters of a particle with  $C(x,y)$  as object centroid: fitted ellipse for determining longest object diameter  $d_{\text{major}}$  and shortest object diameter  $d_{\text{minor}}$ .

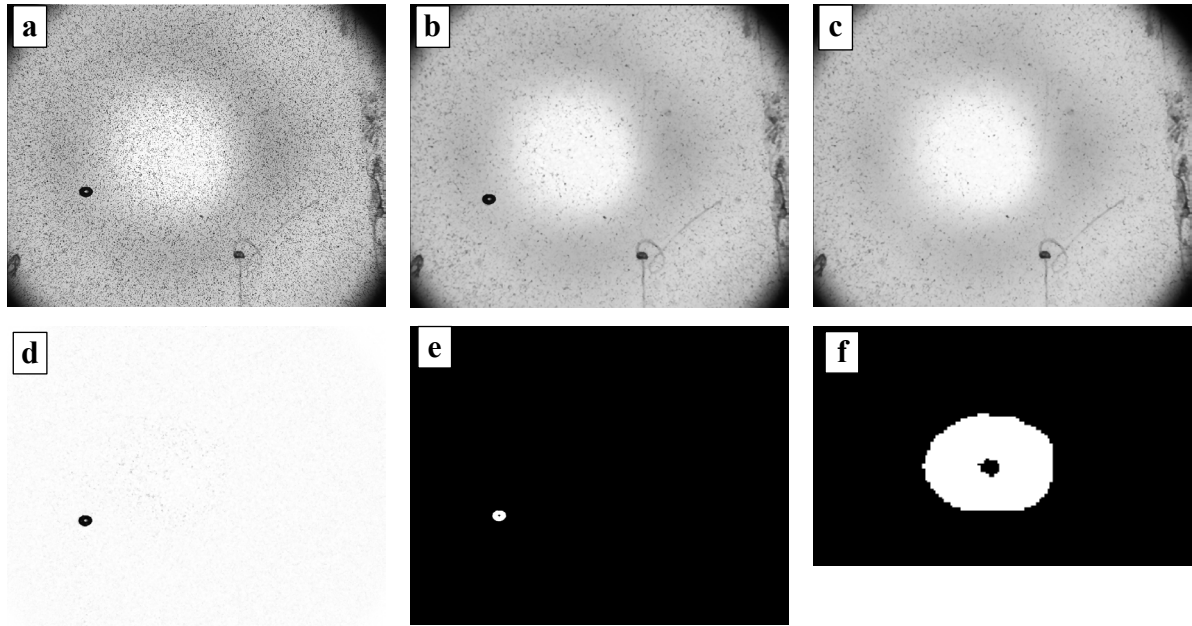


**Fig. 3-8.** Image processing of the automated routine at the example of a rising single bubble: a) original image, b) median filtering, c) maximum intensity projection, d) background subtraction, e) Otsu threshold, f) bubble bitmask (zoomed).

Additionally, the centroid position  $C(x,y)$  of the bitmasks is determined. The centroid is the average of all  $x$  and  $y$  coordinates of all the pixels in the bitmask. The determined  $x$  and  $y$  values can later be used in Excel to visualise the bubble trajectories. Furthermore, the bubble rising velocity is calculated between each frame considering only the motion in vertical  $y$  direction:

$$w_B = \frac{\Delta y}{\Delta t} = \frac{y(t_2) - y(t_1)}{t_2 - t_1} \quad (3-3)$$

The distance  $\Delta y$  is calculated from the determined coordinates of the centroid for two consecutive frames. The time interval  $\Delta t$  between two frames is known, as the camera frame rate (fps) is known.

At the end, all data is exported to an Excel spreadsheet for further data processing using the Excel Writer node (9). The main steps of the image processing are shown in Fig. 3-8.

### 3.2.1.2 Image analysis validation

To validate the accuracy of the developed method, two different procedures are carried out: 1) using static computer generated shapes, 2) using precision grade solid glass spheres. Afterwards, a proof of concept is shown by investigating a rising single bubble in deionized water. All data is analysed with a critical statistical evaluation.

From validation with computer generated geometric shapes varying in size (25–200 px) and aspect ratio (1:1–5:1) it is found that magnification plays an important role for a precise analysis of the objects. Further results may be found in [190]. For a validation under dynamic conditions,

precision grade glass spheres settling in deionized water are analysed. The apparatus used for the experiments is the simplified setup presented in Fig. 3-4 in chapter 3.1.1.2.

The diameter of the precision glass spheres is 0.7 mm, 1.0 mm, 2.0 mm, and 2.5 mm, respectively, with a roundness of  $\geq 0.99$  (tolerances:  $\pm 0.02$  mm in diameter and  $\leq 0.02$  mm in roundness). This procedure is in accordance with BS ISO 13322-2, where calibration tests with at least three different particle sizes are recommended [195]. The spheres are first immersed into deionized water with tweezers and only afterwards released in order to prevent attachment of unwanted gas bubbles on the particle surface. Measurements are carried out using a Shadowgraphy system as explained in chapters 2.3.3.2 and 3.1.1.1.4. A camera frame rate of 500 fps is chosen for the experiments. At least 30 spheres of each size are analysed for a statistical discussion. Possible outliers in the data sets are identified using a combined two-sided and one-sided Dixon's Q test (cf. [190]). To determine the accuracy of the measurements, the particle diameter and elongation are analysed using Eqs. (3-1) and (3-2). The obtained results are compared with the supplier information. Furthermore, the settling velocities of the particles are calculated using Eq. (3-3) and compared with theoretical models from literature.

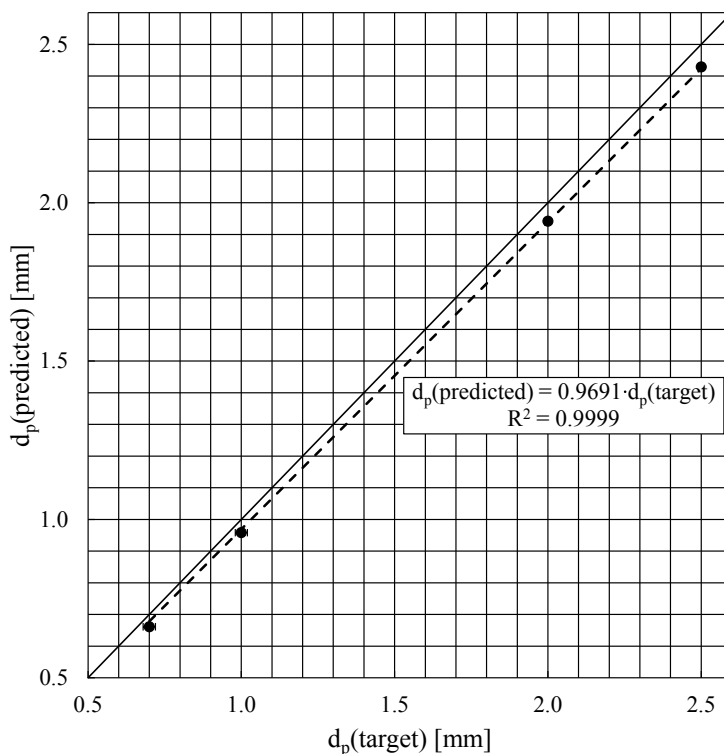


**Fig. 3-9.** Comparison between predicted and target particle diameter  $d_p$ .

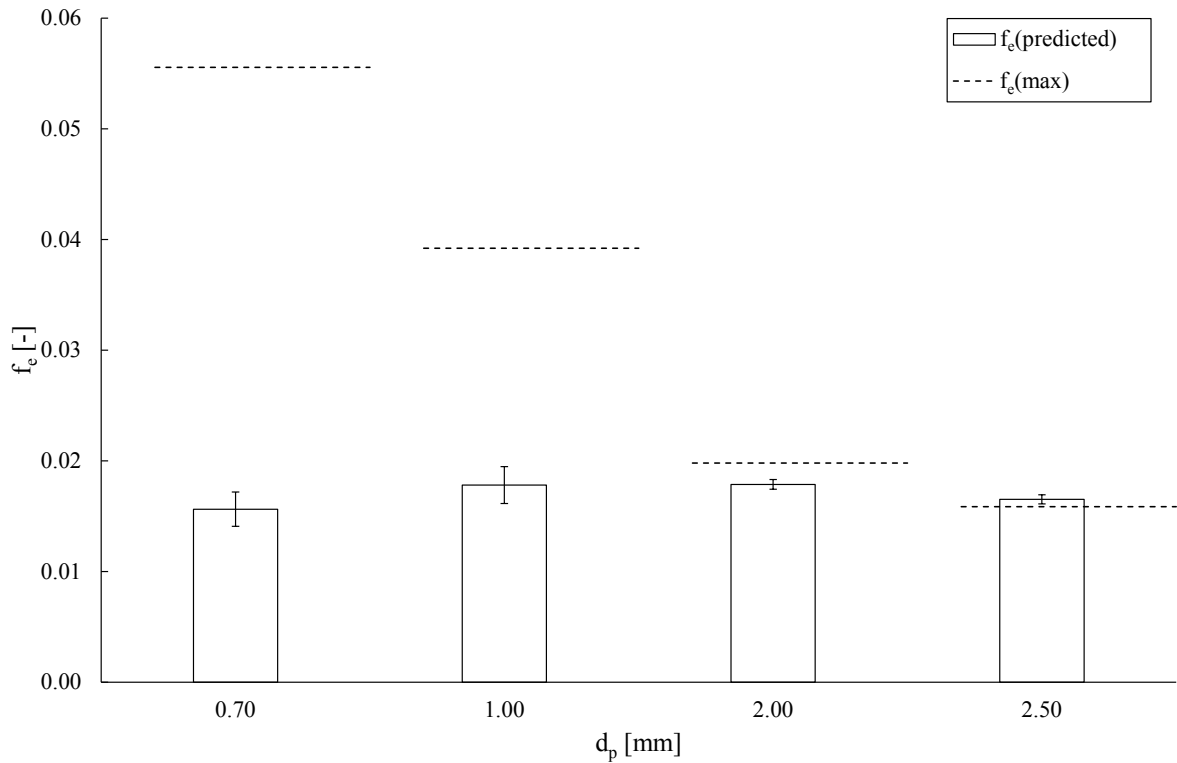


**Fig. 3-10.** Comparison of predicted elongation  $f_e$  for different particle diameters  $d_p$  with maximum allowable elongation  $f_e(\text{max})$  based on the tolerances given by the supplier.

A comparison of the target diameter and the measured (predicted) diameter is shown in Fig. 3-9. The absolute deviation increases with increasing particle diameter. At the maximum target diameter of 2.5 mm the relative error is, however, still minor with a relative difference of 2.8 %. The comparison of the predicted elongation with the maximum allowable elongation of the particles as given by the tolerances of the supplier is presented in Fig. 3-10. The predicted elongation is always below the maximum allowable elongation except for  $d_p=2.5$  mm. The relative deviation between predicted and maximum elongation at this particle diameter is, however, small with about 4 %. Furthermore, the values determined for  $f_e$  are close to zero. Thus, the sphericity of the particles is detected precisely.

As shown in Tab. 3-1 the determined experimental settling velocities are close to theoretical calculations. For calculation of the theoretical terminal settling velocity of a sphere, Eq. (3-4) is used:

$$w_s = \sqrt{\frac{4}{3} \cdot \frac{(\rho_p - \rho_l) \cdot g \cdot d_p}{\rho_l \cdot c_D}} \quad (3-4)$$

In Eq. (3-4),  $\rho_p$  is the density of the particle ( $2500 \text{ kg/m}^3$ ) and  $\rho_l$  is the density of the fluid ( $997 \text{ kg/m}^3$ ). The densities of the solid particles and the deionized water have been determined experimentally with a pycnometer.

The drag coefficient  $c_D$  is a function of the particle Reynolds number  $Re_p$ , which is generally defined as:

$$Re_p = \frac{d_p \cdot w_s \cdot \rho_l}{\eta_l} \quad (3-5)$$

For particles with a diameter of 2.0 mm and 2.5 mm,  $c_D$  is calculated using Kaskas's equation (valid for  $Re_p < 2 \cdot 10^5$ ):

$$c_D = \frac{24}{Re_p} + \frac{4}{\sqrt{Re_p}} + 0.4 \quad (3-6)$$

The particle Reynolds number for particles with a diameter of 0.7 mm and 1.0 mm is calculated with Martin's equation [196], which is valid for  $Re_p < 2 \cdot 10^5$ :

$$Re_p = 18 \cdot \left[ \sqrt{1 + \frac{1}{9} \cdot \sqrt{Ar_p - 1}} \right]^2 = \frac{w_s \cdot d_p}{\nu_l} \quad (3-7)$$

In Eq. (3-7),  $\nu_l$  is the kinematic viscosity of the fluid and  $Ar_p$  is the particle Archimedes number, which is defined as:

$$Ar_p = \frac{g \cdot (\rho_p - \rho_l)}{\nu_l^2 \cdot \rho_l} \cdot d_p^3 \quad (3-8)$$

Although Eqs. (3-6) and Eq. (3-7) have the same limitation for  $Re_p$  and are therefore valid for all investigated sphere diameters, a better fit to the experimental data is found when using Martin's equation for the two smallest particle diameters of 0.7 mm and 1.0 mm. A proof of concept for application of the developed analysis routine has already been presented in Fig. 2-26. From the above presented results it can be concluded that the developed method is precise and robust with relative errors of less than 5 %. Thus, the method can be used for further image analysis in the present work.

**Tab. 3-1.** Comparison of experimental and theoretical terminal settling velocities  $w_s$  of precision glass spheres with varying diameters in deionized water [190].

$d_p$ [mm]	$Re_p$ [-]	$w_s$ [mm/s]		relative error [%]
		experimental	theoretical	
0.7	85	$103.7 \pm 0.2$	103.5	0.1
1.0	168	$152.5 \pm 0.2$	157.5	-3.2
2.0	582	$269.1 \pm 0.8$	273.2	-1.5
2.5	851	$310.9 \pm 0.7$	316.2	-1.7

### 3.2.2 Analysis procedure for Particle Image Velocimetry image sequences

To investigate the liquid flow field induced by the rising bubbles Particle Image Velocimetry (PIV) measurements are carried out. The obtained image sequences are analysed using DynamicStudio v4.00 applying the cross-correlation algorithm [197,198]. Since single rising bubbles are analysed, a transient process is present. The bubbles enter the bottom of the viewing area and leave the area after a time interval  $\Delta t$  depending on the experimental conditions. Therefore, the image sequences have to be analysed time-resolved.

In a preceding feasibility study, the influence of the camera frame rate on the PIV results has been investigated for different volumetric gas flow rates in deionized water. The obtained vector fields have been evaluated subjectively and with respect to the number of invalid and substituted vectors as quantifiable parameter. It has been found that a higher camera frame rate leads to lower percentages of substituted vectors as shown in Tab. 3-2. Therefore, if not indicated otherwise, a camera frame rate of 300 fps will be used for the PIV measurements in the present work. The final interrogation area size is set to  $16 \times 16 \text{ px}^2$  with an overlap of 25 %. For validation of calculated vectors a peak validation factor of 0.5 with a neighbourhood of  $5 \times 5 \text{ px}^2$  and an acceptance of 0.2 are applied. The liquid velocity  $w$  is calculated using the scalar map function in DynamicStudio:

$$w = \sqrt{w_x^2 + w_y^2} \quad (3-9)$$

In Eq. (3-9),  $w_x$  is the velocity in horizontal  $x$  and  $w_y$  the velocity in vertical  $y$  direction. The vorticity is a measure of vortex strength and an indicator for the direction of the flow inside a vortex. Only two-dimensional PIV images of the liquid flow field are present in this work, which is why only the rotation  $\omega_z$  around the out-of-plane  $z$  axis can be calculated. For this purpose, the local velocities  $\partial w_y$  and  $\partial w_x$  are differentiated with respect to the locations  $\partial x$  and  $\partial y$ , respectively:

$$\omega_z = \frac{\partial w_y}{\partial x} - \frac{\partial w_x}{\partial y} \quad (3-10)$$

The vorticity can be used to characterize wake structures and to identify vortex structure patterns, e.g. that of a Kármán vortex street [199].

In addition to the time-resolved analysis, the Vector Statistics method is applied in order to produce the time-averaged mean liquid velocity  $\bar{w}$  including the variances of the velocity components in horizontal  $x$  and vertical  $y$  direction. From these variances an insight into the turbulent kinetic energy (TKE)  $k$  is provided.

**Tab. 3-2.** Mean percentage of substituted vectors in relation to total number of vectors at different camera frame rates (fps) and volumetric gas flow rates  $\dot{V}_g$ . The total number of vectors is 9010 for each frame rate.

$\dot{V}_g$ [mL/min]	Percentage of substituted vectors [%]		
	60 fps	150 fps	300 fps
0.004	$5.7 \pm 0.8$	$4.0 \pm 0.1$	$3.8 \pm 0.2$
0.050	$4.8 \pm 0.6$	$3.5 \pm 0.2$	$3.2 \pm 0.1$
2.000	$26.9 \pm 0.8$	$14.6 \pm 0.7$	$8.6 \pm 0.3$

The TKE is the mean kinetic energy per unit mass associated with vortices in turbulent flow. It is characterised by the measured root-mean-square (RMS) velocity fluctuations ([3], p. 44):

$$k = \frac{1}{2} \cdot (\overline{w_x'^2} + \overline{w_y'^2} + \overline{w_z'^2}) \quad (3-11)$$

In Eq. (3-11),  $\overline{w_x'^2}$ ,  $\overline{w_y'^2}$ , and  $\overline{w_z'^2}$  are the RMS velocity fluctuations in horizontal x, vertical y and out-of-plane z direction, respectively. As stated above, only planar (2D) images are present for an analysis so that the velocity component in z direction is not accessible. Some methods to estimate the missing component are described in literature, e.g. assuming local isotropy [200,201]. Mathematically, the sum of the variances is proportional to the TKE. However, it should be noted that in the analysis of PIV data spatial averaging over the interrogation area is performed. In contrast to this, classic fluid mechanics operate in an infinitely small fluid element ([202], p. 596). Therefore, it is more convenient to say that the measured RMS velocity fluctuations are proportional to the TKE, instead of discussing actual values. Hence, a proportionality constant  $k_{TKE}$  is defined and used for qualitative discussions related to energy content:

$$k_{TKE} \propto k \quad (3-12)$$

Lastly, the Proper Orthogonal Decomposition (POD) technique is applied to extract dynamic phenomena in the present unsteady flows. This technique was first proposed in the context of fluid mechanics by Lumley [203]. It is a multi-variate statistical method, which aims to obtain a reduced order model representing a set of data. With help of POD it is also possible to reveal relevant structures hidden in the data. Due to reasons of computational efficiency, the snapshot POD introduced by Sirovich [204–206] is widely applied [207–212]. Each instantaneous PIV measurement is considered as a snapshot of the flow. In the first step, the mean velocity field is calculated from all snapshots. By subtracting this mean velocity from all snapshots, only the fluctuating parts of the velocity components remain. Application of POD decomposes the flow

field into optimal orthogonal spatial modes, also referred to as *topo*-modes, and optimal orthogonal temporal modes, also referred to as *chrono*-modes:

$$\mathbf{w}'(\mathbf{x},t)=\sum_n^{N_{\text{mod}}} a^{(n)}(t)\cdot\varphi^{(n)}(\mathbf{x}) \quad (3-13)$$

In Eq. (3-13),  $\mathbf{w}'(\mathbf{x},t)$  is a velocity vector,  $N_{\text{mod}}$  is the total number of POD modes,  $a^{(n)}$  are the POD coefficients, which are dependent on time, and  $\varphi^{(n)}$  are the POD eigenfunctions, which are deduced from projection of the instantaneous velocity field onto the corresponding POD coefficient. POD minimises the mean square error of any partial sum of expansion, similarly to, e.g., Fourier decomposition. Each snapshot can be expanded in a series of the POD modes with the POD coefficients  $a^{(n)}$  for each mode  $n$ . Thus, the velocity field can be reconstructed using these coefficients:

$$\mathbf{w}(\mathbf{x},t)=\bar{\mathbf{w}}(\mathbf{x})+\mathbf{w}'(\mathbf{x},t)=\bar{\mathbf{w}}(\mathbf{x})+\sum_n^{N_{\text{mod}}} a^{(n)}(t)\cdot\varphi^{(n)}(\mathbf{x}) \quad (3-14)$$

In Eq. (3-14),  $\bar{\mathbf{w}}(\mathbf{x})$  is the mean velocity and  $\mathbf{w}'(\mathbf{x},t)$  is the fluctuating part, which is described by Eq. (3-13). Fukunaga showed that the eigenvalue of a POD mode is proportional to the amount of total kinetic energy from velocity fluctuations in the snapshots [213]. The calculated POD coefficients  $a^{(n)}$  are always sorted by their size so that the first modes always contain the largest amount of kinetic energy [202,214]. The mean velocity field is considered the zeroth mode of POD. With increasing coefficient number the amount of contained energy of each mode decreases.

Besides the snapshot method, which gives information on the energy distribution in the different modes, a time-resolved analysis of the POD modes is conducted using Fast Fourier Transform (FFT). For this purpose, an Excel spreadsheet with a Visual Basic Application (VBA) macro is developed for an automatic FFT analysis. With the FFT analysis, the dominant frequencies of each mode are determined. In the first step, the sampling frequency  $f_s$  is calculated by dividing the number of the sample data  $N_D$  by the time interval  $\Delta t$  of the sample data:

$$f_s=\frac{N_D}{\Delta t} \quad (3-15)$$

The number of data points operated on must be a number that is a power of two, e.g.  $2^8=256$  or  $2^9=1024$ , because the Excel analysis toolbox uses a discrete Fourier Transform. In the present work,  $N_D$  is always around 200 so that the number of data points is enlarged to 256 data points by zero-padding. This procedure is not affecting the results of the frequency analysis and is a common procedure ([215], p. 178).

In the next step, the FFT complex  $F(\omega)$  is calculated:

$$F(\omega) = \int_{-\infty}^{\infty} f(t) \cdot e^{-i\omega t} dt \quad (3-16)$$

With:

$$e^{i\omega t} = \cos(\omega t) + i \cdot \sin(\omega t) \quad (3-17)$$

In Eq. (3-16),  $f(t)$  is a signal or function,  $i$  is the unity imaginary number, and  $\omega$  is the range of angular frequencies associated with the signal. This is done using the built in FFT analysis function in Excel. Afterwards, the FFT magnitude  $A$  is calculated, which is defined by:

$$A = \frac{2}{N_{D,adjusted}} \cdot |F(\omega)| \quad (3-18)$$

In Eq. (3-18),  $N_{D,adjusted}$  is the sample data adjusted by zero-padding. Lastly, the frequency  $f$  is calculated using Eq. (3-19):

$$f = \frac{f_s}{2} \cdot \frac{2}{N_{D,adjusted}} \cdot t \cdot f_s \quad (3-19)$$

Now, the dominant frequency can be extracted by searching for the maximum magnitude  $A$  and then finding the corresponding frequency  $f$ .

A schematic overview of the complete PIV post-processing procedure is given in Fig. 3-11.

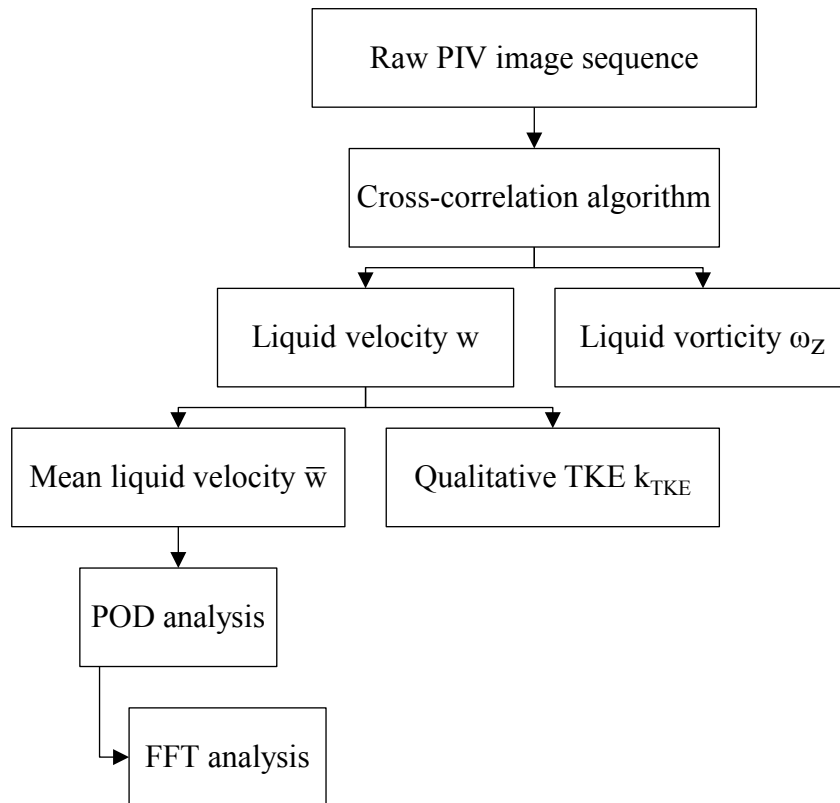


Fig. 3-11. Schematic representation of analysis procedure for PIV image sequences.

### 3.2.3 Fourier Transform Raman spectroscopy

Parts of this chapter have been published in [216]. For experiments with the industrial fluorite flotation system from the Clara mine (see chapter 6.1), an analysis method for quantification of the calcium fluoride ( $\text{CaF}_2$ ) content has to be developed. Several options to determine the  $\text{CaF}_2$  content in a sample are available, e.g. chemical analysis [217,218], potentiometric analysis [85], photometric analysis [219] or X-ray fluorescence spectroscopy (XRF) [87,88]. In industrial plants the latter is commonly applied, as the former methods are time-consuming. XRF is for quantification of fluorine, however, cost-intensive, because special equipment is needed, including a special radiation source and a special detector. Furthermore, X-rays represent a high potential danger, which is why safety precautions have to be considered. Additionally, samples have to be comminuted prior to analysis. Particle sizes of less than  $10\ \mu\text{m}$  are typically used to reduce the influence of X-ray absorption, which reduces the signal intensity [220–222].

Raman spectroscopy in general is on the other hand a very sensitive technique, which requires minimal sample preparation. It can be used on large specimens like crude ore, on fine powders, and even liquids. Thus, spectra from minerals can be obtained from dry solid samples as well as dispersed in liquids [223]. Fourier Transform (FT) Raman spectroscopy is additionally very sensitive towards the crystallinity of solid samples. Due to the many advantages, an analysis method using FT Raman spectroscopy is developed in order to quantify the  $\text{CaF}_2$  content.

First experiments are conducted in an artificial model system consisting of high-purity grades of  $\text{CaF}_2$ ,  $\text{BaSO}_4$ , and  $\text{SiO}_2$  to test the feasibility of FT Raman spectroscopy. Via cross-validation with XRF measurements of an industrial fluorite flotation system the accuracy of the proposed method is tested for  $\text{CaF}_2$  weight fractions ranging from 7 % to 98 %.

#### 3.2.3.1 Methodology

The experimental methodology for the development of the method is depicted schematically in Fig. 3-12. It can be divided into two main parts:

1. investigation of an artificial model system
2. and investigation of a real fluorite system from an industrial production site.

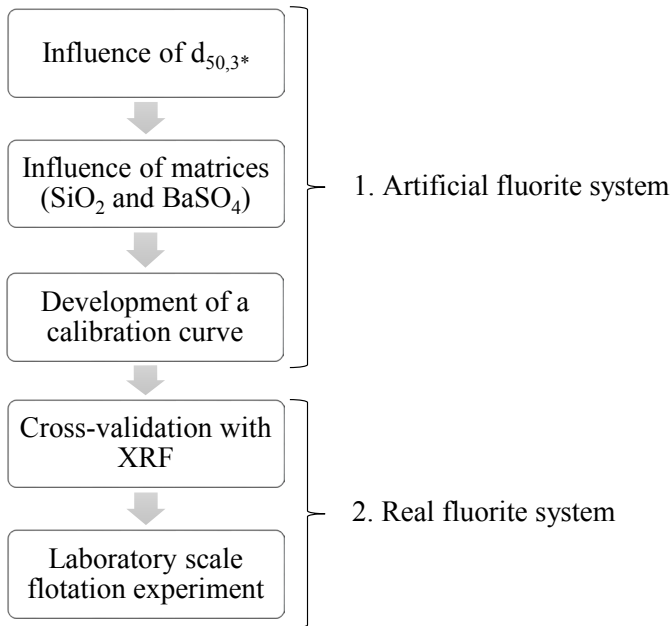


**Fig. 3-12.** Methodology for development and validation of the FT Raman spectroscopy method for quantification of  $\text{CaF}_2$  in solid samples [216].

In the first part, an artificial fluorite system consisting of high-purity grades is investigated to test the feasibility of FT Raman spectroscopy for the given system. High-purity grades of calcium fluoride (99 %), barium sulphate (92 %), and silica (98 %) are used to analyse effects of particle size, aperture, and matrices on the calcium fluoride detection via FT Raman spectroscopy. Furthermore, a calibration curve is established using the high-purity grades for calcium fluoride contents varying from 0 % to 100 %. The obtained results are summarized in the following. A complete overview of the results is given in [216].

The area of the Raman shift of calcium fluoride has been found to increase with increasing median particle diameter  $d_{50,3^*}$  as well as aperture until a threshold is reached. Likewise, a shift towards higher wave numbers is present with increasing aperture and increasing  $d_{50,3^*}$ . These results verify that calcium fluoride can be identified independently of the median particle diameter and the aperture. An investigation of barium sulphate and silica being present besides calcium fluoride as matrices has shown no significant influence on the quantification. Thus, a 10 point calibration curve is established using calcium fluoride and barium sulphate in different weight fractions. The resulting plot is shown in Fig. 3-13. A statistical analysis according to DIN 32645 [224] is carried out at a significance level  $\alpha$  of 99 %. The following process limitations have been determined:

- Detection limit  $w_{dl}=4.58$  %
- Identification limit  $w_{il}=9.15$  %
- Quantification limit  $w_{ql}=10.45$  %

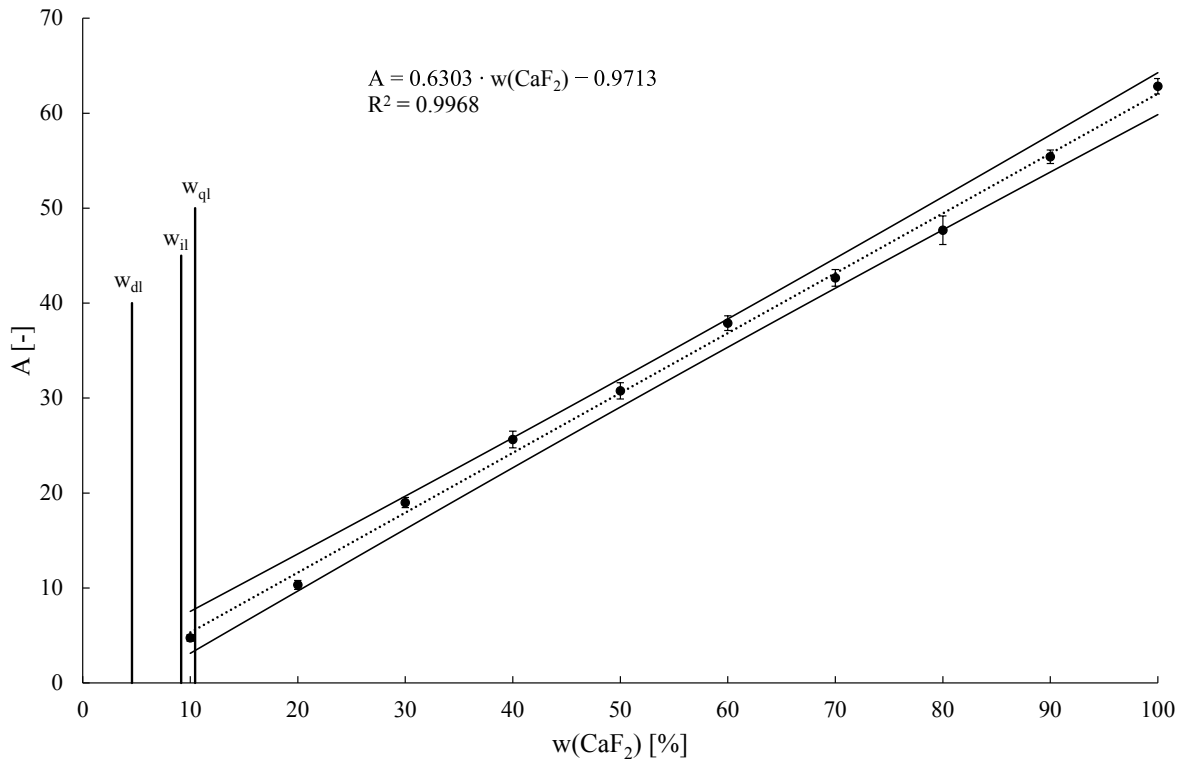


**Fig. 3-13.** Calibration curve with measured peak area  $A$  for calcium fluoride at a Raman shift of  $319.13 \text{ cm}^{-1}$  plotted against calcium fluoride weight fraction  $w(\text{CaF}_2)$  including confidence interval as well as calculated detection limit  $w_{dl}$ , identification limit  $w_{il}$ , and quantification limit  $w_{ql}$ . Assumed significance level  $\alpha=99 \%$  [216].

As the minimum calcium fluoride content is expected to be higher than 50 % in the raw material as well as in the flotation product, a quantification of  $\text{CaF}_2$  for samples of these fractions using this calibration curve is therefore feasible.

During the analysis of the industrial fluorite system, some problems have been encountered, which are thoroughly described and discussed in [216]. Additionally, the calibration curve presented in Fig. 3-13 has been developed for a Raman shift at  $319.13 \text{ cm}^{-1}$ . An exact reproduction of this Raman shift is impossible for the industrial fluorite system, because several components are simultaneously present, which makes comminution of  $\text{CaF}_2$  to the corresponding particle size difficult. Thus, to facilitate determination of the calcium fluoride concentration of varying particle sizes via FT Raman spectroscopy using the developed calibration curve, an empirical model is developed, which incorporates the effect of  $d_{50,3^*}$  on Raman shift and peak area.

The following linear equation is established to determine the weight fraction of calcium fluoride  $w(\text{CaF}_2)$  in a sample regardless of particle size and Raman shift:

$$w(\text{CaF}_2) = 1.59 \cdot \frac{A_{\text{measured}}}{k^*} + 1.54 \quad (3-20)$$

In Eq. (3-20),  $A_{\text{measured}}$  is the measured peak area of the  $\text{CaF}_2$  peak of the sample and  $k^*$  is an area correction factor, which incorporates the change of the Raman peak area with particle diameter.

The area correction factor  $k^*$  is calculated via Eq. (3-21):

$$k^* = 1.72 + \frac{-1.02}{1 + \exp\left[\frac{d_{50,3}^*}{9.25} - 2.23\right]} \quad (3-21)$$

The median particle diameter  $d_{50,3}^*$  in Eq. (3-21) is determined with the following equation:

$$d_{50,3}^* = 9.17 \cdot \ln\left[\frac{-4.68}{\tilde{\nu} - 321.68} - 1\right] + 12.99 \quad (3-22)$$

In Eq. (3-22),  $\tilde{\nu}$  is the measured Raman shift of  $\text{CaF}_2$ . The procedure for analysis of a sample with unknown  $\text{CaF}_2$  is therefore as follows: 1) estimation of the median particle diameter in the sample with Eq. (3-22) using the measured Raman shift  $\tilde{\nu}$  of the  $\text{CaF}_2$  peak in the sample; 2) quantification of the  $\text{CaF}_2$  weight fraction in the sample with Eqs. (3-20) and (3-21) using the measured area of the  $\text{CaF}_2$  peak in the sample.

### 3.2.3.2 Method validation

To validate the developed empirical model and test the feasibility for a real fluorite system, samples from an industrial flotation site with varying calcium fluoride contents are analysed (cf. Fig. 3-14). The samples have been analysed via XRF at the industrial production site after comminution to 5-10  $\mu\text{m}$ .

The results obtained with the developed FT Raman method are compared with the results obtained via XRF in Tab. 3-3. An excellent agreement between both methods is found with only minor absolute differences of less than 5 %. The mean absolute difference is approx. 2.3 %. It has to be noted, however, that the weight fraction of the first sample is larger than the detection limit but lower than the identification and quantification limits (cf. chapter 3.2.3.1).



**Fig. 3-14.** Raw samples for cross-validation of the developed method with XRF measurements. Calcium fluoride content increases from sample 1 to sample 7 from approx. 7 wt% to about 98 wt%.

**Tab. 3-3.** Results of the cross-validation: weight fraction of calcium fluoride  $w(\text{CaF}_2)$  analysed via X-ray fluorescence spectroscopy (XRF) compared to results obtained via FT Raman spectroscopy [216].

sample no.	$w(\text{CaF}_2)$ [%]		absolute difference [%]
	XRF	FT Raman	
1	7.34	6.50	-0.84
2	18.30	14.22	-4.08
3	50.63	52.19	1.56
4	45.08	42.62	-2.46
5	59.23	63.60	4.37
6	91.94	90.09	-1.85
7	98.45	96.61	-1.84

Therefore, a reliable quantification of this sample is according to DIN 32645 infeasible. The cross-validation results prove that the developed model is accurate and a quantification of the  $\text{CaF}_2$  content is possible with respect to the determined process limitations.

Analysis of natural materials, and especially of solid samples, is always affected by a large inhomogeneity due to sampling. With less than 5 % absolute difference between the newly developed method using FT Raman spectroscopy and commonly applied XRF at the industrial site the method can be said to be precise.

## 4 Investigations in two-phase systems

Before measurements are conducted in the three-phase systems, investigations in two-phase systems are carried out. On the one hand, experiments are performed in deionized water to test the influence of the volumetric gas flow rate on the induced liquid velocity field around single rising bubbles. Furthermore, the influence of surface active agents on both bubble characteristics as well as induced liquid flow field are investigated at the example of the surfactants used for the later flotation experiments in the model system consisting of glass particles (see chapter 5).

### 4.1 Experiments in deionized water

In first experiments, single bubbles rising in deionized water are observed in the designed single bubble flotation column (cf. Fig. 3-1) in order to prove the feasibility of the measurement system as well as to investigate the influence of different parameters on the bubble behaviour.

#### 4.1.1 Feasibility test

A critical factor for the investigation of effects on single bubbles is the reproducibility of the bubbles. Generally, each bubble is unique. It is, however, possible to minimize the differences between consecutive bubbles by, e.g., production of bubbles with almost similar bubble diameters. As described in chapter 3.1.1.1.1, PEEK capillaries with varying internal diameters of 130  $\mu\text{m}$ , 250  $\mu\text{m}$ , and 500  $\mu\text{m}$  are used to produce single bubbles in the single bubble flotation column. The capillaries are connected to a precision syringe pump, which enables a high reproducibility of the gas flow rate.

To prove the feasibility of the single bubble flotation column with respect to the reproducibility of the bubbles, the bubble parameters equivalent bubble diameter  $d_B$ , rising velocity  $w_B$ , and elongation  $f_e$  are investigated for seven volumetric gas flow rates  $\dot{V}_g$  ranging from 16  $\mu\text{L}/\text{min}$  up to 1  $\text{mL}/\text{min}$  in deionized water with an electrolytic conductivity  $\kappa$  of 17  $\mu\text{S}/\text{cm}$  from an in-house purification system. For each gas flow rate about 30-50 bubbles are analysed using the automated time-resolved analysis procedure presented in chapter 3.2.1. The data is analysed statistically using a combined two-sided and one-sided Dixon's Q test (cf. [190]). All raw data can be found in the Appendix. The standard deviation of each parameter is below 5 %, which indicates an excellent reproducibility. A summary of the determined range of various bubble parameters is given in Tab. 4-1. The parameters are a function of the volumetric gas flow rate and capillary diameter. This influence is, however, low which is why it is not further discussed at this point.

**Tab. 4-1.** Summary of determined range of bubble parameters for rising single bubbles in deionized water for gas flow rates ranging from 16  $\mu\text{L}/\text{min}$  up to 1  $\text{mL}/\text{min}$ .

Parameter		Range
Bubble diameter	$d_B$ [mm]	1.92-2.42
Rising velocity	$w_B$ [m/s]	0.28-0.32
Elongation	$f_e$ [-]	0.3-0.5
Bubble Reynolds number	$Re_B$ [-]	492-741
Eötvös number	$Eo$ [-]	0.5-0.8
Morton number	$M$ [-]	$2.2 \cdot 10^{-11}$

The elongation  $f_e$  as morphological parameter is in a range between 0.3-0.5. Thus, the analysed bubbles are non-spherically but elongated. This is also confirmed when comparing the determined dimensionless numbers  $Re_B$ ,  $Eo$ , and  $M$  for each bubble with the bubble shape map found in literature (cf. Fig. 4-1a). A comparison with the bubble regimes defined by Clift et al. (cf. Fig. 2-17) shows that the analysed bubbles are all in the region of ellipsoidal/wobbling, which is in consensus with the visual impressions as well as the determined range for  $f_e$  [125].

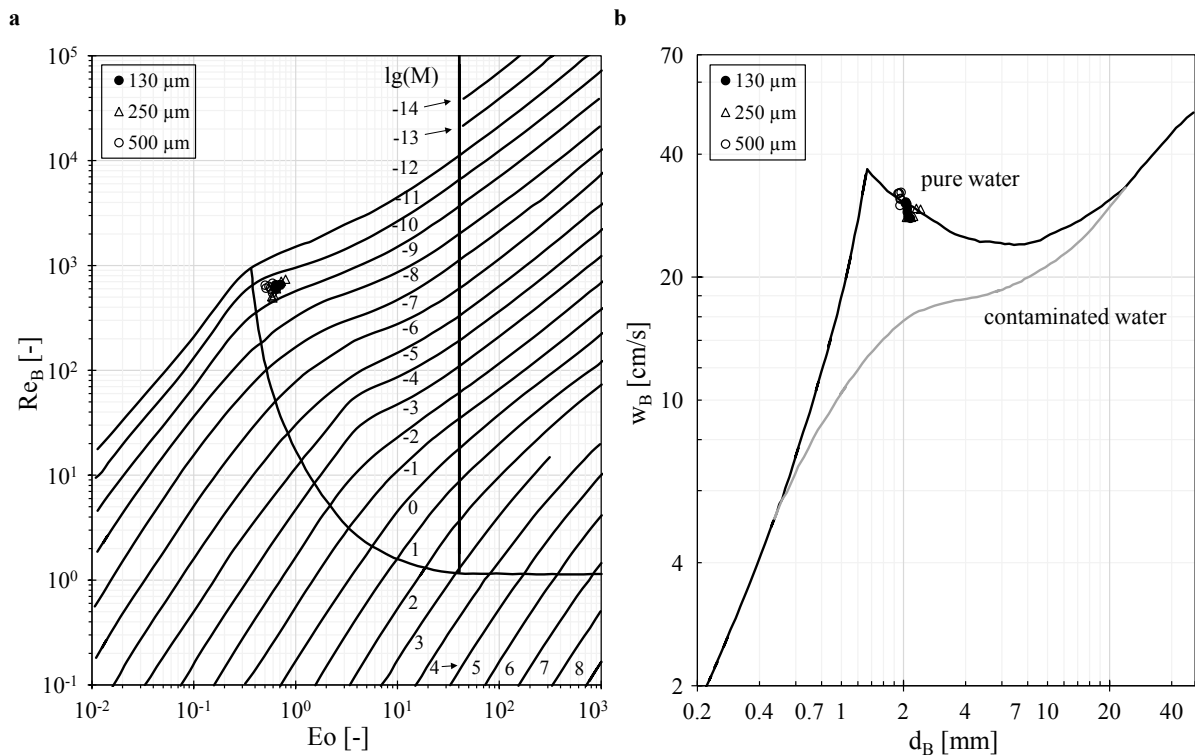


**Fig. 4-1.** Bubble shape map (a) and bubble rising velocity  $w_B$  as a function of bubble diameter  $d_B$  (b) for single bubbles rising in deionized water compared to literature [125].

The measured rising velocities are compared to literature data in Fig. 4-1b (cf. chapter 2.3.1.2). The determined rising velocities are for all capillaries close to the curve for pure water. Therefore, the feasibility of the measurement system with respect to the measurement method as well as the purity of the deionized water is verified.

An empirical model proposed by Al Ba'ba'a et. al. [225] is used to predict the bubble diameter at the varying experimental conditions based on the capillary Reynolds number  $Re_c$  and the capillary Weber number  $We_c$ :

$$d_{B,\text{predicted}} = A \cdot \left( \frac{4 \cdot \dot{V}_g \cdot \rho_g}{\pi \cdot \eta_g \cdot d_c} \right)^B \cdot \left( \frac{16 \cdot \rho_g \cdot \dot{V}_g^2}{\pi^2 \cdot d_c^3 \cdot \sigma} \right)^C = A \cdot Re_c^B \cdot We_c^C \quad (4-1)$$

The variable parameters A, B, and C in Eq. (4-1) are determined using the least-squares method. The resulting equation is then given by:

$$d_{B,\text{predicted}} = 2.49 \cdot Re_c^{0.018} \cdot We_c^{0.010} \quad (4-2)$$

A graphical comparison of measured and predicted equivalent diameter is presented in Fig. 4-2. The developed empirical model in Eq. (4-2) allows a prediction of the bubble equivalent diameter within a tolerance of  $\pm 10\%$ . In literature, estimations with a tolerance of  $\pm 20\%$  are already said to be very good [226].

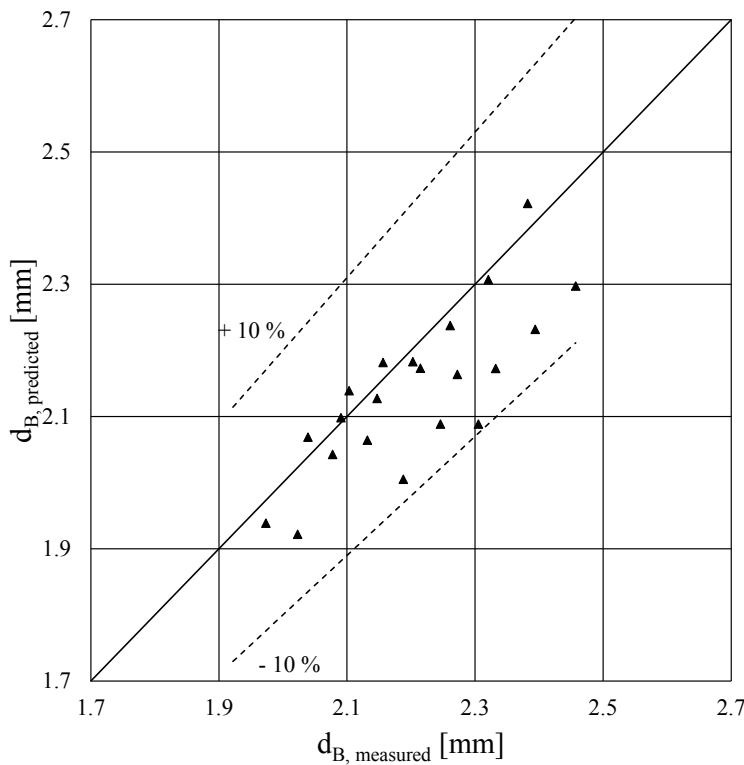


**Fig. 4-2.** Predicted equivalent bubble diameter  $d_{B,\text{predicted}}$  vs. measured equivalent bubble diameter  $d_{B,\text{measured}}$  using Eq. (4-2) including a confidence interval of  $\pm 10\%$ .

#### 4.1.2 Influence of gas flow rate on induced liquid velocity

Parts of this chapter have been published in [227]. The influence of different operational parameters on the bubble characteristics has been presented in chapter 4.1.1. In the next step, the influence of the volumetric gas flow rate on the liquid velocity around the rising single bubbles is investigated. For this purpose, the experimental setup for simplified measurements as presented in chapter 3.1.1.2 is used. Particle Image Velocimetry (PIV) measurements are carried out at ten different gas flow rates ranging from 0.1 mL/min to 2 mL/min. A PEEK capillary with an internal diameter of 500  $\mu\text{m}$  is used. At least five bubbles are analysed for each gas flow rate according to the analysis procedure presented in chapter 3.2.2. To investigate the effects of the gas flow rate on the induced liquid velocities, the vector distributions of the mean vector fields are analysed via histograms. For this purpose ten classes with an equidistant width are defined ranging from 0 m/s-0.020 m/s.

The relationship between the number  $N$  of vectors in different liquid velocity classes and the volumetric gas flow rate  $\dot{V}_g$  is presented in Fig. 4-3. The figure shows the relationship for the first six classes with liquid velocities from 0 m/s-0.012 m/s. The five repetitive measurements show a high reproducibility, because of the low standard deviations.

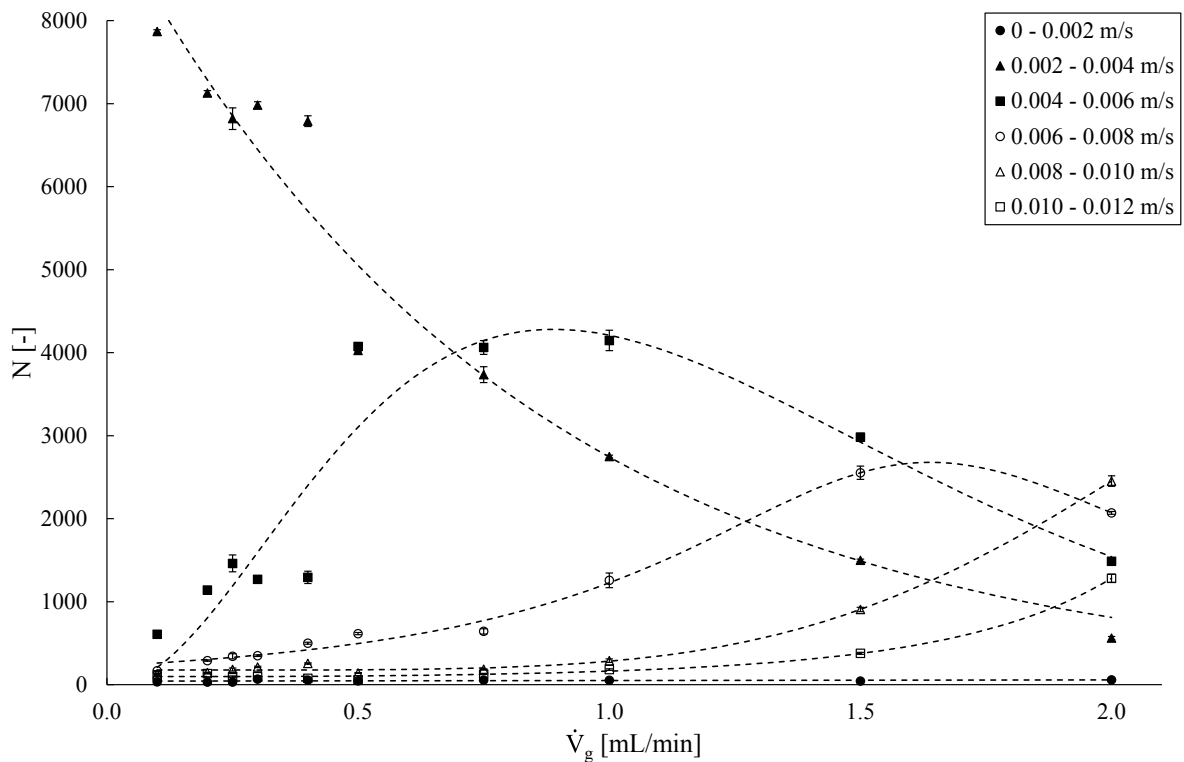


**Fig. 4-3.** Relationship between the number  $N$  of vectors in six different classes from 0-0.012 m/s and volumetric gas flow rate  $\dot{V}_g$ . Dashed lines indicate trends. The number of vectors in each analysed vector field is in total 9010.

The number of vectors in the first class (0 m/s-0.002 m/s), where only a small relative amount of vectors is present with less than 1 % of the total amount of vectors, is unaffected by an increase of the gas flow rate. The second class ranging from 0.002 m/s to 0.004 m/s is the class with the largest amount of vectors at low gas flow rates. With increasing  $\dot{V}_g$  a sharp decline is observed. The initial vector number at  $\dot{V}_g=0.1$  mL/min decreases by a factor of 14 towards the highest investigated gas flow rate of 2 mL/min. The next two classes from 0.004 m/s to 0.006 m/s and 0.006 m/s to 0.008 m/s show similar trends with a shift on the x axis: The number of vectors first increases with increasing  $\dot{V}_g$  until a maximum is reached. Afterwards, the number of vectors in these classes decreases again. While the class with liquid velocities of 0.004-0.006 m/s reaches its maximum at a  $\dot{V}_g$  of approximately 0.88 mL/min, the maximum in the class with liquid velocities of 0.006-0.008 m/s is reached at  $\dot{V}_g \approx 1.68$  mL/min. The classes with liquid velocities of 0.008-0.010 m/s and 0.010-0.012 m/s show a steady increase with increasing  $\dot{V}_g$ . In summary, it can be seen that a shift to higher liquid velocities is present with increasing gas flow rate.

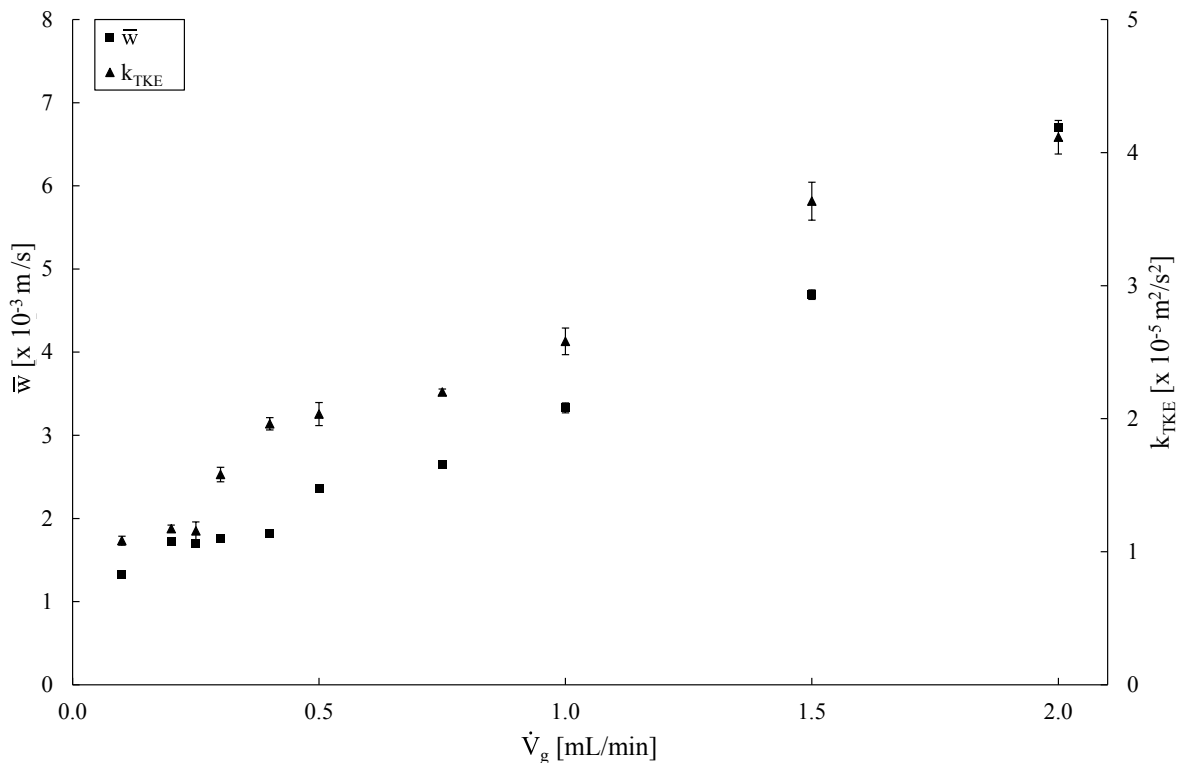


**Fig. 4-4.** Mean liquid velocity  $\bar{w}$  and proportionality constant to the turbulent kinetic energy  $k_{TKE}$  as a function of volumetric gas flow rate  $\dot{V}_g$ .

This trend is also present in Fig. 4-4, which shows the relation between mean liquid velocity  $\bar{w}$  and proportionality constant of the turbulent kinetic energy  $k_{\text{TKE}}$  (cf. chapter 3.2.2) with  $\dot{V}_g$ . The mean liquid velocity increases in the investigated range from 0.1 mL/min to 2 mL/min by a factor of approx. five. The value for  $k_{\text{TKE}}$  also increases with increasing  $\dot{V}_g$  so that more turbulent kinetic energy is induced by the bubbles at a higher gas flow rates. The initial value of  $k_{\text{TKE}}$  increases in the investigated range of  $\dot{V}_g$  by a factor of about four.

Some exemplary instantaneous liquid velocity and vorticity plots for three different volumetric gas flow rates of 4  $\mu\text{L}/\text{min}$ , 0.05 mL/min, and 2 mL/min are presented in Fig. 4-5. Each vector field and scalar map contains 9010 vectors. The liquid velocities and vorticities are shown in all cases 100 ms after the bubble has entered the measurement area. The presented vector maps exhibit a small amount of spurious vectors, especially at the corners of the maps, which can be attributed to image distortion towards the edge of the camera lens. As neither vectors were substituted via interpolation nor a time- or ensemble-average has been calculated, the presence of these spurious vectors is natural. Their contribution to the total liquid flow field is, however, small so that no large error is to be expected. A comparison with literature data shows that the determined liquid velocities are similar to results obtained by Miyahara et al. [228] as well as Böhm and Kraume [229].

The wake structures behind the rising bubbles in Fig. 4-5 can clearly be identified. With increasing  $\dot{V}_g$  the wake expands. The mean liquid velocity in the bubble wake ranges between 0.03 m/s to 0.04 m/s. While at low  $\dot{V}_g$  the liquid velocity in the measurement area is elevated only in the wake region directly behind the rising bubble (Fig. 4-5a&b), a significant expansion is observed at 2 mL/min, where nearly 50 % of the measurement area exhibit liquid velocities larger than 0.01 m/s (Fig. 4-5c). Nevertheless, the main zigzagging bubble trajectory which is representative for the two lower gas flow rates may still be recognized at a gas flow rate of 2 mL/min. The observed bubble motion is in consensus with the statements in Tab. 2-5.

The vorticity plots are useful for the identification of vortices in the bubble wake and the characterization of the wake structure (cf. chapter 3.2.2). In all vorticity plots in Fig. 4-5 clockwise vortices, displayed in blue (negative value), and anti-clockwise vortices, indicated in red (positive values), can be observed. A value near zero means that no rotation is present (displayed in green). All vorticity plots show an alternating pattern according to a Kármán vortex street [199]. This pattern is more pronounced in Fig. 4-5a&b than in Fig. 4-5c, but the Kármán vortex street can be identified nevertheless. This vortex pattern in the wake of rising single bubbles was also observed by, e.g. Böhm and Kraume [229]. In contrast to their investigations, the vortices in the present study are, however, not connected with each other to

form a closed wake region of large clockwise and anti-clockwise rotating vortices. Instead, an alternating shedding pattern of counter-rotating vortices behind the bubble was found. This may be related to the used zoom lens, which allows a more detailed observation of the liquid flow field around and especially in the wake of rising single bubbles. In Böhm and Kraume's work, the bubble area was approx. 0.2 % of the total field of view, while it was 0.4 % in the present work, thus doubling the magnification.

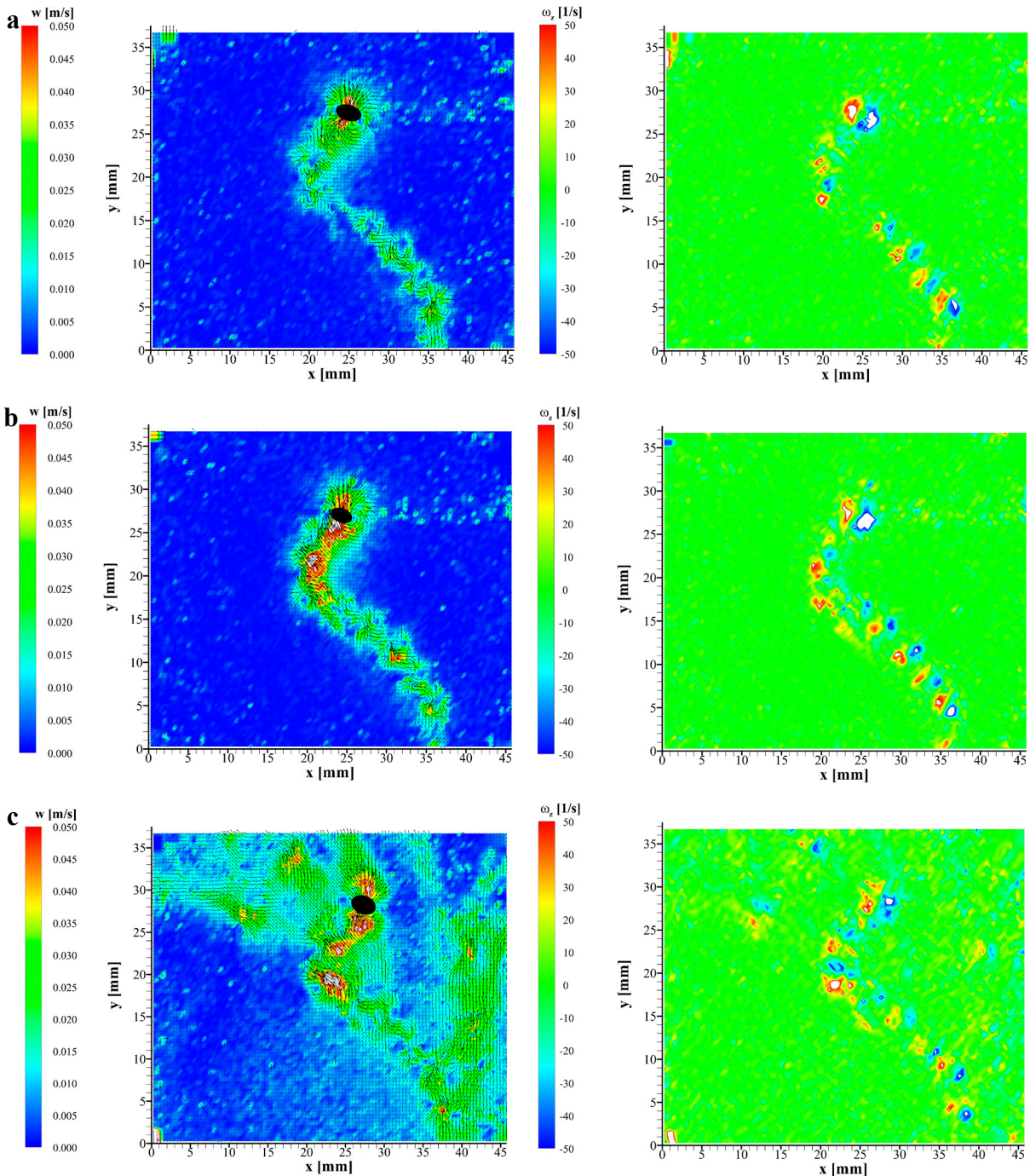


**Fig. 4-5.** Liquid velocity vector fields (left) and liquid vorticity scalar maps (right) for experiments in deionized water at gas flow rates of 4  $\mu\text{L}/\text{min}$  (a), 0.05  $\text{mL}/\text{min}$  (b), and 2  $\text{mL}/\text{min}$  (c). Bubble position and shape are indicated in the liquid velocity fields as black ellipses.

## 4.2 Experiments in surfactant solutions

Parts of this chapter have been published in [230]. As described in chapter 2.3.2, surfactants have a significant influence on the bubble characteristics. Therefore, the influence of the surfactants used as collector and frother in the later flotation experiments with glass particles (see chapter 5) are investigated with both Shadowgraphy (SH) and Particle Image Velocimetry (PIV). By combining the results of the two optical methods the relationship between bubble characteristics and hydrodynamic parameters is examined.

### 4.2.1 Experimental procedure

The experiments are conducted in the experimental setup for simplified measurements, which has been presented in chapter 3.1.1.2. The measurement area is arbitrarily positioned approximately 35 mm above the capillary outlet. The SH sequences are analysed using the automated time-resolved analysing procedure in KNIME<sup>®</sup> as presented in chapter 3.2.1. As bubble parameters the equivalent diameter  $d_B$ , the rising velocity  $w_B$ , and the elongation  $f_e$  are studied. The PIV sequences are analysed in DynamicStudio according to the procedure described in chapter 3.2.2. As hydrodynamic parameters the liquid velocity  $w$  and vorticity  $\omega_z$  are analysed. Furthermore, an information about the turbulent kinetic energy (TKE) in form of the proportionality constant  $k_{TKE}$  (see chapter 3.2.2) is extracted from the mean velocity vector fields. Lastly, the Proper Orthogonal Decomposition (POD) technique is applied to extract dynamic phenomena in the present unsteady flows.

The surfactants hexadecylamine (HDA) and methyl isobutyl carbinol (MIBC) are investigated at varying concentrations. The former is a representative collector for, e.g. quartz flotation, where amines are commonly used ([17], p. 271), while the latter is a common frother used in many industrial flotation processes ([17], p. 279; [30], p. 259). Both of these surfactants are used in the flotation process of glass particles in chapter 5. The pH of HDA is adjusted to six using hydrochloric acid. This ensures a complete protonation of the amine group. HDA as ionic surfactant is used in smaller concentrations in a range of 5.2 to 34.5  $\mu\text{mol/L}$ , while MIBC is used in a concentration range of 79 to 7922  $\mu\text{mol/L}$ .

About 120 mL of the given test liquid are filled into the apparatus. A constant volumetric gas flow rate of 0.1 mL/min is chosen to produce single bubbles with a bubble production time of approx. 0.85 s, hence a bubble production frequency of less than 80 bubbles per minute. According to Rafiei et al. and Sam et al. an interaction between consecutive bubbles can therefore be neglected [137,231]. High-speed image sequences are captured as soon as the gas flow is constant. All experiments are carried out at a room temperature of 22-24 °C.

Shadowgraphy and PIV measurements are conducted subsequently for each experimental condition. Each measurement is repeated at least five times, so that five SH image sequences and five PIV image sequences are obtained for each concentration.

Additionally, surface tension measurements of prepared solutions are carried out at room temperature (22-24 °C) with an automatic force tensiometer (type: Krüss Easy Dyne K20) using the Du Noüy ring method (cf. chapter 2.2.2.2). Each measurement is repeated five times.

## 4.2.2 Results and discussion

In this chapter, the experimental results are presented starting with the surface tension measurements, followed by the rigorous analysis of the bubble characteristics obtained via SH measurements, and concluding with the hydrodynamic characterisation via PIV measurements.

### 4.2.2.1 Surface tension measurements

The results of the surface tension measurements are shown in Fig. 4-6. As recommended in literature, the correction method proposed by Harkins and Jordan [121] has been applied (cf. chapter 2.2.2.2). HDA decreases the surface tension in the investigated concentration range more strongly than MIBC. At a concentration of approx. 35 µmol/L HDA, the initial surface tension of 72.4 mN/m for pure water halved already to 35.7 mN/m. In contrast to this, a decrease by about 12 mN/m compared to deionized water is measured at the highest concentration of MIBC (approx. 7900 µmol/L). In both cases, the critical micelle concentration (CMC) has not been reached. For HDA a CMC of  $8.3 \times 10^{-4}$  mol/L is reported ([232], p. 255), while Drzymala states a value of approx. 0.2 mol/L for MIBC ([32], p. 328).

Using the  $\sigma$ -log  $c$  plot from Fig. 4-6, the area occupied by a surfactant molecule at the bubble interface can be calculated with Eq. (2-36). To do this, the slopes  $\left(\frac{\partial\sigma}{\partial\log c}\right)_T$  have to be determined for HDA and MIBC. For HDA, the slope is determined between 6 µmol/L and 34 µmol/L ( $R^2=0.997$ ), while for MIBC the slope is calculated between 5000 and about 8000 µmol/L ( $R^2=0.987$ ). Hence, an area of about 0.32 nm<sup>2</sup> per molecule is obtained for HDA and  $A=0.38$  nm<sup>2</sup> per molecule for MIBC. The calculated value for MIBC is in excellent agreement with the literature value of 0.38 nm<sup>2</sup> stated by Fong et al. [233]. For HDA no literature data was available. The Frumkin equation, which can be used to estimate the efficiency of surfactant adsorption, stated that a decrease of the surface tension by 20 mN/m indicates a saturation of the surface concentration of approximately 84-99.9 % (cf. chapter 2.2.2.1).

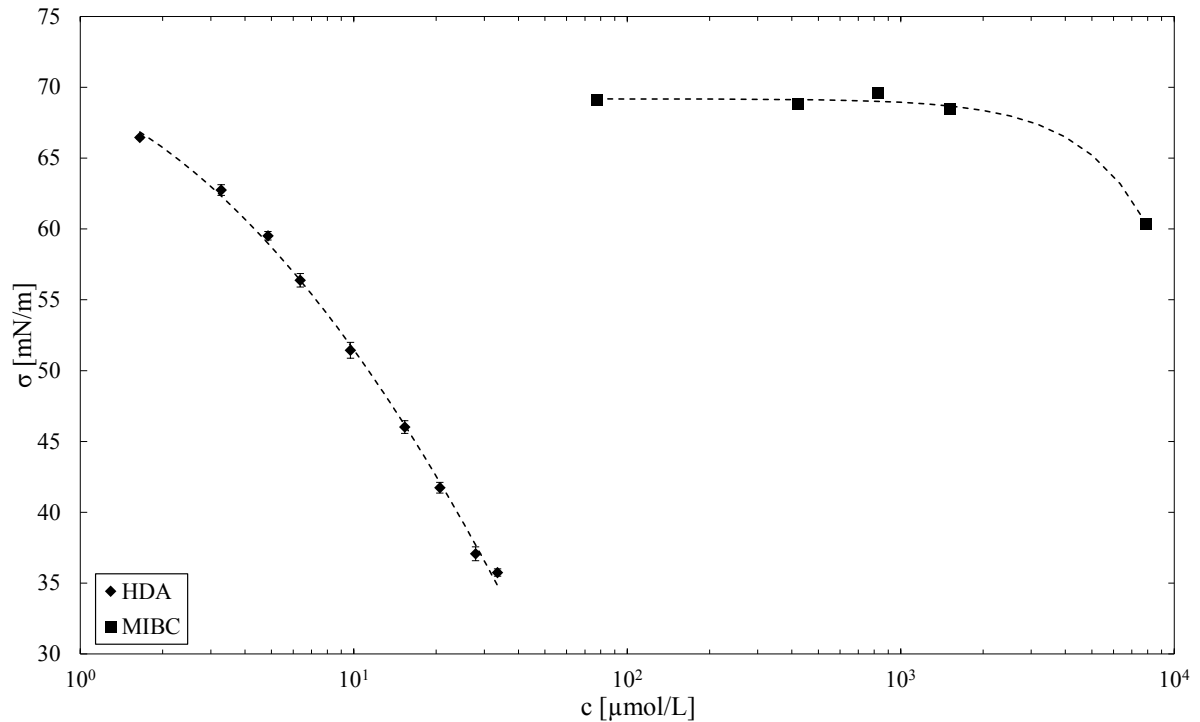


**Fig. 4-6.** Surface tension of hexadecylamine (HDA) and methyl isobutyl carbinol (MIBC) solutions with different concentrations in deionized water. Dashed lines indicate trends [230].

In the present work, a decrease of about 37 mN/m is observed for HDA in the investigated concentration range, while MIBC lowers the surface tension by only about 12 mN/m. This relates to surface saturations of 94 % and 68 % for HDA and MIBC, respectively. As the absolute decrease of the liquid surface tension is lower for MIBC than for HDA, the obtained results are in the expected range.

From the above presented results regarding the surface tension of the liquid it can be concluded that HDA exhibits a better adsorption at the gas-liquid interface than MIBC. This will be discussed further in the following section with respect to the bubble characteristics.

#### 4.2.2.2 Bubble characteristics

The bubble characteristics are found to change with variation of the surfactant concentration as shown in Fig. 4-7. All three bubble parameters, equivalent diameter  $d_B$  (Fig. 4-7a), rising velocity  $w_B$  (Fig. 4-7b), and elongation  $f_e$  (Fig. 4-7c), decrease with increasing surfactant concentration. Both  $w_B$  and  $f_e$  show a sharp drop in the beginning until a threshold is reached (cf. Fig. 4-7b&c). The value of this threshold is for both bubble parameters approximately the same in HDA and MIBC solutions. The rising velocity converges towards a value of 0.18 m/s and the elongation towards a value of 0.08.

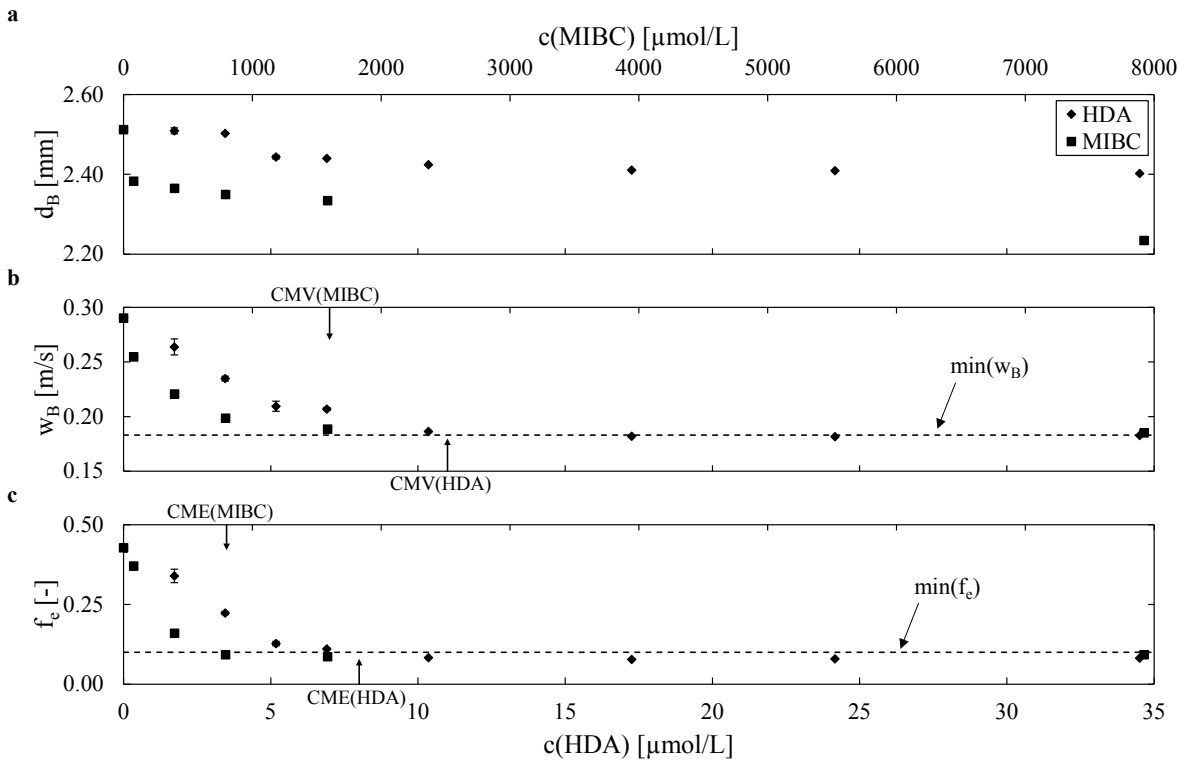


**Fig. 4-7.** Bubble characteristics for varying concentrations of hexadecylamine (HDA) and methyl isobutyl carbinol (MIBC): equivalent bubble diameter  $d_B$  (a), rising velocity  $w_B$  (b), and elongation  $f_e$  as morphological parameter (c). Dashed line in (b) indicates minimum bubble velocity  $\min(w_B)$ , while dashed line in (c) represents the minimum elongation  $\min(f_e)$ . Determined concentration at minimum velocity (CMV) and concentration at minimum elongation (CME) are included in (b) and (c), respectively [230].

As stated in chapter 2.3.2, Tan et al. [139] proposed two different criteria to determine terminal velocities: 1) when velocity at a given concentration reaches minimum with distance; 2) when velocity at a given distance reaches minimum with concentration. As the simplified apparatus with the measurement area close to the capillary outlet is used for the experiments, criterion 2) is applied to determine terminal velocities.

The concentration at the minimum rising velocity (CMV) is determined using the graphical method proposed by Tan et al. [147] (Fig. 4-7b). CMV is determined to be about 1600  $\mu\text{mol/L}$  for MIBC and 11  $\mu\text{mol/L}$  for HDA. A value of 400  $\mu\text{mol/L}$  is stated in literature for CMV of MIBC [139,148], which is approx. only a quarter of the value determined from the present measurements. The value of 400  $\mu\text{mol/L}$  was, however, determined at an arbitrarily chosen position of 3000 mm above the capillary outlet compared to 35 mm in the present experimental procedure (see chapter 4.2.1). Furthermore, the bubble size was with 1.45 mm approx. 60 % smaller than in the present measurements [139]. A difference between the CMV value determined from the present experiments and the value found in literature is therefore expected,

as the time needed to reach terminal velocity will be a function of surfactant concentration and bubble size.

The elongation shows a similar trend as the rising velocity (see Fig. 4-7c). Thus, a new bubble parameter is introduced, which is defined as concentration at the minimum elongation (CME). CME represents the concentration at which the difference between minor and major axis of the bubble is less than 10 %, which is equal to  $f_e=0.1$ . According to Clift et al. ([125], p. 23), bubbles who satisfy this criterion can be assumed spherical (cf. chapter 2.3.1.2). Using the same graphical method as for CMV, a CME of approx. 8  $\mu\text{mol/L}$  is determined for HDA and a CME of approx. 800  $\mu\text{mol/L}$  for MIBC. Comparison of CMV and CME shows that the concentrations determined for CME are lower for both surfactants. Thus, an increase of surfactant concentration after CME does not influence the bubble shape anymore, while  $w_B$  will decrease further until the minimum rising velocity is reached.

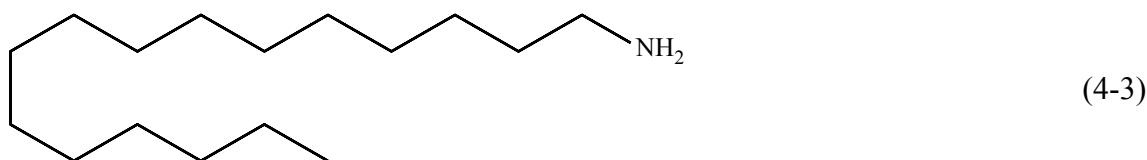
The minimum equivalent bubble diameters, which are obtained at the maximum investigated concentrations of MIBC and HDA, are 2.23 mm and 2.40 mm, respectively. In contrast to  $w_B$  and  $f_e$ , a threshold for  $d_B$  has not been reached yet for both surfactants (cf. Fig. 4-7a). Although Cho and Laskowski found in their study that the bubble size was “not affected at all by a frother if the bubbles cannot collide with each other” [141,142], i.e. production of bubbles from a single-hole sparger, the results of the present measurements and studies of Li et al. [234] as well as Zhu et al. [235] show an influence on all investigated bubble characteristics including  $d_B$ . The effect is, however, small compared to the effect of surfactants in bubble swarms, where a change of  $d_B$  from e.g. 4 to 1 mm is commonly observed [139,142–144].

A comparison of the determined rising velocities with literature shows a shift towards smaller bubble diameters and smaller rising velocities with increasing surfactant concentration (cf. Fig. 4 in [230]). A difference between the determined threshold value of the rising velocity (0.18 m/s) and the curve for contaminated water, where a value of 0.16 m/s is stated, is present for both surfactants. Zhang et al. [138] as well as Tan et al. [139] noted in their studies that the contaminated water curve given by Clift et al. ([125], p. 172, see also Fig. 2-18) seems to underestimate the terminal velocity. Thus, the terminal velocity determined in the present experiments is compared to further correlations for the rising velocity from literature using the model of Karamanev [236,237] and Grace et al. [238]. The velocities obtained by these models are compared to the experimental rising velocities in Tab. 4-2. The determined terminal velocities from the present experiments range between the values predicted by the models of Clift et al. and Grace et al.

**Tab. 4-2.** Comparison of experimentally determined terminal velocities with models proposed in literature [230].

Surfactant	$w_B$ [m/s]			
	Experimental	Clift et al. [125]	Karamanev [236,237]	Grace et al. [238]
MIBC	0.185	0.163	0.233	0.197
HDA	0.183	0.165	0.228	0.194

The presented experimental results show that HDA has a larger effect on all bubble characteristics compared to MIBC, because they are significantly influenced by already very low concentrations of HDA. Higher concentrations of MIBC are necessary to achieve similar effects. As the surface tension changes only sparsely with increasing MIBC concentration (see Fig. 4-6), this does not seem to be the predominant influence factor for bubble characteristics as was also stated by several authors in literature [142,143,239–242]. Instead, the adsorption of the surfactant molecules at the in situ formed gas-liquid interface seems to be of greater importance. As rising bubbles represent a dynamic system, Comley et al. hypothesised that the rate of adsorption has to be the main influence factor [239]. In chapter 4.2.2.1 it has been shown that HDA molecules adsorb better on the bubble surface than MIBC molecules, which is related to differences in molecular architecture. HDA has a straight hydrocarbon chain with 16 carbon atoms and an amino group at terminal position:



MIBC is on the other hand a branched alcohol with a hydroxyl group located in a side chain:



Another explanation for the different adsorption efficiency may be related to the negatively charged bubble surface [243,244]. The negative surface charge is caused due to the better adsorption of the smaller, less hydrated anions compared to the more likely hydrated cations, which have a tendency to remain in the bulk phase ([245], p. 175). Attractive forces are present between the negatively charged bubble surface and protonated HDA molecules so that an adsorption is facilitated compared to the adsorption of non-ionic MIBC molecules [246,247]. At a certain concentration the ionic adsorption will be retarded by electrostatic repulsion effects [113]. However, this effect has not been observed in the present experiments.

A schematic depiction of the adsorption of HDA and MIBC molecules on the bubble surface is shown in Fig. 4-8.

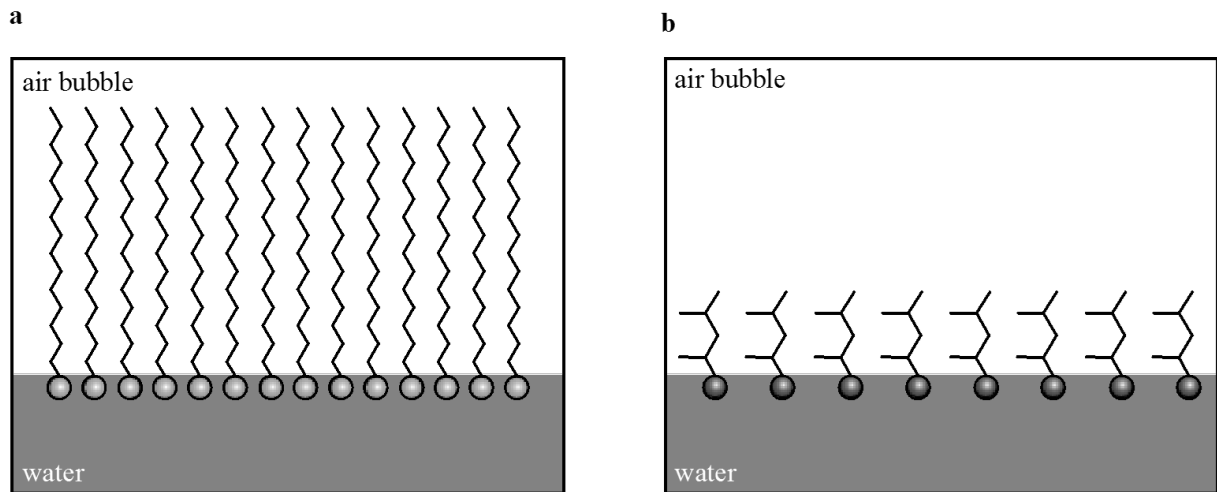


**Fig. 4-8.** Schematic packing density for hexadecylamine (HDA) (a) and methyl isobutyl carbinol (MIBC) (b) at a bubble interface [230].

In accordance with [147,248], HDA allows a higher packing density compared to MIBC due to its straight hydrocarbon chain, which results in a hydrophobic chain-chain interaction.

The packing densities calculated for HDA and MIBC in chapter 4.2.2.1 support this theory. As stated in chapter 2.3.2, the bubble drag increases in presence of surfactants as a result of the Marangoni effect, resulting in a lower rising velocity. The adsorption of HDA at the bubble interface is better and the packing density is higher compared to MIBC, which is why CMV and CME of HDA have to be lower than CMV and CME of MIBC. The results presented in Fig. 4-7 support this theory.

In addition to the bubble characteristics presented in Fig. 4-7, the bubble centroids have been tracked and, thus the bubble trajectories can be reconstructed. The trajectories obtained for bubbles rising in deionized water are presented in Fig. 4-9. The top diagram Fig. 4-9a shows the bubble motion in horizontal  $x$  direction over time. The bubbles exhibit an oscillating rising behaviour in horizontal  $x$  direction. In order to quantify the oscillating behaviour, a sinusoidal fit function according to Eq. (4-5) is applied.

$$x(t) = \hat{A} \cdot \cos(\omega \cdot t + \phi) + C \quad (4-5)$$

In Eq. (4-5),  $\hat{A}$  is the amplitude of the oscillation,  $\omega$  is the oscillation frequency,  $t$  is the time,  $\phi$  is the phase, and  $C$  is a constant defining a mean level. The regression coefficient  $R^2$  of this equation applied to the bubble motion in horizontal  $x$  direction for bubbles in deionized water is 0.983, which shows that an excellent representation of the experimental results is achieved with the model. The trajectory in vertical  $y$  direction (Fig. 4-9b) shows a linear trend, which is supported by an  $R^2$  of 0.999 for a linear approximation. Thus, a nearly constant rising velocity can be assumed in the measurement area. The elongation is nearly constant during the bubble rise (Fig. 4-9c).

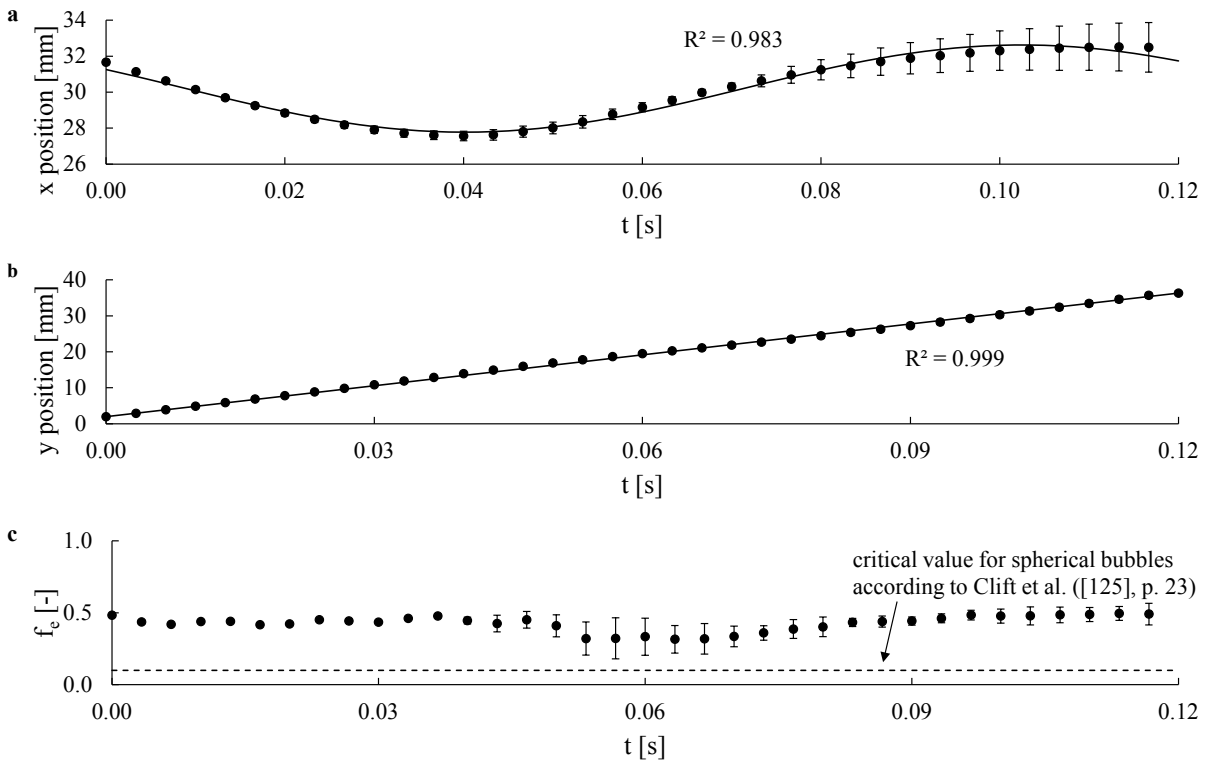


**Fig. 4-9.** Bubble trajectories in horizontal x direction (a) and vertical y direction (b), and time-resolved analysis of the elongation  $f_c$  (c) for rising bubbles in deionized water. Solid line in (a) represents sinusoidal fit function according to  $x(t) = \hat{A} \cdot \cos(\omega \cdot t + \phi) + C$ . Solid line in (b) represents linear fit function according to  $y(t) = m \cdot t + b$ . Dashed line in (c) represents the critical value for spherical bubbles according to Clift et al. ([125], p. 23; [230]).

Some larger standard deviations around  $t = 0.06$  s are referred to the horizontal redirection of the bubbles at this point (cf. Fig. 4-9a). As stated above and in chapter 2.3.1.2, bubbles may be assumed spherical when the difference between major and minor axis of the bubble is less than 10 %, corresponding to an elongation of 0.1. This critical value is included in Fig. 4-9c as dashed line. For bubbles rising in deionized water, the mean elongation is approx. 0.43. Thus, the observed bubbles are highly non-spherical and instead more ellipsoidal, which is in consensus with visual impressions.

The motion amplitude  $\Delta x$  in horizontal x direction is about 5 mm for bubbles in deionized water. With increasing surfactant concentration, both  $\Delta x$  and the standard deviation in x direction for five analysed bubbles per investigated surfactant concentration decrease ( $\Delta x \approx 3$  mm in Fig. 4-10a), resulting in an almost straight rising path. A mean standard deviation in x direction of 0.3 mm and 0.03 mm is observed at the highest investigated concentrations of HDA and MIBC, respectively. All measurement results may be found in the Appendix.

The bubble motion in x direction for the highest investigated MIBC concentration of  $7922 \mu\text{mol/L}$  presented in Fig. 4-10 shows again an oscillating behaviour so that the sinusoidal fit function according to Eq. (4-5) is applied for a quantification.

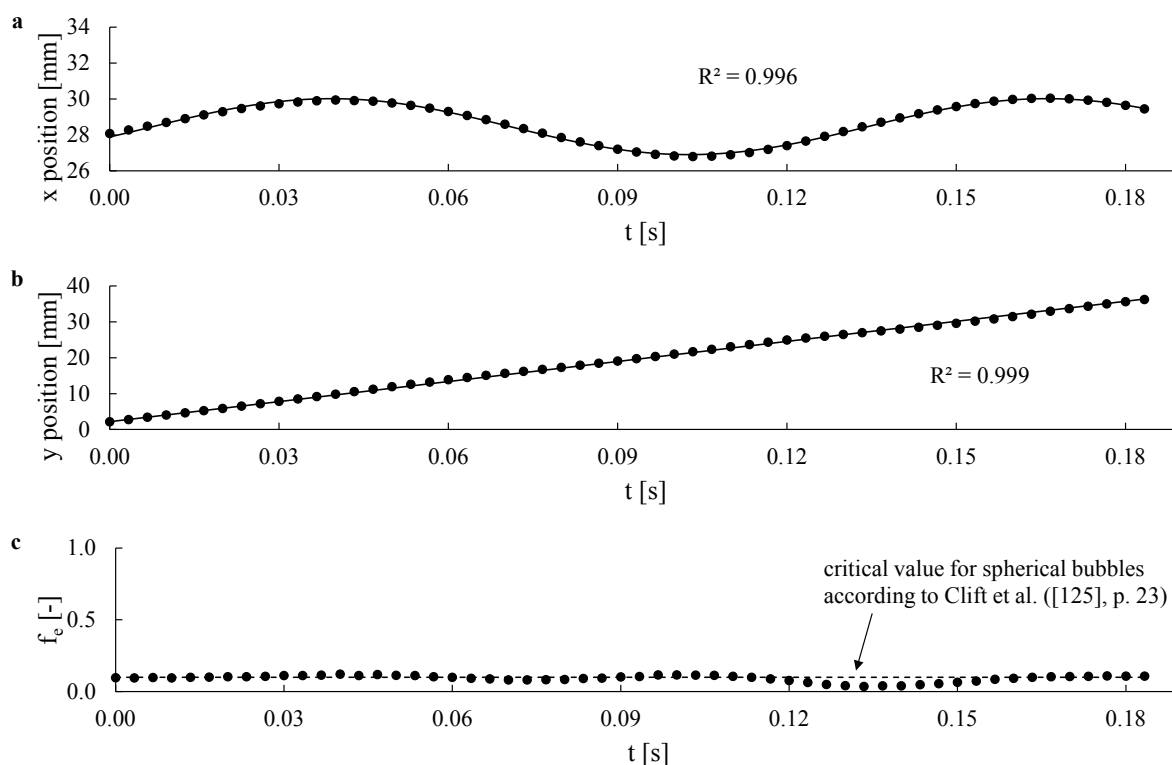


**Fig. 4-10.** Bubble trajectories in horizontal x direction (a) and vertical y direction (b), and time-resolved analysis of the elongation  $f_e$  (c) for rising bubbles in a 7922  $\mu\text{mol/L}$  methyl isobutyl carbinol solution. Solid line in (a) represents sinusoidal fit function according to  $x(t) = \hat{A} \cdot \cos(\omega \cdot t + \phi) + C$ . Solid line in (b) represents linear fit function according to  $y(t) = m \cdot t + b$ . Dashed line in (c) represents the critical value for spherical bubbles according to Clift et al. ([125], p. 23; [230]).

The resulting regression coefficient  $R^2$  of 0.996 proves an excellent agreement with the model. The movement in vertical y direction shows again that the bubbles rise with a nearly constant rising velocity in the measurement area (cf. Fig. 4-10b). The time-resolved analysis of the elongation in Fig. 4-10c shows only small oscillations compared to rising bubbles in deionized water (cf. Fig. 4-9c). Furthermore, the mean elongation is lower than in deionized water with a value of 0.09. According to the definition of Clift et al. ([125], p. 23) the bubbles are spherical, which is in consensus with visual impressions. The calculated amplitudes  $\hat{A}$  and frequencies  $\omega$  of the trajectory oscillations according to the sinusoidal fit function of Eq. (4-5) for bubbles rising in MIBC and HDA solutions with varying concentrations are presented in Fig. 4-11. For both surfactants the amplitude of oscillation decreases with increasing surfactant concentration, whereas the oscillation frequency increases. At a certain surfactant concentration a threshold is reached. The threshold value is approximately the same for both surfactants, namely 1.6 mm as amplitude and 48 Hz as frequency of trajectory oscillation. The concentrations of the surfactant solutions of these thresholds correspond approximately to the concentrations of the thresholds for elongation and rising velocity as presented in Fig. 4-7b&c.

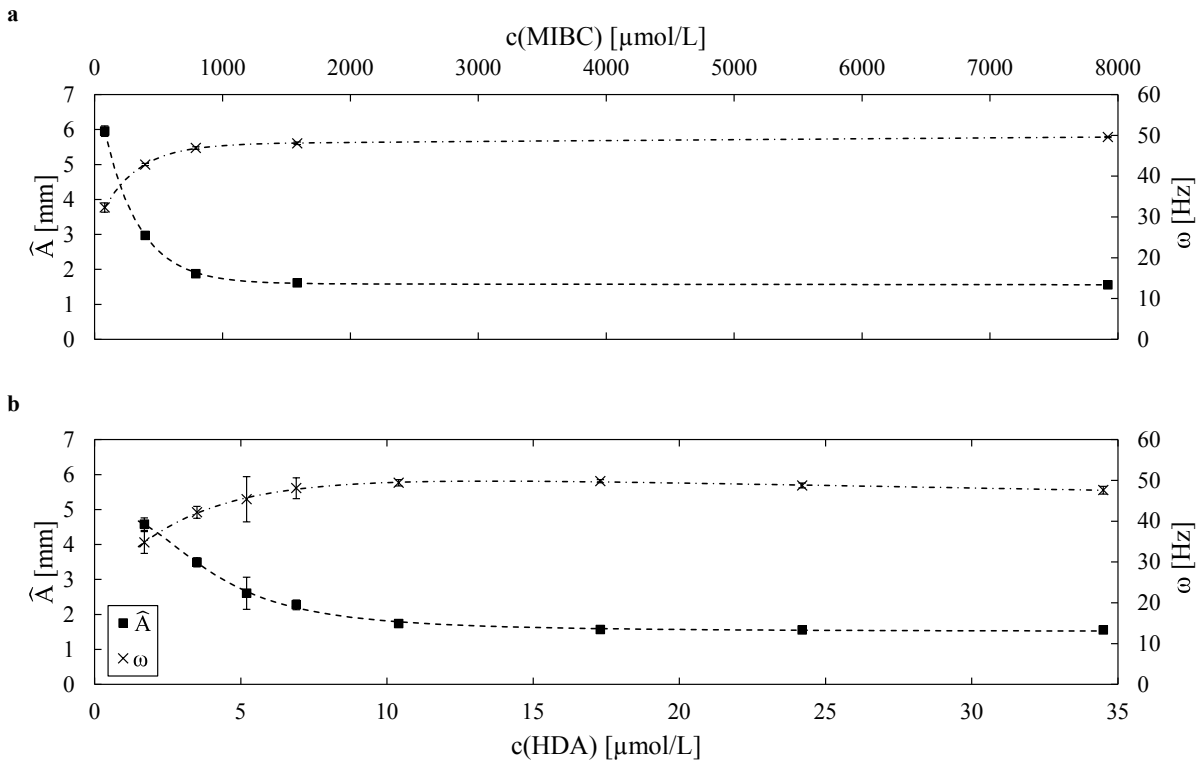


**Fig. 4-11.** Amplitude  $\hat{A}$  and frequency  $\omega$  of trajectory oscillation according to a sinusoidal fit function of the type  $x(t)=\hat{A}\cdot\cos(\omega\cdot t+\phi)+C$  for bubbles rising in methyl isobutyl carbinol (MIBC) solutions (a) and hexadecylamine (HDA) solutions (b). Dashed lines indicate trends [230].

#### 4.2.2.3 Hydrodynamic characterisation

The bubble trajectories and the corresponding mean velocity vector fields for different MIBC concentrations obtained by PIV are presented in Fig. 4-12a&b, Fig. 4-13a&b, and Fig. 4-14a&b. Velocities larger than zero are mainly observed directly in the bubble rising path. Regions left and right of the rising path are unaffected. The vectors in the bubble rising path are oriented in direction of the rising bubble. However, at points of bubble redirection, e.g. at  $x\approx 25$  mm and  $y\approx 9$  mm in Fig. 4-12b, vectors are present, which are directed outwards from the rising path. In these areas pointing outwards from the bubble trajectory, higher liquid velocities with values of about 0.016 m/s are observed. With increasing MIBC concentration the number of regions with velocities larger than zero increases. Furthermore, more regions with liquid velocities higher than 0.012 m/s are observed. Thus, the mean liquid velocity seems to increase with increasing surfactant concentration. Similar results have been obtained for varying HDA concentrations, which are shown in Appendix 9.1.2.

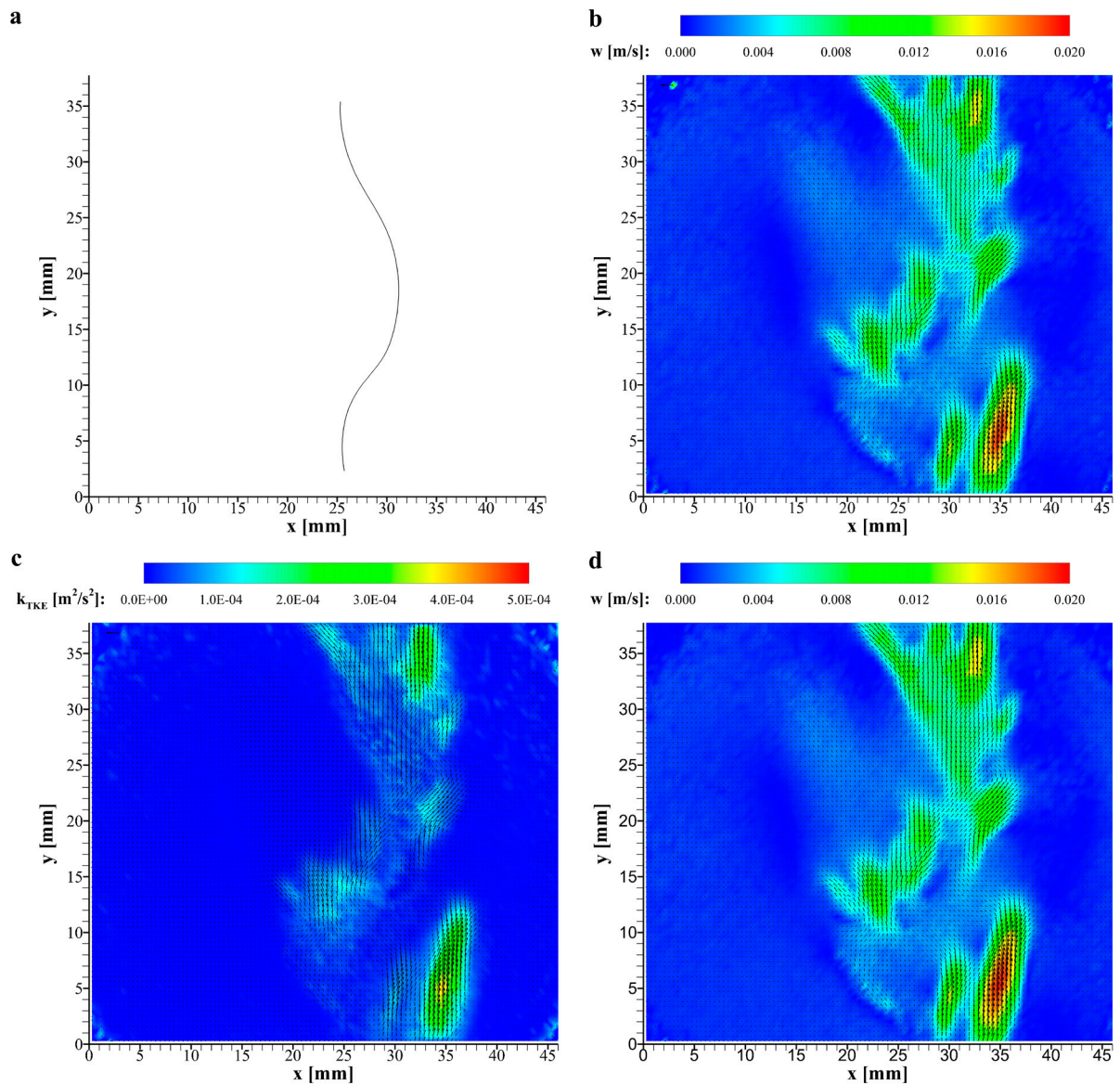


**Fig. 4-12.** Bubble trajectory (a), mean liquid velocity vector field (b), mean vector field as indicator for turbulent kinetic energy  $k_{TKE}$  (c), and reconstructed mean liquid velocity vector field using POD mode 0 coefficient (d) all for 396  $\mu\text{mol/L}$  methyl isobutyl carbinol (blank spots indicate values larger than scale) [230].

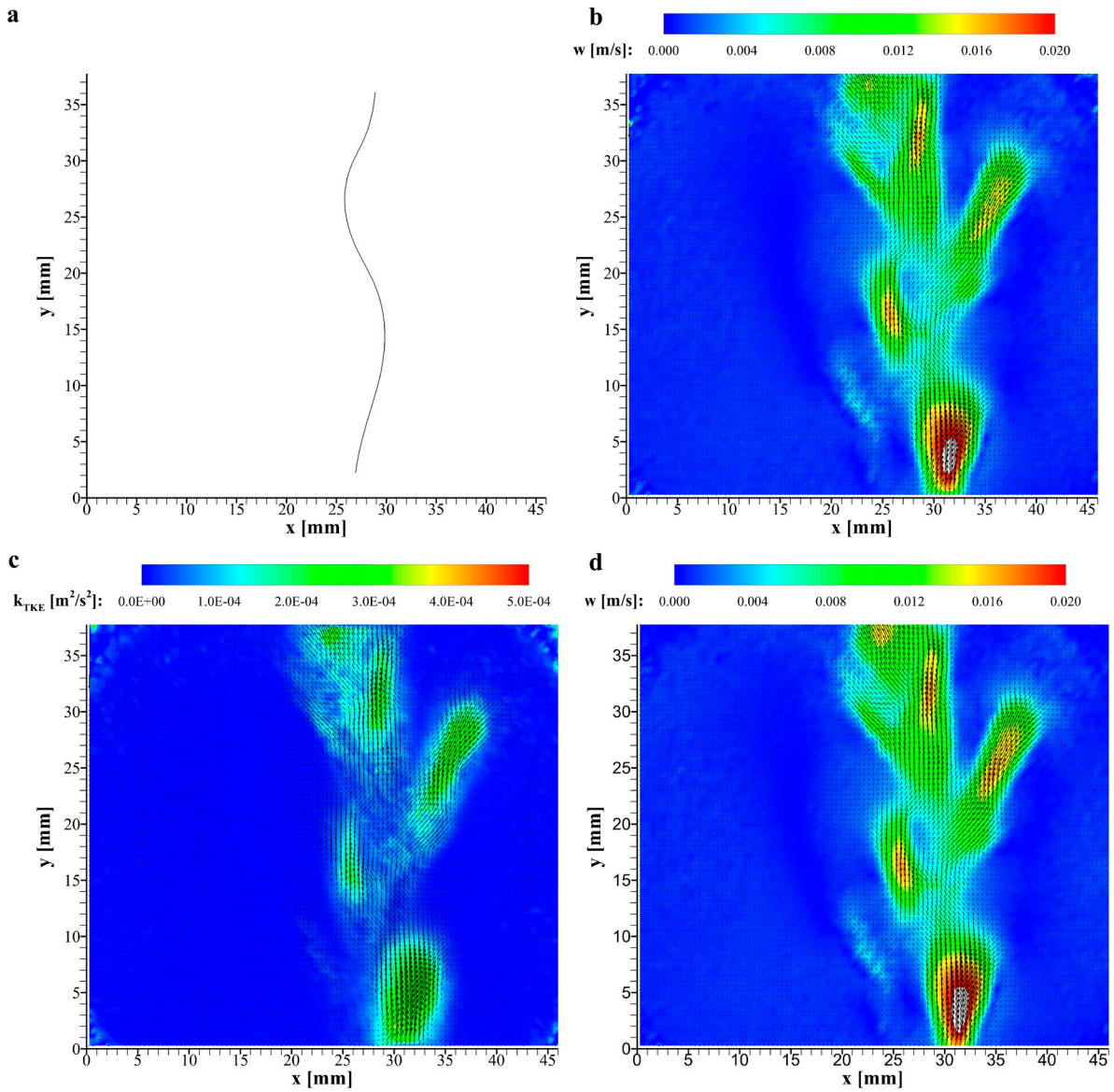


**Fig. 4-13.** Bubble trajectory (a), mean liquid velocity vector field (b), mean vector field as indicator for turbulent kinetic energy  $k_{TKE}$  (c), and reconstructed mean liquid velocity vector field using POD mode 0 coefficient (d) all for 792  $\mu\text{mol/L}$  methyl isobutyl carbinol (blank spots indicate values larger than scale) [230].

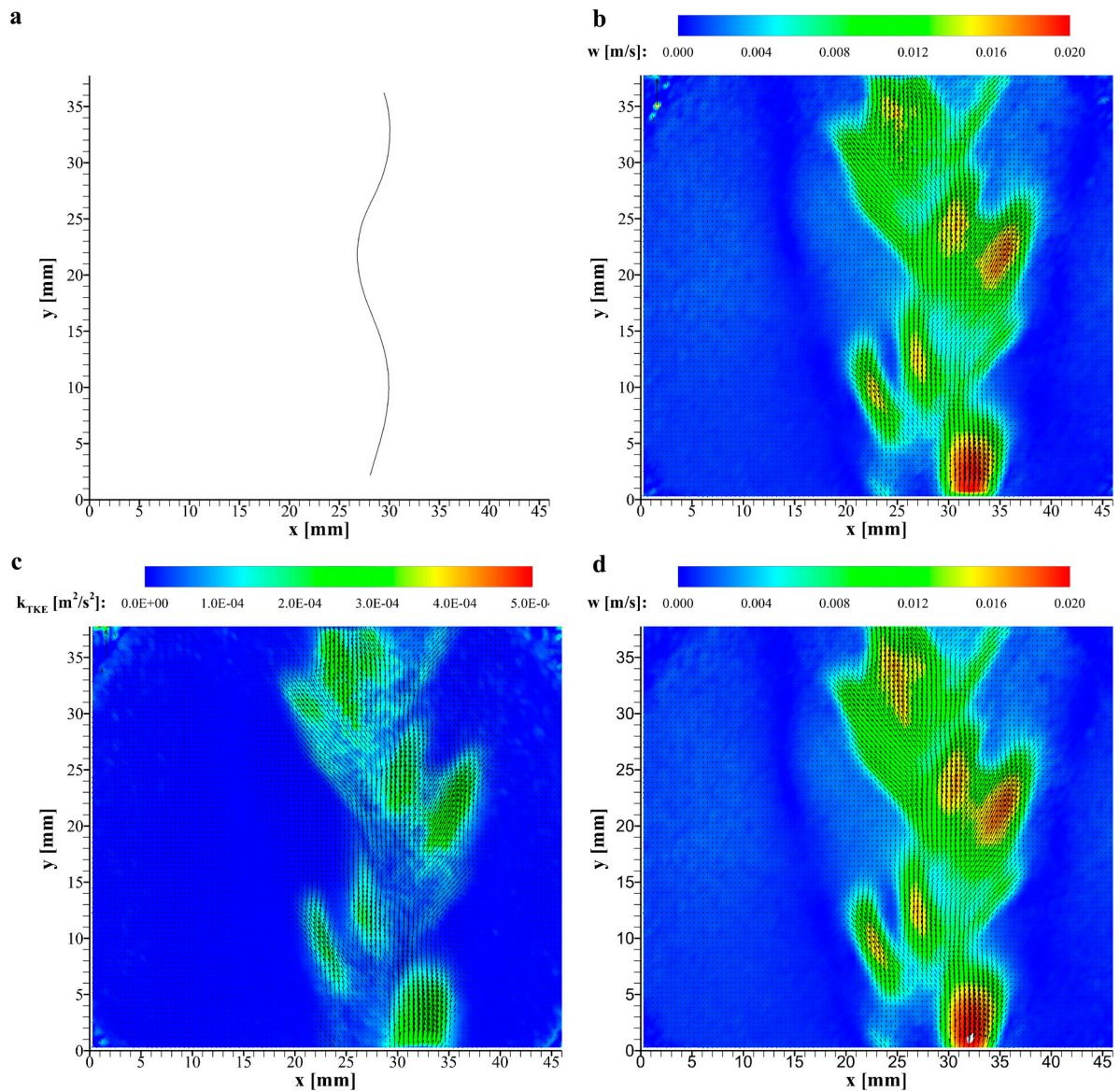


**Fig. 4-14.** Bubble trajectory (a), mean liquid velocity vector field (b), mean vector field as indicator for turbulent kinetic energy  $k_{TKE}$  (c), and reconstructed mean liquid velocity vector field using POD mode 0 coefficient (d) all for 7922  $\mu\text{mol/L}$  methyl isobutyl carbinol (blank spots indicate values larger than scale) [230].

Obtained values for the mean liquid velocity  $\bar{w}$  are compared to the corresponding bubble rising velocities  $w_B$  in Fig. 4-15 for different MIBC and HDA concentrations. The mean liquid velocity increases with increasing surfactant concentration, whereas the bubble rising velocity decreases with increasing surfactant concentration. Because this seems contradictory, further hydrodynamic parameters are investigated.

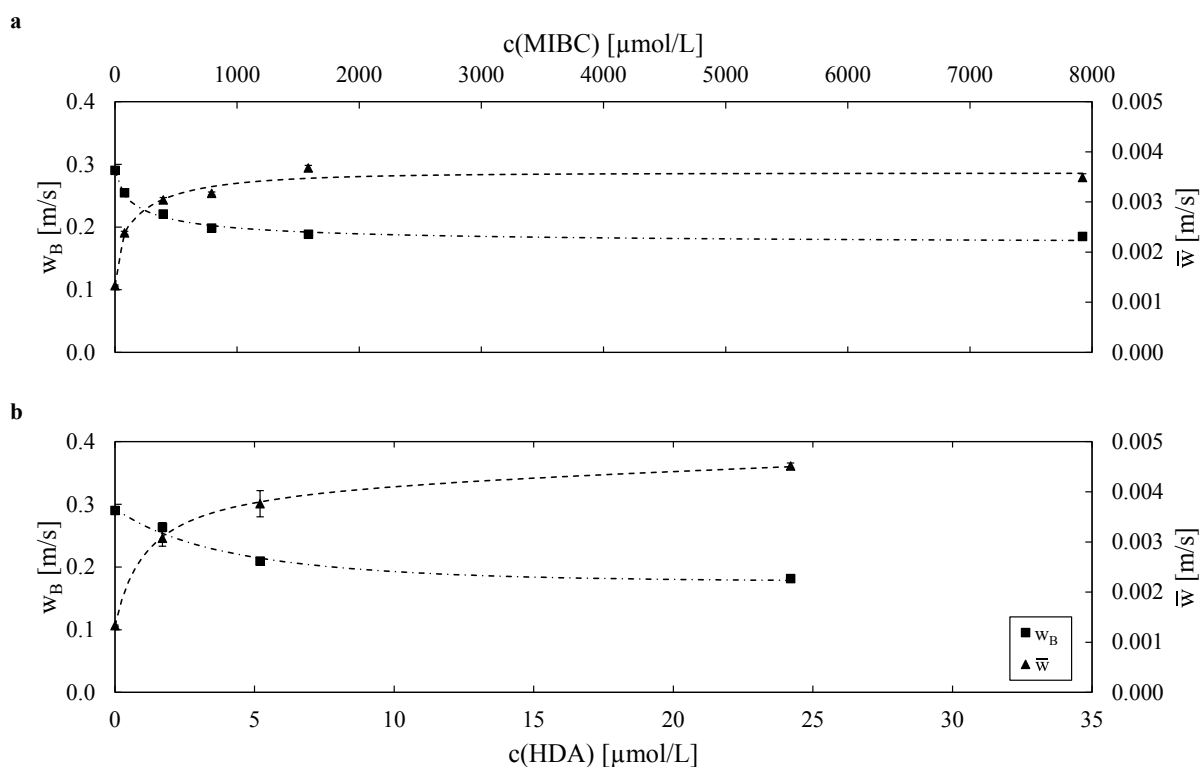


**Fig. 4-15.** Bubble rising velocity  $w_B$  (squares) and mean liquid velocity  $\bar{w}$  (triangles) for rising bubbles in aqueous methyl isobutyl carbinol (MIBC) (a) and hexadecylamine (HDA) solutions (b). Dashed lines indicate trends [230].

Instantaneous liquid vorticity fields for three different MIBC concentrations corresponding to the presented vector fields in Fig. 4-12 to Fig. 4-14 are shown in Fig. 4-16. As has been presented in Fig. 4-7, the bubble rising velocity decreases with increasing surfactant concentration. The vertical bubble position in all vorticity plots in Fig. 4-16 is at approximately  $y=26$  mm so that a comparison between the three plots is feasible. Counter-rotating vortices can be identified for all three MIBC concentrations, which may be linked to a Kármán vortex street [199]. Clockwise rotating vortices are displayed in blue (negative values) and anti-clockwise rotating vortices are indicated in red (positive values). Areas with no rotation have a value of zero and are represented in green. Similar vortex patterns were observed in simulations by Fleckenstein and Bothe for a freely rising contaminated bubble with a diameter of 1 mm [249]. The vorticity plots show that the number of vortices increases with increasing MIBC concentration. Clift et al. found that vortex shedding occurs in surfactant solutions already at  $Re=200$ , while it is delayed in pure systems to  $Re=800$  ([125], p. 185). As a reason for this they named the mobile surface of bubbles in pure water, which prevents vortex shedding due to the internal gas circulation as depicted in Fig. 2-19a. Added surface active reagents adsorb on the bubble surface, which leads to an immobilisation of the surface as well as a decreased internal gas circulation (cf. Fig. 2-19b). Bubbles behave then like rigid spheres so that vortex shedding arises.

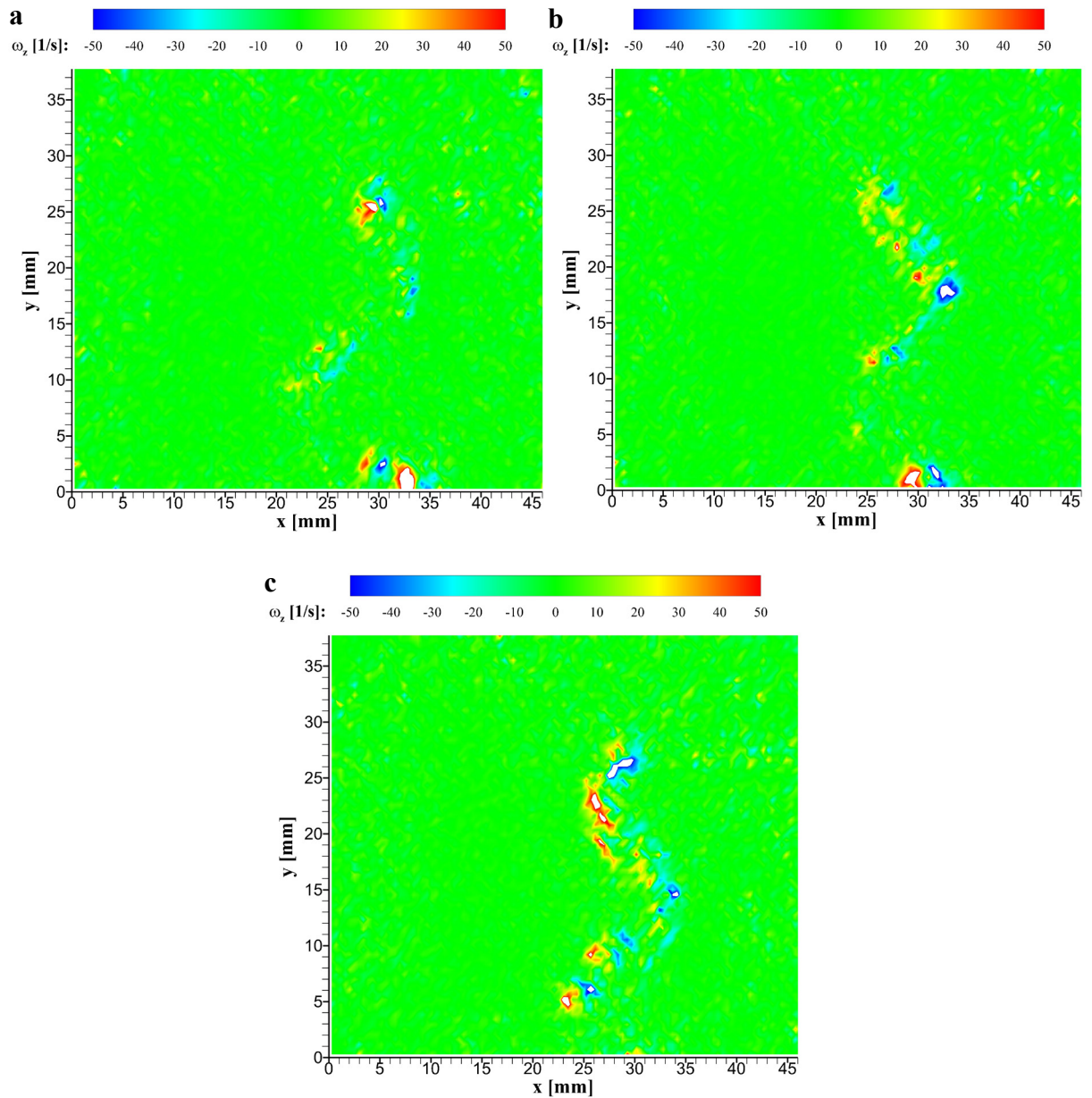


**Fig. 4-16.** Liquid vorticity plots for MIBC concentrations of 396  $\mu\text{mol/L}$  (a), 792  $\mu\text{mol/L}$  (b), and 7922  $\mu\text{mol/L}$  (c). The bubbles are for all plots located at approx.  $y=26$  mm for a better comparison (blank spots indicate values larger than scale) [230].

The rotation frequency of the vortices in Fig. 4-16 is about 30 to 50 Hz. Thus, a good agreement between the rotation frequencies of the vortices and the frequencies of trajectory oscillation, which has been found to range likewise between 30 and 50 Hz (cf. Fig. 4-11), is present.

The mean vector fields for the proportionality constant of the turbulent kinetic energy  $k_{\text{TKE}}$  (see chapter 3.2.2) for three different MIBC concentrations are presented in Fig. 4-12c, Fig. 4-13c, and Fig. 4-14c. The main energy is induced at points of redirection of the bubble in the rising path (cf. Fig. 4-12a, Fig. 4-13a, and Fig. 4-14a). As already observed for the mean liquid velocity, the rest of the measurement area is unaffected. With increasing MIBC concentration the mean value for  $k_{\text{TKE}}$  increases. The coloured area at the bottom of the measurement area at

$x=35$  mm decreases in length with increasing MIBC concentration, but increases in width from approx. 3 mm to 5 mm (cf. Fig. 4-12c, Fig. 4-13c, and Fig. 4-14c). Additionally, the number of areas with values for  $k_{TKE}$  larger than zero increases with increasing MIBC concentration. At 396  $\mu\text{mol/L}$  (Fig. 4-12c) only two larger areas are present, while there are five areas at 792  $\mu\text{mol/L}$  (Fig. 4-13c) and eight areas at 7922  $\mu\text{mol/L}$  (Fig. 4-14c). Furthermore, the vectors in areas with larger kinetic energies are always directed outwards of the bubble rising path. These areas are mainly present at positions of bubble redirection. At these positions vortex shedding occurs as shown in Fig. 4-16. This proves that kinetic energy is induced by vortex shedding. As the number of bubble redirections increases with increasing surfactant concentration, the number of vortices in the measurement area increases. Thus, more kinetic energy is induced in the measurement area, which leads to an increase in the mean liquid velocity  $\bar{w}$  as observed in Fig. 4-15. Similar results have been obtained in HDA solutions (see Appendix 9.1.2).

The bubble characteristics differ between measurements in HDA and MIBC solutions (cf. Fig. 4-7). In order to compare the obtained results in relation with the hydrodynamic parameters  $k_{TKE}$  and  $\bar{w}$ , the dimensionless bubble Strouhal number  $Sr_B$  is introduced:

$$Sr_B = \frac{d_B \cdot \omega}{w_B} \quad (4-6)$$

For calculation of  $Sr_B$  the bubble diameter  $d_B$ , the bubble rising velocity  $w_B$ , and the frequency of trajectory oscillation  $\omega$  as discussed above are used. The relation between  $k_{TKE}$  and  $Sr_B$  is given in Fig. 4-17a and the relation between  $\bar{w}$  and  $Sr_B$  is presented in Fig. 4-17b. With increasing  $Sr_B$  the proportionality constant of the turbulent kinetic energy  $k_{TKE}$  as well as the mean liquid velocity  $\bar{w}$  increase. The results presented above show that  $Sr_B$  increases with increasing surfactant concentration, as the path oscillation frequency  $\omega$  increases and the rising velocity  $w_B$  decreases. Thus, the higher  $Sr_B$ , the higher the surfactant concentration.

In the present study,  $Sr_B$  is less than unity for all investigated surfactant concentrations. Di Marco et al. [250] observed that a bubble Strouhal number smaller than unity is closely related to vortex shedding. Due to vortex shedding, more kinetic energy is introduced in the measurement area, which results in higher mean liquid velocities.

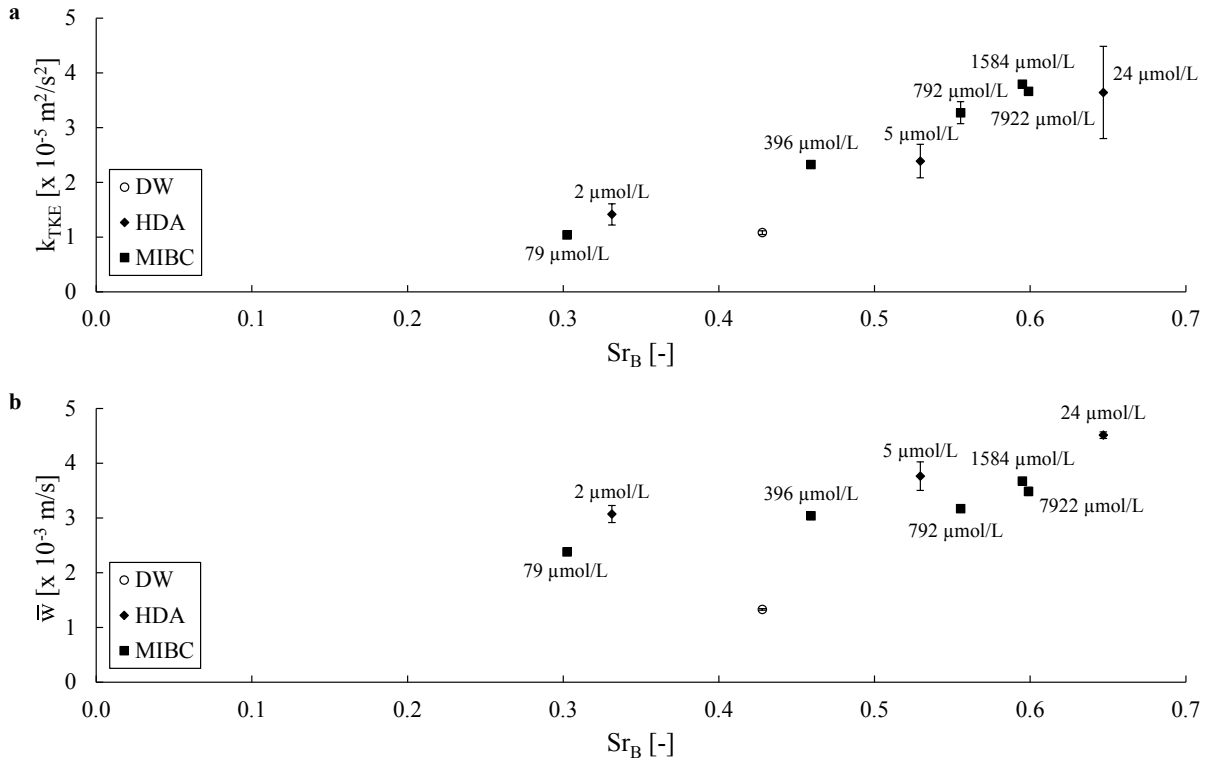


**Fig. 4-17.** Proportionality constant of turbulent kinetic energy  $k_{TKE}$  in dependency of bubble Strouhal number  $Sr_B$  (a) and relationship between mean liquid velocity  $\bar{w}$  and  $Sr_B$  (b) for experiments in deionized water (DW) as well as aqueous hexadecylamine (HDA) and methyl isobutyl carbinol (MIBC) solutions [230].

The vortex shedding is related to the path oscillation frequency  $\omega$  of the rising bubble, which increases with increasing surfactant concentration (cf. Fig. 4-11). Hence,  $\bar{w}$  will increase in the measurement area with increasing surfactant concentration.

Saito et al. also found that addition of surfactants has an influence on vortex shedding [251]. They showed that the intensity and size of vortices increased up to a critical surfactant concentration and decreased afterwards. As a reason for the increase of the intensity they name the Marangoni stress, which is owed to a concentration gradient of the adsorbed surfactant on the bubble surface (see also [134,252,253]).

As shown in the present study, the increase of the hydrodynamic parameters  $k_{TKE}$  and  $\bar{w}$  can be related to the oscillation frequency  $\omega$  of the bubble trajectories, which results in an increased vortex shedding. Due to an adsorption of surfactants on the bubble surface, the bubble motion is nearly rectilinear, which is in consensus with determined  $Re$  numbers (cf. Tab. 2-5). Further addition of surfactants decreases the amplitude of motion in horizontal  $x$  direction, but at the same time increases the frequency of redirections, until a threshold is reached.

Proper Orthogonal Decomposition (POD) is applied in order to investigate dynamic structures of the flow. All results for POD in the following are presented for experiments in MIBC solutions. Similar results have been obtained in HDA solutions with some larger deviations in

only a few cases due to less experimental data (see Appendix 9.1.2). The eigenvalues of calculated modes for MIBC solutions are shown in Fig. 4-18 as cumulative percentage sum of the kinetic energy. As explained in chapter 3.2.2, the calculated modes are sorted by their contribution to the turbulent kinetic energy. Thus, low modes contain a large amount of energy, while higher modes contain low amounts of energy. This can also be seen in Fig. 4-18. For all five MIBC solutions a steep increase is present for the first modes. Afterwards, the amount of energy increases slower with increasing mode number, until 100 % of the energy is represented at mode 169. Furthermore, it can be seen that the amount of energy contained by the same modes is different for different MIBC concentrations. With increasing surfactant concentration the energy content of lower modes increases.

The difference of mode energy dependent on MIBC concentration is summarized in Fig. 4-19, where the number of modes necessary to represent 90 % of the TKE for different MIBC concentrations is shown. The amount of energy contained by lower modes is as already observed in Fig. 4-18 increasing with increasing surfactant concentration. Thus, less modes are needed at higher MIBC concentrations to represent 90 % of the TKE. Furthermore, an analogy to the graphs of rising velocity and elongation presented in Fig. 4-7b&c can be seen: The number of modes for 90 % of TKE decreases with increasing MIBC concentration until a threshold is reached.

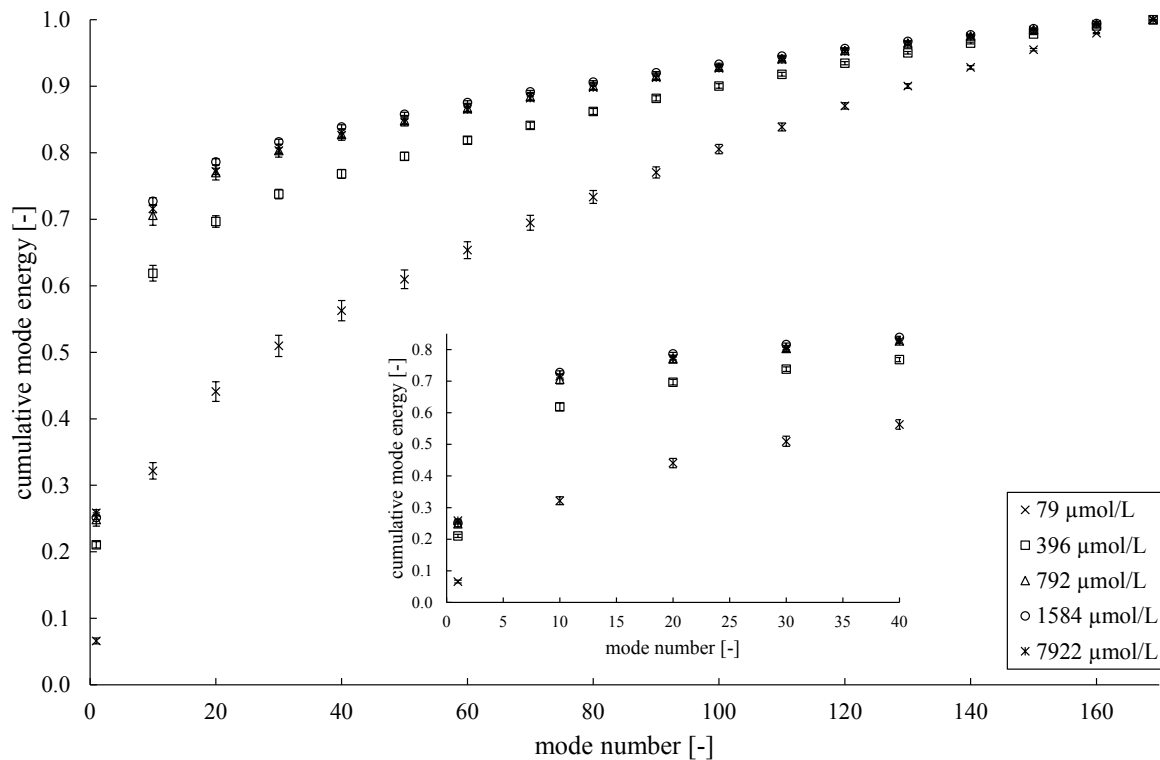


**Fig. 4-18.** Eigenvalues of modes shown as cumulative percentage sum of the turbulent kinetic energy of the fluctuating velocity field for POD analysis of varying MIBC concentrations (every 10<sup>th</sup> value shown) [230].

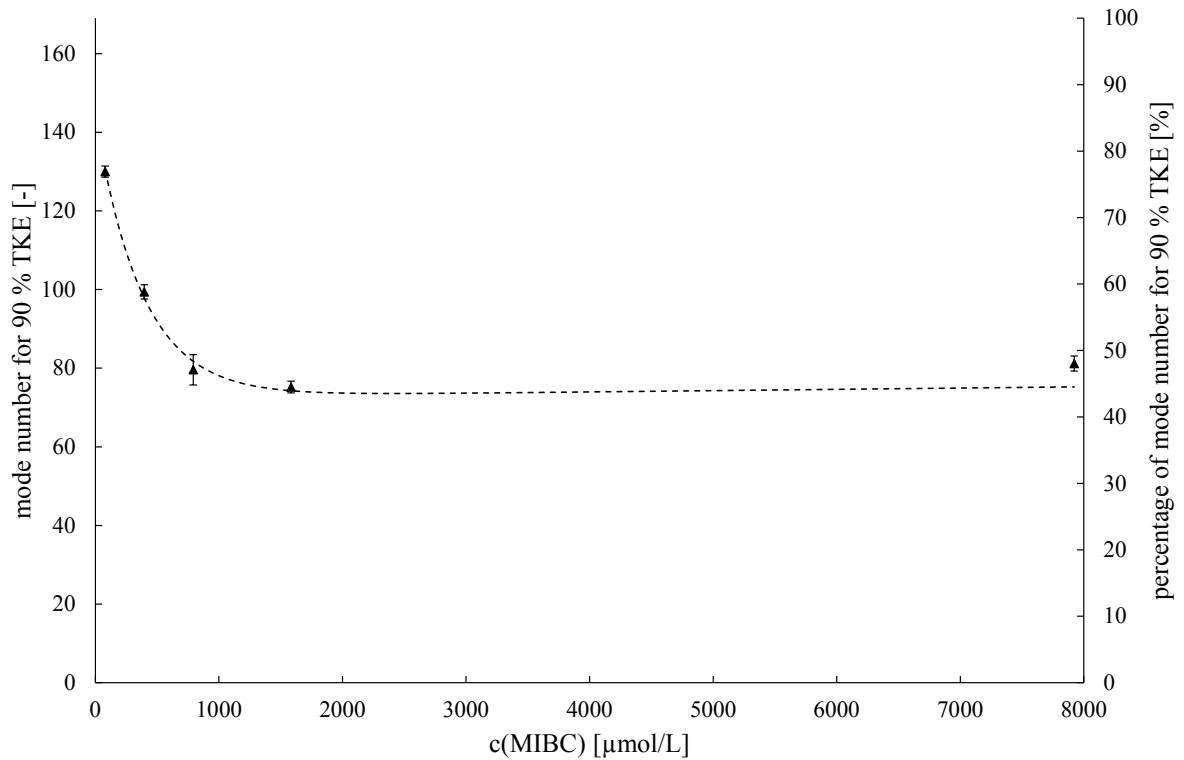


**Fig. 4-19.** Mode number and corresponding percentage necessary to represent 90 % of turbulent kinetic energy (TKE) depending on methyl isobutyl carbinol (MIBC) concentration  $c(\text{MIBC})$  [230].

The zeroth mode contains the information of the mean liquid velocity field (cf. chapter 3.2.2). The reconstructed mean liquid velocity fields using the calculated eigenvalues of the zeroth modes for MIBC concentrations of  $396 \mu\text{mol/L}$ ,  $792 \mu\text{mol/L}$ , and  $7922 \mu\text{mol/L}$  are presented in Fig. 4-12d, Fig. 4-13d, and Fig. 4-14d. A comparison with the experimentally measured mean liquid velocity fields in Fig. 4-12b, Fig. 4-13b, and Fig. 4-14b shows an excellent agreement between the vector fields, as only small differences between the liquid vector fields are observed, e.g. the area at  $x \approx 33 \text{ mm}$  and  $y \approx 35 \text{ mm}$  with a velocity of approx.  $0.015 \text{ m/s}$  in Fig. 4-12 is larger in the POD reconstruction (d) than in the measured mean vector field (b). This emphasises that POD is applicable to the given data set to represent the fluid flow with a reduced order model.

The time-resolved values for modes 1, 10, and 50 for deionized water and an MIBC solution with a concentration of  $7922 \mu\text{mol/L}$  are presented in Fig. 4-20a1-c1. It is clearly visible that a periodic nature is present. In the MIBC solution only one oscillation period is present for mode 1 (Fig. 4-20a1), while there are already five oscillation periods present in mode 10 (Fig. 4-20b1). The oscillation seems to be damped, because the oscillation frequency decreases with increasing time.

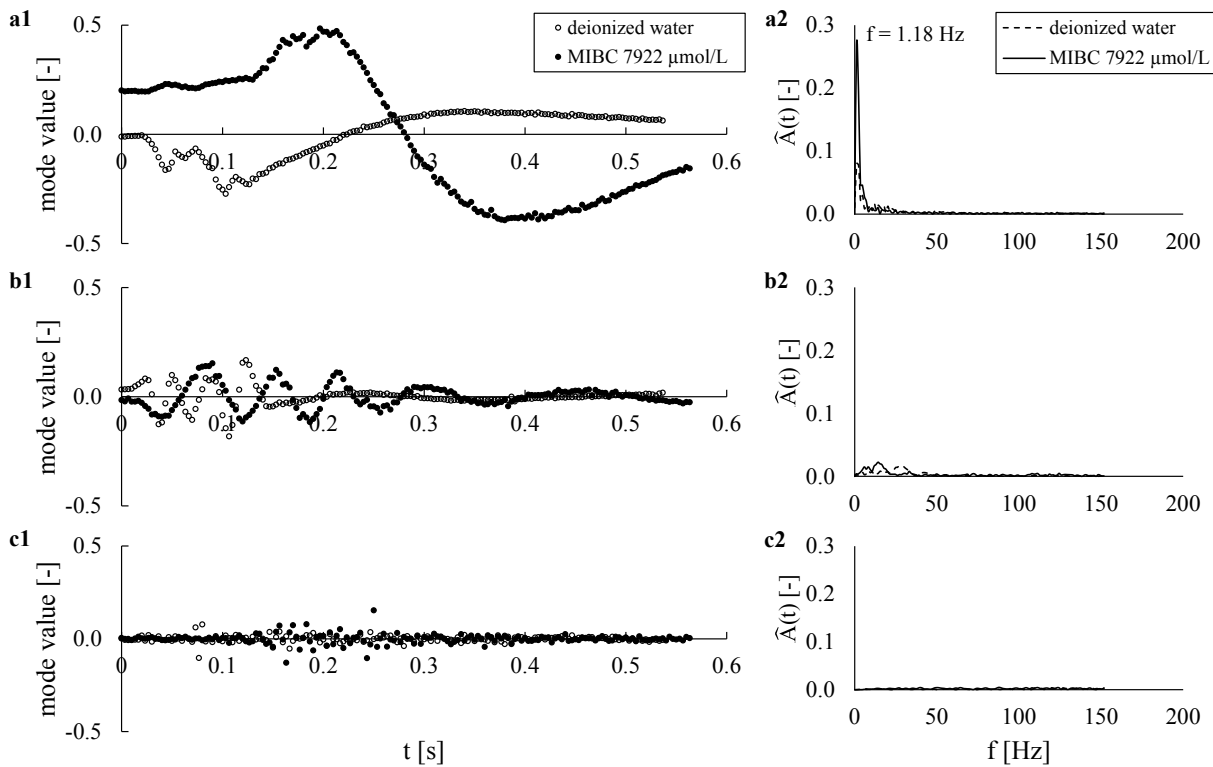


**Fig. 4-20.** Time-resolved values of determined modes (1) for deionized water (open circles) and a methyl isobutyl carbinol concentration of 7922  $\mu\text{mol/L}$  (full circles) and corresponding Fast Fourier Transform (FFT) spectra (2) for POD mode 1 (a), mode 10 (b), and mode 50 (c) [230].

A similar trend is observed for deionized water. Compared to the MIBC modes the number of oscillations as well as the amplitudes are, however, lower. Mode 50 (Fig. 4-20c1) shows a random structure with very small mode values for both deionized water and MIBC solution. The oscillation amplitudes, which correspond to the mode values, decrease with increasing mode number, while the frequency seems to increase.

A temporal analysis of the POD modes via Fast Fourier Transform (FFT) provides information on the periodicity of the features captured by each POD mode (cf. chapter 3.2.2). The FFT spectra corresponding to mode 1, mode 10, and mode 50 are presented in Fig. 4-20a2-c2. A single distinctive signal is observed only for mode 1 at a frequency  $f$  of 1.18 Hz for both deionized water and MIBC. The observed amplitude  $\hat{A}$  is higher for the MIBC solution than for deionized water. The dominant frequency corresponds to the bubble production frequency, which has been observed during the experiments (cf. chapter 4.2.1). Therefore, it is plausible that the dominant frequency should be the same for both liquids. The FFT spectra for mode 10 (Fig. 4-20b2) are multimodal with smaller amplitudes than for mode 1. No characteristic frequency could be determined. However, a shift towards higher frequencies seems to be present. For mode 50, the amplitudes are even smaller and close to zero so that no dominant frequency could be determined. The first modes represent the large scale turbulences, while

higher modes mainly represent small fluctuations in the flow referred to noise (cf. chapter 3.2.2). Thus, higher mode numbers exhibit lower values representing random structures. As mode 1 represents the highest amount of energy in the fluid flow and the frequency of this mode could be connected to the bubble production frequency, it may be concluded that streamwise bubble-induced motions dominate the large scale structures of the liquid velocity field. This was also stated by Aliyu et al. [254]. The differences in mean liquid velocity and turbulent kinetic energy are referred to the vortex shedding process as discussed above.

The reconstructed liquid vector fields using the first four significant POD modes are presented in Fig. 4-21 for an MIBC solution with a concentration of 7922  $\mu\text{mol/L}$ . Mode 1 and mode 2 contain together nearly 50 % of the total energy of the flow. From mode 2 to mode 3 a sharp drop in the energy amount to approx. one third is present. Mode 1 and 2 seem to show the same vector field with a slight shift in upwards direction, e.g. the vortex centre at  $x \approx 35$  mm and  $y \approx 0$  mm in Fig. 4-21a moves to  $x \approx 36$  mm and  $y \approx 4$  mm in Fig. 4-21b. The time-resolved analysis of these modes confirm this as they show the same sinusoidal behaviour with a shift in phase. Furthermore, an increase in the amount of vortices present in the measurement area is observed from mode 2 to mode 4. Comparison of, e.g., position  $x \approx 20$ -25 mm and  $y \approx 5$ -15 mm in Fig. 4-21b with the same location in Fig. 4-21c&d reveals the structure of vortex breakdown. This procedure can be related to the energy cascade model proposed by Richardson ([255], p. 66). From the mean liquid velocity vector fields presented in Fig. 4-12b, Fig. 4-13b, and Fig. 4-14b, this dynamic nature of the flow is not accessible. With POD, however, a detailed insight into the micro processes in the bubble wake is feasible.

From the analysis of the POD results it can be concluded that dominating large scale structures are present independent of surfactant concentration, which correspond to the streamwise bubble-induced motions. Yet the mean liquid velocity and the amount of turbulent kinetic increase with increasing surfactant concentration (see Fig. 4-15 and Fig. 4-17). Therefore, large scale structures cannot be the main reason. As shown in Fig. 4-19, nearly 50 % of the calculated modes are necessary for the highest MIBC concentration to represent 90 % of the TKE of the flow, although the first three modes already contain approx. 60 % of total TKE (cf. Fig. 4-21). Thus, small scale structures represented by higher modes, which correspond to vortex shedding and energy cascading, seem to have a significant influence on the liquid flow field and are the reason for differences in mean liquid velocity and induced kinetic energy.

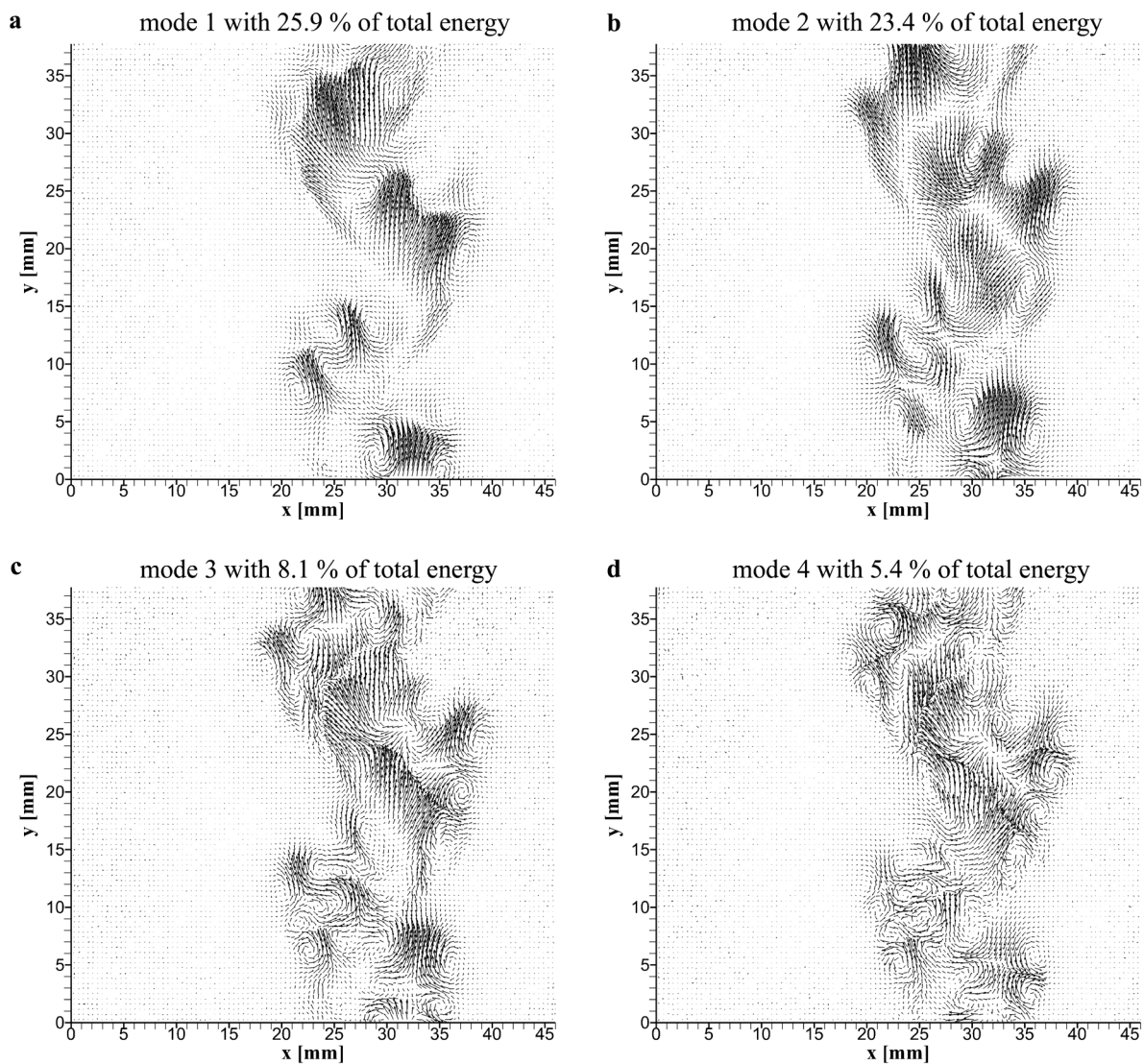


**Fig. 4-21.** Reconstructed liquid vector fields using POD mode 1 with 25.9 % of total energy (a), mode 2 with 23.4 % of total energy (b), mode 3 with 8.1 % of total energy (c), and mode 4 with 5.4 % of total energy (d) for a concentration of 7922  $\mu\text{mol/L}$  methyl isobutyl carbinol [230].

## 5 Investigation of a model three-phase system

In this chapter flotation experiments conducted with glass particles as a model system are presented. These experiments are carried out in order to investigate different influence parameters on the flotation process.

### 5.1 Surface modification of glass

For first flotation tests, a model system consisting of glass particles is used to investigate the influence of different parameters on the flotation process in general. One of the parameters to be investigated is the wettability of the particles. The surface properties of glass particles with respect to the wettability can be manipulated by reaction of the surface with silanes as stated in chapter 2.5. In first tests, the surface modification via silanisation is investigated using glass slides. In doing so, the wettability of the glass surface can be directly determined via contact angle measurements. Based on these results, glass particles are modified for rigorous flotation tests.

#### 5.1.1 Modification of glass slides

Glass slides purchased from Thermo Scientific are modified using four different trialkoxysilanes: ethyltriethoxysilane (ES), n-octyltriethoxysilane (OS), n-dodecyltriethoxysilane (DS) and 1H,1H,2H,2H-perfluorooctyltriethoxysilane (FS). The chemical composition of the glass slides is given in Tab. 5-1.

The glass slides are first cleaned for 24 h in a beaker glass using Caro's acid to remove all organic impurities from the glass surface. Additionally, the surface is activated due to a protonation of the silanol groups at the glass surface (cf. chapter 2.5). The Caro's acid is freshly prepared by mixing three parts concentrated sulphuric acid ( $\text{H}_2\text{SO}_4$ , 96 %) and one part hydrogen peroxide solution ( $\text{H}_2\text{O}_2$ , 30 %).

**Tab. 5-1.** Composition of glass slides [256].

Component	w [%]
Silicon dioxide ( $\text{SiO}_2$ )	72.2
Sodium oxide ( $\text{Na}_2\text{O}$ )	14.3
Calcium oxide ( $\text{CaO}$ )	6.4
Magnesium oxide ( $\text{MgO}$ )	4.3
Others	2.8

The production of peroxymonosulfuric acid is an exothermic reaction and the reaction product is highly instable. Thus, the beaker glass is cooled in an ice bath and the reaction temperature is kept below 50 °C due to safety reasons and to reduce the amount of decomposing peroxymonosulfuric acid. H<sub>2</sub>O<sub>2</sub> is filled into a beaker glass and the concentrated H<sub>2</sub>SO<sub>4</sub> is slowly added to the solution while stirring. Afterwards, the slides are rinsed with deionized water and dried in an oven at 70 °C. In the next step, the glass slides are conditioned in ethanol (EtOH, 96 %) for 24 h, before the silanisation reaction is carried out in 25 mL fresh EtOH (96 %). A ratio of molar amount of silane to available glass surface of approx. 5 mmol/m<sup>2</sup> is then added to the solution.

In order to investigate the influence of reaction time on the wettability, the silanisation process is carried out for one, four, and seven days for each of the four silanes. After the reaction, the glass slides are rinsed with deionized water and dried in an oven at 70 °C. The contact angles are measured using the sessile drop method in order to analyse the change in surface wettability. At least five contact angles using deionized water as test fluid are measured along the entire surface per glass slide. Each drop has a volume of 1 µL, which is dosed automatically by the system to decrease measurement uncertainties due to unequal drop sizes ([117], p. 13ff). The resolution of the measurement system is stated to be ±0.1°. The contact angle measurements are performed at a room temperature of 23 °C and a relative humidity of 49 %. The silanisation reactions for each silane and each reaction time are repeated at least three times.

The resulting mean contact angles for each tested silane with respect to the reaction time  $t_R$  are presented in Fig. 5-1. Contact angles of an unmodified glass surface, which is prior to the measurement cleaned with acetone, a glass slide treated with Caro's acid and a glass slide after the conditioning step with EtOH are presented as reference values. The shown mean values are calculated as weighted averages  $\theta_{\text{wav}}$  ([257], p. 173):

$$\theta_{\text{wav}} = \frac{\sum_i^N w_i \theta_i}{\sum_i^N w_i} \quad (5-1)$$

In this equation,  $\theta_i$  is the arithmetic mean contact angle of the five contact angles for one glass slide and  $w_i$  is the weight defined as reciprocal square of the corresponding uncertainty:

$$w_i = \frac{1}{\sigma_i^2} \quad (5-2)$$

As the standard deviations are very low, homogeneous surfaces are present after silanisation. The silanisation procedure should therefore also be applicable for modification of glass particles and flotation tests.

The unmodified glass surface exhibits a contact angle of  $19.6^\circ \pm 1.7^\circ$ . After the cleaning step using Caro's acid, the contact angle reduces to  $14.8^\circ \pm 1.1^\circ$ .

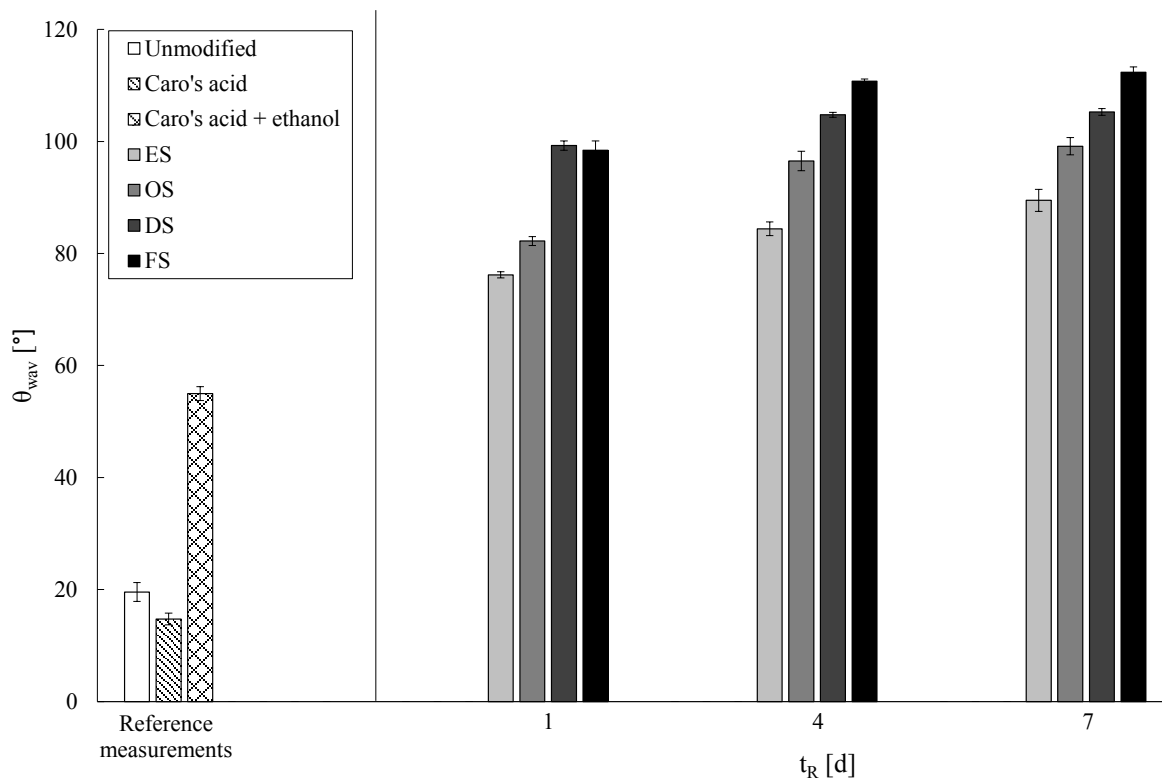


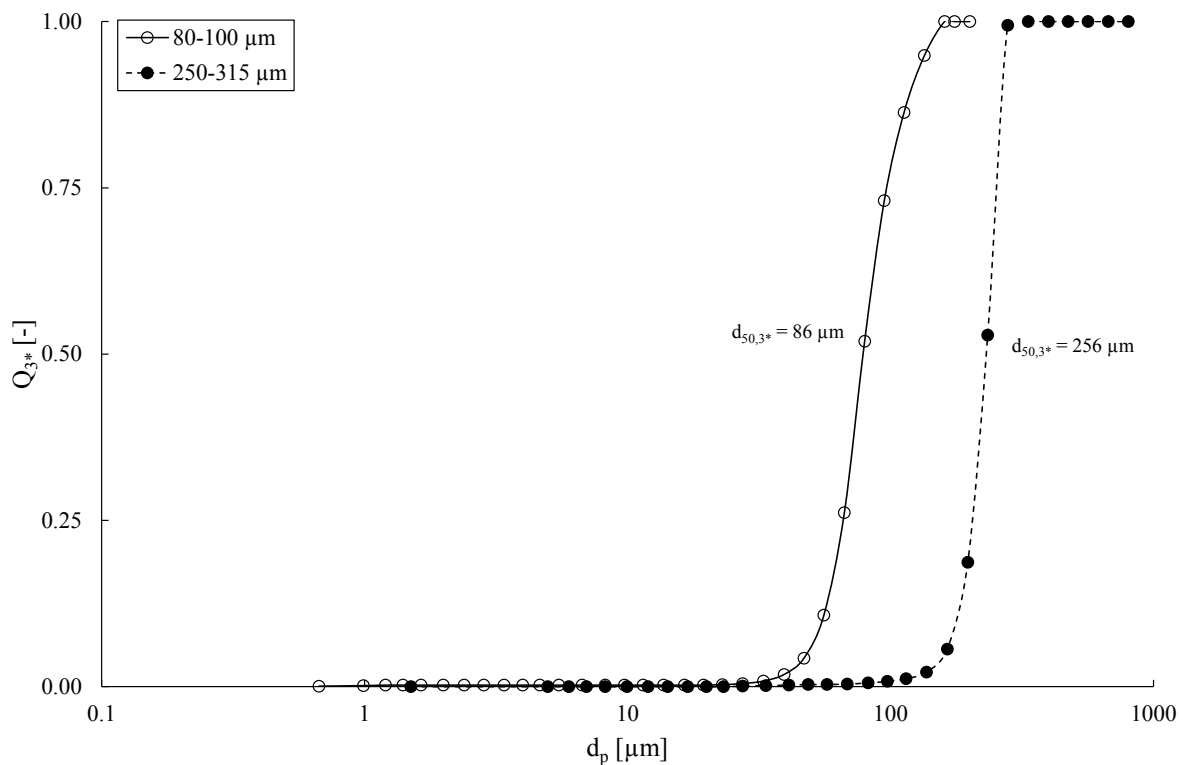
**Fig. 5-1.** Results for equilibrium weighted average contact angle  $\theta_{\text{wav}}$  of glass slides after a reaction time  $t_R$  of one, four, and seven days including reference values for an unmodified glass slide as well as for the pre-treatment with Caro's acid and conditioning with ethanol (ES=ethyltriethoxysilane, OS=n-octyltriethoxysilane, DS=n-dodecyltriethoxysilane, FS=1H,1H,2H,2H-perfluorooctyltriethoxysilane).

Thus, the cleaned surface exhibits a more hydrophilic behaviour (cf. chapter 2.2.1.1). The conditioning with ethanol shows an increase of the contact angle to  $55.0^\circ \pm 1.2^\circ$ . Therefore, the conditioning of the glass slides in EtOH causes already a hydrophobisation of the glass surface. Contact angle measurements on the glass slides after silanisation show a further increase of the hydrophobicity for all tested silanes. For all reaction times  $t_R$ , a relationship between the alkyl chain length and the measured mean contact angle is found: the contact angle increases with increasing alkyl chain length. Furthermore, the trend for each silanisation reaction over time is similar. With increasing  $t_R$ ,  $\theta_{\text{wav}}$  increases until a threshold is reached. A similar trend was found by Balgar et al. [182]. The silanisation reaction starts with the building of small islands. With increasing time, the islands expand until they merge together and finally the complete surface is covered with the silane. This process is in the beginning fast, but slows down with time (cf. chapter 2.5). The measured contact angles for ES and DS for  $t_R=1$  d are in excellent agreement with values stated in literature of  $80^\circ$  for ES [258] and  $100^\circ$  for OS ([181], p. 15), respectively. Kutelova et al. ([185], p. 99) stated  $\theta=114^\circ$  for FS and  $\theta=15^\circ$  after glass slides were treated with Caro's acid. These results also fit excellently to the measurement results presented in Fig. 5-1.

### 5.1.2 Modification of glass beads

In addition to the wettability of the particles, the particle size is one of the influence parameters, which is investigated in the flotation tests (cf. chapter 1.2). For this purpose, the unmodified glass particles are sieved via wet sieving into a fraction of 80-100  $\mu\text{m}$  and a fraction of 250-315  $\mu\text{m}$ . The resulting particle size distributions (PSD) after sieving are shown in Fig. 5-2. The median particle diameters  $d_{50,3^*}$  of these PSD are approx. 86  $\mu\text{m}$  and 256  $\mu\text{m}$ , respectively. The composition of the soda lime glass particles is given in Tab. 5-2. It is similar to the composition of the glass slides from chapter 5.1.1, especially with respect to the silicon dioxide content, which is essential for the surface modification via silanisation (cf. chapter 2.5).

For the surface modification of the glass particles n-octyltriethoxysilane (OS) is chosen as reagent. Preceding tests showed that particles with  $d_{50,3^*}=86 \mu\text{m}$  are already sufficiently hydrophobic after some minutes reaction time  $t_R$ , while an equal hydrophobisation is achieved for particles with  $d_{50,3^*}=256 \mu\text{m}$  after some hours (cf. Appendix). Therefore, a  $t_R$  of ten minutes is chosen for the smaller particles and  $t_R=5 \text{ h}$  for the larger particles. The chosen concentration of the silane is equal to the concentration for modification of the glass slides with 5  $\text{mmol}/\text{m}^2$ . The surface area of the glass particles is calculated under the assumption of spherical particles. The scanning electron microscopy (SEM) images presented in Fig. 5-3 justify this assumption.



**Tab. 5-2.** Composition of used soda lime glass particles [259].

Component	w [%]
Silicon dioxide (SiO <sub>2</sub> )	72.30
Sodium oxide (Na <sub>2</sub> O)	13.30
Calcium oxide (CaO)	8.90
Magnesium oxide (MgO)	4.00
Others	1.50

The procedure for the modification of the glass particles is analogous to the procedure for modification of the glass slides. Fig. 5-3 shows scanning electron microscopy (SEM) images of glass particles before and after treatment with Caro's acid at two different magnification factors. The images clearly show the presence of impurities and contaminations at the particle surface before the treatment, while afterwards a clean and smooth surface is present.

In case of the glass particles, direct contact angle measurements via the sessile drop technique are infeasible, because the particles are too small. Instead, the film flotation method, which has been presented in chapter 2.2.1.2, is used to measure the critical surface tension of wettability  $\bar{\gamma}_c$  as an indicator for the modification of the glass surface.

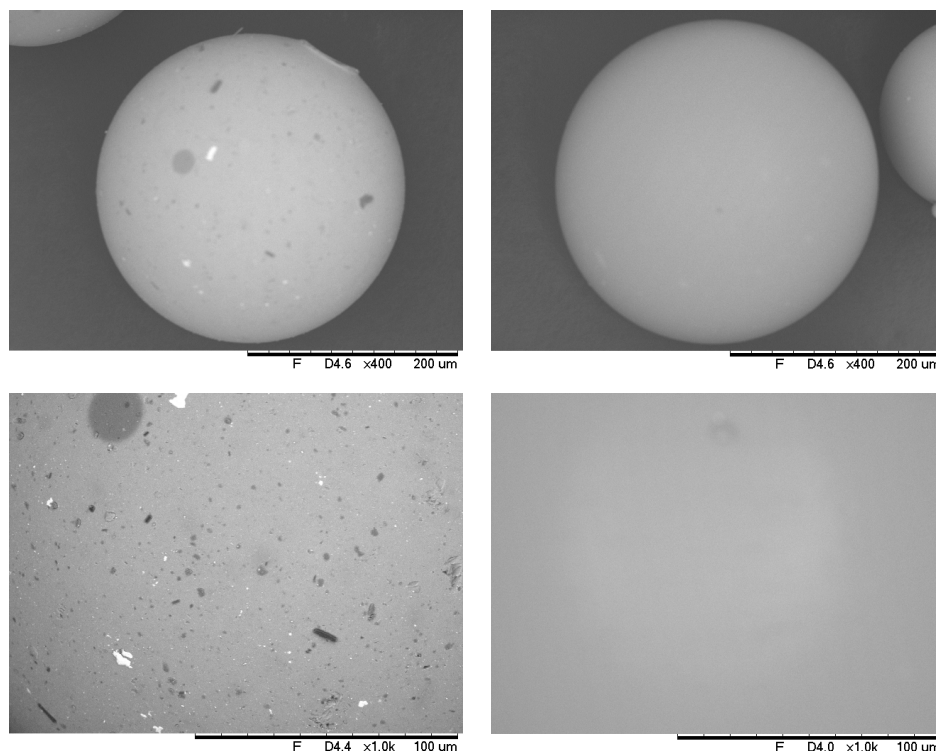


**Fig. 5-3.** Scanning electron microscopy (SEM) images of a glass particle with a median diameter  $d_{50,3^*}$  of 256  $\mu\text{m}$  before (left) and after (right) treatment with Caro's acid at a magnification factor of 400x (top) and a magnification factor of 1000x (bottom).

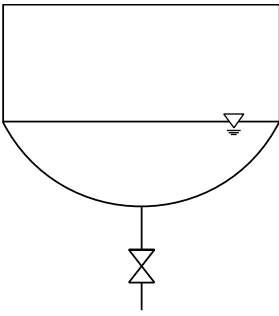


**Fig. 5-4.** Schematic representation of the experimental setup for film flotation experiments.

For this purpose, 0.1 g of the modified particles are weighed using a precision laboratory scale. Mixtures of high purity grade ethanol (99.5 %) and deionized water are prepared with varying weight fractions in order to vary the liquid surface tension. The liquid surface tension for these mixtures is correlated from literature. The corresponding diagram can be found in the Appendix 9.1.3.1. The liquid is filled into a conical apparatus with discharge, which is schematically depicted in Fig. 5-4. The particles are then carefully placed on the liquid surface. Particles with  $\bar{\gamma}_c$  smaller than the liquid surface tension  $\sigma$  will float on the surface, while particles with  $\bar{\gamma}_c$  greater than  $\sigma$  will sink. The process of wetting is spontaneous and will take place directly after the particles are placed on the liquid surface (see chapter 2.2.1.2). The floating particles are carefully removed from the surface using a spatula. The sunken particles are removed from the apparatus via the discharge. Each fraction is collected on a separate petri dish and dried in an oven at 100 °C to constant weight. The masses of each fraction are used to calculate the recovery  $R$  via Eq. (5-3):

$$R = \frac{m_{\text{floating}} + m_{\text{sunken}}}{0.1 \text{ g}} \quad (5-3)$$

The weight fraction of the floating particles  $w_{\text{floating}}$  is calculated via Eq. (5-4) using the determined recovery:

$$w_{\text{floating}} = \frac{m_{\text{floating}}}{R} \quad (5-4)$$

The weight fraction of the floating particles is then related to the corresponding liquid surface tension and a graph as shown in Fig. 2-12 is developed. The critical surface tension of wettability  $\bar{\gamma}_c$  is determined from the intersection with  $w_{\text{floating}}=50\%$  (cf. chapter 2.2.1.2).

As presented in chapter 2.2.1.2, Fuerstenau et al. compared the critical surface tension of wettability of particles with similarly modified flat surfaces. They found that the values of  $\bar{\gamma}_c$  of the particles obtained via film flotation experiments and  $\sigma_c$  of the flat surfaces obtained from the Zisman plot are equal. Thus, for experimental purposes a calibration curve relating the critical surface tension of wettability  $\sigma_c$  of flat glass surfaces with the corresponding contact angle  $\theta$  on the surface using water as testing liquid can be established. Assuming  $\sigma_c = \bar{\gamma}_c$  the

corresponding contact angle of the particles can be estimated ([260], p. 80). For the preparation of the Zisman plot, glass slides are modified with OS for various  $t_R$  in order to create surfaces with different contact angles. Contact angle measurements are then carried out using deionized water, glycerol, ethylene glycol, and toluene as testing liquids. The critical surface tension of wettability  $\sigma_c$  of each glass slide is determined as described in chapter 2.2.1.1. The contact angle  $\theta$  determined using deionized water as testing liquid is then related to the corresponding  $\sigma_c$  to establish the calibration curve presented in Fig. 5-5.

The critical surface tension of wettability  $\bar{\gamma}_c$  of the two modified particle fractions is determined via film flotation experiments as described above. A critical surface tension of wettability for the particles with a median diameter of  $86 \mu\text{m}$  of approx.  $41.1 \text{ mN/m}$  is found, while  $\bar{\gamma}_c \approx 60.4 \text{ mN/m}$  for  $d_{50,3^*} = 256 \mu\text{m}$ . Using the established calibration curve and assuming  $\sigma_c = \bar{\gamma}_c$  the contact angle for the particles with a median diameter of  $86 \mu\text{m}$   $\theta$  is approx.  $59^\circ$ , while  $\theta \approx 21^\circ$  for particles with  $d_{50,3^*} = 256 \mu\text{m}$ .

The film flotation technique is found to be a very precise measurement technique if performed properly. The determined recoveries  $R$  using Eq. (5-3) are found to be above 95 % in all experiments. Repetitive measurements at a constant surface tension also show only very small standard deviations of less than 5 %. The obtained results are therefore reliable.

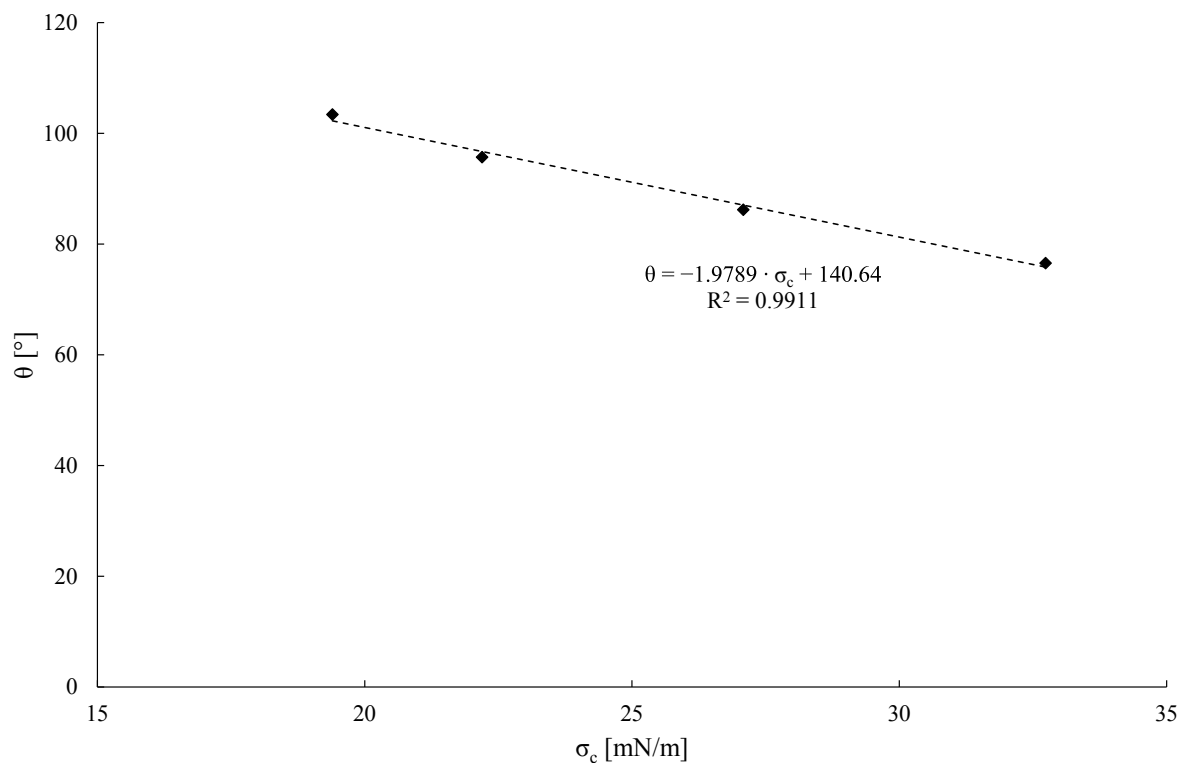


**Fig. 5-5.** Calibration curve for the relation between the contact angle  $\theta$  measured with deionized water as testing liquid on glass slides modified with n-octyltriethoxysilane (OS) and the critical surface tension of wettability  $\sigma_c$  obtained from the Zisman plot.

## 5.2 Establishment of a collector-frother system

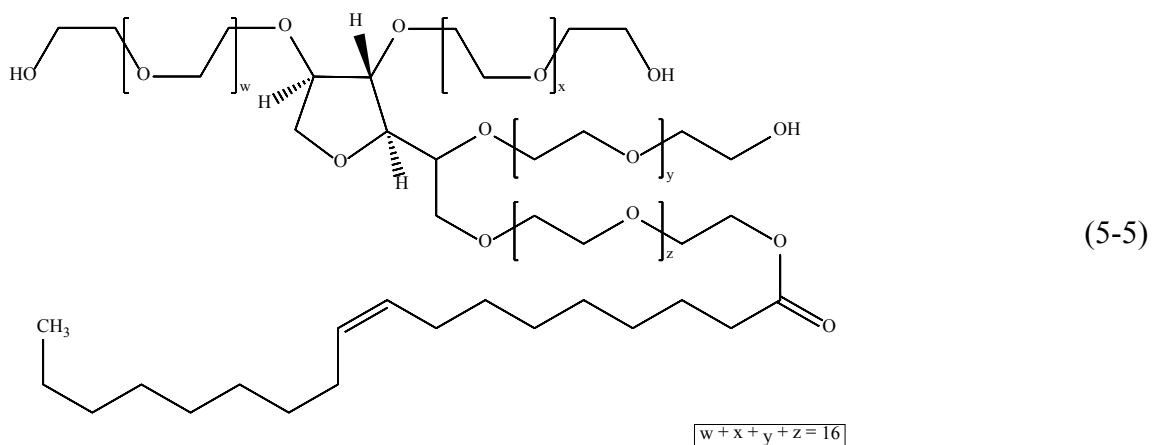
To investigate the flotation process of glass particles, a suitable collector-frother system has to be established. As stated in chapter 2.1.2.2, a collector will always exhibit frothing properties to a certain extent and vice versa frothers will exhibit collecting properties. The intention of the experiments with glass particles is to investigate the influence of collectors and frothers independently. Thus, a collector-frother system has to be found, where a good differentiation between the different flotation agents is feasible.

### 5.2.1 Preliminary tests

To find a suitable frother-collector system with the defined properties, different compounds are tested in the froth flotation cell presented in chapter 3.1.2. The experiments are evaluated with respect to the maximum recovery  $R_{\max}$  of unmodified glass particles with a median particle diameter  $d_{50,3^*}$  of 256  $\mu\text{m}$  at a solids concentration of 1 g/L. Amongst other compounds tested, which showed only negligible recoveries, oleic acid (OA), Tween<sup>®</sup> 80, hexadecylamine (HDA), and methyl isobutyl carbinol (MIBC) are tested in three different combinations:

1. OA as collector and frother (as used in the flotation process of fluorite, cf. chapter 2.1.4.2) at a concentration of  $c=0.047$  mmol/L at pH=8,
2. HDA ( $c=0.012$  mmol/L) as collector and MIBC ( $c=0.80$  mmol/L) as frother,
3. and HDA ( $c=0.012$  mmol/L) as collector and Tween<sup>®</sup> 80 ( $c=0.021$  mmol/L) as frother.

The resulting maximum recoveries  $R_{\max}$  of these three combinations are presented in Fig. 5-6. OA shows the lowest recovery with only 7 %, the combination of HDA and MIBC shows a maximum recovery of 21 %, while the highest recovery of 90 % is observed for the combination of HDA and Tween<sup>®</sup> 80. Thus, the combination of HDA and Tween<sup>®</sup> 80 seems most promising for flotation experiments with glass particles. However, the function of Tween<sup>®</sup> 80 in meanings of a flotation agent is not completely clear. The molecular structure of Tween<sup>®</sup> 80 is presented in Eq. (5-5):



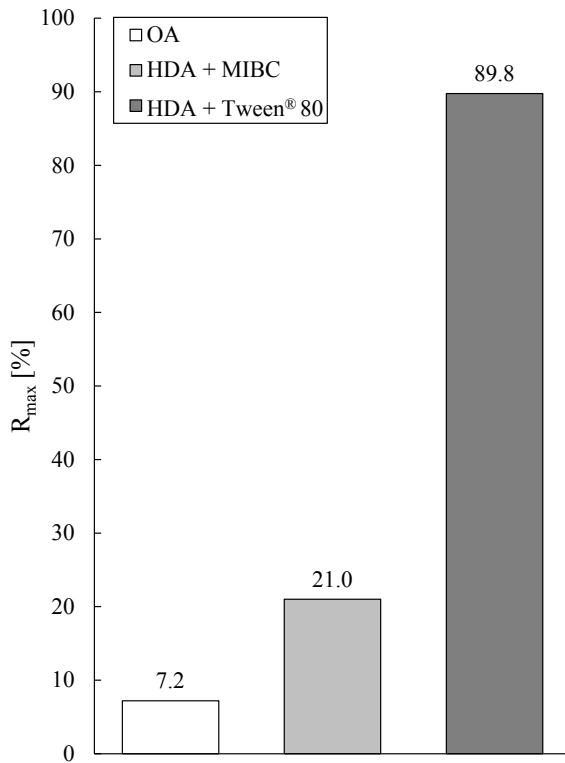


**Fig. 5-6.** Measured maximum recoveries  $R_{\max}$  of glass particles using different flotation chemicals: oleic acid (OA) as collector and frother (white bar), a mixture of hexadecylamine (HDA) used as collector and methyl isobutyl carbinol (MIBC) used as frother (light-grey bar), and a combination of HDA used as collector and Tween<sup>®</sup> 80 used as frother (dark-grey bar).

Tween<sup>®</sup> 80 is a polyoxethylated compound based on sorbitol and oleic acid. It is a non-ionic surfactant with polyethers as hydrophilic groups. Due to its large molecular size, collecting properties are assumed besides frothing properties. In fact, an experiment using only Tween<sup>®</sup> 80 as flotation agent showed already a recovery of approx. 53 % (see Appendix). Thus, the mixture of HDA and Tween<sup>®</sup> 80 cannot be used for flotation experiments and is therefore, rejected.

The low recovery of the glass particles using OA is related to electrostatic repulsion due to the negative charge of both the oleate molecule and the glass surface [261].

Comparison with literature shows that primary amines are commonly used as collector in the flotation process of quartz ([17], p. 271; [262], p. 24; [263–267]). Burdukova and Laskowski [268] as well as Laskowski [269] reported an enhanced adsorption of primary amines on quartz particles in the presence of bubbles. The bubbles act as collector transfer agent by transferring adsorbed primary amines from the bubble surface to solid particles when colliding [111]. When co-surfactants, i.e. frothers, are present, the amine will spread into a molecular film at the liquid-air interface. This activates the bubbles, which will enhance the formation of heterocoagulates [269]. Thus, the collector-frother system consisting of HDA and MIBC is chosen for further investigations.

### 5.2.2 Optimisation of the collector-frother system

Parts of this chapter have been published in [270]. To find the optimum parameters for the concentrations of the collector hexadecylamine (HDA) and the frother methyl isobutyl carbinol (MIBC), a design of experiment (DoE) is performed. For this purpose, the maximum recovery  $R_{\max}$  in the flotation process of unmodified glass particles with  $d_{50,3^*}=256 \mu\text{m}$  at a particle concentration of 1 g/L is analysed. As variable parameters, the collector concentration  $c(\text{HDA})$ , the frother concentration  $c(\text{MIBC})$ , and the volumetric gas flow rate  $\dot{V}_g$  are chosen. Thus, a  $3^k$  DoE as presented in Tab. 5-3 is generated. The centre point experiment ( $N=9$ ) is repeated nine times and each other experimental point is repeated three times, yielding a total number of 33 experiments.

The experiments are conducted in a 2 L laboratory scale flotation apparatus (see chapter 3.1.2) at a room temperature of  $22 \text{ }^\circ\text{C} \pm 2 \text{ }^\circ\text{C}$ . Deionized water is filled into the apparatus to a liquid level of about 180 mm. Separate aqueous stock solutions of HDA and MIBC are produced in volumetric flasks. Hexadecylamine is a crystalline solid, which is insoluble in water ([271], p. 3-304). By addition of hydrochloric acid, the amine group is protonated and hexadecylammonium chloride is formed. To solve HDA in deionized water via formation of hexadecylammonium chloride, 80 mL deionized water are heated while stirring to approx. 50-60  $^\circ\text{C}$ . Afterwards, 0.1 g HDA (92 %) and 0.7 mL concentrated hydrochloric acid (25 %) are added. After all HDA is solved the solution is cooled down to room temperature.

**Tab. 5-3.** Design of experiment (DoE) for optimisation of the collector-frother system of hexadecylamine (HDA) and methyl isobutyl carbinol (MIBC) with volumetric gas flow rate  $\dot{V}_g$  and the concentrations of the collector  $c(\text{HDA})$  and the frother  $c(\text{MIBC})$  as variable parameters.

N	$\dot{V}_g$ [-]	$c(\text{HDA})$ [-]	$c(\text{MIBC})$ [-]	$\dot{V}_g$ [L/min]	$c(\text{HDA})$ [ $\mu\text{mol/L}$ ]	$c(\text{MIBC})$ [ $\mu\text{mol/L}$ ]
1	-1	-1	-1	2.0	5.0	191
2	-1	-1	1	2.0	5.0	765
3	-1	1	-1	2.0	20.0	191
4	-1	1	1	2.0	20.0	765
5	1	-1	-1	5.0	5.0	191
6	1	-1	1	5.0	5.0	765
7	1	1	-1	5.0	20.0	191
8	1	1	1	5.0	20.0	765
9	0	0	0	3.5	12.5	478

The solution is then diluted in a 100 mL volumetric flask. For preparation of the frother stock solution, 5 mL MIBC (99 %) are diluted with deionized water in a 1 L volumetric flask. The gas flow rate is varied between 2 L/min and 5 L/min, the concentration of the collector HDA is varied between 5  $\mu\text{mol/L}$  and 20  $\mu\text{mol/L}$ , and the frother concentration  $c(\text{MIBC})$  is varied between 191  $\mu\text{mol/L}$  and 478  $\mu\text{mol/L}$ . Jameson and Ata investigated the formation of bubble-particle clusters in flotation experiments with silica particles at dodecylamine concentrations between 0 and 750 g/t silica and a constant frother concentration of 25 ppmv. The experiments were conducted in a 12 L mechanically agitated flotation cell at a solids concentration of 10 wt% [272]. The concentrations stated in their work are used as a starting point for the present experiments. In terms of Ata and Jameson, the collector concentration in this study is varied from 1 mg/g  $\text{SiO}_2$  to 4 mg/g  $\text{SiO}_2$ , while the frother concentration is varied from 25 ppmv to 100 ppmv. The chosen minimum collector concentration of 1 mg/g  $\text{SiO}_2$  is equal to the maximum collector concentration used in the study by Ata and Jameson, as HDA has a higher molar mass than dodecylamine. Tests with lower collector and frother concentrations showed very low recoveries, which may be a result of the low solids concentration of 0.1 wt%.

The resulting mean maximum recoveries  $R_{\text{max}}$  of the experiments are shown in Fig. 5-7. All experimental results can be found in the Appendix. A maximum recovery of approx. 21 % is achieved at a gas flow rate of 2 L/min, a collector concentration of 20  $\mu\text{mol/L}$  and a frother concentration of 765  $\mu\text{mol/L}$ . The trend of  $R_{\text{max}}$  inside the design space leads, however, to the assumption of a local maximum being present on one of the four vertical cube edges 1-5, 2-6, 3-7, or 4-8. Thus, additional experiments are performed with three repetitive measurements for each of the four cube edges.

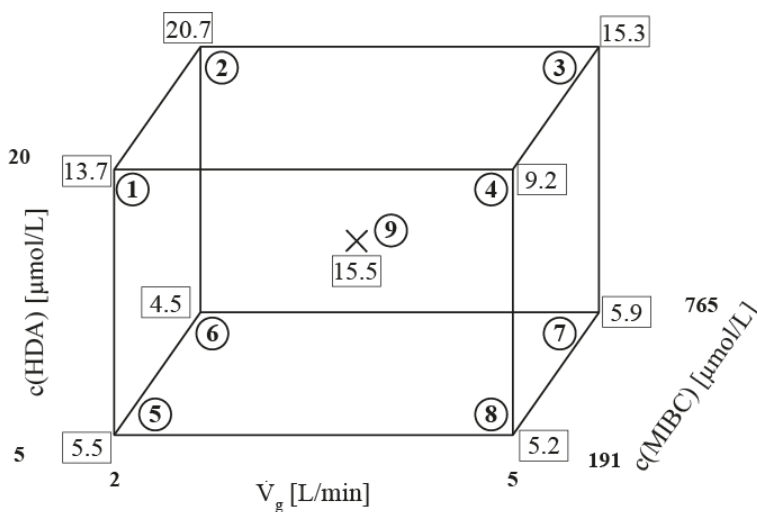


**Fig. 5-7.** Maximum recoveries  $R_{\text{max}}$  of the  $3^k$  design of experiment (rectangles) with centre set point marked with an "X". The measurement points of the design space are numbered from 1 to 9 (circles) according to Tab. 5-3.

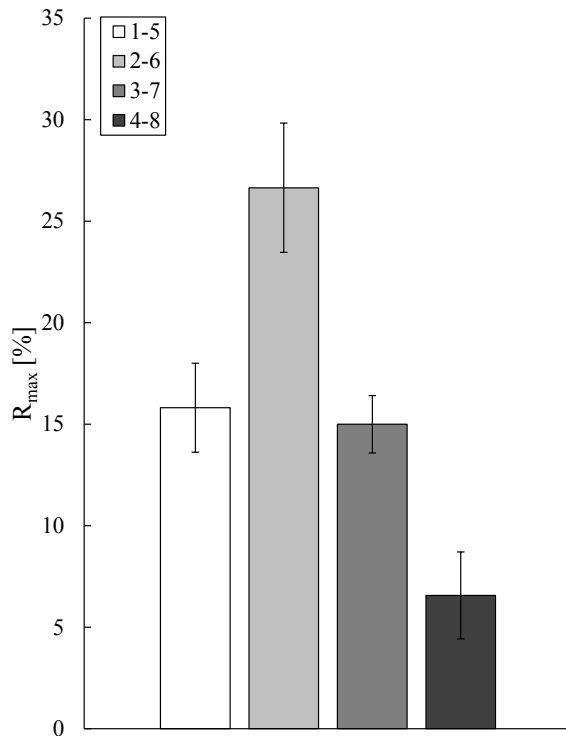


**Fig. 5-8.** Maximum recoveries of the additional experiments for the cube edges 1-5, 2-6, 3-7, and 4-8 as denominated in Fig. 5-7.

The results of these additional measurements are presented in Fig. 5-8. The cube edge 2-6 shows the highest recovery with an  $R_{\max}$  of about 27 %  $\pm$  3 %. This recovery is higher than the previously found  $R_{\max}$  of about 21 % at  $N=2$  (cf. Fig. 5-7). Thus, the assumption of a local maximum being present could successfully be proven. As the recovery is maximised at the cube edge 2-6 the determined concentrations of this experimental set point are said to be optimal. The concentrations of HDA and MIBC at this set point are 12.5  $\mu\text{mol/L}$  and 765  $\mu\text{mol/L}$ , respectively, corresponding to a collector concentration of approx. 2.5 mg HDA per gram glass particles and a frother concentration of about 100 ppmv. As Jameson and Ata did not investigate the recovery in their experiments, the obtained optimal collector and frother concentrations cannot be compared. The determined optimum concentrations will be used in the single bubble flotation experiments presented in chapter 5.3.

### 5.3 Single bubble flotation experiments

In the following chapter, all experiments regarding the model flotation system consisting of glass particles are presented. Various influence parameters on the flotation process are rigorously investigated, analysed and supported via Shadowgraphy measurements.

#### 5.3.1 Determination of flotation kinetics and maximum recovery

In a first step the flotation kinetics of glass particles are determined and the influence of four different operational parameters on the process is analysed. The variable parameters are:

1. median particle diameter  $d_{50,3^*}$ ,
2. volumetric gas flow rate  $\dot{V}_g$ ,
3. wettability of particles,
4. and flotation medium.

Glass particles with two different  $d_{50,3^*}$  of 86  $\mu\text{m}$  and 256  $\mu\text{m}$  (see chapter 5.1.2) and two different  $\dot{V}_g$  of 0.1 mL/min and 2 mL/min are used. The influence of the wettability is investigated using three different particle groups: hydrophilic particles (glass particles treated with Caro's acid, see chapter 5.1.2), unmodified particles, and silanised particles (see chapter 5.1.2). Furthermore, the flotation experiments are conducted in three different media. Experiments are carried out in deionized water to analyse the kinetics as well as to determine the degree of entrainment. The degree of entrainment gives an information on the amount of particles, which is floated naturally without the influence of a collector. The hydrophilic and unmodified particles are both floated in an aqueous flotation solution containing the optimum concentrations of hexadecylamine (HDA) as collector and methyl isobutyl carbinol (MIBC) as frother (cf. chapter 5.2). To analyse the effect of the hydrophobic surfaces of the silanised particles, these particles are floated without the addition of HDA but in presence of MIBC.

##### 5.3.1.1 Experimental procedure

###### 5.3.1.1.1 Preparation of the apparatus

Single bubble flotation experiments are conducted in the flotation column presented in chapter 3.1.1.1. The piping and instrumentation diagram (P&ID) of the experimental setup is given in Fig. 5-9. The complete piping system of the apparatus is made from flexible hoses. To simplify the flow sheet, the hoses are depicted as pipes. In the first step, a capillary for aeration is introduced into the apparatus in the dispersion cell via plug valve HK2.

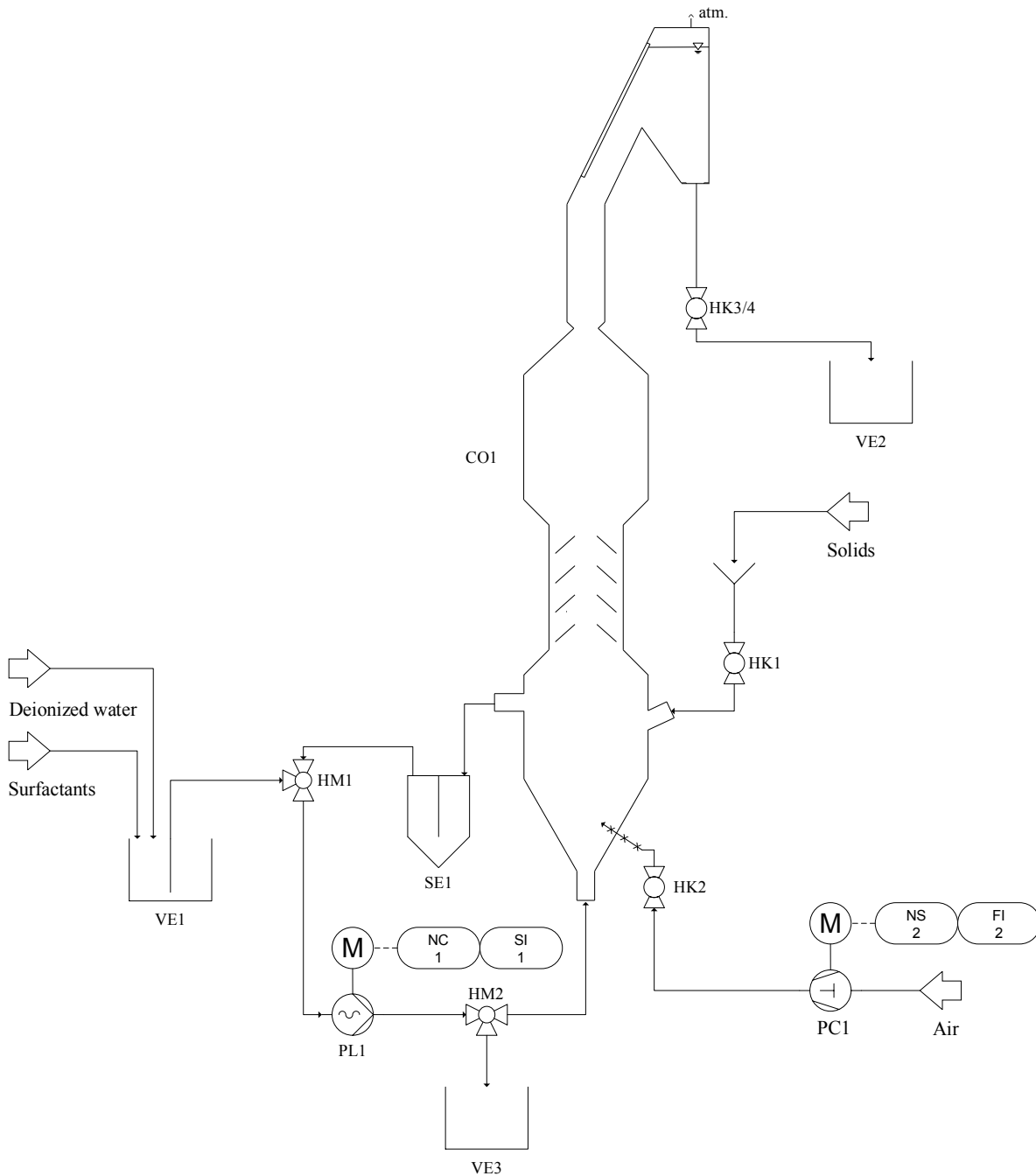


**Fig. 5-9.** P&ID of the single bubble flotation column. All pipes shown in the flow sheet are flexible hoses. Flotation column shown is a simplified model for representation purposes.

The capillary is connected to a gastight syringe, which is filled with ambient air, and a precision syringe pump PC1. Before starting the experiments, the flotation column CO1 is filled with the desired flotation medium. Therefore, the three-way plug valve HM1 is turned 90° so that the flow direction is open from vessel VE1 to the progression cavity pump PL1. The hose system is then filled with the desired medium, up to the suction side of the pump. The suction side hose is afterwards placed into the liquid-filled vessel VE1. The separator SE1, which is used to prevent solids from entering the pump PL1, is manually filled with the flotation medium by removing its lid. Afterwards, HM2 is turned so that the fluid flow is open from the pressure

side of PL1 to the dispersion cell of the flotation column. Furthermore, the plug valves HK1, HK3, and HK4 are closed. In the next step, the pump PL1 is switched on. The apparatus is now filled completely with liquid. Afterwards, the pump PL1 is switched off. Then, HM1 and HM2 are turned 90° so that the flow direction is open from the separator SE1 to vessel VE1 and from the dispersion cell of the flotation column to vessel VE3. This removes the air from the separator as well as from the pressure side of the pump. After the air is completely removed, HM1 and HM2 are turned back so that the flow direction from VE1 to PL1 and from PL1 to the dispersion cell of the flotation column is open again. The pump PL1 is switched on and the apparatus is refilled with liquid. Finally, HM1 is turned to the 180° position so that the fluid flow is open from SE1 to the suction side of PL1. In this configuration, the liquid flow in the dispersion cell is circulated, which is intended for dispersion of the solids in the pulp during the flotation experiments.

#### 5.3.1.1.2 Flotation experiments

The apparatus is first prepared as described in chapter 5.3.1.1.1 so that the liquid circulates inside the dispersion cell. The flotation experiments are conducted in three different types of liquids, namely deionized water (DW), an aqueous solution of hexadecylamine as collector and methyl isobutyl carbinol as frother (HDA-MIBC), and an aqueous solution of MIBC (see Tab. 5-4). The determined optimum concentrations of HDA and MIBC for the flotation of glass particles presented in chapter 5.2.2 are chosen for the present experiments in the single bubble flotation column. Thus, a concentration of 12.4  $\mu\text{mol/L}$  HDA and 765  $\mu\text{mol/L}$  MIBC is employed in 3 L DW in vessel VE1 (see Fig. 5-9). The particles for the experiments are weighed using a precision laboratory scale. The particle mass used for the experiments is always 4 g. The dispersion cell has a volume of 65 mL so that the mass concentration is approx. 62 g/L. Before the particles are added to the flotation column, the frequency of the circulating pump has to be adjusted with respect to the particle size. Information on the calculation of the pump frequency can be found in Appendix 9.1.3.2. Then, plug valve HK1 is opened and the liquid from the apparatus flows into the hose. Afterwards, HK1 is closed again and the weighed glass particles are added via a funnel. The particles are given time to settle to the closed plug valve HK1. Then, HK1 is opened and the particles can settle into the dispersion cell, where they will be dispersed due to the circulating stream of the progression cavity pump (see chapter 5.3.1.1). A gastight syringe with a volume of 50 mL is filled with ambient air. Aeration via the capillary is started by turning on the precision syringe pump at the desired volumetric gas flow rate. The measurement starts as soon as air bubbles start to ascend in the column. The flotation experiments are carried out until no more particles are floated or 30 minutes have elapsed. The

experimental time is chosen arbitrarily. As the flotation kinetics are to be investigated, samples of the flotation product have to be taken at defined times. This is done at least every five minutes. The syringe pump is stopped during the sampling so that no more bubbles are formed. Then, the plug valves HK3 and HK4 are opened and the liquid in the solids deposition cell is drained into vessel VE2 (see Fig. 5-9). The cell is afterwards rinsed several times with deionized water to ensure that all floated particles are removed from the cell. Next, HK3 and HK4 are closed again and HM1 is turned 90° so that the fluid flow is open from VE1 to the suction side of the pump PL1. The flotation column is now refilled to the desired liquid level.

**Tab. 5-4.** Experimental design for single bubble flotation experiments using glass particles with two different median particle diameters  $d_{50,3^*}$  treated with Caro's acid (hydrophilic), unmodified particles, and silanised particles (hydrophobic) in deionized water (DW), a flotation solution containing hexadecylamine (HDA) as collector and methyl isobutyl carbinol (MIBC) as frother or just MIBC at two different gas flow rates  $\dot{V}_g$ .

N	particle class	medium	$d_{50,3^*}$ [ $\mu\text{m}$ ]	$\dot{V}_g$ [mL/min]
1	hydrophilic	DW	86	0.1
2	hydrophilic	DW	86	2.0
3	hydrophilic	DW	256	0.1
4	hydrophilic	DW	256	2.0
5	hydrophilic	HDA-MIBC	86	0.1
6	hydrophilic	HDA-MIBC	86	2.0
7	hydrophilic	HDA-MIBC	256	0.1
8	hydrophilic	HDA-MIBC	256	2.0
9	unmodified	DW	86	0.1
10	unmodified	DW	86	2.0
11	unmodified	DW	256	0.1
12	unmodified	DW	256	2.0
13	unmodified	HDA-MIBC	86	0.1
14	unmodified	HDA-MIBC	86	2.0
15	unmodified	HDA-MIBC	256	0.1
16	unmodified	HDA-MIBC	256	2.0
17	hydrophobic	MIBC	86	0.1
18	hydrophobic	MIBC	86	2.0
19	hydrophobic	MIBC	256	0.1
20	hydrophobic	MIBC	256	2.0

Then, HM1 is turned back to the 180° position so that the liquid is circulated in the dispersion cell and the syringe pump is started again. After the experiment is finished, the collected concentrates are filtrated, washed several times with deionized water and finally dried to constant weight in an oven at 100 °C. The apparatus including all hoses is cleaned using deionized water. Tests showed that 3 L deionized water are sufficient for this purpose, because bubbles exhibited then the morphology and rising velocity of bubbles rising in pure deionized water.

The experimental design is given in Tab. 5-4. All experiments are repeated two times except for measurements in deionized water with hydrophilic particles, which are only conducted once. Thus, a total of 36 experiments are performed. The hydrophilic particles are as stated in chapter 5.1.2 treated with Caro's acid for at least 3 h. The particles are afterwards filtered, washed several times with deionized water and finally dried to constant weight at 100 °C. The flotation tests are performed immediately after the drying process to prevent a deactivation of the surface due to adsorption of hydrocarbons from the surrounding air at the particle surface (cf. chapter 2.5). For flotation experiments with unmodified particles, glass particles as present are taken from the storage containers without any surface treatment.

Hydrophobic particles are attained by silanisation reactions using n-octyltriethoxysilane (OS) as stated in chapter 5.1.2. The reaction time of particles with a median particle diameter  $d_{50,3^*}$  of 256  $\mu\text{m}$  is 5 h, while  $t_R=10$  min for particles with  $d_{50,3^*}=86$   $\mu\text{m}$ . As presented in chapter 5.1.2, film flotation experiments are carried out to determine the critical surface tension of wettability  $\bar{\gamma}_c$ . It has been found that  $\bar{\gamma}_c$  is about 60.4 mN/m for  $d_{50,3^*}=256$   $\mu\text{m}$ , while  $\bar{\gamma}_c \approx 41.1$  mN/m for  $d_{50,3^*}=86$   $\mu\text{m}$ . According to the established calibration curve (cf. Fig. 5-5) this corresponds to contact angles of about 21° and 59° for  $d_{50,3^*}=256$   $\mu\text{m}$  and  $d_{50,3^*}=86$   $\mu\text{m}$ , respectively. Corresponding to the classification by Drelich and Marmur [92], the particles with the median particle diameter of 256  $\mu\text{m}$  are poorly floatable, while the particles with  $d_{50,3^*}$  of 86  $\mu\text{m}$  are high-rate floatable (cf. chapter 2.2.1).

### 5.3.1.2 Flotation results

The experimental data is analysed using chemical analogous kinetic models of type 0<sup>th</sup> order, 1<sup>st</sup> order, and 2<sup>nd</sup> order, as well as empirical models, e.g. the classical model (cf. Tab. 2-3). The flotation rate constant  $k$  in the chemical analogous models is determined via linearisation in Microsoft Excel using the determined experimental recovery  $R_{\max}$  (see chapter 2.1.3.1) after 30 min. For the empirical models  $k$ , the ultimate recovery after infinite flotation time  $R_{\infty}$ , and other model parameters are determined using a MATLAB tool [273]. The empirical model fits are carried out with the restriction  $R_{\infty} \leq 100\%$ .

An overview of the tested kinetic models and the corresponding mean regression coefficients  $\overline{R^2}$  averaged over all 36 experiments is presented in Tab. 5-5. The 0<sup>th</sup> order model gives the best mean regression coefficient for the chemical analogous models with a value of 0.9822. The empirical models show similar mean regression coefficients ( $\overline{R^2} \geq 0.9835$ ), except for the fully mixed model ( $\overline{R^2} = 0.5752$ ). Exemplary fits of the kinetic models to an experimental data set are given in Fig. 5-10, where the graphs are shown for unmodified glass particles with  $d_{50,3^*} = 86 \mu\text{m}$  at  $\dot{V}_g = 0.1 \text{ mL/min}$  in deionized water. The chemical analogous model of 0<sup>th</sup> type gives the best fit. The 1<sup>st</sup> order fit overestimates the recovery in the beginning and underestimates it towards the end. The trend of the 2<sup>nd</sup> order fit is similar to the 1<sup>st</sup> order fit with a faster convergence towards a maximum recovery with a relative deviation of -21 % compared to the experimental data. The classical model, which is shown as an example of the analysed empirical models, shows a fit similarly as good as the 0<sup>th</sup> order model.

**Tab. 5-5.** Mean regression coefficients  $\overline{R^2}$  and minimum and maximum determined regression coefficients  $\min(R^2)$  and  $\max(R^2)$ , respectively, for single bubble flotation experiments.

Kinetic model	$\overline{R^2}$	$\min(R^2)$	$\max(R^2)$
0 <sup>th</sup> order	$0.9822 \pm 0.0191$	0.9169	0.9995
1 <sup>st</sup> order	$0.9545 \pm 0.0390$	0.8653	0.9960
2 <sup>nd</sup> order	$0.8031 \pm 0.0749$	0.6069	0.9191
Classical model	$0.9877 \pm 0.0190$	0.9262	0.9997
Klimpel model	$0.9849 \pm 0.0199$	0.9240	0.9995
Kelsall model	$0.9835 \pm 0.0182$	0.9262	0.9999
Modified Kelsall model	$0.9884 \pm 0.0192$	0.9262	0.9999
Gamma model	$0.9880 \pm 0.0191$	0.9262	0.9997
Fully mixed model	$0.5752 \pm 0.1471$	0.3006	0.9032

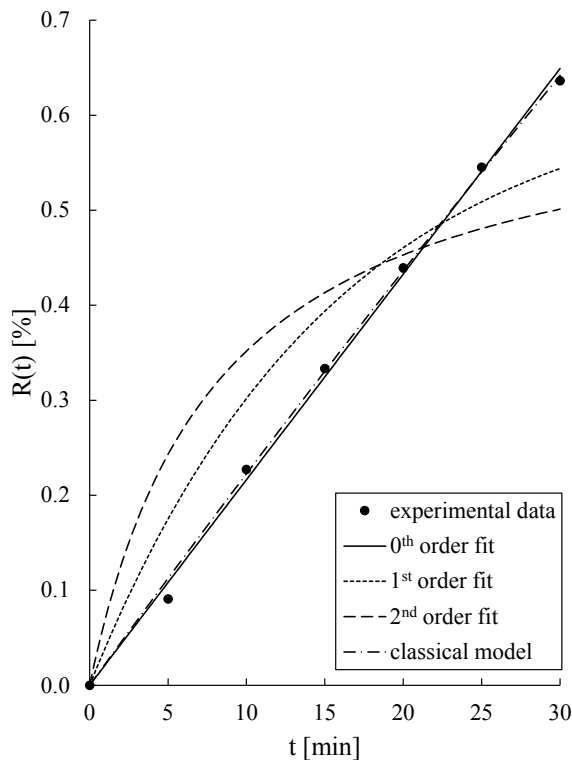


**Fig. 5-10.** Exemplary kinetic fit for unmodified glass particles with a median diameter  $d_{50,3^*}=86 \mu\text{m}$  at a gas flow rate of 0.1 mL/min in deionized water using chemical analogous models of type 0<sup>th</sup> order, 1<sup>st</sup> order, and 2<sup>nd</sup> order, as well as the classical type model as an example for the evaluated empirical models.

Compared to the 0<sup>th</sup> order model the classical model predicts slightly higher recoveries in the beginning and lower recoveries towards the end. The maximum experimental recoveries  $R_{\text{max}}$  for the different experimental conditions are shown in Fig. 5-11.  $R_{\text{max}}$  is in water much lower than in the flotation solutions, regardless of particle diameter, particle class, or volumetric gas flow rate. Furthermore,  $R_{\text{max}}$  increases for all experimental conditions with increasing gas flow rate  $\dot{V}_g$ . This seems plausible, because more bubbles per time interval are present at 2 mL/min than at 0.1 mL/min leading to an increased collision frequency of bubbles with particles. The ultimate recoveries  $R_{\infty}$  show no clear trend and predict oftentimes values of  $R_{\infty}=100 \%$ , e.g. for hydrophilic particles in water. Thus, a discussion of these values is omitted.

As the recovery in water as medium is greater than zero, particle entrainment has to be considered in the analysis of the experiments in the flotation solutions. The masses of floated particles in experiments in the flotation solutions are therefore corrected by the determined entrainment. The results of the experiments in the flotation solutions show an increase of  $R_{\text{max}}$  with increasing  $d_{50,3^*}$  for hydrophilic and unmodified particles (cf. Fig. 5-11a&b). This is referred to an increase in the collision probability with increasing particle diameter (see chapter 2.1.3.2). Furthermore, the hydrophilic particles exhibit a lower  $R_{\text{max}}$  than the unmodified particles at a constant  $d_{50,3^*}$ .

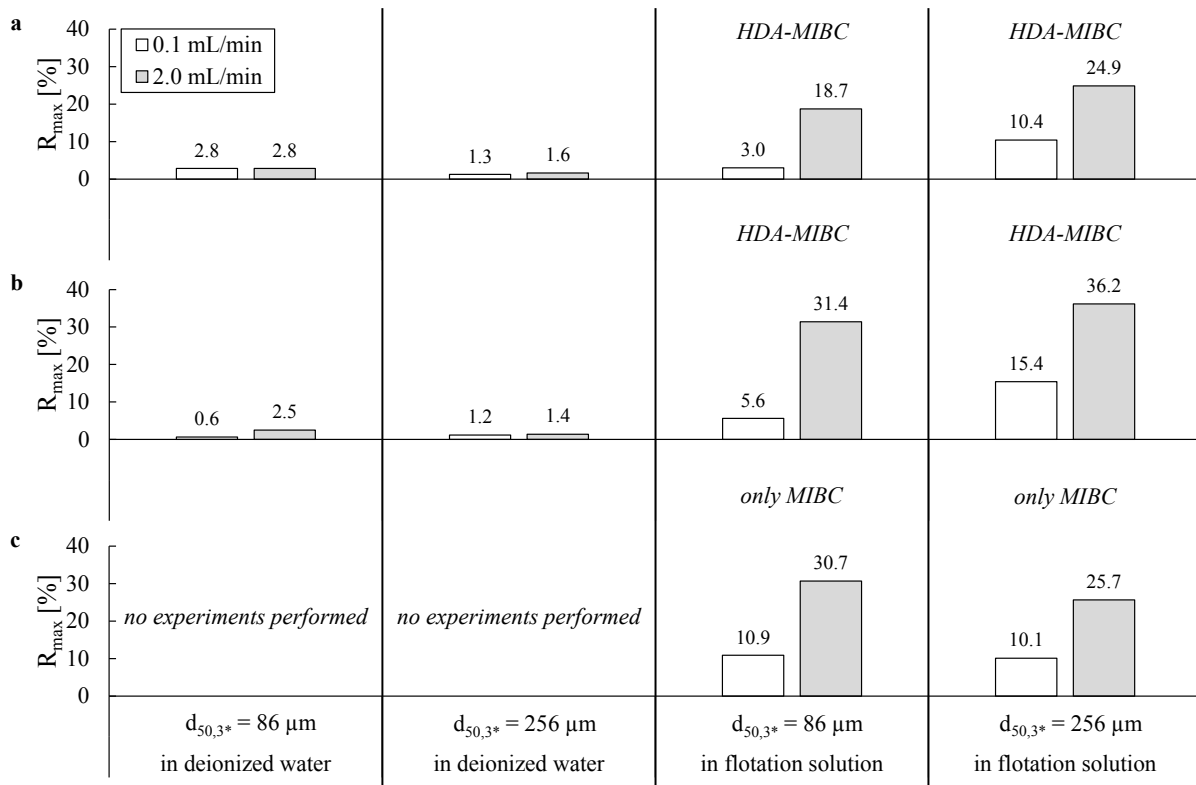


**Fig. 5-11.** Maximum experimental recoveries  $R_{\text{max}}$  for hydrophilic (a), unmodified (b), and hydrophobic (c) glass particles with median diameters  $d_{50,3^*}$  of 86  $\mu\text{m}$  and 256  $\mu\text{m}$  at gas flow rates of 0.1 mL/min (white bars) and 2 mL/min (light-grey bars) in deionized water and flotation solution.

The contact angle of hydrophilic particles is lower than that of unmodified particles, which is why attachment to bubbles and formation of stable bubble-particle heterocoagulates is less probable (see chapter 2.1.3.2).

The maximum recoveries for the hydrophobic particles are shown in Fig. 5-11c. As stated in chapter 5.3.1.1.2 the degree of hydrophobicity of the different particle sizes is unequal. The particles with a median diameter of  $d_{50,3^*}=86 \mu\text{m}$  are more hydrophobic than the particles with a  $d_{50,3^*}$  of 256  $\mu\text{m}$ , resulting in different contact angles of about  $59^\circ$  and about  $21^\circ$ , respectively. Due to the differences in hydrophobicity the recoveries of these two different particle sizes cannot be compared. A comparison of  $R_{\text{max}}$  of the different particle classes obtained at a constant  $d_{50,3^*}$  is, however, feasible.

For  $d_{50,3^*}=86 \mu\text{m}$ , the hydrophobic particles show the highest  $R_{\text{max}}$  at a low gas flow rate with approx. 11 % and at a higher gas flow rate a similar recovery as the unmodified particles with about 31 %. At a low gas flow rate, surface forces become more important, which is why hydrophobic particles will attach easier to bubbles than hydrophilic particles. Additionally, some particle-particle aggregates have been observed during experiments with these particles. This effect has not been observed for hydrophilic and unmodified particles. A collision with a bubble and the successful formation of a heterocoagulate leads in this case also to an increase

in  $R_{\max}$ . At a higher gas flow rate, the effect of surface forces decreases as turbulence increases. Therefore, the collision probability will be more dominant than the attachment probability. As the particle diameter is the same for unmodified and silanised particles,  $R_{\max}$  will be similar. The particles treated with Caro's acid exhibit a much smaller  $R_{\max}$  with 3 % at  $\dot{V}_g=0.1$  mL/min and  $R_{\max}=19$  % at 2 mL/min due to their strong hydrophilic nature.

Hydrophobic particles with a median diameter  $d_{50,3^*}$  of 256  $\mu\text{m}$  show a maximum recovery, which is comparable to the  $R_{\max}$  of the hydrophilic particles for both gas flow rates (approx. 10 % and 26 %, respectively). The unmodified particles yield at this  $d_{50,3^*}$  the highest recoveries with  $R_{\max}=36$  %. As described in chapter 5.3.1.1.2, the hydrophobic particles are floated in the absence of a collector. The hydrophilic particles have a contact angle close to zero, as the treatment with Caro's acid creates a completely fresh glass surface free of any adsorbed hydrocarbons, which would increase the contact angle (cf. chapters 5.1.1 and 5.1.2). Adsorption of the collector on the particle surface increases the contact angle and, thus attachment to bubbles is improved. As  $R_{\max}$  of the hydrophilic particles is similar to that of the silanised particles, it may be assumed that the contact angles are similar. This would mean an increase of  $\theta$  by about  $20^\circ$  due to the adsorption of HDA on the particle surface.

As described in chapter 2.1.3.1, both  $R_{\max}$  and  $k$  are influenced by a change in the experimental conditions. Therefore, the product  $k \cdot R_{\max}$  is commonly used as a parameter to analyse the influence of the experimental conditions on the flotation process ([3], p. 749; [49]). To compare the obtained results for the flotation constant  $k$  and the maximum  $R_{\max}$  the so-called limits kinetic curve is used (cf. Fig. 2-5). The present experiments show an excellent agreement with the 0<sup>th</sup> order chemical analogous kinetic equation (see Tab. 5-5), which is why only the values of  $k$  for the 0<sup>th</sup> order are considered.

The limits kinetic curve for all experimental data assuming 0<sup>th</sup> order kinetics is presented in Fig. 5-12. Using this graph, four regions of flotation can be arbitrarily identified according to [50]: slow-powerless, slow-powerful, fast-powerful, and fast-powerless. The present experiments are all located either in the slow-powerless or fast-powerful regime. Furthermore, it is found that the experimental data forms clusters with respect to the process parameters volumetric gas flow rate and flotation solution. Flotation in deionized water at a low gas flow rate shows the lowest flotation rate constants and the lowest recoveries. With increasing  $\dot{V}_g$  both  $k$  and  $R_{\max}$  increase. As expected, the flotation performance improves significantly, when the medium changes from deionized water to the flotation solutions containing the frother-collector mixture or just the frother (see chapter 5.3.1.1.2). In the flotation solutions, both  $k$  and  $R_{\max}$  are again higher for the higher investigated volumetric gas flow rate.

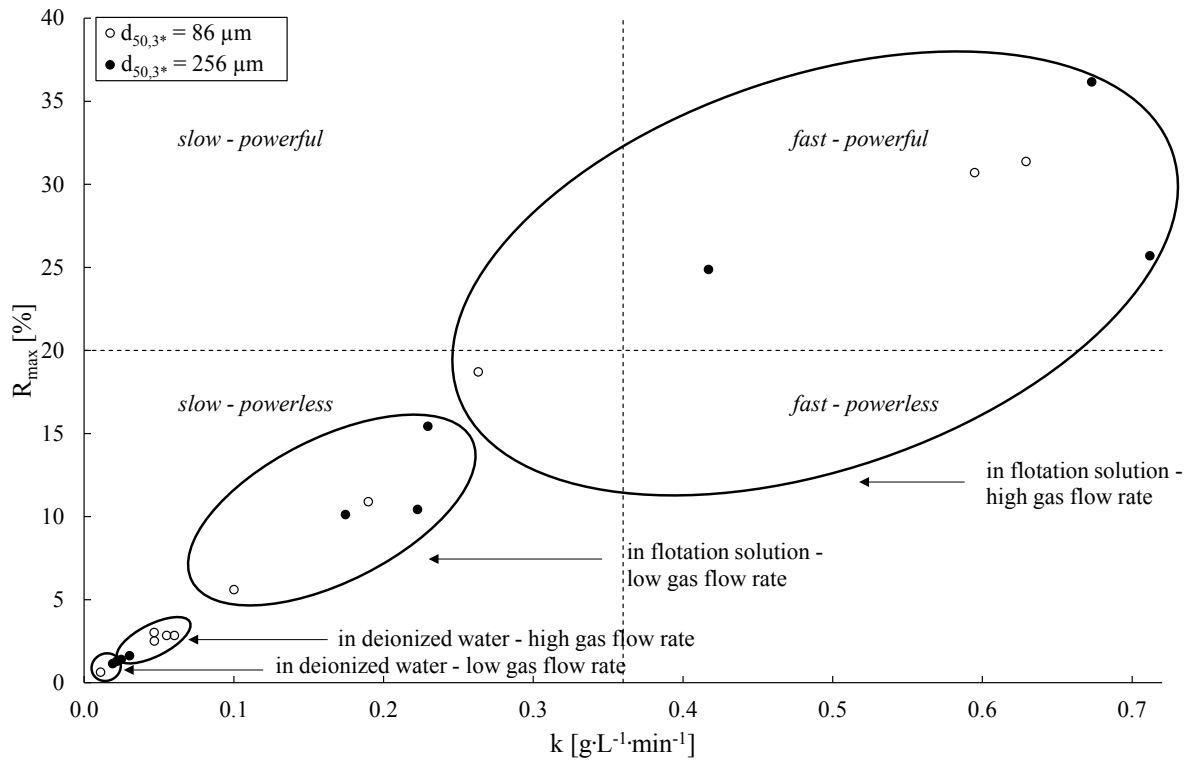


**Fig. 5-12.** Limits kinetic curve for flotation of glass particles with a median diameter  $d_{50,3^*}$  of 86  $\mu\text{m}$  (blank dots) and 256  $\mu\text{m}$  (black dots) for 0<sup>th</sup> order kinetic rate constants  $k$  and maximum experimental recoveries  $R_{\text{max}}$ .

The flotation process can be described as the product of probabilities of the three micro processes collision, attachment, and stabilisation (cf. chapter 2.1.3.2). The observed bubble size during the experiments is approx. 2 mm and the rising velocity is about 0.18 m/s. The collision probability  $P_c$  is calculated using Gaudin's model, Sutherland's model as well as the model for the intermediate range (cf. Tab. 2-4) for various particle diameters  $d_p$  in a range of 50 to 300  $\mu\text{m}$  (cf. Fig. 5-13a). For the particles used in the present experiments,  $P_c$  ranges between 0.1 % and 13 % for  $d_{50,3^*}=86 \mu\text{m}$ , while  $P_c=1-38 \%$  for  $d_{50,3^*}=256 \mu\text{m}$ . The particles with a larger diameter have therefore the higher collision probability at a constant bubble diameter. The actual value of  $P_c$  is, however, unknown, because the actual flow conditions are unknown. As stated in chapter 2.1.3.2.1, Gaudin's equation generally underestimates  $P_c$ , while Sutherland's model overestimates  $P_c$ . The actual value of  $P_c$  is therefore expected in the range described by these two models, which will be close to the intermediate model.

The attachment probability  $P_a$  is calculated with Equations (2-24) and (2-26), which have been presented in chapter 2.1.3.2.2, for the two used median particle diameters of 86 and 256  $\mu\text{m}$  for various contact angles  $\theta$  ranging from 0 to 180° (cf. Fig. 5-13b). The contact angles determined for the silanised particles are marked in the graph. For all  $\theta$ , particles with  $d_{50,3^*}=86 \mu\text{m}$  show a higher  $P_a$  than particles with  $d_{50,3^*}=256 \mu\text{m}$ . The calculated attachment probabilities of the hydrophobised particles are about 92 % and 5 % for 86  $\mu\text{m}$  and 256  $\mu\text{m}$ , respectively.

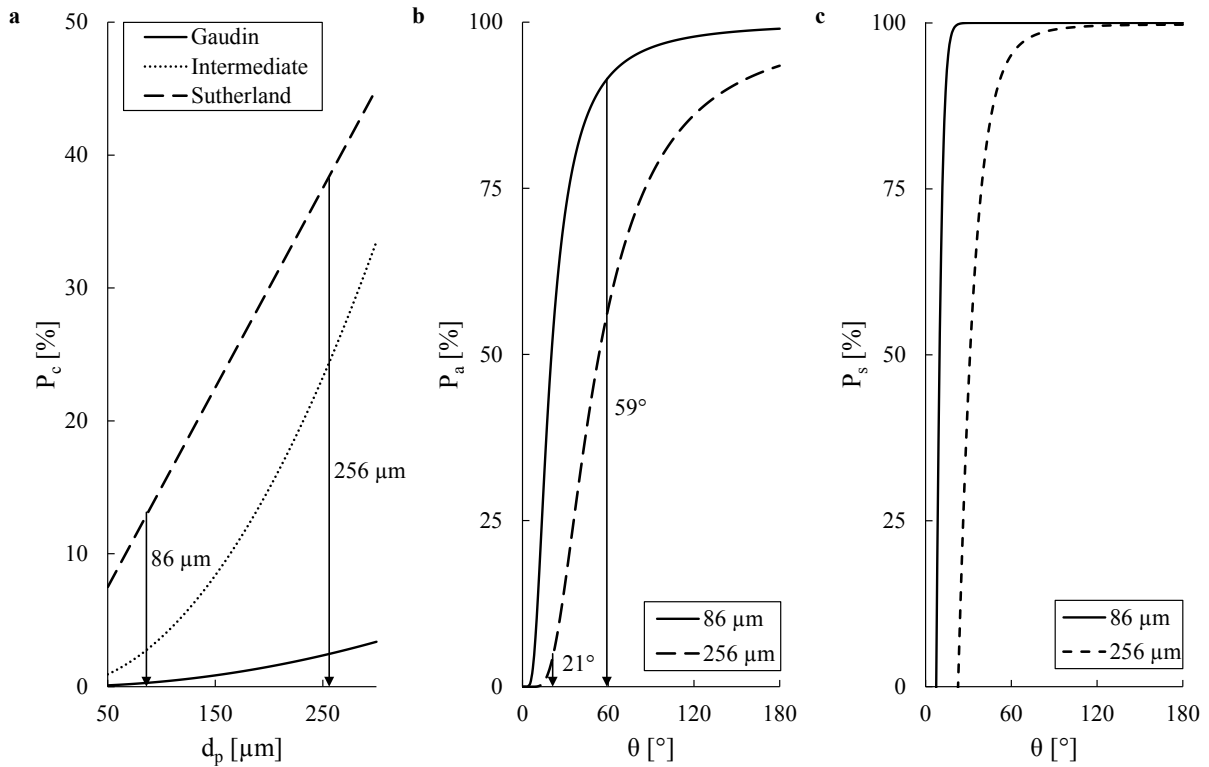


**Fig. 5-13.** Theoretically calculated collision probabilities  $P_c$  for varying particle diameters  $d_p$  (a), attachment probabilities  $P_a$  for particles with a median particle diameter  $d_{50,3^*}$  of 86 μm and 256 μm for varying contact angles  $\theta$  (b), and stability probabilities  $P_s$  for varying  $\theta$  with  $d_B=2$  mm,  $w_B=0.18$  m/s,  $\sigma=0.072$  mN/m, and  $\varepsilon=10$  m<sup>2</sup>/s<sup>2</sup> (c).

The information of the local energy dissipation  $\varepsilon$  is not accessible, which is why an accurate calculation of the stability probability  $P_s$  via Eqs. (2-27) and (2-28) is infeasible. A qualitative comparison of  $P_s$  of the two particle sizes with varying  $\theta$  is, however, possible. Fig. 5-13c shows that smaller particles will lead to formation of stable bubble-particle heterocoagulates even at lower contact angles, while higher  $\theta$  are necessary for larger particles to improve the stability. The presented results from Fig. 5-13 show that collision of small particles with bubbles is less probable than for large particles. The attachment probability will, however, be significantly higher. The experimental results for the maximum recovery  $R_{\max}$  presented in Fig. 5-11a&b have shown an approx. three times higher recovery for particles with  $d_{50,3^*}=256$  μm compared to 86 μm at a low gas flow rate. This difference is in good agreement with the calculated collision probabilities for both particle sizes using Sutherland's model, where a three times higher  $P_c$  has been calculated for the larger particles. The smaller deviations of  $R_{\max}$  at a higher gas flow rate may be attributed to the increased turbulence, which on the one hand will increase  $P_c$ , but will on the other hand also have a significant influence on the stability of the bubble-particle heterocoagulates. A complete theoretical calculation on the basis of flotation probabilities is infeasible, due to the lack of quantitative information on the present flow conditions inside the flotation cell.

### 5.3.1.3 Influence of initial solids concentration in the flotation pulp

To investigate the influence of the initial particle concentration  $c_{p,0}$  in the pulp on the flotation process, additional six experiments are carried out, where the solids concentration in the flotation pulp is halved from 62 g/L to 31 g/L. These experiments are experiments 7, 8, and 13-16 from Tab. 5-4. The determined maximum experimental recoveries  $R_{\max}$  for the two different initial solids concentrations are compared in Fig. 5-14. The influence of  $c_{p,0}$  on  $R_{\max}$  for hydrophilic particles is only investigated for particles with a  $d_{50,3^*}$  of 256  $\mu\text{m}$ . The results in Fig. 5-14a show that  $R_{\max}$  seems to be unaffected by  $c_{p,0}$ . For unmodified particles, however, an increase in  $R_{\max}$  is observed for both particle sizes with decreasing particle concentration in the pulp (Fig. 5-14b). The increase in  $R_{\max}$  is smaller for particles with a median diameter of 86  $\mu\text{m}$  than for particles with  $d_{50,3^*}=256 \mu\text{m}$ .

As explained in chapter 2.1.3.1,  $k$  and  $R_{\max}$  are affected simultaneously by a change in experimental conditions. Therefore, the flotation kinetics are analysed in accordance to the described procedure in chapter 5.3.1.2 with respect to the mean regression coefficient  $\overline{R^2}$ .

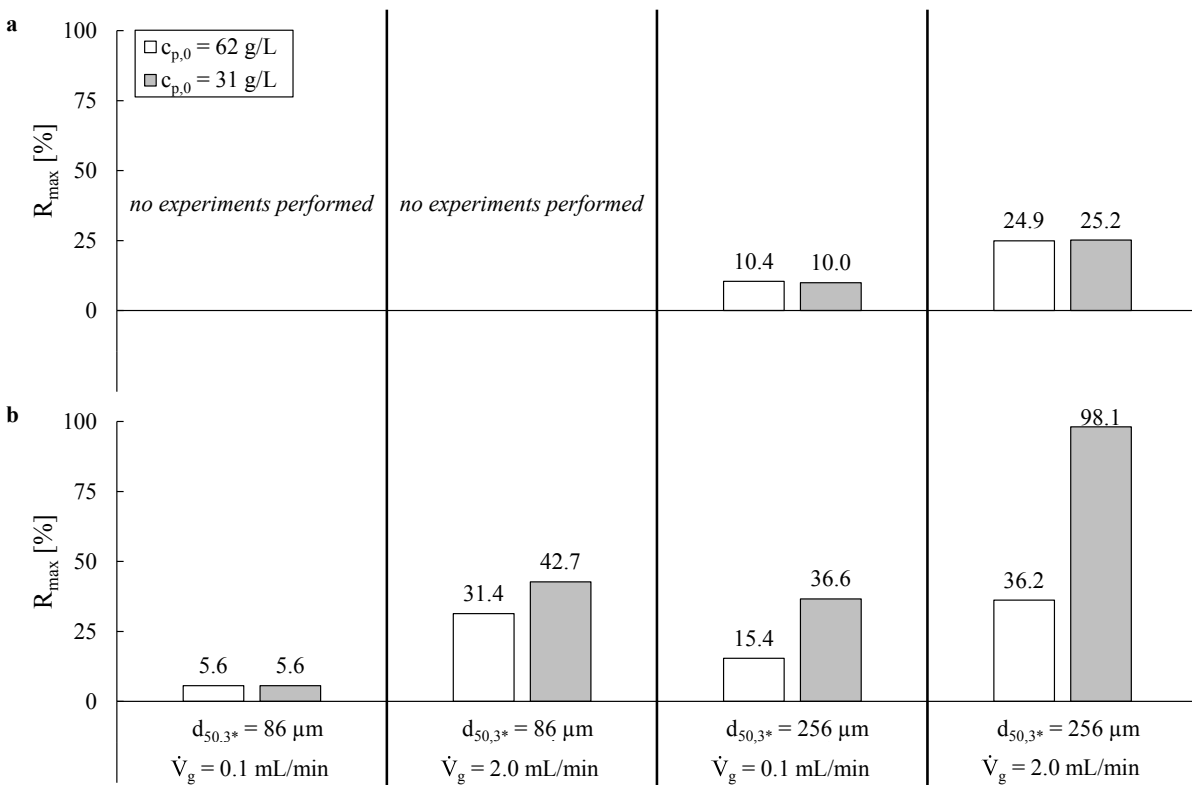


**Fig. 5-14.** Comparison of maximum experimental recovery  $R_{\max}$  for glass particles with median diameters  $d_{50,3^*}$  of 86  $\mu\text{m}$  and 256  $\mu\text{m}$  at gas flow rates of 0.1 mL/min and 2 mL/min with initial solids concentrations  $c_{p,0}$  of 62 g/L (white bars) and 31 g/L (grey bars) treated with Caro's acid (a) and unmodified particles (b) in a flotation solution containing hexadecylamine (HDA) as collector and methyl isobutyl carbinol (MIBC) as frother.

Sekhar and Shanker stated that a change of the experimental conditions may not only result in a change of the value of the flotation kinetic constant  $k$  but also in a shift of the flotation kinetics order  $n$  [40]. The obtained data is therefore additionally analysed with respect to  $n$ . A comparison to the obtained order of flotation kinetics at  $c_{p,0}=62$  g/L and at  $c_{p,0}=31$  g/L is presented in Tab. 5-6.

The order of flotation kinetics for the hydrophilic particles is unaffected by a change in  $c_{p,0}$ . For both initial solids concentrations the 0<sup>th</sup> order kinetic model gives the best fit. The value for the flotation rate constant  $k$  is for  $c_{p,0}=31$  g/L approx. half the value of  $k$  for  $c_{p,0}=62$  g/L, which is in consensus with the observed unchanged  $R_{\max}$  in Fig. 5-14a considering the kinetic equation for the 0<sup>th</sup> order model given in Eq. (2-9).

The unmodified particles with a median particle diameter of 86  $\mu\text{m}$  show a shift from 0<sup>th</sup> order to 1<sup>st</sup> order at a low gas flow rate of 0.1 mL/min. At a higher gas flow rate of 2 mL/min, the experimental data of both initial solids concentrations follows 1<sup>st</sup> order. The flotation process of particles with a  $d_{50,3^*}$  of 86  $\mu\text{m}$  is therefore strongly affected by  $c_{p,0}$ . The shift from 0<sup>th</sup> order to 1<sup>st</sup> order at the low gas flow rate of 0.1 mL/min shows in terms of Tomlinson and Fleming [25,28,40] that at a higher solids concentration the flotation process is predominantly inhibited, while free flotation is the main mechanism at a lower solids concentration.

In contrast to this, no change in the order of flotation kinetics is observed for particles with  $d_{50,3^*}=256$   $\mu\text{m}$  at a low gas flow rate of 0.1 mL/min. For both investigated initial solids concentrations the data is best described by the 0<sup>th</sup> order chemical kinetic analogous model. The value for the flotation rate constant  $k$  is similar for both initial solids concentrations. Thus,  $R_{\max}$  is approx. two times higher at  $c_{p,0}=31$  g/L compared to  $c_{p,0}=62$  g/L (cf. Fig. 5-14b).

**Tab. 5-6.** Comparison of order of flotation kinetics  $n$  for an initial solids concentration  $c_{p,0}$  of 62 g/L in the pulp as presented in chapter 5.3.1.2 and a reduced concentration of  $c_{p,0}=31$  g/L.

N	Particle class	$d_{50,3^*}$ [ $\mu\text{m}$ ]	$\dot{V}_g$ [mL/min]	n for	
				$c_{p,0}=62$ g/L	$c_{p,0}=31$ g/L
7	hydrophilic	256	0.1	0	0
8	hydrophilic	256	2.0	0	0
13	unmodified	86	0.1	0	1
14	unmodified	86	2.0	1	1
15	unmodified	256	0.1	0	0
16	unmodified	256	2.0	0.5	0.7

At a higher gas flow rate, the regression coefficients for  $c_{p,0}=62$  g/L are similar for the 0<sup>th</sup> order model ( $R^2=0.9801$ ) and the 1<sup>st</sup> order model ( $R^2=0.9890$ ). At  $c_{p,0}=31$  g/L a larger difference between these two models is found with  $R^2=0.9562$  and  $R^2=0.9800$  for 0<sup>th</sup> order and 1<sup>st</sup> order model, respectively. However, the regression coefficient for the 1<sup>st</sup> order model shows that the fit of the experimental data is not completely accurate. Therefore, both investigated initial solids concentrations of experiment N=16 are analysed using the fractional order kinetic model, which is given in Eq. (2-12). As a result, the order of flotation kinetics at  $c_{p,0}=62$  g/L is found to be 0.5 ( $R^2=0.9907$ ), while the order changes to 0.7 for  $c_{p,0}=31$  g/L ( $R^2=0.9914$ ). Thus, a change in the order of flotation kinetics is present at a higher gas flow rate of 2 mL/min. However, this change seems to be minor compared to the change from 0<sup>th</sup> order to 1<sup>st</sup> order – or rather from inhibited flotation to free flotation – for particles with a median particle diameter of 86  $\mu\text{m}$ .

At a high solids concentration, the ratio between the number of air bubbles and the number of particles  $N_B/N_p$  is small. As the number of bubbles in the flotation pulp is far lower compared to the number of particles, the bubbles will be completely covered by particles (cf. Fig. 5-18a), resulting in an inhibited flotation mechanism according to Tomlinson and Fleming (see chapter 2.1.3.1). With decreasing solids concentration the ratio between  $N_B/N_p$  increases, so that more bubbles per particle are present in the flotation pulp. As a result, the bubbles are no longer completely covered by particles, which changes the predominant flotation mechanism from inhibited flotation to free flotation. Although halving  $c_{p,0}$  changes  $N_p$  equally for the particles with  $d_{50,3^*}=86$   $\mu\text{m}$  and 256  $\mu\text{m}$  to half the initial particle number, the impact on the kinetics of particles with a median particle diameter of 86  $\mu\text{m}$  is more pronounced than for particles with  $d_{50,3^*}=256$   $\mu\text{m}$ . Under the assumption of spherical particles, halving  $c_{p,0}$  leads to an absolute reduction from approx. 5 million particles to 2.5 million particles for  $d_{50,3^*}=86$   $\mu\text{m}$ , while for particles with a median diameter of 256  $\mu\text{m}$  a change of only about  $\Delta N_p=90,000$  is present. Thus, it is only plausible that the influence on the flotation kinetics of particles with a smaller  $d_{50,3^*}$  is more significant than for particles with a larger median particle diameter.

### 5.3.2 Optical investigations

The experimental conditions have a significant influence on the flotation behaviour with respect to the maximum recovery  $R_{\max}$  as well as the flotation kinetic constant  $k$  and order of flotation kinetics  $n$  (see chapters 5.3.1.2 and 5.3.1.3). Optical investigations via Shadowgraphy (SH) are conducted to analyse the influence of the particle-bubble interaction at the capillary outlet. In addition, the rising heterocoagulates formed under different experimental conditions are analysed with the two optical methods SH and Particle Image Velocimetry (PIV). The former is used to characterise the formed heterocoagulates, while the latter is used to analyse the induced hydrodynamics.

#### 5.3.2.1 Bubble-particle interaction during the bubble formation process

One of the main influence factors on the flotation kinetics, which emerged from the analysis in chapters 5.3.1.2 and 5.3.1.3, is the volumetric gas flow rate  $\dot{V}_g$ . The bubble formation time  $t_f$ , which is the time from bubble formation at the capillary outlet up to the time of bubble detachment from the capillary, varies with variation of  $\dot{V}_g$ . At a low gas flow rate of 0.1 mL/min,  $t_f$  is approx. 0.15 s, while  $t_f \approx 0.05$  s at 2 mL/min. To make sure that the bubble production time has no significant influence on the flotation kinetics, Shadowgraphy (SH) measurements are carried out at the capillary outlet in order to analyse the bubble-particle interaction during the bubble formation process.

An exemplary image sequence of the bubble formation at the capillary outlet during the flotation process of unmodified glass particles with a median particle diameter of 256  $\mu\text{m}$  at a gas flow rate of 0.1 mL/min in the flotation solution containing hexadecylamine (HDA) and methyl isobutyl carbinol (MIBC) at the optimum concentrations (cf. chapter 5.2.2) is shown in Fig. 5-15. Particles tend to settle on the capillary and even to some extent on the capillary outlet (Fig. 5-15a). Although particles seem able to adsorb on the bubble surface (Fig. 5-15b-d), the interacting forces are too weak for formation of a stable bubble-particle heterocoagulate, because the particles desorb from the bubble surface just before the bubble detachment (Fig. 5-15e). Therefore, no particles are initially adsorbed on the bubble surface due to a bubble-particle interaction during the bubble formation process, proving that the flotation kinetics will be unaffected by the bubble formation time (Fig. 5-15f). The heterocoagulate formation process must therefore occur elsewhere in the apparatus.

At a higher gas flow rate, the residence time of the bubble at the capillary outlet is even lower due to a significantly lower bubble formation time. Hence, the influence of bubble-particle interaction during the bubble formation process is even lower. No bubble-particle interaction

has been observed at the higher gas flow rate of 2 mL/min during the experiments. Therefore, it can be concluded that the influence of particles adsorbed on the bubble surface prior to bubble detachment is negligible.

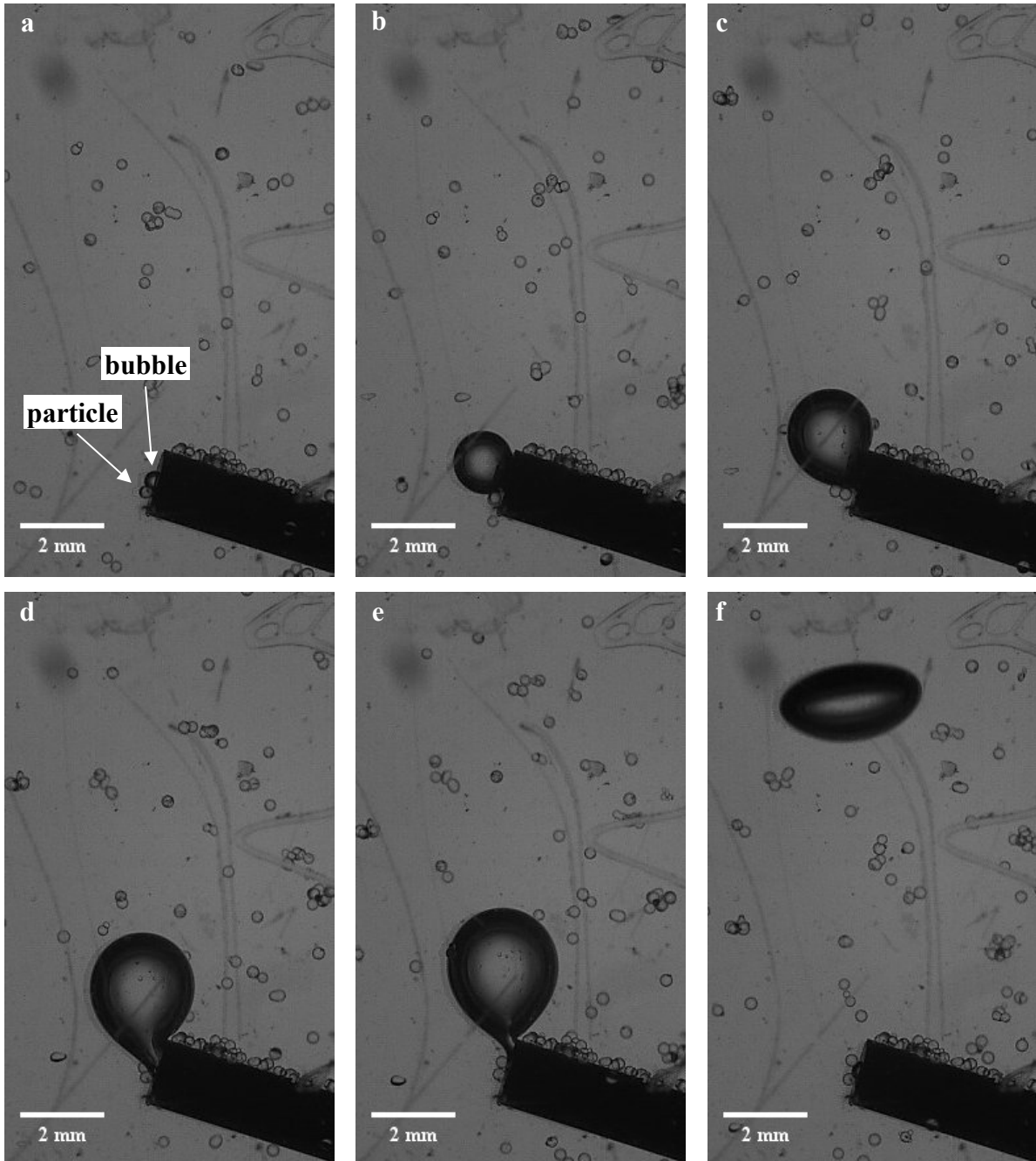


**Fig. 5-15.** Bubble formation at the capillary during the flotation process of unmodified glass particles with a median particle diameter of 256  $\mu\text{m}$  at a gas flow rate of 0.1 mL/min in a flotation solution containing hexadecylamine and methyl isobutyl carbinol. Bubble formation time  $t_f=0.15$  s.

### 5.3.2.2 Shadowgraphy measurements of rising single bubble heterocoagulates

For each experimental condition in Tab. 5-4 in chapter 5.3.1.1.2, Shadowgraphy (SH) measurements of the rising single bubble heterocoagulates are performed. The optical analysis of the heterocoagulates should help to understand the flotation behaviour with respect to the determined maximum recoveries  $R_{\max}$  and the flotation kinetics in form of the rate constant  $k$  at the different experimental conditions (cf. chapter 5.3.1.2). In all image sequences presented in this chapter, glass particles with a median particle diameter of  $256 \mu\text{m}$  are presented, because these particles provide a better visualisation due to their larger diameter compared to the particles with  $d_{50,3^*}=86 \mu\text{m}$ . The effects observed for both particle sizes are, however, the same. All raw image sequences can be found in the Appendix.

An exemplary sequence of a rising single bubble heterocoagulate in the HDA-MIBC flotation solution with unmodified particles attached at the bubble rear is presented in Fig. 5-16. The approximate time interval between the images (a) to (c) is 0.07 s. The image sequence shows a nearly rectilinear rising path of the single bubble heterocoagulate, with only a small rocking motion in horizontal  $x$  direction. This is in consensus with the motion of freely rising bubbles in Tab. 2-5. The particles attached to the bubble rear are always aligned opposite the direction of movement of the bubble. In Fig. 5-16a, the bubble rocks to the left-hand side, while the particles align on the right-hand side of the bubble rear. In Fig. 5-16b, a neutral position of the bubble is present. Therefore, the particles are positioned at the centre of the bubble rear. In Fig. 5-16c the bubble moves to the right-hand side. Thus, the particles position themselves at the left-hand side of the bubble rear.

From this image sequence it can be concluded that only minor rocking motions are present for single bubble heterocoagulates formed from unmodified glass particles. It is, however, unclear if this motion is induced by the bubble and balanced by the particles, or vice versa. From the results of the investigations in the two-phase system (see chapters 4.1 and 4.2) it may, however, be assumed that the motion is induced by the bubbles and compensated by the particles.

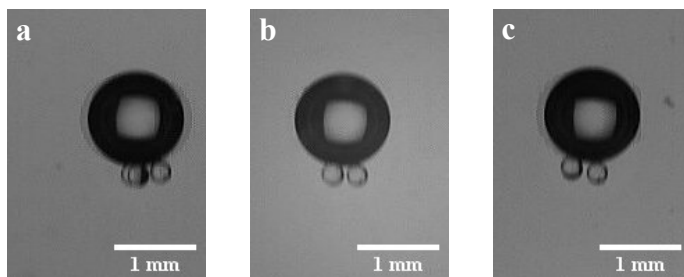


**Fig. 5-16.** Rise of a single bubble heterocoagulate in the HDA-MIBC flotation solution with attached unmodified particles of a median particle diameter  $d_{50,3^*}$  of  $256 \mu\text{m}$  filmed in the observation cell. Time interval between (a) and (c) is approx. 0.07 s.

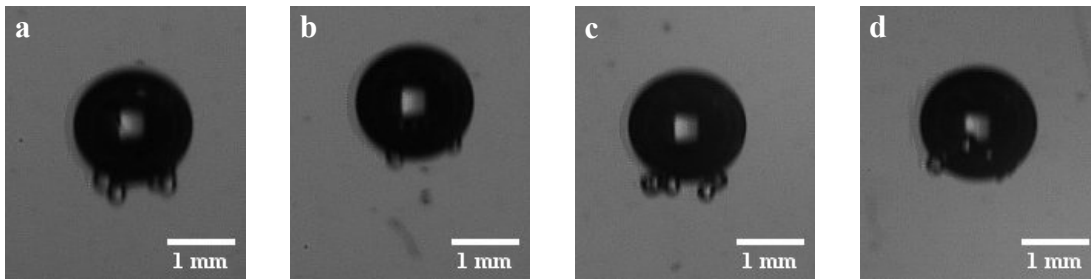


**Fig. 5-17.** Rise of a single bubble heterocoagulate in the HDA-MIBC flotation solution with attached hydrophilic particles of a median particle diameter  $d_{50,3^*}$  of 256  $\mu\text{m}$  filmed in the observation cell. Time interval between (a) and (d) is approx. 0.07 s.

An image sequence of a rising single bubble heterocoagulate in the HDA-MIBC flotation solution formed from hydrophilic particles is shown in Fig. 5-17. The time interval between the presented images (a) to (d) is approximately 0.07 s. The image sequence shows a high mobility of the glass particles on the bubble surface. This motion is strongly three-dimensional, as the particles move not only to the back (b) and front (d) of the bubble, but also to the left and right. The contact angle of this particle class could not be determined via film flotation experiments, because no liquid more hydrophilic than deionized water has been present during the experiments. However, contact angle measurements on equally hydrophilic glass slides showed a contact angle of approx.  $14.8^\circ$  (cf. chapter 5.1.1). The attachment stability of these particles on the bubble surface will therefore be low, consequently enabling them to move freely on the bubble surface. This visual impression underlines the fact that hydrophilic particles exhibit a very small maximum recovery. Due to the high mobility of the particles and the small attachment forces, already minor disturbances, e.g. turbulence and/or collision with other heterocoagulates or the wall of the apparatus, can easily lead to a detachment of the particles from the bubble surface. Furthermore, the attachment probability is in accordance with Eq. (2-26) low due to the low contact angle, which decreases the flotation kinetics (cf. chapter 2.1.3.2.2).

For hydrophobic particles, larger bubble-particle aggregates up to a clustering of multiple bubbles and particles are observed (see Fig. 5-18). During the experiments with hydrophobic particles in the flotation solution containing only the frother MIBC, an aggregation of the particles has been observed in the dispersion cell. This aggregation is related to the strongly hydrophobic nature of the particles, which prevents a wetting of the particles. The strong particle-particle interactions occur due to the hydrophobic nature of the particles and lead to the formation of aggregates. The flotation of these formed larger aggregates is, however, more complicated, because the weight force is higher than for single particles, thus requiring a higher buoyant force. The bubble production frequency and capillary outlet diameter are kept constant

during the experiments, so that the bubble size is approximately constant and, thus the buoyant force. The bubbles induced in the dispersion cell exhibit also a hydrophobic surface, which is why the hydrophobic glass particles will be attracted towards the bubble surface. Due to the hydrophobic property of the bubble and the additional effect of the hydrophobic particles, bubbles may be fully covered by particles as shown in Fig. 5-18a. In this case, the bubble is not able to float to the top of the single bubble flotation column anymore. The fully covered bubbles are observed to be moving up and down in the dispersion cell. With adsorption of particles on the bubble surface the mean density of the heterocoagulate increases up to the point, where the density is close to the density of the surrounding liquid. If the densities are similar, the heterocoagulate will hover and follow the flow induced by the circulating pump in the dispersion cell. As new bubbles are induced into the dispersion cell, a collision between the fully covered bubble-particle heterocoagulates and the newly formed bubbles is possible. Due to the hydrophobic nature of the particles, the attachment to air bubbles is increased (Fig. 5-18b&c). The more bubbles attach to the already existing heterocoagulate, the higher the buoyant force of the heterocoagulate becomes. As soon as the buoyant force is greater than the weight force, the heterocoagulate will rise to the top of the single bubble column. If only a small number of particles aggregates and the buoyant force of an attached bubble is large enough to overcome the weight force, flotation of these already larger bubble-particle heterocoagulates is also feasible (see Fig. 5-18d).

The results of the SH measurements are in consensus with the results presented in Fig. 5-11. It is observed that the number of particles attached to the bubble surface of rising heterocoagulates is larger for hydrophobic particles than for unmodified or hydrophilic particles. The determined low values for  $R_{\max}$  and  $k$  for hydrophilic particles (cf. chapter 5.3.1) can be attributed to the high mobility of the particles on the bubbles surface. Due to this mobility, the stability of the bubble-particle heterocoagulates is low, resulting in a higher detachment probability of the particles. Compared to this, determined values for  $R_{\max}$  and  $k$  for unmodified particles are higher, but still low compared to hydrophobic particles, which is a result of the formed larger bubble-particle aggregates and the hydrophobic particle-particle interaction.

The finding of completely loaded bubbles in the dispersion cell (cf. Fig. 5-18a) may be another explanation why the maximum recovery  $R_{\max}$  of the hydrophobic particles with a median particle diameter  $d_{50,3^*}$  of 256  $\mu\text{m}$  is lower compared to  $R_{\max}$  of the unmodified particles (cf. Fig. 5-11). As described above, heavily loaded bubbles will have a density close to the surrounding liquid, which is why they are unable to float. Only if more bubbles attach to the heterocoagulate will the density be lowered again so that the heterocoagulates will rise to the solids deposition cell at the top of the apparatus.

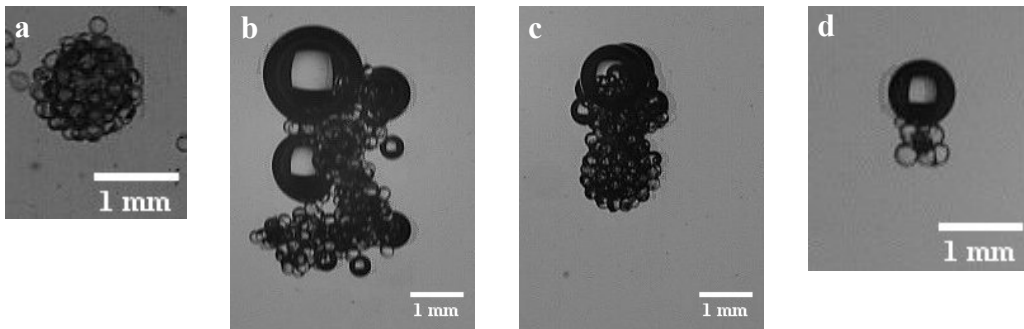


**Fig. 5-18.** Formation of larger bubble-particle heterocoagulates in an aqueous MIBC solution of particles with a median diameter  $d_{50,3^*}$  of 256  $\mu\text{m}$  using hydrophobic particles. Image (a) shows a fully covered bubble in the dispersion cell, which is unable to rise, while (b)-(d) show rising heterocoagulates in the observation cell.

For small flotation times  $R_{\text{max}}$  may therefore be low. If the flotation time is prolonged, however, the attachment of further bubbles on the heterocoagulates may result in the flotation of the heavily loaded bubbles, and thus increase  $R_{\text{max}}$  significantly.

### 5.3.2.3 Hydrodynamic characterisation of rising heterocoagulates

As stated in chapter 1.2, the aim of the present work is the analysis of freely rising heterocoagulates. The experimental setup presented in chapter 3.1.1.1 explained the necessity of a circulating pump for the dispersion of the solid particles in the pulp of the flotation column located in the dispersion cell (cf. chapter 3.1.1.1.1). A distance of approx. 380 mm between the dispersion cell and the observation cells has been considered to reduce the influence of the circulating pump on the optical investigations to a minimum. To analyse the influence of the circulating pump on the hydrodynamics in the observation cells, Particle Image Velocimetry (PIV) measurements are carried out without solids and bubbles in the observation cells. Afterwards, flotation experiments as described in chapter 5.3.1 are carried out for unmodified glass particles with two different particles sizes at two different volumetric gas flow rates at a constant collector and frother concentration. The formed single bubble heterocoagulates are observed and analysed using the optical methods Shadowgraphy (SH) and PIV simultaneously.

#### 5.3.2.3.1 Experimental procedure

The single bubble flotation column is prepared as described in chapter 5.3.1.1.1 and the experimental procedure for the flotation of the glass particles is analogous to the description in chapter 5.3.1.1.2. For the measurements regarding the influence of the circulating pump, no solid particles are added to the liquid and the syringe pump is turned off. PIV measurements are then conducted for volumetric liquid flow rates  $\dot{V}$  of zero to investigate the gravitational influence as well as for the volumetric flow rates calculated for the dispersion of the glass

particles with a median diameter  $d_{50,3^*}$  of 86  $\mu\text{m}$  and 256  $\mu\text{m}$  (see Appendix 9.1.3.2). The PIV measurements are conducted at steady-state and approx. 300 images are analysed.

Rising heterocoagulates are investigated for the experiments N=13-16 stated in Tab. 5-4 in chapter 5.3.1.1.2. The stated volumetric gas flow rate  $\dot{V}_g$  of 2 mL/min for experiments N=14 and N=16 is, however, too high for an investigation via PIV. Preceding studies have shown that the time interval between two consecutive rising heterocoagulates is too small at this gas flow rate. Therefore,  $\dot{V}_g$  is reduced to 1 mL/min instead, which reduces the interaction between two consecutive rising heterocoagulates and, thus enables the analysis of these.

Four grams of unmodified glass particles with a median particle diameter  $d_{50,3^*}$  of 86  $\mu\text{m}$  and 256  $\mu\text{m}$  are floated at two different gas flow rates  $\dot{V}_g$  of 0.1 mL/min and 1 mL/min in an aqueous HDA-MIBC flotation solution with the optimised concentrations stated in chapter 5.2.2. SH and PIV measurements are conducted simultaneously to allow an analysis of the geometric parameters of the heterocoagulates and their influence on the induced hydrodynamics as well as a counting of the attached particles. Preceding experiments have shown that the tracer-particles do not adsorb on the bubble surface, neither in deionized water nor in surfactant solutions. Thus, a systematic error due to floated tracer particles does not have to be considered. The number of particles attached to the bubbles are counted manually from the SH image sequences. The PIV image sequences are analysed as stated in chapter 3.2.2.

### 5.3.2.3.2 Results

In the first step, the influence of gravitational effects and the effect of the volumetric liquid flow rate  $\dot{V}$  induced by the circulating pump in the dispersion cell are analysed. The results are presented in Tab. 5-7. The determined mean liquid velocities  $\bar{w}$  are in all three cases smaller by a factor of ten compared to PIV results of rising single bubbles in deionized water and aqueous surfactant solutions (cf. chapters 4.1.2 and 4.2). To evaluate the influence magnitude of these background effects on the actual measurements, the ratio of  $\bar{w}$  and the minimum observed bubble rising velocity  $w_B$  in surfactant systems (cf. chapter 2.3.1.2), as well as the ratio of  $\bar{w}$  and the average liquid flow velocity  $\bar{w}^*$  around rising single bubbles observed in the two-phase system (cf. chapter 4.1.2) are calculated. The former ratio shows that the influence of  $\bar{w}$  on the rising velocity is less than 1 % and therefore negligible. The latter ratio shows also a low effect on the average liquid flow velocity around rising single bubbles with an influence of less than 3 % in all investigated experimental conditions. Thus, it can be concluded that all measurements regarding single bubble heterocoagulates in the flotation column will be acquired without the influence of the circulating pump.

**Tab. 5-7.** Mean liquid velocity  $\bar{w}$  measured in the observation cell under the influence of gravity ( $\dot{V}=0$ ) as well as the two different circulating pump volumetric flow rates  $\dot{V}$  used for dispersion of the solid particles in the dispersion cell of the single bubble flotation column (cf. Appendix 9.1.3.2).

$\dot{V}$	$\bar{w}$ [ $\times 10^{-4}$ m/s]	$\frac{\bar{w}_1}{w_B}$ [%]	$\frac{\bar{w}_2}{\bar{w}^*}$ [%]
0	2.2	0.1	0.6
$d_{50,3^*}=86 \mu\text{m}$	8.5	0.5	2.4
$d_{50,3^*}=256 \mu\text{m}$	9.9	0.6	2.8

The resulting frequency distributions  $q_0$  for the two different gas flow rates are shown in Fig. 5-19. The manual counting of the particles attached to bubbles is only carried out for particles with a  $d_{50,3^*}$  of 256  $\mu\text{m}$ , because the smaller particles cannot be counted accurately due to their low particle size.

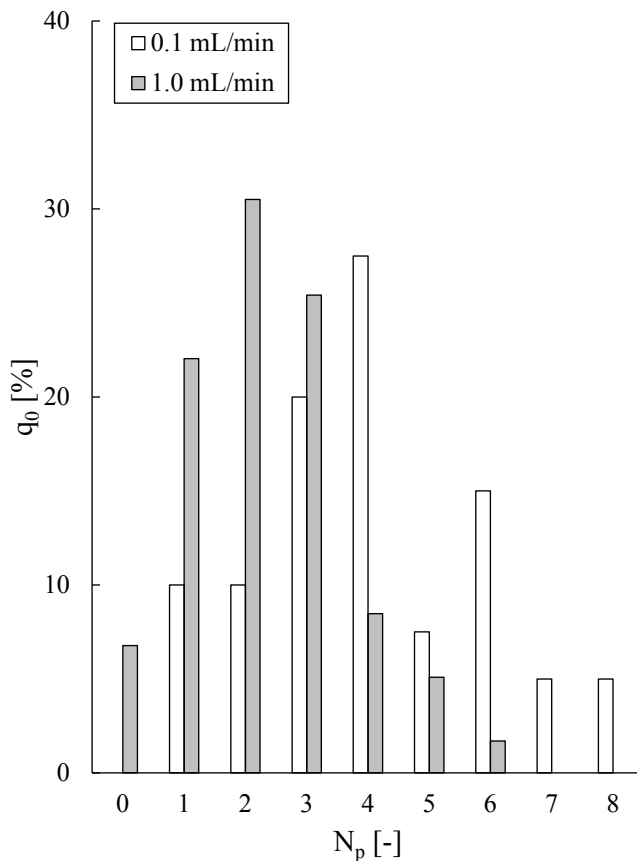


**Fig. 5-19.** Frequency distribution  $q_0$  of the number of particles  $N_p$  attached to a rising bubble at volumetric gas flow rates of 0.1 mL/min (white bars) and 1.0 mL/min (grey bars) for unmodified particles with a median diameter  $d_{50,3^*}$  of 256  $\mu\text{m}$  in the HDA-MIBC flotation solution. Approximately 100 bubbles have been counted.

<sup>1</sup> A rising velocity of  $w_B=0.18$  m/s is assumed, which corresponds to the minimum rising velocity of the bubbles in the experimental range (cf. chapter 2.3.1.2).

<sup>2</sup> A mean liquid flow velocity  $\bar{w}^*$  around rising bubbles of 0.035 m/s is assumed (cf. chapter 4.1.2).

The number of particles  $N_p$  attached to the bubbles decreases with increasing gas flow rate  $\dot{V}_g$ . This seems plausible, because the probability of formation of a stable bubble-particle heterocoagulate will decrease due to an increased turbulence (cf. chapter 2.1.3.2.3). At  $\dot{V}_g=0.1$  mL/min, the maximum of the frequency distribution is at  $N_p=4$ , while the maximum is at  $N_p=2$  for  $\dot{V}_g=1$  mL/min. Furthermore, it is striking that at the higher gas flow rate bubbles are observed, which have no particles attached to the bubble surface. According to the model for the probability of the stability  $P_s$  of the bubble-particle heterocoagulates given by Eq. (2-28) in chapter 2.1.3.2.3, the stability will decrease with increasing turbulence in the flotation pulp. Thus, the finding of bubbles without attached particles may be related to the higher turbulence in the flotation pulp due to the increased gas flow rate and, consequently, the increase of the induced liquid velocity (cf. chapter 4.1.2).

The results of the mean liquid velocity  $\bar{w}$  in the observation cell 2 (cf. Fig. 3-1) at two different volumetric gas flow rates  $\dot{V}_g$  of 0.1 mL/min and 1 mL/min for the single bubble-particle heterocoagulates with median particle diameters  $d_{50,3^*}=86$   $\mu\text{m}$  and 256  $\mu\text{m}$  are compared to unloaded bubbles in deionized water (DW) and the collector-frother solution (HDA-MIBC) in Fig. 5-20.

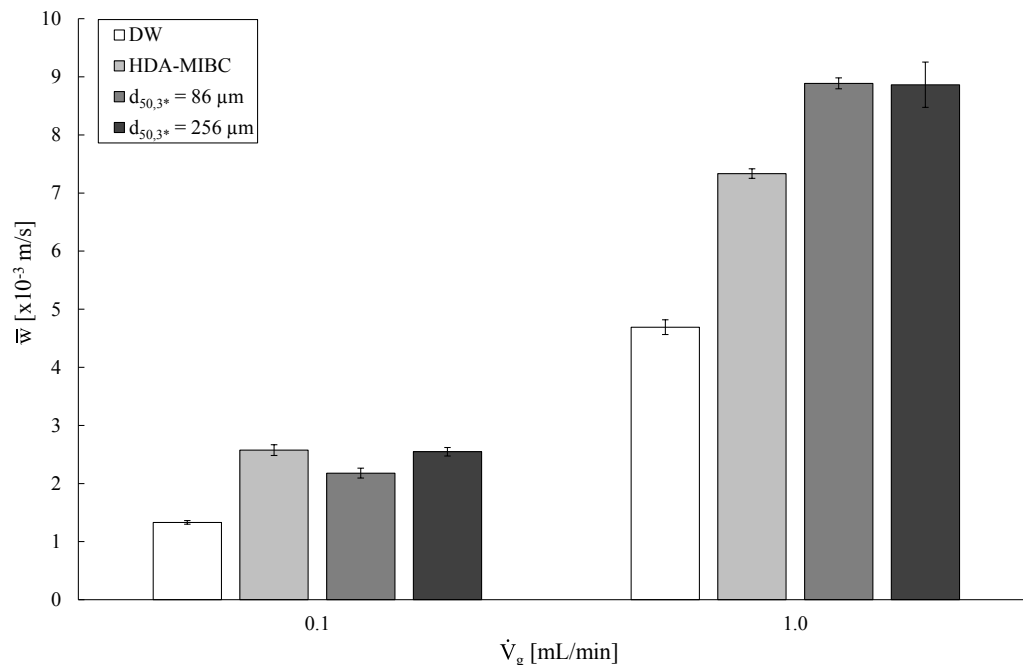


**Fig. 5-20.** Comparison of mean liquid velocities  $\bar{w}$  for gas flow rates  $\dot{V}_g$  of 0.1 mL/min and 1.0 mL/min for measurements in deionized water (DW, white bars), the hexadecylamine-methyl isobutyl carbinol-solution used in absence of particles (HDA-MIBC, light-grey bars), as well as freely rising heterocoagulates with particles with a median diameter  $d_{50,3^*}$  of 86  $\mu\text{m}$  (grey bars) and particles with  $d_{50,3^*}=256$   $\mu\text{m}$  (dark-grey bars).

For measurements in DW and the HDA-MIBC solution the mean value of five bubbles is presented, while the average of approximately 30 bubbles is presented for all particle loadings. An increase of  $\bar{w}$  from  $\dot{V}_g=0.1$  mL/min to 1.0 mL/min is present for all four experimental conditions. Furthermore, measurements in DW show always the lowest  $\bar{w}$ . At a low  $\dot{V}_g$ , a clear trend between unloaded bubbles in the HDA-MIBC solution and the bubble-particle heterocoagulates is not present. The mean liquid velocity for bubbles in the HDA-MIBC solution is equal to  $\bar{w}$  for heterocoagulates with particles of a median diameter of 256  $\mu\text{m}$ . The mean liquid velocity for heterocoagulates with  $d_{50,3^*}=86$   $\mu\text{m}$  is approx. 17 % lower than for  $d_{50,3^*}=256$   $\mu\text{m}$  at  $\dot{V}_g=0.1$  mL/min. At the higher gas flow rate of 1 mL/min, a clear trend between loaded and unloaded bubbles is observed. The mean liquid velocity is the lowest for measurements in DW, followed by rising unloaded bubbles in the HDA-MIBC solution. The heterocoagulates exhibit the highest  $\bar{w}$ . A significant difference between the two different particle sizes is, however, not observed.

## 6 Flotation experiments with fluorite minerals

In this chapter, flotation experiments with an industrial fluorite mineral system and a fluorescent fluorite mineral are presented.

### 6.1 Industrial fluorite mineral from Clara mine

#### 6.1.1 Experimental procedure

A fluorite flotation system from the Clara mine in Oberwolfach, Germany, provided by Sachtleben Bergbau GmbH is investigated using a design of experiment (DoE) with respect to the total recovery  $R_{\max}$ , the flotation rate constant  $k$ , and the calcium fluoride content  $w(\text{CaF}_2)$  in the concentrate using the developed FT Raman spectroscopy method (see chapter 3.2.3). A  $3^k$  DoE with pH value, oleic acid concentration  $c(\text{OA})$ , stirrer speed  $n$ , and volumetric gas flow rate  $\dot{V}_g$  as variable parameters is set up as presented in Tab. 6-1. The centre point experiment ( $N=17$ ) is repeated nine times and each other experimental point is repeated three times, yielding a total number of 57 experiments.

The experiments are conducted in a 2 L laboratory scale flotation apparatus (see chapter 3.1.2) at a room temperature of  $22\text{ °C} \pm 2\text{ °C}$ . Deionized water is filled into the apparatus to a liquid level of about 180 mm. Afterwards oleic acid and starch are added while stirring. Starch is used as depressant for barium sulphate in the experiments. Its concentration is kept constant at 0.4 mg/g crude ore in all 57 experiments, which is in the typical concentration range stated in literature (see chapter 2.1.4.2). The oleic acid concentration is varied between 0.047 mmol/L and 0.17 mmol/L, which corresponds to 0.4-1.4 kg OA per tonne crude ore. The chosen range of  $c(\text{OA})$  is therefore in the common range reported in literature (cf. chapter 2.1.4.2). The pH value is measured using an immersed pH-electrode (cf. Fig. 3-5) and manipulated using a 1N sodium hydroxide solution. Afterwards, 60 g of the dry fluorite ore are given into the liquid solution, yielding a solids concentration of 3 wt%. The Raman analysis of the crude ore shows a calcium fluoride concentration of approx. 50 wt%. After 1 min conditioning time, air is introduced into the apparatus via a porous frit. The air flow rate is adjusted using a variable area flowmeter. The duration of the experiments is monitored with a stop watch.

The formed froth is skimmed manually into a glass beaker. Every five minutes, a new beaker is used to facilitate a time-resolved analysis of the flotation process. At the same time, the present pH value is noted. The experiments are stopped when no more froth is formed or 30 minutes have elapsed. Afterwards, the concentrate is filtered and washed several times with deionized water. The particles are then dried to constant weight in an oven at 100 °C.

**Tab. 6-1.** Design of experiment (DoE) for investigation of the fluorite flotation system from the Clara Mine in Oberwolfach, Germany, provided by Sachtleben Bergbau GmbH with pH value, oleic acid concentration  $c(\text{OA})$ , stirrer speed  $n$ , and volumetric gas flow rate  $\dot{V}_g$  as variable parameters.

N	pH	$c(\text{OA})$	$n$	$\dot{V}_g$	pH	$c(\text{OA})$	$n$	$\dot{V}_g$
	[-]	[-]	[-]	[-]		[-]	[mmol/L]	[1/min]
1	-1	-1	-1	-1	8	0.047	250	2.0
2	-1	-1	-1	1	8	0.047	250	5.0
3	-1	-1	1	-1	8	0.047	450	2.0
4	-1	-1	1	1	8	0.047	450	5.0
5	-1	1	-1	-1	8	0.170	250	2.0
6	-1	1	-1	1	8	0.170	250	5.0
7	-1	1	1	-1	8	0.170	450	2.0
8	-1	1	1	1	8	0.170	450	5.0
9	1	-1	-1	-1	12	0.047	250	2.0
10	1	-1	-1	1	12	0.047	250	5.0
11	1	-1	1	-1	12	0.047	450	2.0
12	1	-1	1	1	12	0.047	450	5.0
13	1	1	-1	-1	12	0.170	250	2.0
14	1	1	-1	1	12	0.170	250	5.0
15	1	1	1	-1	12	0.170	450	2.0
16	1	1	1	1	12	0.170	450	5.0
17	0	0	0	0	10	0.109	350	3.5

For the FT Raman analysis, approx. 0.5 g of the dried sample are filled into a vial. The measurements are carried out as described in chapter 3.2.3. If the amount of a fraction is smaller than 0.5 g it is mixed with the next fraction and measured as an average of the sample times. To investigate the effect of  $c(\text{OA})$  on the flotation performance, supplementary film flotation experiments are conducted. In these experiments, high-purity grade calcium fluoride with a  $\text{CaF}_2$  content of at least 99 wt% is used. Suspensions of 5 g  $\text{CaF}_2$  and the minimum and maximum oleic acid concentrations investigated in the DoE, namely 0.047 mmol/L and 0.170 mmol/L, are setup in 50 mL beaker glasses. The pH is adjusted to 8 using a 1N sodium hydroxide solution. The suspensions are stirred for 10 min with a magnetic stirrer. Afterwards, the suspensions are filtrated, the calcium fluoride is rinsed several times with deionized water, and finally dried in an oven at 100 °C to constant weight. The procedure of the film flotation experiments is analogous to the procedure described in chapter 5.1.2.

## 6.1.2 Results and discussion

The results of the design of experiment (DoE) are first analysed with respect to the flotation kinetics. Afterwards, a rigorous statistical analysis is carried out for the design of experiment in order to investigate the influence of the different operational parameters on the overall flotation process. Lastly, results of additionally conducted optical measurements are presented in order to relate these results with the flotation results.

### 6.1.2.1 Analysis of flotation kinetics

The experimental results are analysed with respect to the flotation kinetics as stated in chapter 6.1.1. For this purpose chemical analogous kinetic models of type 0<sup>th</sup> order, 1<sup>st</sup> order, and 2<sup>nd</sup> order, as well as empirical models, e.g. the classical model, are evaluated. The former models are analysed via linearisation in Microsoft Excel using the determined experimental recovery  $R_{\max}$  (see chapter 2.1.3.1), while the kinetic parameters of the latter are determined using a MATLAB tool [273]. The empirical model fits are carried out with the restriction  $R_{\infty} \leq 100\%$ .

An overview of the tested kinetic models and the corresponding mean regression coefficients  $\overline{R^2}$  is given in Tab. 6-2. The 1<sup>st</sup> order model gives the best mean regression coefficient for the chemical analogous models with a value of 0.9907. The empirical models show mean regression coefficients with similar values ( $\overline{R^2} \geq 0.9898$ ) with exception of the fully mixed model, which has a mean regression coefficient of 0.9445.

**Tab. 6-2.** Mean regression coefficients  $\overline{R^2}$  and minimum and maximum determined regression coefficients  $\min(R^2)$  and  $\max(R^2)$ , respectively, for flotation experiments of the industrial fluorite mineral.

Kinetic model	$\overline{R^2}$	$\min(R^2)$	$\max(R^2)$
0 <sup>th</sup> order	$0.9227 \pm 0.0414$	0.8534	0.9857
1 <sup>st</sup> order	$0.9907 \pm 0.0133$	0.9461	0.9999
2 <sup>nd</sup> order	$0.8479 \pm 0.0843$	0.6577	0.9752
Classical model	$0.9970 \pm 0.0024$	0.9929	0.9998
Klimpel model	$0.9929 \pm 0.0047$	0.9857	0.9992
Kelsall model	$0.9928 \pm 0.0076$	0.9768	1.0000
Modified Kelsall model	$0.9996 \pm 0.0008$	0.9974	1.0000
Gamma model	$0.9995 \pm 0.0009$	0.9966	1.0000
Fully mixed model	$0.9445 \pm 0.0777$	0.7659	0.9999

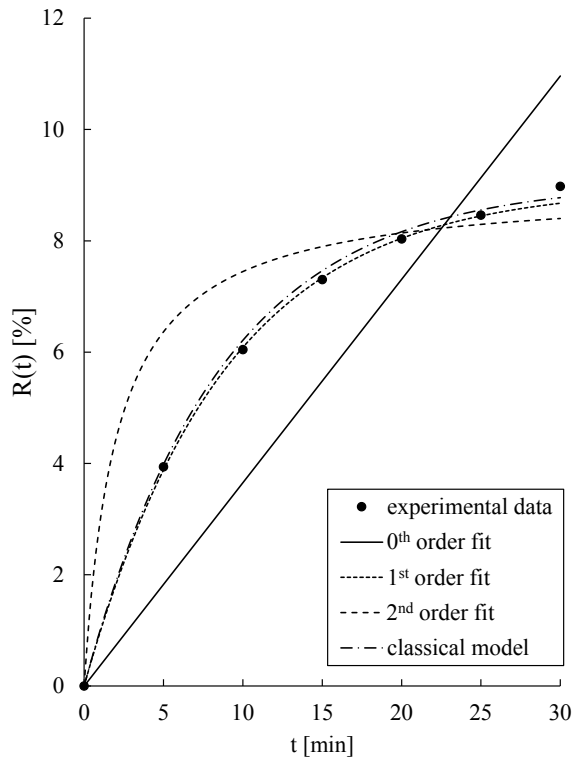


**Fig. 6-1.** Exemplary kinetic fit for fluorite flotation at a pH of 8, a concentration of oleic acid of 0.047 mmol/L, a stirrer frequency of 450 min<sup>-1</sup> and a gas flow rate of 5 L/min using chemical analogous models of type 0<sup>th</sup> order, 1<sup>st</sup> order, and 2<sup>nd</sup> order, as well as the classical type model as an example for the evaluated empirical models.

Exemplary fits of the kinetic models to an experimental data set is given in Fig. 6-1, where the data from the experimental design at N=4 (cf. Tab. 6-1) are presented for fluorite flotation at pH=8 with  $c(\text{OA})=0.047$  mmol/L at a stirrer speed of 450 min<sup>-1</sup> and  $\dot{V}_g=5$  L/min. The chemical analogous model of 1<sup>st</sup> order gives the best fit. The 0<sup>th</sup> order fit underestimates the recovery in the beginning and overestimates it towards the end with an absolute deviation of 2 % at  $t=30$  min, which represents a relative error of 21 %. The 2<sup>nd</sup> order fit overestimates the recovery up to approx.  $t=20$  min and underestimates it afterwards with an absolute difference of 2.6 %. The classical model, which is shown as an example for the evaluated empirical models, shows a fit similarly as good as the 1<sup>st</sup> order chemical analogous model. Compared to the 1<sup>st</sup> order model the classical model predicts a slightly higher recovery at  $t=30$  min (8.78 % vs. 8.68 %). From the obtained data it can be concluded that the flotation process of fluorite generally follows 1<sup>st</sup> order kinetics for the investigated process parameters. Wills and Finch ([17], p. 297) as well as many other researchers [35–39] state that the order of flotation kinetics generally follows 1<sup>st</sup> order (cf. chapter 2.1.3.1). According to Nguyen and Schulze first-order kinetics apply to flotation of single minerals or diluted pulps, while second-order kinetics apply to flotation of low grade ores as well as more concentrated pulps ([3], p. 749). The initial solids concentration in the pulp in the present experiments is 3 wt% with a calcium fluoride

concentration of  $w(\text{CaF}_2) \approx 50 \text{ wt}\%$  (cf. chapter 6.1.1). Batch-flotation tests presented in literature state solids concentrations ranging from diluted solutions with 1-4 wt% [39,274] and intermediate concentrations of approx. 10-20 wt% [24,36,42,275–277] up to concentrated pulps with about 30-40 wt% solids in the pulp [41,46,278]. The pulp concentration in the present experiments is low so that a diluted solution may be assumed. Wills and Finch recommend a low pulp density to avoid an overloading of the bubbles, which would result in an inhibited flotation according to Tomlinson and Fleming (cf. chapter 2.1.3.1). However, they state that in commercial roughers most commonly pulps with 25-40 wt% solids are used, although their concentration can vary to a minimum of 8 wt% and up to a maximum of 55 wt%. Diluted pulps are preferred in cleaner stages to take advantage of increased selectivity ([17], p. 320). In the industrial flotation process of fluorite, a solids concentration of 25-32 wt% in the pulp is reported. The process is commonly conducted in 5-10 mechanical cells per bank, meaning five to ten flotation cells in series ([77], p. 1209). Therefore, comparison of batch-flotation experiments in laboratory scale with industrial processes is complicated.

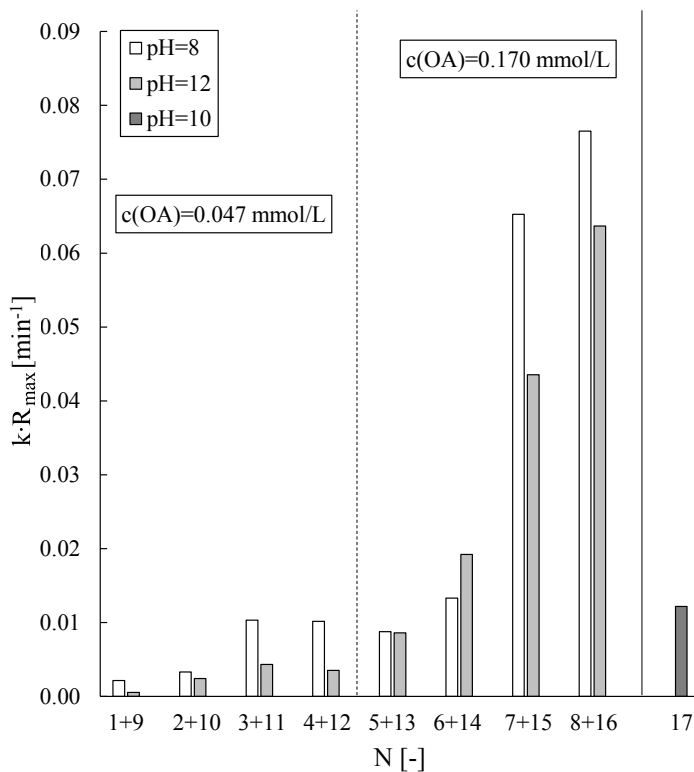


**Fig. 6-2.** Comparison of the product of flotation rate constant and maximum experimental recovery  $k \cdot R_{\max}$  at pH=8 (white bars), pH=12 (light-grey bars), and pH=10 (grey bars) for the experiment numbers  $N$  stated in the experimental design in Tab. 6-1. The flotation rate constants  $k$  used for the calculations are all taken from the results of the 1<sup>st</sup> order chemical analogous reaction model fit.

It has been stated in chapter 2.1.3.1 that a change in experimental conditions will simultaneously affect the flotation rate constant  $k$  and the maximum recovery  $R_{\max}$ . Thus, the product of these two parameters  $k \cdot R_{\max}$  is more suitable for a comparison of the flotation process at varying experimental conditions. A comparison of the determined  $k \cdot R_{\max}$  for the conducted experiments is shown in Fig. 6-2. For all calculations presented in this diagram, the determined 1<sup>st</sup> order flotation rate constants  $k$  from the chemical analogous model are used.

At pH=8, the product  $k \cdot R_{\max}$  is always greater than at pH=12, with exception of N=6+14. Furthermore, an increase of  $c(\text{OA})$  always yields higher values for  $k \cdot R_{\max}$ , e.g. comparison of N=1+9 with N=5+13, which have the same stirrer speed  $n$  of  $250 \text{ min}^{-1}$  and same gas flow rate  $\dot{V}_g$  of 2 L/min, shows an approx. four times higher value at pH=8 and an about 16 times higher value at pH=12 with an increase of  $c(\text{OA})$  from 0.047 mmol/L to 0.17 mmol/L. Additionally, an increase of  $n$  results in an increase of  $k \cdot R_{\max}$  (cf. Fig. 6-2 for, e.g. N=1+9 and N=3+11). The gas flow rate shows no clear trend at the low oleic acid concentration, as  $k \cdot R_{\max}$  increases from, e.g. N=1+9 to N=2+10, but decreases from N=3+11 to N=4+12. At  $c(\text{OA})=0.17 \text{ mmol/L}$ ,  $k \cdot R_{\max}$  increases with increasing  $\dot{V}_g$  for all experimental data sets (cf. Fig. 6-2 for, e.g. N=5+12 and N=6+14). The product of flotation rate constant and maximum recovery at the centre point of the DoE (N=17) is similar to the value obtained at N=5+13.

From Fig. 6-2 it can be concluded that a low pH value of 8, a high oleic acid concentration of 0.17 mmol/L, and a high stirrer speed of  $n=450 \text{ min}^{-1}$  are favourable to increase the kinetics and the recovery. The gas flow rate seems to have an influence on  $k \cdot R_{\max}$  only at a higher  $c(\text{OA})$ . At this set point,  $\dot{V}_g$  should then be high (5 L/min) to increase  $k \cdot R_{\max}$ . Although a discussion of the process parameter is feasible using Fig. 6-2, there is, however, no information on the concentrate grade given in this diagram, which is why these set points do not necessarily have to be the optimal flotation parameters. In order to investigate the influence of the process parameters on the flotation process including the product quality, a statistical analysis is carried out in the following chapter.

### 6.1.2.2 Statistical analysis of the design of experiment

The summarized results of the design of experiment are presented in Tab. 6-3. The results for the flotation responses maximum recovery  $R_{\max}$ , first-order flotation rate constant  $k$ , and calcium fluoride content  $w(\text{CaF}_2)$  in the concentrate are the mean values of the three and nine repetitive measurements, respectively (see chapter 6.1.1). The presented results for  $k$  are the 1<sup>st</sup> order flotation rate constants obtained from the kinetic analysis using the chemical analogous model, as this model has been found to represent the flotation kinetics best (cf. chapter 6.1.2.1). The maximum recovery ranges from 0.4 % to 42 %, the 1<sup>st</sup> order flotation rate constant ranges from  $1.6 - 4.0 \cdot 10^{-3} \text{ s}^{-1}$ , and the calcium fluoride content in the concentrate ranges from 36 % to 91 %.

**Tab. 6-3.** Resulting mean maximum recovery  $\bar{R}_{\max}$ , mean first-order kinetic constant  $\bar{k}$ , and mean weight fraction of calcium fluoride in the concentrate  $\bar{w}(\text{CaF}_2)$  of the design of experiment as well as the parameter product  $\bar{R}_{\max} \cdot \bar{w}(\text{CaF}_2)$ .

N	pH	c(OA)	n	$\dot{V}_g$	$\bar{R}_{\max}$	$\bar{k}$	$\bar{w}(\text{CaF}_2)$	$\bar{R}_{\max} \cdot \bar{w}(\text{CaF}_2)$
	[-]	[mmol/L]	[1/min]	[L/min]	[%]	[ $\times 10^{-3} \text{ s}^{-1}$ ]	[%]	[%]
1	8	0.047	250	2.0	1.18	3.04	75.73	0.89
2	8	0.047	250	5.0	1.79	3.07	78.22	1.40
3	8	0.047	450	2.0	8.36	2.06	83.56	6.99
4	8	0.047	450	5.0	8.98	1.89	91.22	8.19
5	8	0.170	250	2.0	7.65	1.91	83.38	6.38
6	8	0.170	250	5.0	8.32	2.67	83.28	6.93
7	8	0.170	450	2.0	42.44	2.56	87.74	37.24
8	8	0.170	450	5.0	38.36	3.33	84.41	32.38
9	12	0.047	250	2.0	0.38	2.45	36.36	0.14
10	12	0.047	250	5.0	1.01	3.99	47.01	0.48
11	12	0.047	450	2.0	4.41	1.64	57.64	2.54
12	12	0.047	450	5.0	2.96	1.98	47.44	1.40
13	12	0.170	250	2.0	5.69	2.52	72.68	4.14
14	12	0.170	250	5.0	11.64	2.75	75.48	8.79
15	12	0.170	450	2.0	20.83	3.48	60.01	12.50
16	12	0.170	450	5.0	26.86	3.95	61.68	16.57
17	10	0.109	350	3.5	11.37	1.78	79.27	9.02

The influence of the variable parameters pH value, oleic acid concentration  $c(\text{OA})$ , stirrer speed  $n$ , and volumetric gas flow rate  $\dot{V}_g$  on the maximum recovery  $R_{\max}$ , the flotation rate constant  $k$ , and the calcium fluoride content  $w(\text{CaF}_2)$  in the concentrate is analysed via a statistical analysis in Minitab v18.1.0.0. All analyses are carried out at a significance level  $\alpha$  of 99 %.

The analysis of the standardized effects in form of a Pareto chart for  $R_{\max}$  is shown in Fig. 6-3. The Pareto chart is used to determine the magnitude and the significance of the effects. Only bars, which cross the reference line are statistically significant. The position of the reference line depends on the chosen significance level. A previous analysis showed that the volumetric gas flow rate (factor D) as well as all two-factor interactions with  $\dot{V}_g$  (AD, BD, and CD) are insignificant, which is why these factors are not shown in Fig. 6-3. Due to their insignificance, these parameters have to be excluded for all further analyses.

From Fig. 6-3 it can be seen that the concentration of oleic acid has the largest influence on  $R_{\max}$ , the stirrer speed the second largest effect, and the two-factor interaction effect  $c(\text{OA}) \cdot n$  the third largest effect. The two-factor interaction effect  $\text{pH} \cdot c(\text{OA})$  is just insignificant. The Pareto chart displays, however, only the absolute values of the effects. Thus, it cannot be determined if the significant effects have a positive or negative effect on  $R_{\max}$ .

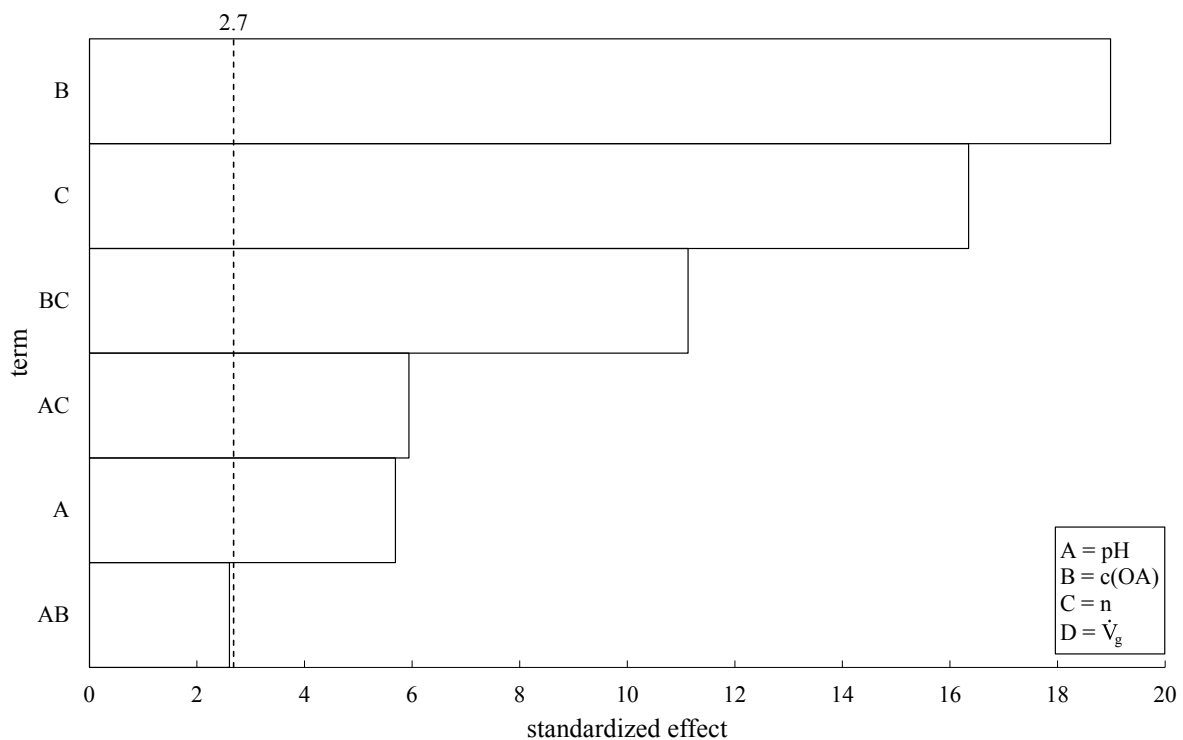


**Fig. 6-3.** Pareto chart of the standardized effects for the maximum recovery  $R_{\max}$  at a significance level  $\alpha$  of 99 %. Dashed line at a standardized effect of 2.7 shows reference value at which effects become significant.

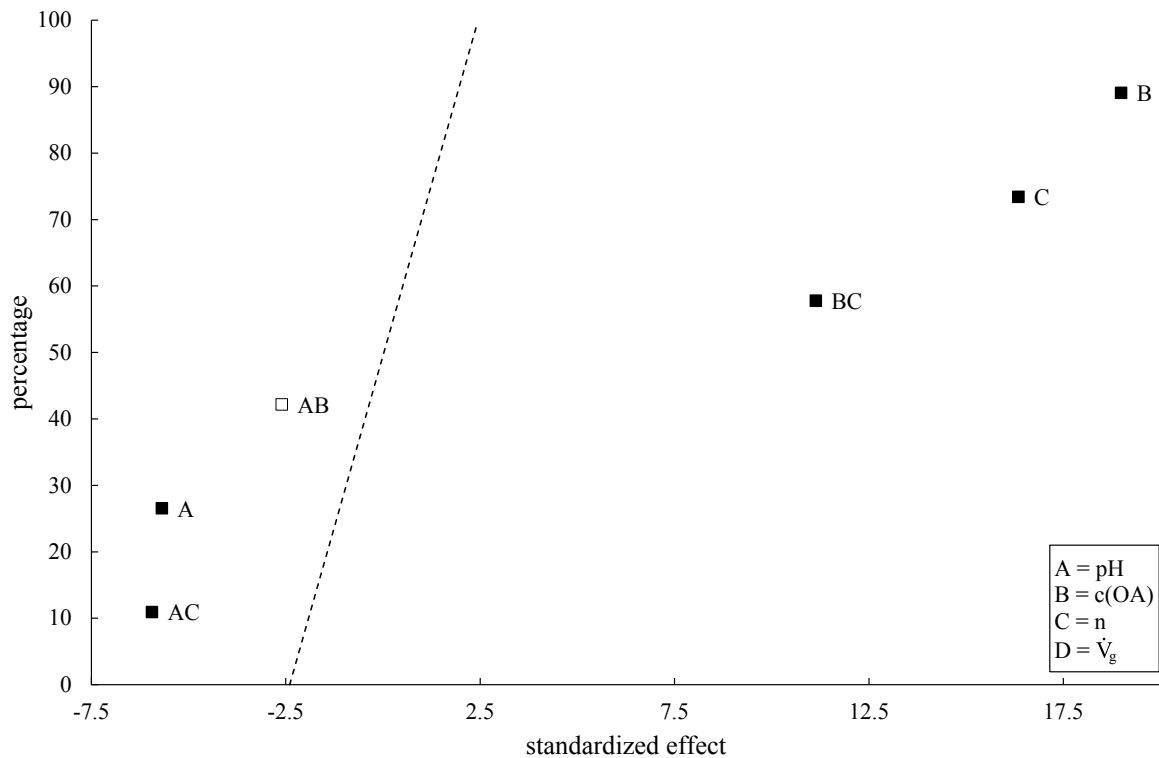


**Fig. 6-4.** Normal plot of the standardized effects for the maximum recovery  $R_{\max}$  at a significance level  $\alpha$  of 99 %. Dashed line shows reference value at which effects become positive. Hollow symbols indicate insignificant effects.

For this purpose, the normal plot of the standardized effects for  $R_{\max}$  as presented in Fig. 6-4 is analysed. Significant effects on the left-hand side of the dashed line in Fig. 6-4 have a negative effect on  $R_{\max}$ , while significant effects on the right-hand side have a positive effect on  $R_{\max}$ . The previously determined three largest effects B, C, and BC all show a positive effect. Thus, an increase in  $c(\text{OA})$  and  $n$  will result in a higher maximum recovery. On the other hand, an increase in pH will result in a decrease of  $R_{\max}$ , because the two-factor interaction effect pH· $n$  has a negative effect on  $R_{\max}$ . The contour plot of this two-factor interaction effect in Fig. 6-5b helps to understand this effect in detail. At a constant pH value  $R_{\max}$  increases with increasing stirrer speed. This effect is more pronounced at a lower pH value than at a higher pH value. Inversely,  $R_{\max}$  decreases with increasing pH value at a constant stirrer speed. At a low stirrer speed, this effect is negligible, while a sharp decrease in  $R_{\max}$  is present at a high stirrer speed.

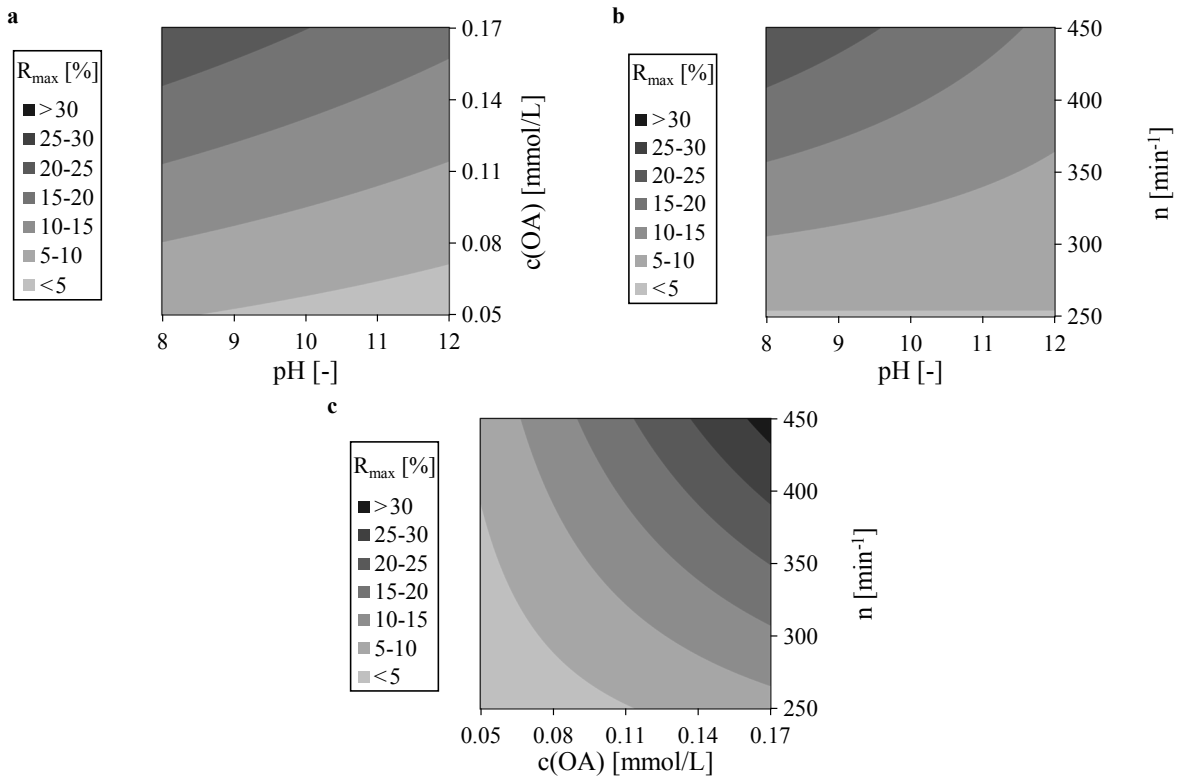


**Fig. 6-5.** Contour plots for maximum recovery  $R_{\max}$  based on the DoE results: interaction of pH value and oleic acid concentration  $c(\text{OA})$  at a constant stirrer speed  $n$  of  $350 \text{ min}^{-1}$  (a), interaction of pH value and  $n$  at a constant  $c(\text{OA})$  of  $0.109 \text{ mmol/L}$  (b), and interaction of  $c(\text{OA})$  and stirrer speed at a constant pH value of 10 (c).

The contour plot of the two-factor interaction effect  $\text{pH} \cdot c(\text{OA})$ , which is shown in Fig. 6-5a, shows as Fig. 6-5b larger values for  $R_{\max}$  at a low pH value of 8. Furthermore,  $R_{\max}$  increases at a constant pH value, if the oleic acid concentration increases. Fig. 6-5c shows the contour plot of the two-factor interaction effect  $c(\text{OA}) \cdot n$ . Both a high concentration of oleic acid as well as a high stirrer speed are preferable for a high maximum recovery. These results are in consensus with the discussion of  $k \cdot R_{\max}$  presented in Fig. 6-2.

The statistical analysis of the flotation rate constant and the calcium fluoride content in the concentrate are carried out analogously to the statistical analysis of the maximum recovery  $R_{\max}$  as presented above. Therefore, only the contour plots will be presented here. All other resulting plots can be found in the Appendix.

As shown in chapter 6.1.2.1, the flotation process of fluorite generally follows first-order kinetics in the investigated parameter range. The statistical discussion of  $k$  is therefore carried out for the determined values using the 1<sup>st</sup> order chemical analogous model (cf. chapter 6.1.2.1). The analysis of the standardized effects in form of a Pareto chart shows that only the two-factor interaction effect  $c(\text{OA}) \cdot n$  is statistically significant. According to the normal plot of the standardized effects this effect is positive. Thus,  $k$  increases with increasing oleic acid concentration as well as increasing stirrer speed.

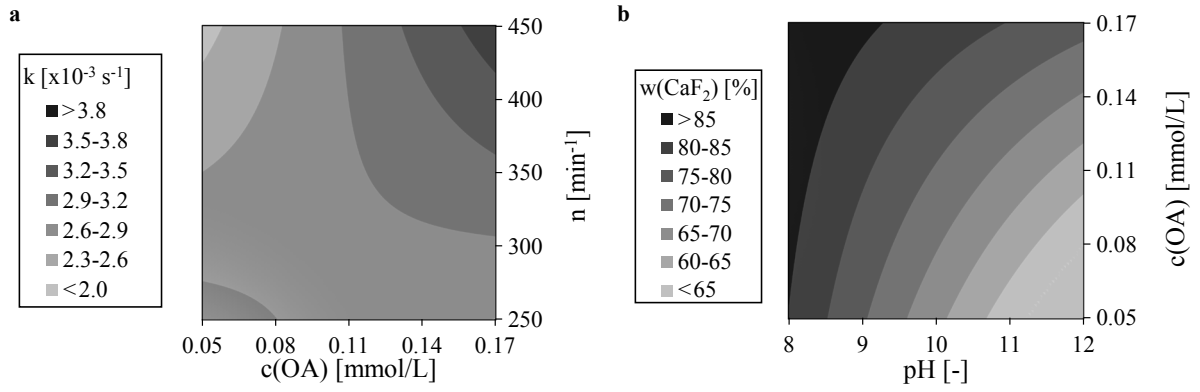


**Fig. 6-6.** Contour plot for 1<sup>st</sup> order flotation rate constant  $k$  (a) and calcium fluoride purity  $w(\text{CaF}_2)$  in the concentrate (b) based on the DoE results: interaction of oleic acid concentration  $c(\text{OA})$  and stirrer speed  $n$  (a) and interaction of pH value and  $c(\text{OA})$  (b).

A detailed insight is provided by the contour plot of  $c(\text{OA}) \cdot n$ , which is presented in Fig. 6-6a. For the investigated parameter range,  $k$  is maximised at a high oleic acid concentration in combination with a high stirrer speed.

From the Pareto chart of the standardized effects for  $w(\text{CaF}_2)$  it is found that pH value, oleic acid concentration, and the two-factor interaction effect  $\text{pH} \cdot c(\text{OA})$  are statistically significant. The amount of influence on  $w(\text{CaF}_2)$  decreases according to  $\text{pH} > c(\text{OA}) > \text{pH} \cdot c(\text{OA})$ . The influence of  $c(\text{OA})$  and the two-factor interaction effect on  $w(\text{CaF}_2)$  are positive, while an increase of pH results in a decrease of  $w(\text{CaF}_2)$ . The contour plot of  $\text{pH} \cdot c(\text{OA})$  is presented in Fig. 6-6b. At a constant pH value, an increase of  $c(\text{OA})$  results in an increase of the calcium fluoride content in the concentrate. Inversely, an increase of the pH value at a constant oleic acid concentration results in a decrease of  $w(\text{CaF}_2)$ .

A summary of the obtained results from the statistical analysis is given in Tab. 6-4. The table provides an overview of the factor levels, which have been determined as optimum in order to maximise the flotation responses  $R_{\max}$ ,  $k$ , and  $w(\text{CaF}_2)$ .

**Tab. 6-4.** Factor levels for maximisation of the recovery  $R_{\max}$ , first-order flotation rate constant  $k$ , and calcium fluoride content  $w(\text{CaF}_2)$  in the concentrate as well as the parameter product  $R_{\max} \cdot w(\text{CaF}_2)$ .

Parameter	Factor level for maximisation of			
	$R_{\max}$	$k$	$w(\text{CaF}_2)$	$R_{\max} \cdot w(\text{CaF}_2)$
pH	↓	arbitrary	↓	↓
$c(\text{OA})$	↑	↑	↑	↑
$n$	↑	↑	arbitrary	↑
$\dot{V}_g$	arbitrary	arbitrary	arbitrary	arbitrary

The presented statistical analysis shows that the volumetric gas flow rate has no significant effect on all three flotation responses in the investigated parameter range. Therefore, its factor level for maximisation of  $R_{\max}$ ,  $k$ , and  $w(\text{CaF}_2)$  in the investigated experiments is arbitrary.

The maximum recovery is influenced by all remaining three parameters, namely pH value, oleic acid concentration, and stirrer speed. In order to maximise  $R_{\max}$ , the pH value should be low, while  $c(\text{OA})$  and  $n$  should be high (cf. Fig. 6-5). The first-order flotation rate constant  $k$  is only significantly affected by the oleic acid concentration and the stirrer speed. Both of these factors should be high in order to maximise  $k$ . The calcium fluoride content in the concentrate is only dependent on the pH value and  $c(\text{OA})$ . To increase the grade of  $\text{CaF}_2$  in the concentrate, the pH value should be low, while the concentration of oleic acid should be high. For industrial flotation plants, the flotation variables  $R_{\max}$  and  $w(\text{CaF}_2)$  are of great economic importance, because both a high recovery as well as a high product purity is desired. The statistical analysis of  $R_{\max} \cdot w(\text{CaF}_2)$  shows in accordance with the previously presented results that the influence of  $\dot{V}_g$  is insignificant, while  $c(\text{OA})$  and  $n$  should be high and the pH value should be low.

In conclusion, the flotation process of fluorite is found to be most efficient at a low pH value, a high concentration of oleic acid and a high stirrer speed in the investigated parameter range. To discuss the reasons for these identified factor levels, further experimental data is analysed and the obtained parameters are compared to literature.

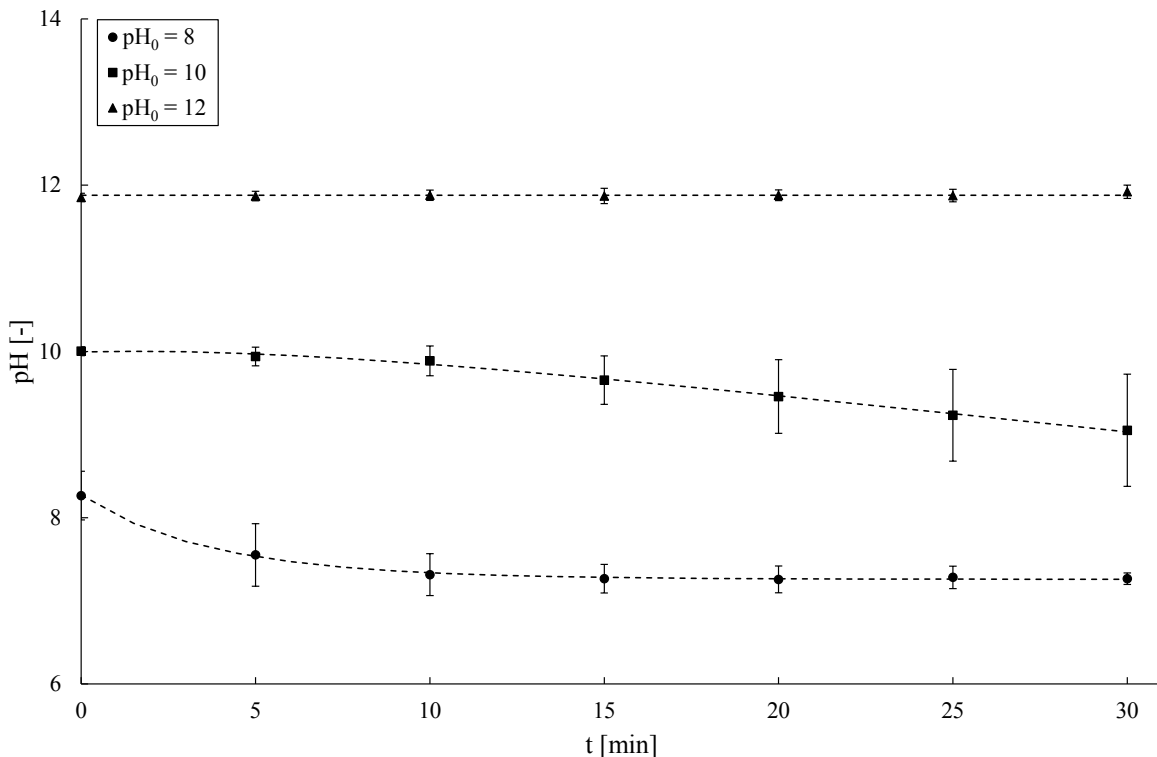


**Fig. 6-7.** Observed pH as a function of experimental time for the three different initial  $\text{pH}_0$  values (dashed lines indicate trends).

The pH value of the flotation pulp in the present experiments is monitored over time using an immersed pH-electrode (see chapter 6.1.1). The mean trends of the pH value for the three different initial  $\text{pH}_0$  values are shown in Fig. 6-7. For an initial pH value  $\text{pH}_0=8$  the pH value decreases in the beginning sharply until a threshold is reached at about 15 min with  $\text{pH}=7$ . At the highest investigated initial pH value of  $\text{pH}_0=12$ , no change is observed over time so that the pH value remains constant throughout the experimental time. Likewise, no change is observed for  $\text{pH}_0=10$  up to  $t \approx 10$  min. At  $t > 10$  min, the pH value decreases to a final value of  $\text{pH}=9$  after 30 min.

The pH value in the experiments is adjusted to the specified  $\text{pH}_0$  using a 1N sodium hydroxide solution (see chapter 6.1.1). The initial pH value is measured after oleic acid and starch are added to the deionized water but before addition of the solid particles. The reduction in pH for  $\text{pH}_0=8$  and  $\text{pH}_0=10$  may therefore be attributed to reactions of the metallic ions from the solid particles with the hydroxide ions. Furthermore, the surface charge of gas bubbles is generally negative due to an increased adsorption of hydroxide ions on the bubble surface ([78], p. 248; [244,279]). During the flotation experiments, particles are floated to the surface of the apparatus under formation of heterocoagulates with the bubbles. A three-phase froth consisting of floated particles, air bubbles with adsorbed hydroxide ions ( $\text{OH}^-$ ), and liquid between the lamella is produced at the surface of the flotation cell, which is skimmed manually (see chapter 6.1.1). Thus, the concentration of  $\text{OH}^-$  ions in the flotation cell will decrease with time, resulting in a decreasing pH value. Compared to a  $\text{pH}_0$  of 8, the initial concentration of  $\text{OH}^-$  ions at  $\text{pH}_0=12$  is larger by a factor of  $10^4$ . To see a change in pH value at this concentration, more hydroxide ions would have to be discharged as at  $\text{pH}_0=8$ . The experimental results in Tab. 6-3 show that the maximum recovery is always worse at  $\text{pH}=12$  compared to  $\text{pH}=8$ . Therefore, less  $\text{OH}^-$  are removed from the flotation cell so that no decrease in pH value is observed. A statistical discussion of the trend of  $\text{pH}_0=10$  is infeasible due to the overlapping error bars.

The results of the conducted film flotation experiments of high-purity grade calcium fluoride particles in solutions containing the minimum and maximum oleic acid concentrations, which have been investigated in the DoE (cf. chapter 6.1.1), are presented in Fig. 6-8. Calcium fluoride particles without conditioning in aqueous oleic acid solution showed a hydrophilic character, as no particles were floating on pure deionized water. In contrast to this, particles conditioned in the two aqueous oleic acid solutions were nearly completely floating in deionized water.

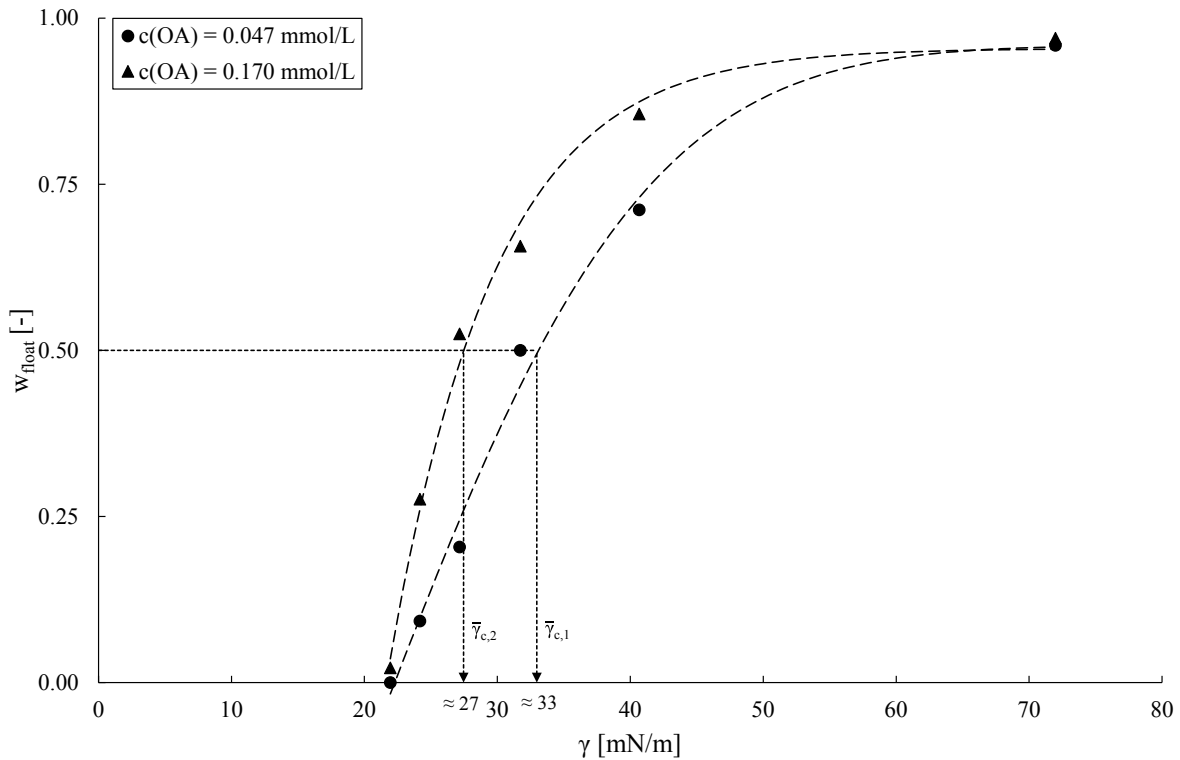


**Fig. 6-8.** Resulting film flotation curves for high-purity grade calcium fluoride particles conditioned in solutions containing the minimum and maximum oleic acid concentrations, which have been investigated in the DoE, at a pH value of 8.

Thus, the calcium fluoride particles become more hydrophobic due to the adsorption of oleic acid on the particle surface. The determined critical surface tension of wettability  $\bar{\gamma}_c$  for  $\text{CaF}_2$  particles conditioned in oleic acid solutions decreases with increasing  $c(\text{OA})$ . At the minimum oleic acid concentration of 0.047 mmol/L,  $\bar{\gamma}_c \approx 33$  mN/m and at  $c(\text{OA})=0.170$  mmol/L the critical surface tension of wettability is approx. 27 mN/m. Thus,  $\bar{\gamma}_c$  decreases by approximately 19 % with an increase of the oleic acid by a factor of 3.6. Additionally, the heterogeneity of  $\bar{\gamma}_c$  decreases with increasing  $c(\text{OA})$ . The minimum concentration of 0.047 mmol/L shows a broader distribution than the maximum concentration, which shows a steeper increase of the floated particle fraction  $w_{\text{float}}$  between  $\gamma=22-40$  mN/m.

The influence of pH value and oleic acid concentration on the performance of the fluorite flotation process is discussed elaborately in literature. For example, Zhao et al. investigated the influence of the pH value of the flotation pulp on the fluorite recovery [280]. They stated an optimum pH value for a maximum recovery of calcium fluoride in the concentrate in the range of 9.5-10.0, although their presented recovery at pH=8 is similar to the ones obtained at pH=9 to 10 (cf. Fig. 6-9).

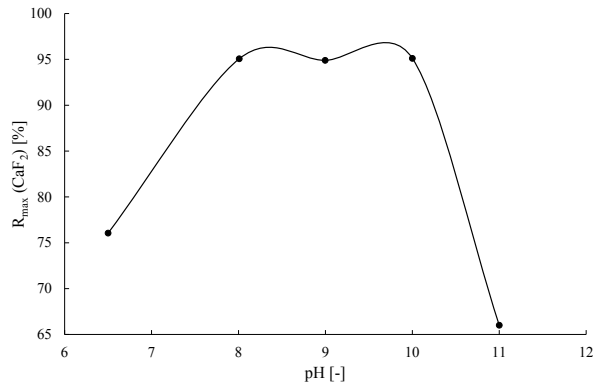


**Fig. 6-9.** Relationship between recovery of fluorite  $R_{\max}(\text{CaF}_2)$  and pH value (adopted from [280]).

Zhang et al. investigated the influence of the oleic acid concentration and pH value on fluorite recovery in presence of quartz [281]. They found that with increasing pH value the recovery of fluorite decreased steadily, with a sharp drop at pH=11 (see Fig. 6-10a). A similar drop of the fluorite recovery at a pH value of 11 was observed by Zheng et al. [282]. The flotation recovery of quartz was very low compared to fluorite, but increased slightly with increasing pH value. The optimum pH value for maximum recovery of fluorite in their experiments is between 7 and 8. Up to a sodium oleate concentration of approx.  $5 \cdot 10^{-5}$  mol/L the fluorite recovery increased continuously with increasing sodium oleate concentration  $c(\text{NaOl})$ . Afterwards, the recovery remained constant so that further addition of NaOl did not improve the recovery (see Fig. 6-10b). Quartz was nearly unaffected by the concentration of NaOl, as its recovery was again low compared to fluorite. However, a small increase is present at concentrations of  $c(\text{NaOl}) > 4.5 \cdot 10^{-5}$  mol/L.

A pH range of 8 to 9 for maximum fluorite recovery was also identified by Zheng et al. [282], Pugh [283], Pugh and Stenius [284], and Schubert et al. [285].

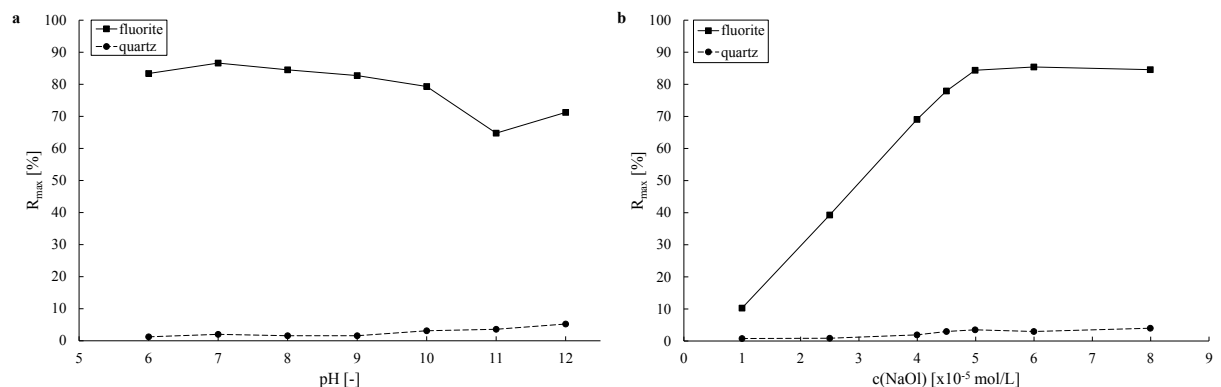


**Fig. 6-10.** Dependency of fluorite and quartz recovery  $R_{\max}$  on pH value (a) and concentration of sodium oleate  $c(\text{NaOl})$  (b) (adapted from [281]).

The optimum pH value for fluorite recovery corresponds well to the surface tension behaviour of aqueous NaOl solutions. The surface tension of the aqueous sodium oleate solution exhibits a minimum of approx. 40 mN/m at pH=8-9 [283,284,286,287]. At higher pH values, the surface tension increases with a maximum at pH=11. A low surface tension relates to a high surfactant adsorption at the gas-liquid interface (cf. chapter 2.2.2.1). The bubble-particle attachment probability and the stability of formed heterocoagulates are thereby increased, leading to higher recoveries.

In addition to the influence on the surface tension, the sodium oleate concentration has also a significant impact on the Zeta potential [281,283,288]. Some exemplary Zeta potential measurements by Chen et al. [289] are shown in Fig. 6-11. The isoelectric points (IEP) for barite and fluorite were determined to be 9.5 and 4.5, respectively. Barite has therefore in the investigated pH range of 8-12 always a negative surface charge. Fluorite on the other hand shows a positive surface charge at pH=8 and negative surface charges only for pH>9.5. Qualitatively similar trends and same values for the IEPs were stated by other authors [79,281,282,288,290,291]. Chen et al. also investigated the effect of NaOl on the Zeta potential of fluorite and barite, which is included in the graphs in Fig. 6-11.

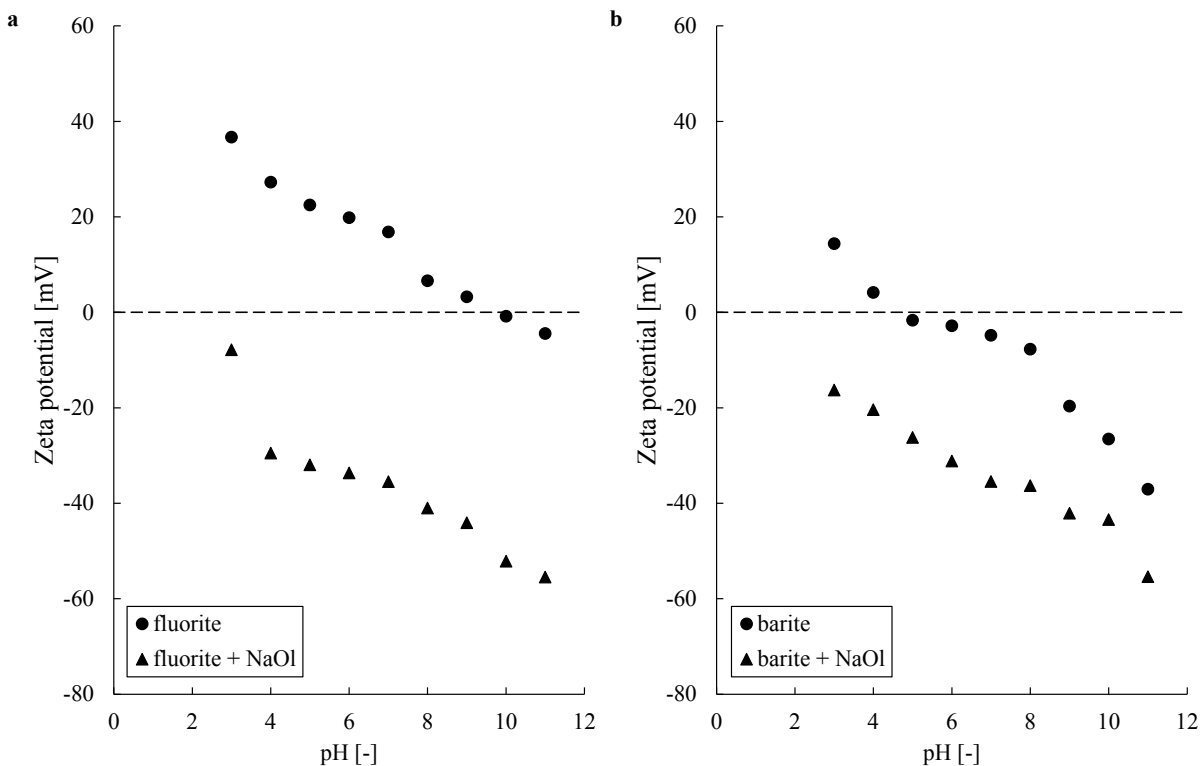


**Fig. 6-11.** Zeta potential of fluorite (a) and barite (b) in absence and presence of sodium oleate (NaOl) at a concentration of  $13 \cdot 10^{-2}$  mmol/L (adopted from [289]).

Addition of sodium oleate shifts the curves down along the y axis towards more negative surface charges. Sreedevi et al. showed that the Zeta potential decreases with increasing pH value as well as increasing sodium oleate concentration. Furthermore, the IEP shifts towards lower pH values with increasing  $c(\text{NaOl})$  [288]. This negative surface charge is attributed to adsorbed oleate species, which is interacting with the positively charged  $\text{Ca}^{2+}$  and  $\text{Ba}^{2+}$  ions, respectively, on the mineral surfaces. Thus, a more negatively charged surface corresponds to a higher adsorption density of oleate species on the mineral surfaces.

The depicted Zeta potential trends underline in addition to the aforementioned effect of the decrease of surface tension that the recovery as well as the grade of fluorite is higher at low pH values. As described in chapter 2.1.4.2, sodium oleate is not entirely selective towards fluorite in the presence of barite due to a concurrent physical co-adsorption on  $\text{CaF}_2$  and  $\text{BaSO}_4$  [82]. The oleate ion is negatively charged and therefore attracted towards positive surface charges. As fluorite exhibits a positive surface charge at  $\text{pH}=8$ , while the barite surface is already negatively charged, the adsorption of oleate is selective towards fluorite, thus resulting in a higher  $R_{\text{max}}$  and a higher  $w(\text{CaF}_2)$  in the concentrate (cf. Tab. 6-3). At  $\text{pH}=12$ , both mineral surfaces are negatively charged so that repulsive forces are dominant. Therefore, the flotation is 1) less effective due to less adsorbed oleate on the mineral surface; 2) less selective as both mineral surfaces exhibit a negative surface with repulsive forces.

The obtained results from the DoE in Tab. 6-3 show that the calcium fluoride content in the concentrate is lower than 80 % at  $\text{pH}=12$  for all experimental points, but between 75 and 91 % at  $\text{pH}=8$ . As stated in chapter 2.1.4.2 fluorite products are classified depending on their calcium fluoride content as acid grade, metallurgical grade, and ceramic grade. The minimum calcium fluoride content for metallurgical grade and ceramic grade is 80 %, while a content of at least 97 % is required for acid grade fluorite. The obtained concentrates at  $\text{pH}=12$  are therefore not classifiable, while the products at  $\text{pH}=8$  are in the range of metallurgical grade and ceramic grade. As the  $\text{SiO}_2$  content could not be measured with the present analysis procedure, a differentiation between these two categories cannot be made. The obtained fluorite grade in the present study at  $\text{pH}=8$  corresponds well to the results from Zhao et al. [280] as well as Zhang et al. [281]. Chen et al. found that addition of starch decreased the recovery of barite significantly, while simultaneously a small decrease in the fluorite recovery was observed [289]. As the starch concentration was kept constant throughout all experiments, this influence is present in all measurements.

To summarize, a detailed understanding of the identified factor levels for optimal performance of the fluorite flotation process could be provided by analysing additional surface phenomena. An excellent correlation between the presented results and literature was found.

### 6.1.2.3 Optical investigations

Shadowgraphy (SH) measurements are conducted to analyse the influence of pH value, oleic acid concentration  $c(\text{OA})$ , stirrer speed  $n$ , and volumetric gas flow rate  $\dot{V}_g$  on the bubble size distribution. For this purpose, an isokinetic bubble sampler similar to the one presented in chapter 2.3.3.1 is designed from transparent PMMA. An image of the experimental setup is provided in the Appendix. In order to evaluate the influence of each of the aforementioned four process parameters separately, only one of the parameters is changed at a time. Comparison with a reference case, which is setup at  $\text{pH}=8$ ,  $c(\text{OA})=0.047$  mmol/L,  $n=250$  min<sup>-1</sup>, and  $\dot{V}_g=2$  L/min, provides then an information of the influence of the changed parameter on the bubble size distribution.

The resulting bubble size distributions in form of frequency distributions  $q_0$  are shown in Fig. 6-12. For each experimental condition approx. 100 bubbles have been manually analysed. The reference case (white bars) shows a very broad bubble size distribution with a maximum bubble diameter at  $d_B=2$  to 3 mm.

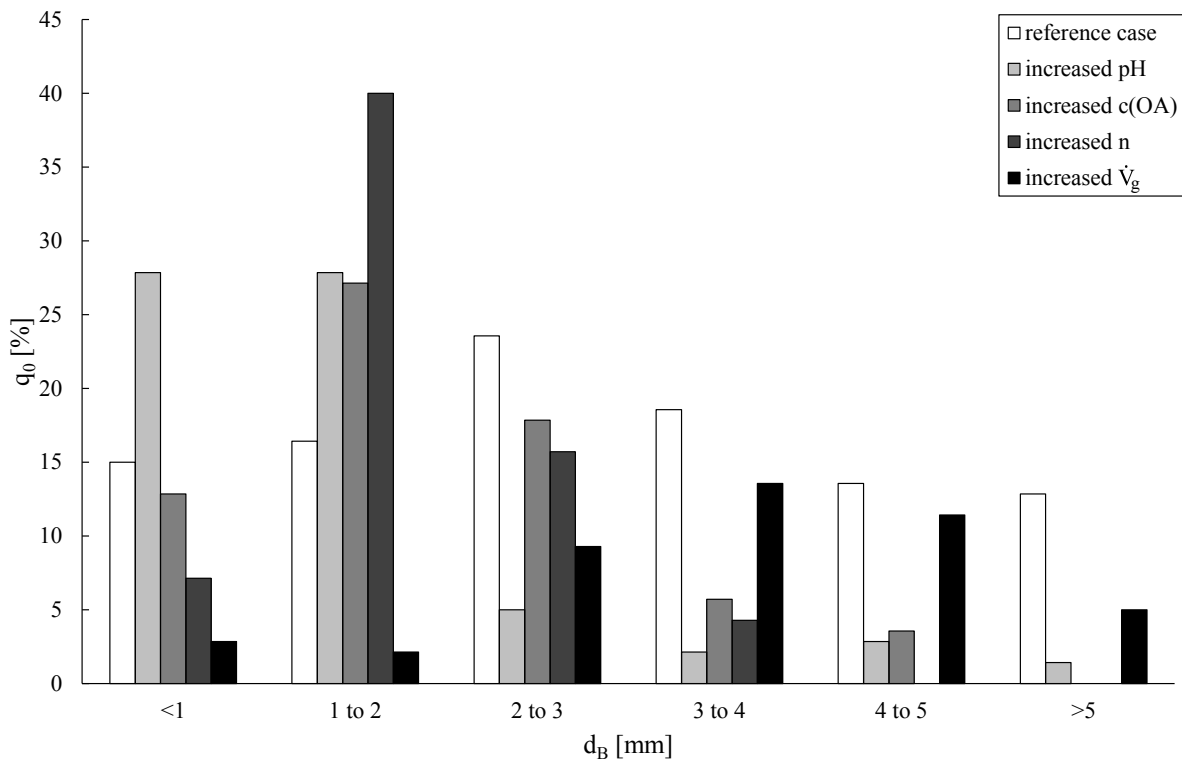


**Fig. 6-12.** Influence of investigated experimental parameters on frequency distribution  $q_0$  of bubble diameters obtained via Shadowgraphy: reference case with  $\text{pH}=8$ ,  $c(\text{OA})=0.047$  mmol/L,  $n=250$  min<sup>-1</sup>, and  $\dot{V}_g=2$  L/min (white bars), change of pH value to 12 (light-grey bars), increasing oleic acid concentration to 0.17 mmol/L (grey bars), adjusting stirrer speed to 450 min<sup>-1</sup> (dark-grey bars), and changing volumetric gas flow rate to 5 L/min (black bars).

**Tab. 6-5.** Mean bubble diameter  $\overline{d_B}$  and mean elongation  $\overline{f_e}$  for different experimental conditions.

Case	$\overline{d_B}$ [mm]	$\overline{f_e}$ [-]
Reference case	2.95	0.31
Increased pH	1.31	0.21
Increased c(OA)	2.02	0.15
Increased n	1.74	0.13
Increased $\dot{V}_g$	3.47	0.28

An increase of the pH value from 8 to 12, while keeping all other parameters constant, shows a significant shift of the bubble size distribution towards smaller bubble diameters, where approx. 60 % of the bubbles have a bubble diameter of 1 to 2 mm (light-grey bars). The bubble size distributions for a higher concentration of oleic acid (grey bars) and a higher stirrer speed (dark-grey bars) show also a narrower distribution compared to the reference case with a maximum around 2 mm. Increasing the volumetric gas flow rate shows an increase in the mean bubble diameter, with a maximum at about 4 mm (black bars). This increase in  $d_B$  is expected.

The mean bubble diameter  $\overline{d_B}$  and the mean elongation  $\overline{f_e}$  for the different experimental conditions are presented in Tab. 6-5. The mean elongations show that bubbles assume a nearly spherical form for the experiments conducted at an increased oleic acid concentration as well as an increased stirrer speed. In contrast to this, bubbles are more ellipsoidal at the reference case and after increasing  $\dot{V}_g$ .

To increase the pH value in the experiments, a sodium hydroxide solution is added to the flotation pulp (see chapter 6.1.1). Craig et al. investigated the influence of various electrolytes on bubbles [292–294]. They found that some electrolytes prevented bubble coalescence, thus resulting in smaller bubble diameters. Sodium hydroxide was found to be one of these electrolytes preventing coalescence. Likewise, oleic acid shows besides its collecting properties also frothing properties (cf. chapter 2.1.2.2). Oleic acid molecules can adsorb on the bubble surface leading to bubble retardation, meaning the bubble surface is immobilised (cf. chapter 2.3.2). The immobilisation leads to an increased stability of the bubbles, which prevents bubble coalescence. Therefore, the obtained narrower bubble size distributions with smaller mean bubble diameters  $\overline{d_B}$  are to be expected (cf. Fig. 6-12 and Tab. 6-5). An increase of n increases the shear force inside the flotation pulp leading to bubble break-up. As stated above, both sodium hydroxide as well as oleic acid prevent bubble coalescence. Therefore, the comminuted bubbles are conserved due to adsorption of these species on the bubble surface, leading to smaller bubble diameters.

The volumetric gas flow rate is linked to the stirrer speed via the dimensionless air flow number (cf. Tab. 2-2). If the stirrer speed is constant and the gas flow rate increases,  $Q$  will increase likewise. The distribution of the bubbles in the flotation cell will become less homogeneous. Further increasing of  $\dot{V}_g$  will finally result in the so-called “flooding” of the stirrer. At this point, the bubbles are only found along the stirrer shaft ([295], p. 261ff.). Thus, with increasing gas flow rate, while the stirrer speed remains constant, bubbles will be less and more inhomogeneously comminuted, resulting in a broader bubble size distribution with a larger mean bubble diameter. The results presented in Fig. 6-12 and Tab. 6-5 are therefore conclusive. Generally, smaller bubbles increase the rate of flotation [296]. The results in Tab. 6-5 show therefore that an enhancement of pH value, stirrer speed, and oleic acid concentration should increase the rate of flotation. However, only oleic acid concentration and stirrer speed have been identified as significant parameters for the first-order flotation rate constant in the statistical analysis of the flotation responses (cf. Fig. 6-6a). This may be related to the fact that the overall performance of the fluorite flotation is worse at higher pH values, resulting in a lower maximum recovery (cf. Tab. 6-3).

## 6.2 Fluorescent mineral

Some of the naturally occurring fluorite minerals are fluorescent under UV irradiation (cf. chapter 2.1.4.1). For optical investigations of the fluorite flotation process, this property could be useful to distinguish valuable fluorite mineral particles from gangue particles attached to bubbles. To evaluate the applicability of this idea, a feasibility study is carried out using a fluorescent fluorite mineral. The mineral exhibits at daylight a greenish colour, while a blue fluorescence is observed under UV irradiation. (cf. Fig. 2-9).

An aqueous suspension of these fluorite particles has been investigated via fluorescence spectroscopy. For this purpose, the signal intensity of the emission at 420 nm, which corresponds to the visually observed blue fluorescence of the particles (cf. Fig. 2-9b), has been investigated for an irradiation between 240 nm to 400 nm (see Appendix 9.1.4). An increased signal intensity is found between 350 nm and 390 nm. For the fluorescence investigations, a UV lamp with an irradiation wavelength of 365 nm is present. At this constant excitation, the highest emission intensity is found between 400 nm and 450 nm (cf. see Appendix 9.1.4). Therefore, a red-shift is present, which is typical for fluorescence emission ([297], p. 14). As stated in chapter 3.1.1.1, UV-permeable PMMA is used in the design of the single bubble flotation column. The transmission spectrum presented in Appendix 9.1.1 shows a transmission of approx. 90 % at the desired excitation wavelength of 365 nm. Thus, the apparatus is feasible for the fluorescence investigations.

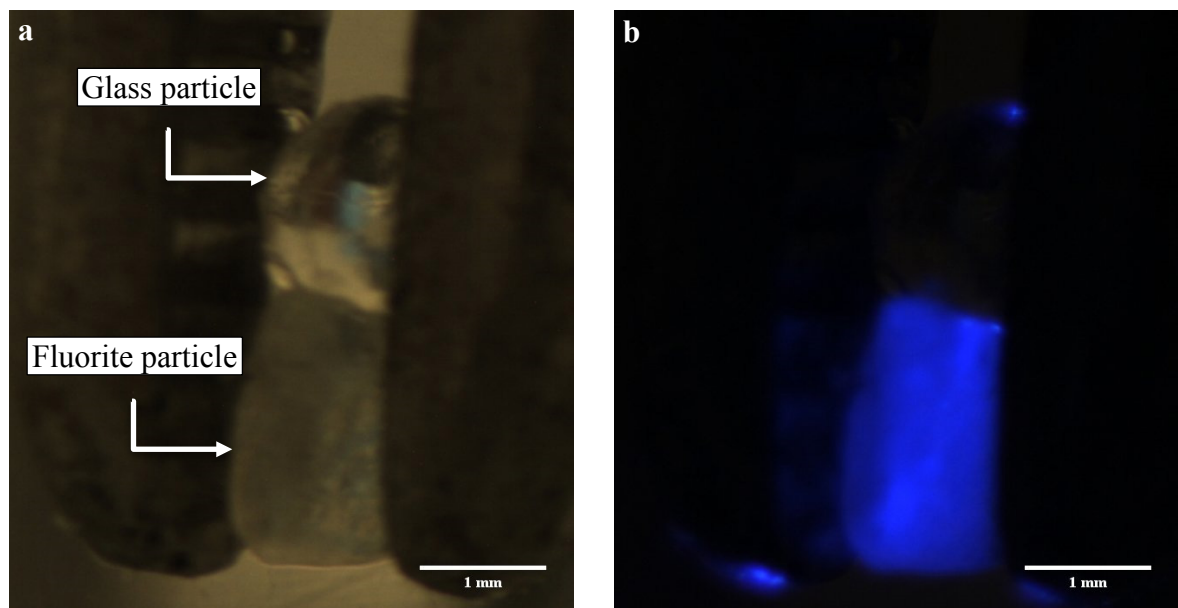


**Fig. 6-13.** Fluorescent fluorite mineral particle and glass particle both with a diameter of approx. 1.2 mm at daylight (a) and under UV irradiation at 365 nm (b). The particles are immersed in deionized water with tweezers.

In a preliminary investigation, the detection of a fluorescent fluorite mineral particle in the presence of a glass particle is tested. Larger specimens with diameters of approx. 1.2 mm are immersed with tweezers in the dispersion cell, which is filled with deionized water. The resulting images at daylight and under UV irradiation at a wavelength of 365 nm are presented in Fig. 6-13.

This test shows that minor reflections of the UV irradiation are present on the surface of the glass particle (cf. Fig. 6-13b, upper part). The fluorescence of the fluorite is, however, in case of large specimens distinguishable from this reflection so that a discrimination between fluorescent particles and reflections seems to be feasible. The RGB values of the fluorescence as well as the reflection are analysed using the histogram function in ImageJ for an area of  $16 \times 16 \text{ px}^2$ . The resulting graphs are presented in Fig. 6-14. In both graphs, the values for the R-channel (red), the G-channel (green), and the B-channel (blue) are shown. The values are typically ranging from 0 to 255. Thus, a distinction between 256 values for each colour channel is feasible [194]. The histogram of the fluorescence in Fig. 6-14a shows clear and distinguishable peaks for each of the three channels, with counts greater than 15. In contrast to this, the histogram of the reflection given in Fig. 6-14b shows broad distributions for all three colour channels.

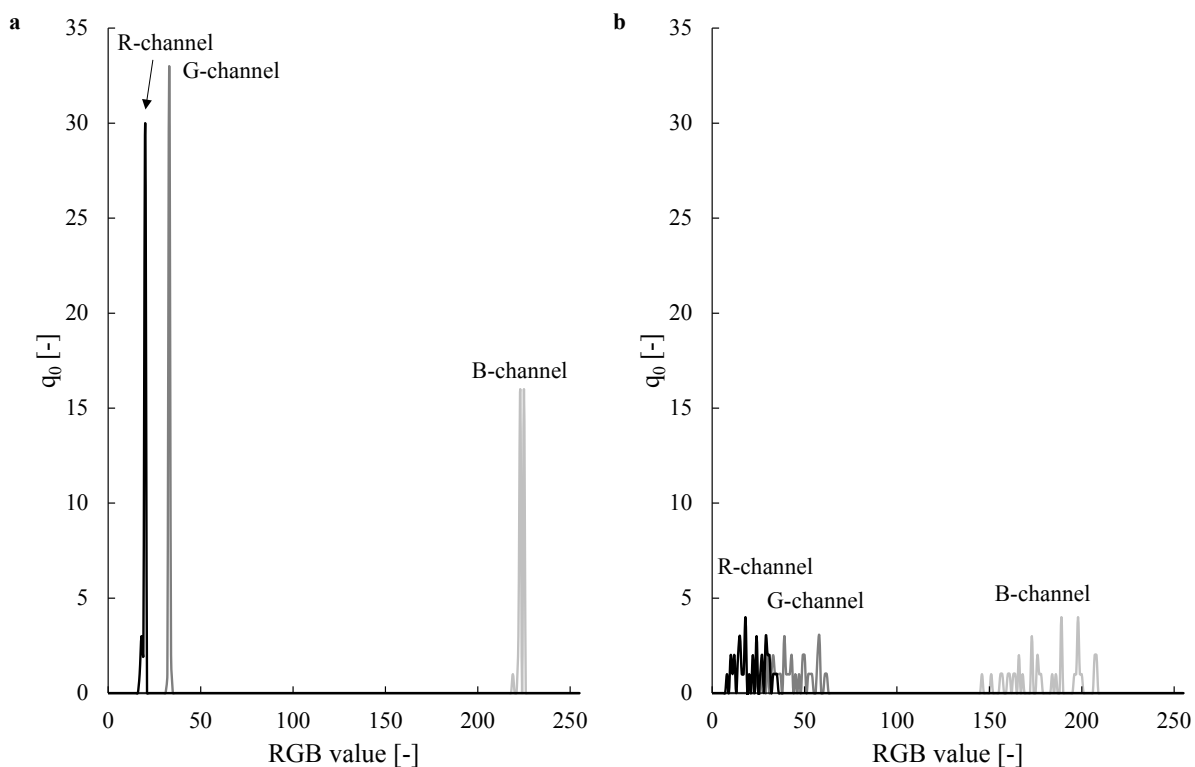


**Fig. 6-14.** RGB histogram for an area of  $16 \times 16 \text{ px}^2$  of the fluorescence of the fluorite particle (a) and of the reflection on the surface of the glass particle (b).

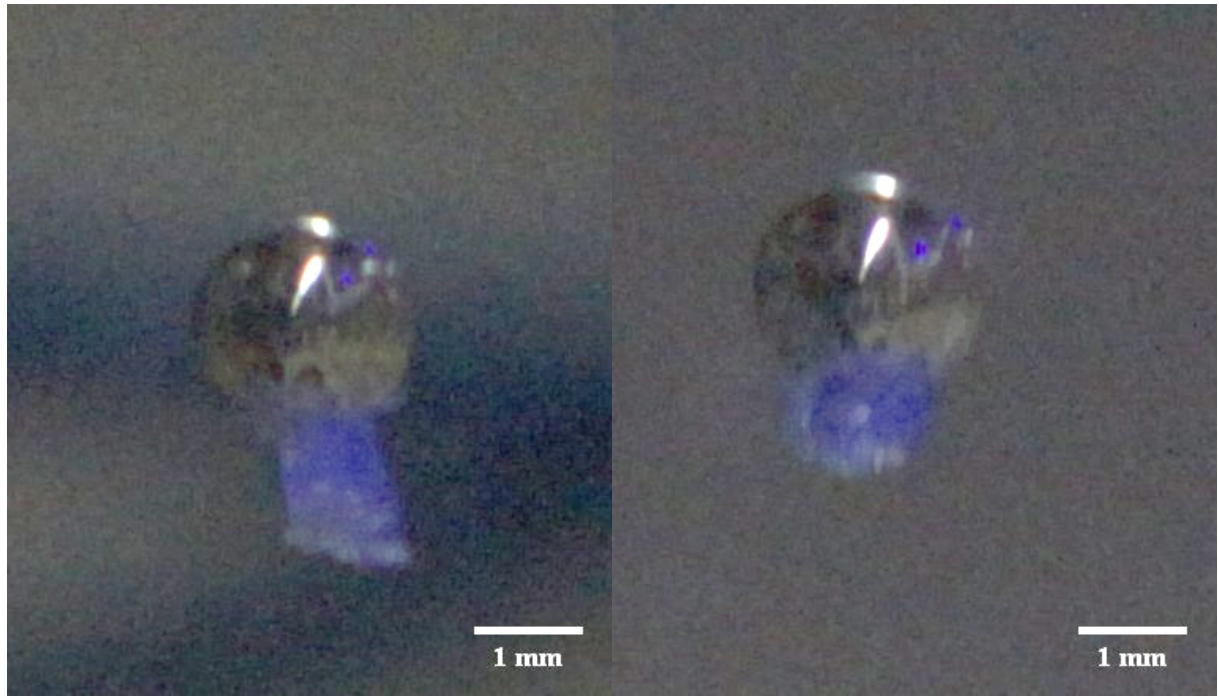


**Fig. 6-15.** Rising single bubble heterocoagulates with attached fluorescent fluorite mineral under UV irradiation at a wavelength of 365 nm. UV irradiation comes from the top right.

Additionally, the R-channel and G-channel show an overlap, thus making a distinction impossible. Furthermore, the signal counts are lower than 5 for each colour channel, resulting in a noisy spectrum instead of clear signals. Hence, the difference between actual fluorescence and reflection is also quantifiable by analysing the RGB values.

Next, flotation tests are conducted using the fluorescent fluorite mineral particles. For this purpose the particles are first comminuted using a rotary ball mill and then sieved to obtain different particle fractions. For the flotation experiments, particles of a fraction between 200  $\mu\text{m}$  and 315  $\mu\text{m}$  are used. The particles are introduced into the single bubble flotation column analogous to the description in chapter 5.3.1.1. Oleic acid is used as a collector at a concentration of 0.17 mmol/L at pH=8.

Two exemplary rising single bubble heterocoagulates with fluorescent fluorite mineral particles attached to the bubble surface are presented in Fig. 6-15. The fluorescence of the particles can clearly be seen, which shows the feasibility of the procedure. Again, some reflections of the UV irradiation can be seen on the bubble surface. The UV-LED is positioned on the same side as the camera. The irradiation comes from the top right. Therefore, the reflections on the bubble surface are expected. The colour and size of the reflection are, however, distinguishable from the actual fluorescence of the particles so that a distinction is possible.

## 7 Summary and outlook

In the present work, the advanced optical methods Particle Image Velocimetry (PIV) and Shadowgraphy (SH) have been applied to investigate complex multiphase flows at the example of the fluorite flotation process. Measurements have been conducted both in two-phase and three-phase systems. The aim has been to facilitate a deeper insight into the dominating mechanisms during the flotation process. To do so, optical investigations have been coupled with flotation experiments, where flotation kinetics, grades, and recoveries have been analysed. Thus, a relation between bubble-particle behaviour and flotation process performance has been found.

### 7.1 Main results from the two-phase system investigations

In the first step, the two-phase system consisting of rising single air bubbles in deionized water has been investigated. Shadowgraphy (SH) measurements have been conducted to investigate the bubble characteristics, like equivalent bubble diameter  $d_B$ , rising velocity  $w_B$ , and the morphology of the bubbles in form of the elongation  $f_e$ . To facilitate an automatic and time-resolved analysis of the obtained image sequences, an analysing procedure has been established and validated with high-precision grade solid glass spheres under dynamic (settling) conditions (cf. chapter 3.2.1). The procedure has then been used to analyse rising single air bubbles in deionized water produced by polyether ether ketone (PEEK) capillaries with varying diameters at various volumetric gas flow rates  $\dot{V}_g$  (cf. chapter 4.1.1). The bubble diameter ranges between 2 to 2.5 mm. The results show an excellent correlation to literature data for both bubble shape, which is in the wobbling/ellipsoidal regime, determined via the dimensionless bubble Reynolds number  $Re_B$ , Eötvös number  $Eo$ , and Morton number  $M$ , and data for rising velocities of single bubbles in pure water. Furthermore, the reproducibility of the bubbles at constant experimental conditions has been verified, as very low standard deviations of less than 5 % have been observed for the bubble characteristics between approx. 30-50 consecutive bubbles at constant experimental conditions. The high reproducibility of the bubbles allows the deduction of trends. The volumetric gas flow rate has been found to have a strong influence on the induced liquid velocity field observed via Particle Image Velocimetry (PIV) measurements. With increasing  $\dot{V}_g$  the mean liquid velocity  $\bar{w}$  in the measurement area increases. In the investigated range from 0.1 mL/min to 2 mL/min an increase by a factor of about five in  $\bar{w}$  and by a factor of approx. four in the proportionality constant to the turbulent kinetic energy  $k_{TKE}$ , which is a qualitative indicator for the induced kinetic energy into the system, has been observed (cf. chapter 4.1.2). The vorticity plots have revealed the presence of a Kármán vortex street in the bubble wake

with separated counter-rotating vortices. This vortex pattern is pronounced at lower gas flow rates, while the vortex street is to some extent still recognizable at higher gas flow rates.

In accordance with literature, the addition of surface active agents to deionized water has been found to change the bubble characteristics significantly. Two different flotation surfactants, namely methyl isobutyl carbinol (MIBC), which is a common non-ionic frother in flotation processes, and hexadecylamine (HDA), which is a common ionic collector in the flotation process of quartz, have been investigated at various concentrations  $c$  (cf. chapter 4.2). Based on surface tension measurements, theoretical calculations for the adsorption efficiency at the gas-liquid interface have been carried out. The calculations show a considerably better adsorption of the ionic collector HDA compared to MIBC. This is also verified by optical investigations via SH. The bubble characteristics change already significantly at far smaller concentrations in case of HDA compared to MIBC. The adsorption behaviour could be related to the attraction forces between the slightly negatively charged bubble surface and the positively charged HDA molecules as well as the favourable steric orientation of HDA compared to MIBC. While the former is a linear molecule, the latter is branched. Thus, a more compact adsorption of HDA molecules at the gas-liquid interface leading to a higher packing density is feasible.

SH measurements have been performed to investigate the influence of surfactant concentration on the bubble characteristics. While the bubble diameter  $d_B$  decreased only by approx. 5-10 %, a steep decrease in both rising velocity  $w_B$  and elongation  $f_e$  by about 40 % and 80 %, respectively, has been observed. Furthermore, the surfactants decreased the amplitude of the zigzagging bubble motion in horizontal  $x$  direction with increasing  $c$ , which led to higher oscillation frequencies  $\omega$ . Although  $w_B$  decreased considerably with increasing  $c$ ,  $\bar{w}$  and  $k_{TKE}$  have been found to increase with increasing  $c$ . The increase of  $\omega$  has been found to be responsible for this contradictory behaviour. An additional analysis of the data via Proper Orthogonal Decomposition (POD) revealed the process of energy cascading, which is mainly present at points of bubble redirection. An increase in  $c$  results in an increase of  $\omega$  so that more bubble redirections occur. Consequently, both  $\bar{w}$  and  $k_{TKE}$  increase with increasing  $c$ .

## 7.2 Main results from the three-phase system investigations

For optical investigations in the three-phase systems, a simplified system consisting of single bubble-particle heterocoagulates has been chosen in order to allow an optical analysis with respect to different operational parameters. For this purpose, a single bubble flotation column made from transparent poly(methyl methacrylate) (PMMA) with full optical accessibility has been developed (cf. chapter 3.1.1.1). The apparatus facilitates optical measurements of single bubble-particle heterocoagulates via SH as well as of the induced liquid velocity by application

of PIV. Additionally, the apparatus is fully functioning as flotation column. Thus, flotation recoveries  $R_{\max}$  and kinetics in form of the order of flotation kinetics  $n$  and the flotation rate constant  $k$  can be determined, which allows the establishment of a relationship between optical investigations of the flotation process and flotation results.

Single bubble flotation experiments in a model system consisting of glass particles have been carried out in order to investigate the influence of different operational parameters on the flotation process (cf. chapter 5.3). These parameters are namely the median particle diameter  $d_{50,3^*}$ , the volumetric gas flow rate  $\dot{V}_g$ , the wettability of the particles  $\bar{\gamma}_c$ , the flotation medium and the initial particle concentration  $c_{p,0}$  in the flotation pulp. On the one hand,  $R_{\max}$  as well as  $n$  and  $k$  of the flotation kinetics have been investigated, while on the other hand optical measurements have been conducted using SH and PIV in order to link the visual impressions with the general flotation behaviour. The maximum recovery has been found to increase with increasing  $\dot{V}_g$  as well as increasing  $d_{50,3^*}$ . Furthermore,  $R_{\max}$  is low in deionized water with recoveries below 3 % compared to measurements in a flotation solution containing a collector-frother mixture. The wettability of the particles shows also a significant influence on the flotation performance. Hydrophilic particles showed lower  $R_{\max}$  and slower flotation kinetics compared to unmodified and hydrophobised particles. The optical investigation via SH showed that hydrophilic particles are highly mobile on the bubble surface. From a theoretical point of view, both attachment efficiency and stability of these particles on the bubble surface are low. Thus, attachment of these particles will be less probable and already small disturbances and impacts on the single bubble-particle heterocoagulate will result in a detachment of the particles, consequently resulting in lower values for  $k$  and  $R_{\max}$ . The initial particle concentration has been found to change the order of the flotation kinetics. At a lower concentration, a shift from 0<sup>th</sup> order towards 1<sup>st</sup> order has been observed. The magnitude of this shift depends, however, on the median particle diameter. A hydrodynamic characterization of the flow field around rising single-bubble heterocoagulates via PIV has shown an increased  $\bar{\omega}$  compared to measurements for unloaded bubbles in deionized water and surfactant solutions. As a reason for this, the increased oscillation frequency  $\omega$  of particle loaded bubbles in horizontal  $x$  direction has been attributed, similar to the influence of surfactants on the bubble motion (cf. chapter 7.1). The induced liquid velocity increases with increasing gas flow rate. A difference between the induced liquid velocity fields based on the median particle diameter in the heterocoagulates has, however, not been observed.

For the investigation of an industrial fluorite flotation system, a novel quantitative analysis method using Fourier Transform (FT) Raman spectroscopy has been developed. The method has been successfully cross-validated with X-ray fluorescence spectroscopy (XRF)

measurements using samples with varying calcium fluoride content. Only minor absolute differences of 5 % have been observed so that the novel method is robust and precise.

An industrial fluorite flotation system from the Clara Mine in Oberwolfach, Germany, provided by Sachtleben Bergbau GmbH, containing mainly barium sulphate and silica as gangue materials, has been investigated via a design of experiment (DoE). The influence of pH value, stirrer speed  $n$ , volumetric gas flow rate  $\dot{V}_g$ , and the concentration of oleic acid  $c(\text{OA})$ , which is used as collector, on the overall process has been statistically analysed. To quantify the influence, the maximum recovery  $R_{\max}$ , the flotation kinetics in form of the order of flotation kinetics  $n$  and the flotation rate constant  $k$ , as well as the concentrate grade with respect to the calcium fluoride weight fraction  $w(\text{CaF}_2)$  have been analysed. The flotation process generally follows 1<sup>st</sup> order kinetics. The gas flow rate has been found to have no statistically significant influence on all observed flotation parameters in the investigated range. To maximise  $R_{\max}$ , a slightly alkaline pH value, a high  $c(\text{OA})$  as well as a high  $n$  are favourable. This could be related to the increased hydrophobicity of the fluorite particles with increasing  $c(\text{OA})$  as well as the higher collision probability of particles with bubbles with increasing  $n$ . The optimum pH value relates excellently to the surface tension behaviour of aqueous sodium oleate solutions, which exhibits a minimum in the determined pH range. A low surface tension relates to a high surfactant adsorption, which increases attachment and stabilisation probability. To increase the rate of flotation, both collector concentration and stirrer speed should be high. This is again referred to an increased collision and attachment probability. The collector concentration should also be high, while the pH value should be only slightly alkaline, if  $w(\text{CaF}_2)$  in the concentrate is to be maximised. The influence of the pH value is attributed to the concurrent adsorption of oleic acid on fluorite and barite. Zeta potential measurements presented in literature show a similarly negative surface charge for adsorbed sodium oleate on fluorite and barite at a highly alkaline pH value. At a slightly alkaline pH value, the concurrent adsorption of sodium oleate is shifted in favour of adsorption on fluorite due to a positive surface charge at this pH value. Due to the attracting forces, the adsorption of negatively charged sodium oleate molecules is enhanced. In summary, a slightly alkaline pH value, a high collector concentration, and a high stirrer speed are favourable in order to optimise the flotation process of fluorite with respect to  $R_{\max}$ ,  $k$ , and  $w(\text{CaF}_2)$  in the investigated parameter range.

Lastly, a fluorescent fluorite mineral has been tested for the purpose of optical investigations. The idea has been to distinguish valuable fluorescent fluorite particles from non-fluorescent gangue particles. Distinguishing the fluorescent particles from gangue particles has been demonstrated under static conditions. Furthermore, first single bubble-particle heterocoagulates with attached fluorescent fluorite particles have been presented as proof of concept.

### 7.3 Outlook

Although the present work extended the insights into the micro processes of the flotation process, there is still a broad field for further investigations.

On the one hand, the analysis of flotation kinetics is a promising area for further experiments, because these play a major role in the development and optimisation of industrial processes. The current flotation tests have all been performed in batch-mode with manual skimming of the froth. In future investigations, fed-batch experiments, where the collector and frother concentrations are held constant over time, or continuous experiments should be performed in order to represent real industrial processes more accurately. Furthermore, the removal of the froth should be as far as possible automatised in order to reduce the influence of the experimenter. Additionally, the number of data points should be increased to facilitate a deeper insight into possibly present shifts in the order of flotation kinetics. This would require either higher solids concentrations or a smaller cell volume. Moreover, the design of experiments used in the present work could be extended by increasing the range of the already investigated parameters, e.g. to higher gas flow rates or higher solids concentrations, as well as by implementation of new parameters, which have been kept constant so far, e.g. the concentration of starch as depressant during the fluorite flotation.

On the microscale, the underlying main mechanisms for flotation, that is bubble-particle collision, attachment, and detachment/stabilisation, could be investigated using the optical measurement techniques SH and PIV. Furthermore, the analysis of rising single bubble-particle heterocoagulates should be extended to investigate the influence of different particle characteristics, e.g. particle size, wettability, and shape, on the induced liquid flow field. Mixtures of particles with differences in above mentioned particle characteristics could be simultaneously used in flotation tests. For this purpose, glass particles are most promising due to the possibility to specifically change the wettability of the particles via silanisation reactions. Using fully coloured glass particles with different colours for different particle characteristics would facilitate an easy optical distinction and analysis. To gain detailed information of the particle motion on the bubble surface as well as to be able to accurately determine the number of particles attached per bubble, multi-camera systems as presented in e.g. [298,299] should be used in future experiments. For this purpose, a new single bubble flotation column would have to be designed.

Such a possible design is presented schematically in Fig. 7-1. The proposed experimental design would enable simultaneous stereo SH and planar PIV measurements or vice versa stereo PIV and planar SH measurements, depending on the purpose of the experiments. The simultaneous investigation via SH and PIV is facilitated using light sources with different

wavelengths as well as using optical filters for the cameras. The depiction in Fig. 7-1 shows the experimental setup for stereo SH and planar PIV measurements. The LED backlight illuminations emit red light at a wavelength of approx.  $\lambda=625$  nm. The continuous wave laser, which has already been used in the present work, emits green light at  $\lambda=532$  nm. The SH cameras are directed towards the apparatus in an angle of  $135^\circ$  with the LEDs positioned on the opposite site, while the PIV camera is positioned perpendicularly to the laser. The PIV camera is equipped with a shortpass filter, which only allows a transmission below 600 nm and the SH cameras are equipped with longpass filters, which allow transmission for light with a wavelength  $\lambda \geq 625$  nm. Thus, the PIV camera does not see the red LED backlight illuminations, while the SH cameras do not see the green laser. In this experimental setup, the two optical methods SH and PIV can be carried out simultaneously without influencing each other.

Furthermore, if the cameras, the LEDs, and the laser would be installed on a movable sliding carriage, the measurements could be performed during the complete bubble ascent. This would enable dynamic investigations instead of static investigations at a fixed measurement window as presented in the present work, which could provide a deeper insight into changes of the bubble behaviour and the hydrodynamics including vortex shedding with time and height of the apparatus.

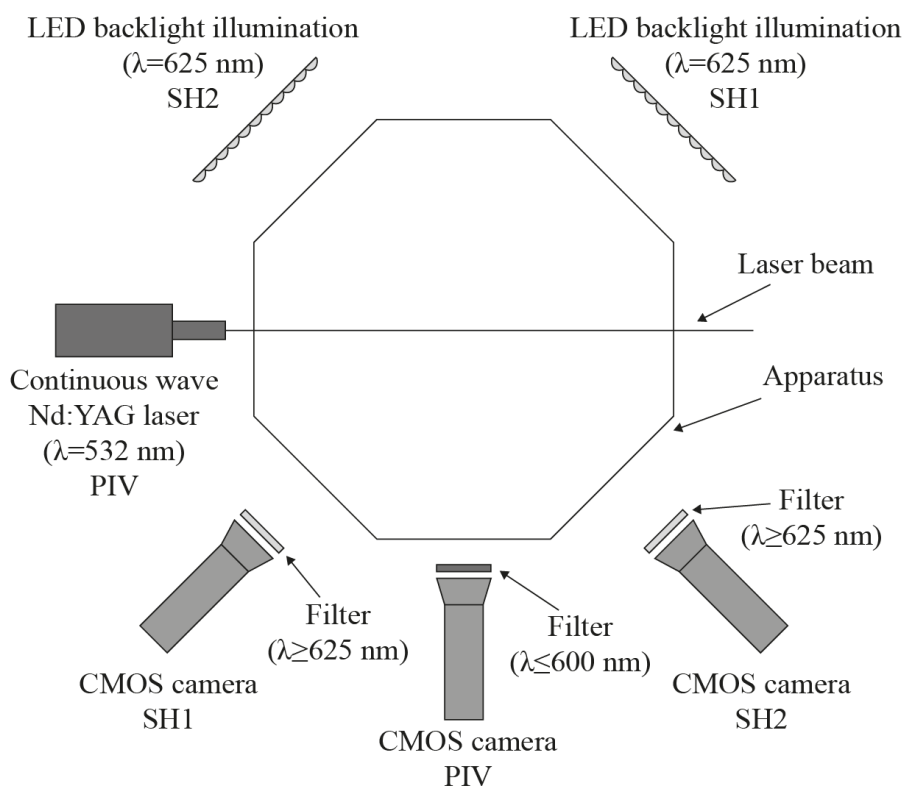


**Fig. 7-1.** Schematic proposal for an experimental setup facilitating simultaneous stereo Shadowgraphy (SH) and planar Particle Image Velocimetry (PIV) measurements. Setup is shown with view from the top.

## 8 References

- [1] J.N. Mohanty, S.K. Biswal, P.S.R. Reddy, V.N. Misra (Eds.), *Role of Chemical Engineering in Processing of Minerals and Materials*, 1st ed., Allied Publishers Pvt. Limited, New Delhi, 2003.
- [2] B.K. Parekh, J.D. Miller (Eds.), *Advances in Flotation Technology*, 1st ed., Society for Mining, Metallurgy and Exploration, Littleton, Colorado, 1999.
- [3] A. Nguyen, H.J. Schulze, *Colloidal Science of Flotation*, Chapman and Hall/CRC, Boca Raton, 2003.
- [4] D.W. Moolman, C. Aldrich, van Deventer, J. S. J., W.W. Stange, Digital image processing as a tool for on-line monitoring of froth in flotation plants, *Minerals Engineering* 7 (9) (1994) 1149–1164. [https://doi.org/10.1016/0892-6875\(94\)00058-1](https://doi.org/10.1016/0892-6875(94)00058-1).
- [5] European Commission, *Report on critical raw materials for the EU: Report of the ad hoc working group on defining critical raw materials*, 2014.
- [6] A.V. Nguyen, G.M. Evans, Attachment interaction between air bubbles and particles in froth flotation, *Experimental Thermal and Fluid Science* 28 (5) (2004) 381–385. <https://doi.org/10.1016/j.expthermflusci.2002.12.001>.
- [7] G. Cheng, C. Shi, X. Yan, Z. Zhang, H. Xu, Y. Lu, A study of bubble-particle interactions in a column flotation process. 856 kB / *Physicochemical Problems of Mineral Processing*; ISSN 2084-4735 (2017). <https://doi.org/10.5277/PPMP170102>.
- [8] D. Hewitt, D. Fornasiero, J. Ralston, Bubble-Particle Attachment, *Journal of the Chemical Society, Faraday Transactions* 91 (13) (1995) 1997–2001. <https://doi.org/10.1039/FT9959101997>.
- [9] A.V. Nguyen, J. Ralston, H.J. Schulze, On modelling of bubble–particle attachment probability in flotation, *International Journal of Mineral Processing* 53 (4) (1998) 225–249. [https://doi.org/10.1016/S0301-7516\(97\)00073-2](https://doi.org/10.1016/S0301-7516(97)00073-2).
- [10] Q. Min, Y.-Y. Duan, X.-F. Peng, A.S. Mujumdar, C. Hsu, D.-J. Lee, Froth Flotation of Mineral Particles: Mechanism, *Drying Technology* 26 (8) (2008) 985–995. <https://doi.org/10.1080/07373930802115628>.
- [11] Y. Xing, X. Gui, L. Pan, B.-E. Pinchasik, Y. Cao, J. Liu, M. Kappl, H.-J. Butt, Recent experimental advances for understanding bubble-particle attachment in flotation, *Adv. Colloid Interface Sci.* 246 (2017) 105–132. <https://doi.org/10.1016/j.cis.2017.05.019>.
- [12] L.L. Schramm, *Emulsions, foams, and suspensions: Fundamentals and applications*, 1st ed., Wiley-VCH, Weinheim, Great Britain, 2010.
- [13] K.J. Ives (Ed.), *The Scientific Basis of Flotation*, 1st ed., Springer, Dordrecht, 1983.

- [14] M.C. Fuerstenau, Froth Flotation: The First Ninety Years, in: B.K. Parekh, J.D. Miller (Eds.), *Advances in Flotation Technology*, 1st ed., Society for Mining, Metallurgy and Exploration, Littleton, Colorado, 1999, pp. xi–xxxiii.
- [15] H. Baldauf, Flotationsapparate, in: K. Luckert (Ed.), *Handbuch der mechanischen Fest-Flüssig-Trennung*, Vulkan-Verl., Essen, 2004, pp. 131–142.
- [16] B. Yarar, Flotation, in: *Ullmann's encyclopedia of industrial chemistry*, Wiley, Chichester, 2010, pp. 237–267.
- [17] B.A. Wills, J.A. Finch, *Wills' mineral processing technology: An introduction to the practical aspects of ore treatment and mineral recovery*, 8th ed., Butterworth-Heinemann, Oxford, UK, Waltham, MA, 2016.
- [18] J. Aigueperse, P. Mollard, D. Devilliers, M. Chemla, R. Faron, R. Romano, J.P. Cuer, Fluorine Compounds, Inorganic, in: *Ullmann's encyclopedia of industrial chemistry*, Wiley, Chichester, 2010, pp. 397–441.
- [19] K. Wiese, J. Schmitz, G. Wollmann, *Das Mineral-Anreicherungsverfahren Flotation: Ein Überblick*, 1st ed., Karlsruhe, 1978.
- [20] M. Zlokarnik, *Rührtechnik: Theorie und Praxis*, Springer, Berlin, Heidelberg, 1999.
- [21] S.M. Bulatovic, *Handbook of flotation reagents*, 1st ed., Elsevier, Amsterdam, 2007.
- [22] W. Zhang, The Effects of Frothers and Particles on the Characteristics of Pulp and Froth Properties in Flotation—A Critical Review, *JMMCE* 04 (04) (2016) 251–269. <https://doi.org/10.4236/jmmce.2016.44023>.
- [23] E. Małysa, K. Małysa, J. Czarnecki, A method of comparison of the frothing and collecting properties of frothers, *Colloids and Surfaces* 23 (1-2) (1987) 29–39. [https://doi.org/10.1016/0166-6622\(87\)80247-0](https://doi.org/10.1016/0166-6622(87)80247-0).
- [24] F. Hernáinz, M. Calero, Froth flotation: Kinetic models based on chemical analogy, *Chemical Engineering and Processing: Process Intensification* 40 (3) (2001) 269–275. [https://doi.org/10.1016/S0255-2701\(00\)00125-2](https://doi.org/10.1016/S0255-2701(00)00125-2).
- [25] N. Ahmed, G.J. Jameson, Flotation Kinetics, *Mineral Processing and Extractive Metallurgy Review* 5 (1-4) (1989) 77–99. <https://doi.org/10.1080/08827508908952645>.
- [26] P.W. Atkins, J. de Paula, *Physical chemistry: Thermodynamics, structure, and change*, 10th ed., Oxford University Press, New York, 2014.
- [27] A. Gupta, D.S. Yan, *Mineral processing design and operations: An introduction*, 2nd ed., Elsevier, Amsterdam, 2016.
- [28] M. Szatkowski, Some comments on flotation kinetics, *Chemical Engineering Science* 42 (10) (1987) 2475–2478. [https://doi.org/10.1016/0009-2509\(87\)80123-9](https://doi.org/10.1016/0009-2509(87)80123-9).

- [29] H. García-Zuñiga, The efficiency obtained by flotation is an exponential function of time, *Boletín Minero* 47 (1935) 83–86.
- [30] M. Fuerstenau, G. Jameson, R.-H. Yoon, *Froth Flotation: A Century of Innovation*, 1st ed., Society for Mining, Metallurgy and Exploration, Littleton, 2007.
- [31] P. Amelunxen, K. Runge, Innovations in Froth Flotation Modeling, in: C.G. Anderson, R.C. Dunne, J.L. Uhrig (Eds.), *Mineral processing and extractive metallurgy: 100 years of innovation*, Society for Mining, Metallurgy and Exploration, Englewood, Colo., 2014, pp. 177–192.
- [32] J. Drzymala, A. Swatek, *Mineral processing: Foundations of theory and practice of minerallurgy*, 1st ed., University of Technology, Wroclaw, 2007.
- [33] X. Bu, G. Xie, Y. Peng, L. Ge, C. Ni, Kinetics of flotation. Order of process, rate constant distribution and ultimate recovery, *Physicochemical Problems of Mineral Processing* 53 (1) (2017) 342–365. <https://doi.org/10.5277/PPMP170128>.
- [34] M.A. Fichera, M.W. Chudacek, Batch cell flotation models — A review, *Minerals Engineering* 5 (1) (1992) 41–55. [https://doi.org/10.1016/0892-6875\(92\)90005-T](https://doi.org/10.1016/0892-6875(92)90005-T).
- [35] D. Chipfunhu, M. Zanin, S. Grano, Flotation behaviour of fine particles with respect to contact angle, *Chemical Engineering Research and Design* 90 (1) (2012) 26–32. <https://doi.org/10.1016/j.cherd.2011.06.021>.
- [36] M. Polat, S. Chander, First-order flotation kinetics models and methods for estimation of the true distribution of flotation rate constants, *International Journal of Mineral Processing* 58 (1-4) (2000) 145–166. [https://doi.org/10.1016/S0301-7516\(99\)00069-1](https://doi.org/10.1016/S0301-7516(99)00069-1).
- [37] S. Szczerkowska, A. Wiertel-Pochopien, J. Zawala, E. Larsen, P.B. Kowalczyk, Kinetics of froth flotation of naturally hydrophobic solids with different shapes, *Minerals Engineering* 121 (2018) 90–99. <https://doi.org/10.1016/j.mineng.2018.03.006>.
- [38] D. Kosior, P.B. Kowalczyk, J. Zawala, Surface roughness in bubble attachment and flotation of highly hydrophobic solids in presence of frother – experiment and simulations. *Physicochemical Problems of Mineral Processing*; ISSN 2084-4735 (2018). <https://doi.org/10.5277/PPMP1815>.
- [39] M. Yekeler, I. Sönmez, Effect of the hydrophobic fraction and particle size in the collectorless column flotation kinetics, *Colloids and Surfaces A: Physicochemical and Engineering Aspects* 121 (1) (1997) 9–13. [https://doi.org/10.1016/S0927-7757\(96\)03942-8](https://doi.org/10.1016/S0927-7757(96)03942-8).
- [40] D. Sekhar, R. Shanker, Flotation Kinetics: An Overview, *Process and Plant Engineering* 19 (5) (2001) 80–84.

- [41] R.D. Stanojlović, J.M. Sokolović, A Study of the Optimal Model of the Flotation Kinetics of Copper Slag from Copper Mine BOR, *Archives of Mining Sciences* 59 (3) (2014) 821–834. <https://doi.org/10.2478/amsc-2014-0057>.
- [42] H. Zhang, J. Liu, Y. Cao, Y. Wang, Effects of particle size on lignite reverse flotation kinetics in the presence of sodium chloride, *Powder Technology* 246 (2013) 658–663. <https://doi.org/10.1016/j.powtec.2013.06.033>.
- [43] R.R. Klimpel, Selection of chemical reagents for flotation, in: A.L. Mular, R.B. Bhappu (Eds.), *Mineral Processing Plant Design*, 2nd ed., Society of Mining Engineers of the American Institute of Mining Metallurgical and Petroleum Engineers, New York, 1980, pp. 907–934.
- [44] B.K. Loveday, Analysis of froth flotation kinetics, *Trans. Inst. Min. Metall* 75 (1966) C219-C225.
- [45] M. Gharai, R. Venugopal, Modeling of flotation process – an overview of different approaches, *Mineral Processing and Extractive Metallurgy Review* 16 (851) (2015) 1197. <https://doi.org/10.1080/08827508.2015.1115991>.
- [46] E.C. Dowling, R.R. Klimpel, F.F. Aplan, Model Discrimination in the Flotation of a Porphyry Copper Ore, *Mining, Metallurgy & Exploration* 2 (2) (1985) 87–101. <https://doi.org/10.1007/BF03402602>.
- [47] D.F. Kelsall, Application of probability in the assessment of flotation systems, *Transactions of the Institution of Mining and Metallurgy* 70 (4) (1961) 191–204.
- [48] A. Jowett, Resolution of flotation recovery curves by a differential plot method, *Trans. Inst. Min. Metall* 85 (1974) C263-C266.
- [49] M. Xu, Modified flotation rate constant and selectivity index, *Minerals Engineering* 11 (3) (1998) 271–278. [https://doi.org/10.1016/S0892-6875\(98\)00005-3](https://doi.org/10.1016/S0892-6875(98)00005-3).
- [50] J. Drzymala, T. Ratajczak, P. Kowalczyk, Kinetic separation curves based on process rate considerations, *Physicochemical Problems of Mineral Processing* 53 (2) (2017) 983–995. <https://doi.org/10.5277/ppmp170224>.
- [51] A.V. Nguyen, Particle-bubble interaction in flotation, in: R. Miller, L. Liggieri (Eds.), *Bubble and drop interfaces*, Brill, Leiden, The Netherlands, 2011, pp. 351–384.
- [52] R.-H. Yoon, The role of hydrodynamic and surface forces in bubble–particle interaction, *International Journal of Mineral Processing* 58 (1-4) (2000) 129–143. [https://doi.org/10.1016/S0301-7516\(99\)00071-X](https://doi.org/10.1016/S0301-7516(99)00071-X).
- [53] N.O. Egiebor, Z.A. Zhou, K. Nyavor, Development of a Particle-Bubble Collision Model for Flotation Columns, *Developments in Chemical Engineering and Mineral Processing* 5 (1-2) (1997) 21–42. <https://doi.org/10.1002/apj.5500050205>.

- [54] K.L. Sutherland, Physical Chemistry of Flotation. XI. Kinetics of the Flotation Process, *J. Phys. Chem.* 52 (2) (1948) 394–425. <https://doi.org/10.1021/j150458a013>.
- [55] M.E. Weber, Collision efficiencies for small particles with a spherical collector at intermediate Reynolds numbers, *J. Separation Process Technol.* 2 (1981) 29–33.
- [56] M. Weber, D. Paddock, Interceptional and gravitational collision efficiencies for single collectors at intermediate Reynolds numbers, *Journal of Colloid and Interface Science* 94 (2) (1983) 328–335. [https://doi.org/10.1016/0021-9797\(83\)90270-9](https://doi.org/10.1016/0021-9797(83)90270-9).
- [57] B. Shahbazi, B. Rezai, S.M. Javad Koleini, The effect of hydrodynamic parameters on probability of bubble–particle collision and attachment, *Minerals Engineering* 22 (1) (2009) 57–63. <https://doi.org/10.1016/j.mineng.2008.03.013>.
- [58] Z. Dai, D. Fornasiero, J. Ralston, Particle–bubble collision models - a review, *Adv. Colloid Interface Sci.* 85 (2-3) (2000) 231–256. [https://doi.org/10.1016/S0001-8686\(99\)00030-5](https://doi.org/10.1016/S0001-8686(99)00030-5).
- [59] A.V. Nguyen, D.-A. An-Vo, T. Tran-Cong, G.M. Evans, A review of stochastic description of the turbulence effect on bubble-particle interactions in flotation, *International Journal of Mineral Processing* 156 (2016) 75–86. <https://doi.org/10.1016/j.minpro.2016.05.002>.
- [60] B. Wang, Y. Peng, The effect of saline water on mineral flotation - A critical review, *Minerals Engineering* 66-68 (2014) 13–24. <https://doi.org/10.1016/j.mineng.2014.04.017>.
- [61] R.-H. Yoon, J.L. Yordan, Induction time measurements for the quartz-amine flotation system, *Journal of Colloid and Interface Science* 141 (2) (1991) 374–383. [https://doi.org/10.1016/0021-9797\(91\)90333-4](https://doi.org/10.1016/0021-9797(91)90333-4).
- [62] J. Ralston, D. Fornasiero, R. Hayes, Bubble–particle attachment and detachment in flotation, *International Journal of Mineral Processing* 56 (1-4) (1999) 133–164. [https://doi.org/10.1016/S0301-7516\(98\)00046-5](https://doi.org/10.1016/S0301-7516(98)00046-5).
- [63] Dai, Z., et al., Particle-Bubble Attachment in Mineral Flotation, *Journal of Colloid and Interface Science* 217 (1) (1999) 70–76. <https://doi.org/10.1006/jcis.1999.6319>.
- [64] W. Wang, Z. Zhou, K. Nandakumar, Z. Xu, J.H. Masliyah, Attachment of individual particles to a stationary air bubble in model systems, *International Journal of Mineral Processing* 68 (1-4) (2003) 47–69. [https://doi.org/10.1016/S0301-7516\(02\)00050-9](https://doi.org/10.1016/S0301-7516(02)00050-9).
- [65] D.I. Verrelli, W.J. Bruckard, P.T. Koh, M.P. Schwarz, B. Follink, Particle shape effects in flotation. Part 1: Microscale experimental observations, *Minerals Engineering* 58 (2014) 80–89. <https://doi.org/10.1016/j.mineng.2014.01.004>.

- [66] B. Albijanic, O. Ozdemir, A.V. Nguyen, D. Bradshaw, A review of induction and attachment times of wetting thin films between air bubbles and particles and its relevance in the separation of particles by flotation, *Adv. Colloid Interface Sci.* 159 (1) (2010) 1–21. <https://doi.org/10.1016/j.cis.2010.04.003>.
- [67] P. Koh, M.P. Schwarz, CFD modelling of bubble–particle attachments in flotation cells, *Minerals Engineering* 19 (6-8) (2006) 619–626. <https://doi.org/10.1016/j.mineng.2005.09.013>.
- [68] B. Shahbazi, B. Rezai, S.M. Javad Koleini, Bubble–particle collision and attachment probability on fine particles flotation, *Chemical Engineering and Processing: Process Intensification* 49 (6) (2010) 622–627. <https://doi.org/10.1016/j.cep.2010.04.009>.
- [69] H.J. Schulze, W. Stöckelhuber, Flotation as a Heterocoagulation Process: Possibilities of Calculating the Probability of the Microprocesses, Rupture of the Intervening Thin Liquid Film, and Progress in Modeling of the Overall Process, in: H. Stechemesser, B. Dobiáš (Eds.), *Coagulation and Flocculation*, CRC Press, Boca Raton, 2005, pp. 455–518.
- [70] G. Wang, A.V. Nguyen, S. Mitra, J.B. Joshi, G.J. Jameson, G.M. Evans, A review of the mechanisms and models of bubble-particle detachment in froth flotation, *Separation and Purification Technology* 170 (2016) 155–172. <https://doi.org/10.1016/j.seppur.2016.06.041>.
- [71] T.T. Chau, W.J. Bruckard, P.T.L. Koh, A.V. Nguyen, A review of factors that affect contact angle and implications for flotation practice, *Adv. Colloid Interface Sci.* 150 (2) (2009) 106–115. <https://doi.org/10.1016/j.cis.2009.07.003>.
- [72] B. Pyke, D. Fornasiero, J. Ralston, Bubble particle heterocoagulation under turbulent conditions, *Journal of Colloid and Interface Science* 265 (1) (2003) 141–151. [https://doi.org/10.1016/S0021-9797\(03\)00345-X](https://doi.org/10.1016/S0021-9797(03)00345-X).
- [73] T. Bide, G. Gunn, T. Brown, D. Rayner, *Fluorspar Mineral Profil*, British Geological Survey (2011).
- [74] M. Bertau, A. Müller, P. Fröhlich, M. Katzberg, *Industrielle anorganische Chemie*, Wiley-VCH Verlag GmbH & Co. KGaA, Weinheim, 2013.
- [75] M. Robbins, *The Collector's Book of Fluorescent Minerals*, 1st ed., Springer, Boston, MA, 1983.
- [76] P.G. Jeffrey, Rare earth content of green fluorite - a new source of Europium, *Nature* 215 (1967) 496–497.

- [77] K.R. Wood, Flotation Equipment Selection and Plant Layout, in: A.L. Mular (Ed.), Mineral processing plant design, practice, and control: Proceedings, 1st ed., Society for Mining, Metallurgy and Exploration, Littleton, Colo., 2002, pp. 1204–1217.
- [78] S.R. Rao, Surface Chemistry of Froth Flotation: Volume 1: Fundamentals, Springer, Boston, MA, 2004.
- [79] X. Zhang, H. Du, X. Wang, J. Miller, Surface chemistry considerations in the flotation of rare-earth and other semisoluble salt minerals, *Minerals and Metallurgical Processing* 30 (1) (2013) 24–37.
- [80] W. Gründer, Erzaufbereitungsanlagen in Westdeutschland: Ein Führer durch die wichtigsten Betriebe für die Aufbereitung von Erzen und anderen mineralischen Rohstoffen, 1st ed., Springer Berlin Heidelberg, Berlin, Heidelberg, s.l., 1955.
- [81] I.H. Redeker, E.H. Bentzen, Plant and laboratory practice in nonmetallic mineral flotation, 1986.
- [82] A. Peck, M. Wadsworth, An infrared study of the flotation of Hematite with Oleic Acid and Sodium Oleate, *Transactions of the American Institute of Mining, Metallurgical, and Petroleum Engineers* (1964) 235–301.
- [83] E. Brunner, Über die Flotation von Alkali- und Erdalkalisalzen. Dissertation, ETH Zürich, 1945.
- [84] Hiçyılmaz und Ghaemi, The effect of inorganic agents on the flotation of barite and fluorite, in: M. Kemal (Ed.), Changing scopes in mineral processing: Proceedings of the 6th International Mineral Processing Symposium, Kusadasi, Turkey, 24 - 26 September 1996, 1st ed., Balkema, Rotterdam, 1996, pp. 261–264.
- [85] The British Standards Institution, BS 5659 - Acid-grade fluorspar - Part 5: Determination of available fluorine content, 1978.
- [86] ASTM International, Standard Test Method for Determination of Calcium Fluoride in Fluorspar by Complexometric Titration, 2004.
- [87] A. Lubecki, K. Wiese, Testing of a new on-line x-ray fluorescence method for barite analysis in fluorspar flotation, *Erzmetall* 35 (1982) 423–428.
- [88] M. Geisler, Routinebestimmung von Kalziumfluorid im Flußspatbergbau durch Röntgenfluoreszenzanalyse mit Radionuklidenanregung, *Neue Bergbautechnik* 2 (6) (1972) 448–452.
- [89] G. Wedler, Lehrbuch der physikalischen Chemie, 5th ed., Wiley-VCH, Weinheim, 2010.
- [90] A.M. Dupré, Théorie mécanique de la chaleur, 1st ed., Gauthier-Villars, Paris, 1869.
- [91] M.E. Schrader, Young-Dupre Revisited, *Langmuir* 11 (9) (1995) 3585–3589.  
<https://doi.org/10.1021/la00009a049>.

- [92] J.W. Drelich, A. Marmur, Meaningful Contact Angles in Flotation Systems: Critical Analysis and Recommendations, *Surface Innovations* (2017) 1–45. <https://doi.org/10.1680/jsuin.17.00037>.
- [93] W. Bigelow, D. Pickett, W. Zisman, Oleophobic monolayers: I. Films adsorbed from solution in non-polar liquids, *Journal of Colloid Science* 1 (6) (1946) 479–553. [https://doi.org/10.1016/0095-8522\(46\)90059-1](https://doi.org/10.1016/0095-8522(46)90059-1).
- [94] A.W. Neumann, R.J. Good, Techniques of Measuring Contact Angles, in: R.J. Good, R.R. Stromberg (Eds.), *Surface and Colloid Science: Volume 11: Experimental Methods*, Springer US, Boston, MA, 1979, pp. 31–91.
- [95] Y. Yuan, T.R. Lee, Contact Angle and Wetting Properties, in: G. Bracco, B. Holst (Eds.), *Surface science techniques*, Springer, Berlin, 2013, pp. 3–34.
- [96] W.A. Zisman, Relation of the Equilibrium Contact Angle to Liquid and Solid Constitution, in: F.M. Fowkes (Ed.), *Contact angle, wettability and adhesion*, American Chemical Society, Washington, D.C., 1964, pp. 1–51.
- [97] A. Taggart, T. Taylor, C. Ince, Experiments with flotation reagents, *Transactions of the American Institute of Mining, Metallurgical and Petroleum Engineers* 87 (1930) 285–368.
- [98] K. Mittal, *Advances in contact angle, wettability and adhesion: Volume 3, 1st ed.*, Scrivener Publishing, Hoboken, NJ, 2018.
- [99] N. Stevens, *Contact Angle Measurements on Particulate Systems*. Ph.D. thesis, University of South Australia, Adelaide, 2005.
- [100] C.W. Extrand, S.I. Moon, Contact angles on spherical surfaces, *Langmuir* 24 (17) (2008) 9470–9473. <https://doi.org/10.1021/la801091n>.
- [101] D.W. Fuerstenau, M.C. Williams, A new method for Characterization of the Surface Energy of Hydrophobic Particles, *Particle & Particle Systems Characterization* 4 (1-4) (1987) 7–13. <https://doi.org/10.1002/ppsc.19870040103>.
- [102] M.C. Williams, D.W. Fuerstenau, A simple flotation method for rapidly assessing the hydrophobicity of coal particles, *International Journal of Mineral Processing* 20 (1-2) (1987) 153–157. [https://doi.org/10.1016/0301-7516\(87\)90023-8](https://doi.org/10.1016/0301-7516(87)90023-8).
- [103] D.W. Fuerstenau, J. Diao, M.C. Williams, Characterization of the wettability of solid particles by film flotation 1. Experimental investigation, *Colloids and Surfaces* 60 (1991) 127–144. [https://doi.org/10.1016/0166-6622\(91\)80273-Q](https://doi.org/10.1016/0166-6622(91)80273-Q).
- [104] A. Marmur, W. Chen, G. Zografis, Characterization of particle wettability by the measurement of floatability, *Journal of Colloid and Interface Science* 113 (1) (1986) 114–120. [https://doi.org/10.1016/0021-9797\(86\)90211-0](https://doi.org/10.1016/0021-9797(86)90211-0).

- [105] H.-J. Butt, K. Graf, M. Kappl, *Physics and chemistry of interfaces*, 1st ed., Wiley-VCH, Weinheim, 2003.
- [106] J. Leja, *Surface Chemistry of Froth Flotation*, 1st ed., Springer US, Boston, MA, 1982.
- [107] M.J. Rosen, J.T. Kunjappu, *Surfactants and interfacial phenomena*, 4th ed., Wiley, Hoboken N.J., 2012.
- [108] R.J. Farn, *Chemistry and technology of surfactants*, Blackwell Pub, Oxford, Ames Iowa, 2006.
- [109] T.F. Tadros, *Applied surfactants: Principles and applications*, 2nd ed., Wiley-VCH, Weinheim, 2008.
- [110] A.N. Martin, P.J. Sinko, Y. Singh, *Martin's physical pharmacy and pharmaceutical sciences: Physical chemical and biopharmaceutical principles in the pharmaceutical sciences*, 6th ed., Lippincott Williams & Wilkins, Baltimore MD, 2011.
- [111] W. Xuming, J.D. Miller, Dodecyl amine adsorption at different interfaces during bubble attachment/detachment at a silica surface. *Physicochemical Problems of Mineral Processing*; ISSN 2084-4735 (2018). <https://doi.org/10.5277/PPMP1809>.
- [112] L. Shen, H. Wang, Properties of fatty acid/dodecylamine mixtures and their application in steam coal reverse flotation. *Physicochemical Problems of Mineral Processing*; ISSN 2083-3989 (2016). <https://doi.org/10.5277/PPMP160126>.
- [113] C.-H. Chang, E.I. Franses, Adsorption dynamics of surfactants at the air/water interface: A critical review of mathematical models, data, and mechanisms, *Colloids and Surfaces A: Physicochemical and Engineering Aspects* 100 (1995) 1–45. [https://doi.org/10.1016/0927-7757\(94\)03061-4](https://doi.org/10.1016/0927-7757(94)03061-4).
- [114] M.C. Fuerstenau, P. Somasundaran, Flotation, in: K.N. Han, M.C. Fuerstenau (Eds.), *Principles of mineral processing*, Society for Mining, Metallurgy and Exploration, Littleton, Colo, 2009, pp. 245–306.
- [115] A. Frumkin, Die Kapillarkurve der höheren Fettsäuren und die Zustandsgleichung der Oberflächenschicht, *Zeitschrift für Physikalische Chemie* 116U (1) (1925) 466–484. <https://doi.org/10.1515/zpch-1925-11629>.
- [116] T. Cosgrove, *Colloid science: Principles, methods and applications*, Blackwell Pub, Oxford UK, Ames Iowa, 2005.
- [117] K.-Y. Law, H. Zhao, *Surface wetting: Characterization, contact angle, and fundamentals*, 1st ed., Springer International Publishing, Cham, Heidelberg, New York, Dordrecht, 2016.

- [118] S. Ebnesajjad, Surface Tension and Its Measurement, in: S. Ebnesajjad (Ed.), Handbook of Adhesives and Surface Preparation: Technology, Applications and Manufacturing, Elsevier, Oxford, 2011, pp. 21–30.
- [119] P.L. Du Nouy, An interfacial tensiometer for universal use, The Journal of General Physiology 7 (5) (1925) 625–631. <https://doi.org/10.1085/jgp.7.5.625>.
- [120] International Organization for Standardization, ISO 304 - Surface active agents - Determination of surface tension by drawing up liquid films, 1985.
- [121] W. Harkins, H. Jordan, A method for the determination of surface and interfacial tension from the maximum pull in a ring, Journal of the American Chemical Society 52 (5) (1930) 1751–1772. <https://doi.org/10.1021/ja01368a004>.
- [122] N. Rübiger, M. Schlüter, Formation and Movement of Bubbles and Drops, in: P. Stephan, S. Kabelac, M. Kind, H. Martin, D. Mewes, K. Schaber (Eds.), VDI heat atlas, 2nd ed., Springer-Verlag, Berlin Heidelberg, 2010, pp. 1239–1254.
- [123] H. Voit, R. Zeppenfeld, A. Mersmann, Calculation of primary bubble volume in gravitational and centrifugal fields, Chem. Eng. Technol. 10 (1) (1987) 99–103. <https://doi.org/10.1002/ceat.270100113>.
- [124] E. Michaelides, Particles, bubbles & drops: Their motion, heat and mass transfer, 1st ed., World Scientific, Hackensack, NJ, 2006.
- [125] R. Clift, J.R. Grace, M.E. Weber, Bubbles, drops, and particles, 3rd ed., Acad. Press, New York, NY, 1992.
- [126] L.-S. Fan, K. Tsuchiya, H. Brenner, Bubble Wake Dynamics in Liquids and Liquid-Solid Suspensions: Principles and Selected Applications, 1st ed., Elsevier Science, Burlington, 1990.
- [127] W.L. Haberman, R.K. Morton, An experimental investigation of the drag and shape of air bubbles rising in various liquids. Report 802, Armed Services Technical Information Agency (1953) 1–55.
- [128] D. Bröder, Anwendung optischer Messtechniken zur Untersuchung disperser Gas-Flüssigkeits-Strömungen. Dissertation, Martin-Luther Universität, Halle-Wittenberg, 2003.
- [129] D. Möbius, R. Miller (Eds.), Drops and bubbles in Interfacial Research, Elsevier, Amsterdam, 1998.
- [130] B.E. Rapp, Microfluidics: Modeling, mechanics, and mathematics, William Andrew, Kidlington, United Kingdom, 2017.
- [131] L. Prandtl, K. Oswatitsch, K. Wieghardt, Führer durch die Strömungslehre, 9th ed., Vieweg+Teubner Verlag, Wiesbaden, 1990.

- [132] J.T. Lindt, On the periodic nature of the drag on a rising bubble, *Chemical Engineering Science* 27 (10) (1972) 1775–1781. [https://doi.org/10.1016/0009-2509\(72\)85039-5](https://doi.org/10.1016/0009-2509(72)85039-5).
- [133] Y. Zhang, J.A. Finch, A note on single bubble motion in surfactant solutions, *J. Fluid Mech.* 429 (2001) 63–66. <https://doi.org/10.1017/S0022112000002755>.
- [134] J. Huang, T. Saito, Influences of gas–liquid interface contamination on bubble motions, bubble wakes, and instantaneous mass transfer, *Chemical Engineering Science* 157 (2017) 182–199. <https://doi.org/10.1016/j.ces.2016.05.013>.
- [135] S. Takagi, Y. Matsumoto, Surfactant Effects on Bubble Motion and Bubbly Flows, *Annu. Rev. Fluid Mech.* 43 (1) (2011) 615–636. <https://doi.org/10.1146/annurev-fluid-122109-160756>.
- [136] C. Pesci, A. Weiner, H. Marschall, D. Bothe, Computational analysis of single rising bubbles influenced by soluble surfactant, *J. Fluid Mech.* 856 (2018) 709–763. <https://doi.org/10.1017/jfm.2018.723>.
- [137] A. Sam, C. Gomez, J.A. Finch, Axial velocity profiles of single bubbles in water/frother solutions, *International Journal of Mineral Processing* 47 (1996) 177–196. [https://doi.org/10.1016/0301-7516\(95\)00088-7](https://doi.org/10.1016/0301-7516(95)00088-7).
- [138] Y. Zhang, A. Sam, J. Finch, Temperature effect on single bubble velocity profile in water and surfactant solution, *Colloids and Surfaces A: Physicochemical and Engineering Aspects* 223 (1-3) (2003) 45–54. [https://doi.org/10.1016/S0927-7757\(03\)00189-4](https://doi.org/10.1016/S0927-7757(03)00189-4).
- [139] Y.H. Tan, A.A. Rafiei, A. Elmahdy, J.A. Finch, Bubble size, gas holdup and bubble velocity profile of some alcohols and commercial frothers, *International Journal of Mineral Processing* 119 (2013) 1–5. <https://doi.org/10.1016/j.minpro.2012.12.003>.
- [140] S.S. Dukhin, R. Miller, G. Loglio, Physico-chemical hydrodynamics of rising bubble, in: D. Möbius, R. Miller (Eds.), *Drops and bubbles in Interfacial Research*, Elsevier, Amsterdam, 1998, pp. 367–432.
- [141] Y.S. Cho, J.S. Laskowski, Bubble coalescence and its effect on dynamic foam stability, *Can. J. Chem. Eng.* 80 (2) (2002) 299–305. <https://doi.org/10.1002/cjce.5450800216>.
- [142] Y. Cho, J. Laskowski, Effect of flotation frothers on bubble size and foam stability, *International Journal of Mineral Processing* 64 (2-3) (2002) 69–80. [https://doi.org/10.1016/S0301-7516\(01\)00064-3](https://doi.org/10.1016/S0301-7516(01)00064-3).

- [143] C. Aldrich, D. Feng, The effect of mothers on bubble size distributions in flotation pulp phases and surface froths, *Minerals Engineering* 13 (10-11) (2000) 1049–1057. [https://doi.org/10.1016/S0892-6875\(00\)00089-3](https://doi.org/10.1016/S0892-6875(00)00089-3).
- [144] J. Laskowski, Testing flotation frothers, *Physicochemical Problems of Mineral Processing* 38 (2004) 13–22.
- [145] Y.H. Tan, J.A. Finch, Frother structure-property relationship: Effect of hydroxyl position in alcohols on bubble rise velocity, *Minerals Engineering* 92 (2016) 1–8. <https://doi.org/10.1016/j.mineng.2016.02.003>.
- [146] Y.H. Tan, J.A. Finch, Frother structure–property relationship: Effect of alkyl chain length in alcohols and polyglycol ethers on bubble rise velocity, *Minerals Engineering* 95 (2016) 14–20. <https://doi.org/10.1016/j.mineng.2016.05.012>.
- [147] Y.H. Tan, J.A. Finch, Frothers and gas dispersion: A review of the structure-property-function relationship. *Physicochemical Problems of Mineral Processing* 54 (1) (2018) 40–53. <https://doi.org/10.5277/PPMP1814>.
- [148] P.B. Kowalczyk, J. Zawala, J. Drzymala, Concentration at the Minimum Bubble Velocity (CMV) for Various Types of Flotation Frothers, *Minerals* 7 (7) (2017) 118. <https://doi.org/10.3390/min7070118>.
- [149] A. Yasunishi, M. Fukuma, K. Muroyama, Measurement of behavior of gas bubbles and gas holdup in a slurry bubble column by a dual electroresistivity probe method, *Journal of Chemical Engineering of Japan* 19 (5) (1986) 444–449. <https://doi.org/10.1252/jcej.19.444>.
- [150] W. Hilgert, H. Hofmann, Characterization of gas phase flow in bubble columns at low gas velocities with the aid of an ultrasonic Doppler technique, *Chemie Ingenieur Technik* 58 (3) (1986) 228–229. <https://doi.org/10.1002/cite.330580313>.
- [151] J.A. Raper, M.S. Kearny, J.M. Burgess, D.J.D. Fell, The structure of industrial sieve tray froths, *Chemical Engineering Science* 37 (4) (1982) 501–506. [https://doi.org/10.1016/0009-2509\(82\)80112-7](https://doi.org/10.1016/0009-2509(82)80112-7).
- [152] S. Miskovic, An investigation of the gas dispersion properties of mechanical flotation cells: an in-situ approach. Ph.D. thesis, Virginia Polytechnic Institute and State University, Blacksburg, Virginia, 2011.
- [153] H.I. de Lasa, S.L.P. Lee, M.A. Bergougnou, Measurement in Three-Phase Fluidized Beds using a U-Shaped Optical Fiber, *Canadian Journal of Chemical Engineering* 62 (2) (1984) 165–169.

- [154] S. Saberi, K. Shakourzadeh, D. Bastoul, J. Militzer, Bubble-Size and Velocity-Measurement in Gas-Liquid Systems - Application of Fiber Optic Technique to Pilot-Plant Scale, *Canadian Journal of Chemical Engineering* 73 (2) (1995) 253–257. <https://doi.org/10.1002/cjce.5450730213>.
- [155] E.W. Randall, C.M. Goodall, P.M. Fairlamb, P.L. Dold, C.T. O'Conner, A method for measuring the sizes of bubbles in two- and three-phase systems, *Journal of Physics E: Scientific Instruments* 22 (10) (1989) 827–833. <https://doi.org/10.1088/0022-3735/22/10/005>.
- [156] J.P. Tucker, D.A. Deglon, J.-P. Franzidis, M.C. Harris, C.T. O'Connor, An evaluation of a direct method of bubble size distribution measurement in a laboratory batch flotation cell, *Minerals Engineering* 7 (5-6) (1994) 667–680. [https://doi.org/10.1016/0892-6875\(94\)90098-1](https://doi.org/10.1016/0892-6875(94)90098-1).
- [157] R. Grau, K. Heiskanen, Visual technique for measuring bubble size in flotation machines, *Minerals Engineering* 15 (7) (2002) 507–513. [https://doi.org/10.1016/S0892-6875\(02\)00074-2](https://doi.org/10.1016/S0892-6875(02)00074-2).
- [158] C.O. Gomez, J.A. Finch, Gas dispersion measurements in flotation cells, *International Journal of Mineral Processing* 84 (1-4) (2007) 51–58. <https://doi.org/10.1016/j.minpro.2007.03.009>.
- [159] J.E. Nasset, J.R. Hernandez-Aguilar, C. Acuna, C.O. Gomez, J.A. Finch, Some gas dispersion characteristics of mechanical flotation machines, *Minerals Engineering* 19 (6-8) (2006) 807–815. <https://doi.org/10.1016/j.mineng.2005.09.045>.
- [160] J. Hernandez-Aguilar, R. Coleman, C. Gomez, J. Finch, A comparison between capillary and imaging techniques for sizing bubbles in flotation systems, *Minerals Engineering* 17 (1) (2004) 53–61. <https://doi.org/10.1016/j.mineng.2003.09.011>.
- [161] R.T. Rodrigues, J. Rubio, New basis for measuring the size distribution of bubbles, *Minerals Engineering* 16 (8) (2003) 757–765. [https://doi.org/10.1016/S0892-6875\(03\)00181-X](https://doi.org/10.1016/S0892-6875(03)00181-X).
- [162] E. Matiolo, F. Testa, J. Yianatos, J. Rubio, On the gas dispersion measurements in the collection zone of flotation columns, *International Journal of Mineral Processing* 99 (1-4) (2011) 78–83. <https://doi.org/10.1016/j.minpro.2011.03.002>.
- [163] J. Yianatos, L. Bergh, P. Condori, J. Aguilera, Hydrodynamic and metallurgical characterization of industrial flotation banks for control purposes, *Minerals Engineering* 14 (9) (2001) 1033–1046. [https://doi.org/10.1016/S0892-6875\(01\)00109-1](https://doi.org/10.1016/S0892-6875(01)00109-1).

- [164] P.K. Panigrahi, K. Muralidhar, Laser Schlieren and Shadowgraph, in: P.K. Panigrahi, K. Muralidhar (Eds.), Schlieren and shadowgraph methods in heat and mass transfer, Springer, New York, NY, 2012, pp. 23–46.
- [165] R.W. Johnson, Handbook of Fluid Dynamics, 2nd ed., CRC Press, Boca Raton, FL, 2016.
- [166] M. Legrand, J. Nogueira, A. Lecuona, A. Hernando, Single camera volumetric shadowgraphy system for simultaneous droplet sizing and depth location, including empirical determination of the effective optical aperture, *Experimental Thermal and Fluid Science* 76 (2016) 135–145. <https://doi.org/10.1016/j.expthermflusci.2016.03.018>.
- [167] J. Klinner, C. Willert, Tomographic shadowgraphy for three-dimensional reconstruction of instantaneous spray distributions, *Exp Fluids* 53 (2) (2012) 531–543. <https://doi.org/10.1007/s00348-012-1308-2>.
- [168] R. Castrejón-García, J.R. Castrejón-Pita, G.D. Martín, I.M. Hutchings, The shadowgraph imaging technique and its modern application to fluid jets and drops, *Revista Mexicana de física* 57 (3) (2011) 266–275.
- [169] K. Gersten, Einführung in die Strömungsmechanik, 2nd ed., Springer Fachmedien, Wiesbaden, 1981.
- [170] M. Raffel, C.E. Willert, F. Scarano, C.J. Kähler, S.T. Wereley, J. Kompenhans, Particle Image Velocimetry: A Practical Guide, 3rd ed., Springer International Publishing, Cham, 2018.
- [171] C.T. Crowe, T.R. Troutt, J.N. Chung, Particle Interactions with Vortices, in: S.I. Green (Ed.), Fluid Vortices, Springer Science+Business Media, Dordrecht, 1995, pp. 829–861.
- [172] R.J. Adrian, J. Westerweel, Particle image velocimetry, 1st ed., Cambridge Univ. Press, Cambridge, 2011.
- [173] N.G. Deen, B.H. Hjertager, T. Solberg, Comparison of PIV and LDA Measurement Methods Applied to the Gas-Liquid Flow in a Bubble Column, 10th International Symposium on Application of Laser Techniques to Fluid Mechanics (2000).
- [174] M.R. Brady, Multiphase Hydrodynamics in Flotation Systems. Ph.D. thesis, Virginia Polytechnic Institute and State University, Blacksburg, Virginia, 2009.
- [175] E.J. Stamhuis, Basics and principles of particle image velocimetry (PIV) for mapping biogenic and biologically relevant flows, *Aquat Ecol* 40 (4) (2006) 463–479. <https://doi.org/10.1007/s10452-005-6567-z>.
- [176] La Vision, FlowMaster: Advanced PIV/PTV Systems for Quantitative Flow Field Analysis. [http://www.piv.de/documents/BR\\_FlowMaster.pdf](http://www.piv.de/documents/BR_FlowMaster.pdf) (accessed 29 January 2019).

- [177] B. Sokoray-Varga, J. Józsa, Particle tracking velocimetry (PTV) and its application to analyse free surface flows in laboratory scale models, *Per. Pol. Civil Eng.* 52 (2) (2008) 63. <https://doi.org/10.3311/pp.ci.2008-2.02>.
- [178] A.F. Holleman, E. Wiberg, N. Wiberg, *Lehrbuch der anorganischen Chemie*, 102nd ed., de Gruyter, Berlin, 2007.
- [179] P. Schönherr, *Multiple Oberflächenfunktionalisierung von Mischgläser- und Siliciumdioxidpartikeln als Komponenten für Kompositmaterialien*. Dissertation, Technische Universität Chemnitz, Chemnitz, 2012.
- [180] C. Wüstner, *Selbstorganisierte Strukturen mit Saturn-Partikeln*. Dissertation, Technische Universität Chemnitz, Chemnitz, 2014.
- [181] B. Arkles, *Hydrophobicity, Hydrophilicity and Silane Surface Modification: Product data sheet*, 2nd ed., 2011.
- [182] T. Balgar, R. Bautista, N. Hartmann, E. Hasselbrink, An AFM study of the growth kinetics of the self-assembled octadecylsiloxane monolayer on oxidized silicon, *Surface Science* 532-535 (2003) 963–969. [https://doi.org/10.1016/S0039-6028\(03\)00101-8](https://doi.org/10.1016/S0039-6028(03)00101-8).
- [183] X. Liu, J. Thomason, F. Jones, The Concentration of Hydroxyl Groups on Glass Surfaces and their Effect on the Structure of Silane Deposits, in: K.L. Mittal (Ed.), *Silanes and other coupling agents: Volume 5*, VSP, Leiden, 2009, pp. 25–39.
- [184] A. Carré, V. Lacarrière, W. Birch, Molecular interactions between DNA and an aminated glass substrate, *Journal of Colloid and Interface Science* 260 (1) (2003) 49–55. [https://doi.org/10.1016/S0021-9797\(02\)00147-9](https://doi.org/10.1016/S0021-9797(02)00147-9).
- [185] Z. Kutelova, H. Mainka, K. Mader, W. Hintz, J. Tomas, *Glass Spheres: Functionalization, Surface Modification and Mechanical Properties*, in: H. Altenbach, N.F. Morozov (Eds.), *Surface Effects in Solid Mechanics: Models, Simulations and Applications*, Springer, Berlin, 2013, pp. 95–104.
- [186] K. Jradi, C. Daneault, B. Chabot, Chemical surface modification of glass beads for the treatment of paper machine process waters, *Thin Solid Films* 519 (13) (2011) 4239–4245. <https://doi.org/10.1016/j.tsf.2011.02.080>.
- [187] J. Böing, *Modifizierung von Glas- und Titanoberflächen zur Verbesserung der Biokompatibilität*. Dissertation, Technische Hochschule Aachen, Aachen, 2003.
- [188] G. Arslan, M. Özmen, B. Gündüz, X. Zhang, M. Ersöz, Surface modification of glass beads with an aminosilane monolayer, *Turk. J. Chem.* 30 (2) (2006) 203–210.
- [189] L.T. Zhuravlev, Surface characterization of amorphous silica—a review of work from the former USSR, *Colloids and Surfaces A: Physicochemical and Engineering Aspects* 74 (1) (1993) 71–90. [https://doi.org/10.1016/0927-7757\(93\)80399-Y](https://doi.org/10.1016/0927-7757(93)80399-Y).

- [190] B. Lewandowski, M. Ulbricht, G. Krekel, An automated image analysing routine for estimation of equivalent diameter in high-speed image sequences with high accuracy and its validation, *Experimental Thermal and Fluid Science* 98 (2018) 158–169.  
<https://doi.org/10.1016/j.expthermflusci.2018.05.016>.
- [191] S. Perreault, P. Hébert, S. Perreault, P. Hebert, Median Filtering in Constant Time, *IEEE Transactions on Image Processing* 16 (9) (2007) 2389–2394.  
<https://doi.org/10.1109/TIP.2007.902329>.
- [192] N. Otsu, A Threshold Selection Method from Gray-Level Histograms, *IEEE Transactions on systems, man, and cybernetics* 9 (1) (1979) 62–66.  
<https://doi.org/10.1109/TSMC.1979.4310076>.
- [193] R.A. Grau, An investigation of the effect of physical and chemical variables on bubble generation and coalescence in laboratory scale flotation cells. Ph.D. thesis, Helsinki University of Technology, Helsinki, Finland, 2005.
- [194] T. Ferreira, W. Rasband, *ImageJ User Guide: IJ 1.46r*, 2012.
- [195] The British Standards Institution, *BS ISO 13322-2 - Particle size analysis - Image analysis methods - Part 2: Dynamic image analysis methods*, 2006.
- [196] H. Martin, Wärme- und Stoffübertragung in der Wirbelschicht, *Chemie Ingenieur Technik* 52 (3) (1980) 199–209. <https://doi.org/10.1002/cite.330520303>.
- [197] R.J.M. Bastiaans, *Cross-correlation PIV: theory, implementation and accuracy - Research report*, Eindhoven University of Technology, 1993.
- [198] R.D. Keane, R.J. Adrian, Theory of cross-correlation analysis of PIV images, *Applied Scientific Research* 49 (3) (1992) 191–215. <https://doi.org/10.1007/BF00384623>.
- [199] T. von Kármán, *Aerodynamics: Selected topics in the light of their historical development*, Dover Publ, Mineola, N.Y., 2004.
- [200] A. Delafosse, M.-L. Collignon, M. Crine, D. Tuye, Estimation of the turbulent kinetic energy dissipation rate from 2D-PIV measurements in a vessel stirred by an axial Mixel TTP impeller, *Chemical Engineering Science* 66 (8) (2011) 1728–1737.  
<https://doi.org/10.1016/j.ces.2011.01.011>.
- [201] D. Xu, J. Chen, Accurate estimate of turbulent dissipation rate using PIV data, *Experimental Thermal and Fluid Science* 44 (2013) 662–672.  
<https://doi.org/10.1016/j.expthermflusci.2012.09.006>.
- [202] Dantec Dynamics A/S, *DynamicStudio: User's Guide 2015a*, Skovlunde, 2015.
- [203] J.L. Lumley, *Stochastic Tools in Turbulence*, 1st ed., Elsevier Science, Burlington, 1970.

- [204] L. Sirovich, Turbulence and the Dynamics of coherent structures: Part I: Coherent structures, *Quarterly of Applied Mathematics* 45 (3) (1987) 561–571.  
<https://doi.org/10.1090/S0033-569X-1987-0910462-6>.
- [205] L. Sirovich, Turbulence and the Dynamics of coherent structures: Part II: Symmetries and transformations, *Quarterly of Applied Mathematics* 45 (3) (1987) 573–582.  
<https://doi.org/10.1090/S0033-569X-1987-0910463-9>.
- [206] L. Sirovich, Turbulence and the Dynamics of coherent structures: Part III: Dynamics and scaling, *Quarterly of Applied Mathematics* 45 (3) (1987) 583–590.  
<https://doi.org/10.1090/qam/910464>.
- [207] S.J. Yi, S.M. Kim, H.D. Kim, J.W. Kim, K.C. Kim, Spatial and temporal structures of turbulent bubble-driven flows in a rectangular water tank, *J Mech Sci Technol* 24 (9) (2010) 1819–1827. <https://doi.org/10.1007/s12206-010-0628-5>.
- [208] H.D. Kim, S.J. Yi, J.W. Kim, K.C. Kim, Structure analysis of bubble driven flow by time-resolved PIV and POD techniques, *J Mech Sci Technol* 24 (4) (2010) 977–982.  
<https://doi.org/10.1007/s12206-010-0210-1>.
- [209] S.M. Kim, S.J. Yi, H.D. Kim, J.W. Kim, K.C. Kim, Dynamic analysis of bubble-driven liquid flows using time-resolved particle image velocimetry and proper orthogonal decomposition techniques, *J Vis* 13 (3) (2010) 213–220. <https://doi.org/10.1007/s12650-010-0029-y>.
- [210] I. Cosadia, J. Borée, P. Dumont, Coupling time-resolved PIV flow-fields and phase-invariant proper orthogonal decomposition for the description of the parameters space in a transparent Diesel engine, *Exp Fluids* 43 (2-3) (2007) 357–370.  
<https://doi.org/10.1007/s00348-007-0338-7>.
- [211] L.-H. Feng, J.-J. Wang, C. Pan, Proper orthogonal decomposition analysis of vortex dynamics of a circular cylinder under synthetic jet control, *Physics of Fluids* 23 (1) (2011) 14106. <https://doi.org/10.1063/1.3540679>.
- [212] M. Jensch, M. Brede, A. Leder, O. Frederich, F. Thiele, Use of proper orthogonal decomposition to visualize coherent structures from time resolved PIV data, 14th International Symposium on Application of Laser Techniques to Fluid Mechanics, Lisbon (2008).
- [213] K. Fukunaga, *Introduction to Statistical Pattern Recognition*, 2nd ed., Academic Press, San Francisco, 1990.
- [214] K.E. Meyer, D. Cavar, J.M. Pedersen, POD as tool for comparison of PIV and LES data, 7th International Symposium on Particle Image Velocimetry, Rome (2007).

- [215] W.Y. Yang, *Signals and Systems with MATLAB*, Springer-Verlag, Berlin Heidelberg, 2009.
- [216] B. Lewandowski, B. Ben Said, M. Ulbricht, G. Krekel, Application of Raman spectroscopy to the flotation process of fluorite, *Minerals Engineering* 135 (2019) 129–138. <https://doi.org/10.1016/j.mineng.2019.02.038>.
- [217] G. Lundell, J.I. Hoffman, The analysis of fluorspar, *Bureau of Standards Journal of Research* 2 (4) (1929) 671–683.
- [218] W. Zönnchen, M. Mehlhorn, K. Volke, Beitrag zur Kalziumfluoridbestimmung in Spaten, *Freiberger Forschungshefte / Reihe A, Geotechnik, Ingenieurgeologie, Bergbautechnik, Verfahrenstechnik* 389 (1966) 35–50.
- [219] C. Harzdorf, Zur photometrischen Titration von Fluorid mit Lanthan (Cer, Yttrium), *Z. Anal. Chem. (Fresenius' Zeitschrift für Analytische Chemie)* 233 (5) (1967) 348–355. <https://doi.org/10.1007/BF00507477>.
- [220] Y. Maruyama, K. Ogawa, T. Okada, M. Kato, Particle size effect in X-ray fluorescence and its implications to planetary XRF spectroscopy, *Lunar and Planetary Science* 38 (1186) (2007).
- [221] Y. Maruyama, K. Ogawa, T. Okada, M. Kato, Laboratory experiments of particle size effect in X-ray fluorescence and implications to remote X-ray spectrometry of lunar regolith surface, *Earth Planet Sp* 60 (4) (2008) 293–297. <https://doi.org/10.1186/BF03352794>.
- [222] J.W. Criss, Particle size and composition effects in x-ray fluorescence analysis of pollution samples, *Analytical Chemistry* 48 (1) (1976) 179–186.
- [223] G.A. Hope, R. Woods, C.G. Munce, Raman microprobe mineral identification, *Minerals Engineering* 14 (12) (2001) 1565–1577. [https://doi.org/10.1016/S0892-6875\(01\)00175-3](https://doi.org/10.1016/S0892-6875(01)00175-3).
- [224] Deutsches Institut für Normung, *Chemische Analytik: Nachweis-, Erfassungs- und Bestimmungsgrenze unter Wiederholungsbedingungen 71.040.01*, 2008.
- [225] H.B. Al Ba'ba'a, T. Elgammal, R.S. Amano, Correlations of Bubble Diameter and Frequency for Air–Water System Based on Orifice Diameter and Flow Rate, *J. Fluids Eng* 138 (11) (2016) 114501. <https://doi.org/10.1115/1.4033749>.
- [226] M. Lichti, H.-J. Bart, Bubble size distributions with a shadowgraphic optical probe, *Flow Measurement and Instrumentation* 60 (2018) 164–170. <https://doi.org/10.1016/j.flowmeasinst.2018.02.020>.

- [227] B. Lewandowski, M. Fertig, G. Krekel, M. Ulbricht, Analysis of wake structures in bubbly flows using Particle Image Velocimetry (PIV), *Chemical & Process Engineering* 40 (1) (2019) 49–55. <https://doi.org/10.24425/cpe.2018.124996>.
- [228] T. Miyahara, S. Kaseno, T. Takahashi, Studies on chains of bubbles rising through quiescent liquid, *Can. J. Chem. Eng.* 62 (2) (1984) 186–193. <https://doi.org/10.1002/cjce.5450620205>.
- [229] L. Böhm, M. Kraume, Investigation of single bubbles rising in narrow rectangular channels with Particle Image Velocimetry, 16th International Symposium on Application of Laser Techniques to Fluid Mechanics, Lisbon (2012).
- [230] B. Lewandowski, M. Fertig, M. Ulbricht, G. Krekel, Relationship between bubble characteristics and hydrodynamic parameters for single bubbles in presence of surface active agents, *Chemical Engineering Science* 199 (2019) 179–198. <https://doi.org/10.1016/j.ces.2019.01.026>.
- [231] A. Rafiei, M. Robbertze, J. Finch, Gas holdup and single bubble velocity profile, *International Journal of Mineral Processing* 98 (1-2) (2011) 89–93. <https://doi.org/10.1016/j.minpro.2010.10.011>.
- [232] K.N. Han, M.C. Fuerstenau (Eds.), *Principles of mineral processing*, Society for Mining, Metallurgy and Exploration, Littleton, Colo, 2009.
- [233] C. Fong, T.L. Greaves, T.W. Healy, C.J. Drummond, The effect of structural modifications on the solution and interfacial properties of straight and branched aliphatic alcohols: the role of hydrophobic effects, *Journal of Colloid and Interface Science* 449 (2015) 364–372. <https://doi.org/10.1016/j.jcis.2015.01.045>.
- [234] Y. Li, T. Zhu, Y. Liu, Y. Tian, H. Wang, Effects of surfactant on bubble hydrodynamic behavior under flotation-related conditions in wastewater, *Water science and technology* 65 (6) (2012) 1060–1066. <https://doi.org/10.2166/wst.2012.933>.
- [235] H. Zhu, A.L. Valdivieso, J. Zhu, S. Song, F. Min, M.A. Corona Arroyo, A study of bubble size evolution in Jameson flotation cell, *Chemical Engineering Research and Design* 137 (2018) 461–466. <https://doi.org/10.1016/j.cherd.2018.08.005>.
- [236] D.G. Karamanev, Equations for calculation of the terminal velocity and drag coefficient of solid spheres and gas bubbles, *Chemical Engineering Communications* 147 (1) (1996) 75–84. <https://doi.org/10.1080/00986449608936496>.
- [237] D.G. Karamanev, Rise of gas bubbles in quiescent liquids, *AIChE J.* 40 (8) (1994) 1418–1421. <https://doi.org/10.1002/aic.690400814>.
- [238] J.R. Grace, Shapes and velocities of single drops and bubbles moving freely through immiscible liquids, *Chem. Eng. Res. Des.* 54 (1976) 167–173.

- [239] B. Comley, P. Harris, D. Bradshaw, M. Harris, Frother characterisation using dynamic surface tension measurements, *International Journal of Mineral Processing* 64 (2-3) (2002) 81–100. [https://doi.org/10.1016/S0301-7516\(01\)00065-5](https://doi.org/10.1016/S0301-7516(01)00065-5).
- [240] J.A. Finch, J.E. Nasset, C. Acuña, Role of frother on bubble production and behaviour in flotation, *Minerals Engineering* 21 (12-14) (2008) 949–957. <https://doi.org/10.1016/j.mineng.2008.04.006>.
- [241] R.A. Grau, J.S. Laskowski, Role of Frothers in Bubble Generation and Coalescence in a Mechanical Flotation Cell, *The Canadian Journal of Chemical Engineering* 84 (2) (2006) 170–182. <https://doi.org/10.1002/cjce.5450840204>.
- [242] V. Machon, A.W. Pacek, A.W. Nienow, Bubble Sizes in Electrolyte and Alcohol Solutions in a Turbulent Stirred Vessel, *Chemical Engineering Research and Design* 75 (3) (1997) 339–348. <https://doi.org/10.1205/026387697523651>.
- [243] C. Yang, T. Dabros, D. Li, J. Czarnecki, J.H. Masliyah, Measurement of the Zeta Potential of Gas Bubbles in Aqueous Solutions by Microelectrophoresis Method, *Journal of Colloid and Interface Science* 243 (1) (2001) 128–135. <https://doi.org/10.1006/jcis.2001.7842>.
- [244] W. Jia, S. Ren, B. Hu, Effect of Water Chemistry on Zeta Potential of Air Bubbles, *International Journal of Electrochemical Science* 8 (2013) 5828–5837.
- [245] D.J. Shaw, *Introduction to colloid and surface chemistry*, 4th ed., Butterworth-Heinemann, Oxford, 1999.
- [246] S. Paria, C. Manohar, K.C. Khilar, Kinetics of Adsorption of Anionic, Cationic, and Nonionic Surfactants, *Ind. Eng. Chem. Res.* 44 (9) (2005) 3091–3098. <https://doi.org/10.1021/ie049471a>.
- [247] C. Yan, A. Angus-Smyth, C.D. Bain, Adsorption kinetics of non-ionic surfactants in micellar solutions: Effects of added charge, *Faraday Discuss* 160 (2013) 45–61. <https://doi.org/10.1039/C2FD20118F>.
- [248] S. Gélinas, J.A. Finch, M. Gouet-Kaplan, Comparative real-time characterization of frother bubble thin films, *Journal of Colloid and Interface Science* 291 (1) (2005) 187–191. <https://doi.org/10.1016/j.jcis.2005.04.094>.
- [249] S. Fleckenstein, D. Bothe, Simplified modeling of the influence of surfactants on the rise of bubbles in VOF-simulations, *Chemical Engineering Science* 102 (2013) 514–523. <https://doi.org/10.1016/j.ces.2013.08.033>.
- [250] P. Di Marco, W. Grassi, G. Memoli, Experimental study on rising velocity of nitrogen bubbles in FC-72, *International Journal of Thermal Sciences* 42 (5) (2003) 435–446. [https://doi.org/10.1016/S1290-0729\(02\)00044-3](https://doi.org/10.1016/S1290-0729(02)00044-3).

- [251] T. Saito, K. Sakakibara, Y. Miyamoto, M. Yamada, A study of surfactant effects on the liquid-phase motion around a zigzagging-ascent bubble using a recursive cross-correlation PIV, *Chemical Engineering Journal* 158 (1) (2010) 39–50.  
<https://doi.org/10.1016/j.cej.2008.07.021>.
- [252] Y. Tagawa, S. Takagi, Y. Matsumoto, Surfactant effect on path instability of a rising bubble, *J. Fluid Mech.* 738 (2014) 124–142. <https://doi.org/10.1017/jfm.2013.571>.
- [253] A. Alke, D. Bothe, 3D numerical modeling of soluble surfactant at fluidic interfaces based on the volume-of-fluid method, *FDMP* 1 (2009) 1–29.
- [254] A.M. Aliyu, H. Seo, H. Kim, K.C. Kim, Characteristics of bubble-induced liquid flows in a rectangular tank, *Experimental Thermal and Fluid Science* 97 (2018) 21–35.  
<https://doi.org/10.1016/j.expthermflusci.2018.04.003>.
- [255] L.F. Richardson, *Weather prediction by numerical process*, 2nd ed., Cambridge Mathematical Library, Cambridge, 2007.
- [256] Thermo Scientific, *Objektträger: product data sheet*, 2015.
- [257] J.R. Taylor, *An introduction to error analysis: The study of uncertainties in physical measurements*, 2nd ed., University Science Books, Sausalito, Calif., 1997.
- [258] P.S. Noonan, A. Shavit, B.R. Acharya, D.K. Schwartz, Mixed alkylsilane functionalized surfaces for simultaneous wetting and homeotropic anchoring of liquid crystals, *ACS Appl. Mater. Interfaces* 3 (11) (2011) 4374–4380.  
<https://doi.org/10.1021/am201026r>.
- [259] Sigmund Lindner GmbH, *SiLibeads SOLID Micro Glass Beads: product data sheet*, 2017.
- [260] T. Miettinen, *Fine Particle Flotation*. Ph.D. thesis, University of South Australia, Adelaide, 2007.
- [261] Y. Gu, D. Li, The  $\zeta$ -Potential of Glass Surface in Contact with Aqueous Solutions, *Journal of Colloid and Interface Science* 226 (2) (2000) 328–339.  
<https://doi.org/10.1006/jcis.2000.6827>.
- [262] P. Somasundaran, A. Lou, *Oxide Mineral Flotation Fundamentals*, in: B.K. Parekh, J.D. Miller (Eds.), *Advances in Flotation Technology*, 1st ed., Society for Mining, Metallurgy and Exploration, Littleton, Colorado, 1999, pp. 23–44.
- [263] X. Zhou, Y.H. Tan, J.A. Finch, Effect of pH and time on hydrodynamic properties of dodecylamine, *Physicochemical Problems of Mineral Processing* 54 (4) (2018) 1237–1244. <https://doi.org/10.5277/ppmp18165>.
- [264] J.L. Scott, R.W. Smith, Diamine flotation of quartz, *Minerals Engineering* 4 (2) (1991) 141–150. [https://doi.org/10.1016/0892-6875\(91\)90030-Y](https://doi.org/10.1016/0892-6875(91)90030-Y).

- [265] R.W. Smith, J.L. Scott, Mechanisms of Dodecylamine Flotation of Quartz, *Mineral Processing and Extractive Metallurgy Review* 7 (2) (1990) 81–94.  
<https://doi.org/10.1080/08827509008952667>.
- [266] A.M. Vieira, A.E. Peres, The effect of amine type, pH, and size range in the flotation of quartz, *Minerals Engineering* 20 (10) (2007) 1008–1013.  
<https://doi.org/10.1016/j.mineng.2007.03.013>.
- [267] P.B. Kowalczyk, M. Siedlarz, S. Szczerkowska, M. Wojcik, Facile determination of foamability index of non-ionic and cationic frothers and its effect on flotation of quartz, *Separation Science and Technology* 53 (8) (2017) 1198–1206.  
<https://doi.org/10.1080/01496395.2017.1293100>.
- [268] E. Burdukova, J.S. Laskowski, Effect of insoluble amine on bubble surfaces on particle-bubble attachment in potash flotation, *Can. J. Chem. Eng.* 87 (3) (2009) 441–447. <https://doi.org/10.1002/cjce.20177>.
- [269] J.S. Laskowski, From amine molecules adsorption to amine precipitate transport by bubbles: A potash ore flotation mechanism, *Minerals Engineering* 45 (2013) 170–179.  
<https://doi.org/10.1016/j.mineng.2013.02.010>.
- [270] B. Lewandowski, C. Nielsen, M. Ulbricht, G. Krekel, Investigation of formation and characteristics of heterocoagulates in flotation processes with Shadowgraphy, in: *7th European Young Engineers Conference Monograph*, Warsaw University of Technology, Faculty of Chemical and Process Engineering, Warsaw, 2018, pp. 205–214.
- [271] L.I. Berger, A.K. Covington, K. Fischer et al., Physical Constants of Organic Compounds, in: R.D. Lide (Ed.), *CRC Handbook of Chemistry and Physics*, 85th ed., CRC Press, Boca Raton, 2005, 3-1 - 3-740.
- [272] S. Ata, G.J. Jameson, The formation of bubble clusters in flotation cells, *International Journal of Mineral Processing* 76 (1-2) (2005) 123–139.  
<https://doi.org/10.1016/j.minpro.2004.12.007>.
- [273] I. Brezani, F. Zelenak, MATLAB® tool for modeling first order flotation kinetics, 2010.
- [274] B.P. Radoev, L.B. Alexandrova, S.D. Tchaljovska, On the kinetics of froth flotation, *International Journal of Mineral Processing* 28 (1-2) (1990) 127–138.  
[https://doi.org/10.1016/0301-7516\(90\)90031-S](https://doi.org/10.1016/0301-7516(90)90031-S).
- [275] P.B. Kowalczyk, Flotation and hydrophobicity of quartz in the presence of hexylamine, *International Journal of Mineral Processing* 140 (2015) 66–71.  
<https://doi.org/10.1016/j.minpro.2015.05.002>.

- [276] F. Hernáinz, M. Calero, G. Blázquez, Kinetic considerations in the flotation of phosphate ore, *Advanced Powder Technology* 16 (4) (2005) 347–361.  
<https://doi.org/10.1163/1568552054194203>.
- [277] F. Hernáinz Bermúdez De Castro, M. Calero De Hocés, Flotation rate of celestite and calcite, *Chemical Engineering Science* 51 (1) (1996) 119–125.  
[https://doi.org/10.1016/0009-2509\(95\)00235-9](https://doi.org/10.1016/0009-2509(95)00235-9).
- [278] E. Yalcin, S. Kelebek, Flotation kinetics of a pyritic gold ore, *International Journal of Mineral Processing* 98 (1-2) (2011) 48–54. <https://doi.org/10.1016/j.minpro.2010.10.005>.
- [279] J.K. Beattie, A.M. Djerdjev, A. Gray-Weale, N. Kallay, J. Lützenkirchen, T. Preočanin, A. Selmani, pH and the surface tension of water, *Journal of Colloid and Interface Science* 422 (2014) 54–57. <https://doi.org/10.1016/j.jcis.2014.02.003>.
- [280] W.J. Zhao, D.W. Liu, H.S. Li, Q.C. Feng, G.Y. Xu, J.J. Yuan, X.D. Jia, Influence of Pulp pH on Flotation of Fluorite and Calcite, *Advanced Materials Research* 616-618 (2013) 614–618. <https://doi.org/10.4028/www.scientific.net/AMR.616-618.614>.
- [281] G. Zhang, Y. Gao, W. Chen, D. Liu, The Role of Water Glass in the Flotation Separation of Fine Fluorite from Fine Quartz, *Minerals* 7 (9) (2017) 157.  
<https://doi.org/10.3390/min7090157>.
- [282] R. Zheng, Z. Ren, H. Gao, Y. Qian, Flotation Behavior of Different Colored Fluorites Using Sodium Oleate as a Collector, *Minerals* 7 (9) (2017) 159.  
<https://doi.org/10.3390/min7090159>.
- [283] R.J. Pugh, The role of the solution chemistry of dodecylamine and oleic acid collectors in the flotation of fluorite, *Colloids and Surfaces* 18 (1) (1986) 19–41.  
[https://doi.org/10.1016/0166-6622\(86\)80191-3](https://doi.org/10.1016/0166-6622(86)80191-3).
- [284] R. Pugh, P. Stenius, Solution chemistry studies and flotation behaviour of apatite, calcite and fluorite minerals with sodium oleate collector, *International Journal of Mineral Processing* 15 (3) (1985) 193–218. [https://doi.org/10.1016/0301-7516\(85\)90035-3](https://doi.org/10.1016/0301-7516(85)90035-3).
- [285] H. Schubert, H. Baldauf, W. Kramer, J. Schoenherr, Further development of fluorite flotation from ores containing higher calcite contents with oleoylsarcosine as collector, *International Journal of Mineral Processing* 30 (3-4) (1990) 185–193.  
[https://doi.org/10.1016/0301-7516\(90\)90014-P](https://doi.org/10.1016/0301-7516(90)90014-P).
- [286] Hernáinz Bermúdez de Castro, F, A.G. Borrego, Modification of Surface Tension in Aqueous Solutions of Sodium Oleate According to Temperature and pH in the Flotation Bath, *Journal of Colloid and Interface Science* 173 (1) (1995) 8–15.  
<https://doi.org/10.1006/jcis.1995.1290>.

- [287] K. Theander, R.J. Pugh, The Influence of pH and Temperature on the Equilibrium and Dynamic Surface Tension of Aqueous Solutions of Sodium Oleate, *Journal of Colloid and Interface Science* 239 (1) (2001) 209–216. <https://doi.org/10.1006/jcis.2000.7543>.
- [288] P. Sreedevi, K. Chennakesavulu, M. Kavitha, G.B. Raju, S. Prabhakar, Electrokinetic Behavior of Fluorite, *Journal of Dispersion Science and Technology* 32 (9) (2011) 1306–1310. <https://doi.org/10.1080/01932691.2010.505813>.
- [289] Z. Chen, Z. Ren, H. Gao, Y. Qian, R. Zheng, Effect of modified starch on separation of fluorite from barite using sodium oleate, *Physicochemical Problems of Mineral Processing* 54 (2) (2018) 228–237. <https://doi.org/10.5277/ppmp1806>.
- [290] Z. Ren, F. Yu, H. Gao, Z. Chen, Y. Peng, L. Liu, Selective Separation of Fluorite, Barite and Calcite with Valonea Extract and Sodium Fluosilicate as Depressants, *Minerals* 7 (2) (2017) 24. <https://doi.org/10.3390/min7020024>.
- [291] R.W. Smith, D. Shonnard, Electrokinetic study of the role of modifying agents in flotation of salt-type minerals, *AIChE J.* 32 (5) (1986) 865–868. <https://doi.org/10.1002/aic.690320519>.
- [292] V.S. Craig, B.W. Ninham, R.M. Pashley, Effect of electrolytes on bubble coalescence, *Nature* 364 (6435) (1993) 317.
- [293] V.S.J. Craig, B.W. Ninham, R.M. Pashley, The effect of electrolytes on bubble coalescence in water, *J. Phys. Chem.* 97 (39) (1993) 10192–10197. <https://doi.org/10.1021/j100141a047>.
- [294] C.L. Henry, C.N. Dalton, L. Scruton, V.S.J. Craig, Ion-Specific Coalescence of Bubbles in Mixed Electrolyte Solutions, *J. Phys. Chem. C* 111 (2) (2007) 1015–1023. <https://doi.org/10.1021/jp066400b>.
- [295] W. Müller, *Mechanische Verfahrenstechnik und ihre Gesetzmäßigkeiten*, 2nd ed., Oldenbourg, München, 2014.
- [296] A. Atrafí, C.O. Gomez, J.A. Finch, M. Pawlik, Frothing behavior of aqueous solutions of oleic acid, *Minerals Engineering* 36-38 (2012) 138–144. <https://doi.org/10.1016/j.mineng.2012.03.020>.
- [297] M. Sauer, J. Hofkens, J. Enderlein, *Handbook of fluorescence spectroscopy and imaging: From single molecules to ensembles*, Wiley-VCH, Weinheim, 2011.
- [298] A.-E. Sommer, M. Nikpay, S. Heitkam, M. Rudolph, K. Eckert, A novel method for measuring flotation recovery by means of 4D particle tracking velocimetry, *Minerals Engineering* 124 (2018) 116–122. <https://doi.org/10.1016/j.mineng.2018.05.006>.

- 
- [299] M.J. Sathe, I.H. Thaker, T.E. Strand, J.B. Joshi, Advanced PIV/LIF and shadowgraphy system to visualize flow structure in two-phase bubbly flows, *Chemical Engineering Science* 65 (8) (2010) 2431–2442. <https://doi.org/10.1016/j.ces.2009.11.014>.
- [300] G. Vázquez, E. Alvarez, J.M. Navaza, Surface Tension of Alcohol Water + Water from 20 to 50°C, *J. Chem. Eng. Data* 40 (3) (1995) 611–614. <https://doi.org/10.1021/je00019a016>.

## 9 Appendix

### 9.1 Supporting information

All of the supporting information including the raw data files can be found on the external hard drive in Prof. Dr. Krekel's office at Niederrhein University of Applied Sciences in Krefeld.

#### 9.1.1 Materials, chemicals, and software

In the following tables, all used materials, chemicals, and software, which were used in this work, are listed.

##### *Materials*

<b>Material</b>	<b>Type</b>	<b>Supplier</b>
Acrifix <sup>®</sup>	1R 0192	Evonik Industries AG
Circulation air dryer	FP 53	Binder
Continuous wave laser	Nd:YAG, 532 nm, 5 W	Dantec Dynamics
Fluorescence Photometer	Cary Eclipse	Agilent Technologies
Frame grabber	Xtium-CL MX4	Teledyne Dalsa
FT Raman spectrometer	Nicolet NXR with an InGaAs detector and a CaF <sub>2</sub> beam splitter	Thermo Scientific
Gas tight syringes	glass	Hamilton
Glass slides	76 x 26 mm, cut edges	Thermo Scientific
High-speed camera	Olympus iSpeed TR	Olympus
High-speed camera	VC-2MC-C340E0-CM	Vieworks
Laser diffraction	Helos KR	Sympatec
LED backlight illumination	80x730, 120 W	Dantec Dynamics
LED backlight illumination	50x50-LLUB-Q-1R-24V	Phlox
Lense attachment	0.5x	Navitar
Micro glass spheres	SiLibeads Type S	Sigmund Lindner GmbH
Optical microscope	DM2500	Leica
Overhead stirrer	T25D	IKA GmbH & Co. KG
Planetary ball mill	PM 100	Retsch
Poly(methyl methacrylate) (PMMA)	Acryglass Solar 2458	Evonik Industries AG

<b>Material</b>	<b>Type</b>	<b>Supplier</b>
Polyether ether ketone (PEEK) capillaries	1/16" outer diameter, varying inner diameter	Techlab
Precision grade glass spheres	SiLibeads Type P	Sigmund Lindner GmbH
Progressing cavity pump	JP-7115.2 GM	Jessberger
Reflex camera	DS126311	Canon
Stirrer	Rushton turbine, d <sub>R</sub> =70 mm	IKA
Scale	LE1003S	Sartorius
Scanning electron microscope	TM3000	Hitachi
Sieves	varying sieve openings	Retsch
Syringe pump	KD200P	Cole-Parmer
Telescope goniometer	OCA 15EC	DataPhysics Instruments GmbH
Ultrasonic cleaning bath	SONOREX SUPER RK 106	Bandelin
UV-Vis-NIR spectrophotometer	Cary 5000	Agilent Technologies
Vacuum pump	PC3001 Vario	Vacuu Brand
Variable area flowmeter	LTMR, 0-10 L/min	Cole-Parmer
Vibration sieving machine	AS 200	Retsch
XTXRF-spectrometer	S2 PICOFOX	Bruker
Zoom lense	12x, C-Mount	Navitar
Zoom lense adapter	2x, F-Mount	Navitar

### Chemicals

<b>Chemical</b>	<b>Supplier</b>	<b>Quality</b>
1H,1H,2H,2H-Perfluorooctyltriethoxysilane	Alfa Aesar	97 %
Barium sulphate	metallpulver24	92 %
Calcium fluoride	Alfa Aesar	99 %
Deionized water	In-house purification	$\kappa=17 \mu\text{S/cm}$
Ethanol abs.	Bernd Kraft	99.5 %
Ethanol technical grade	Bernd Kraft	96 %
Ethylenglycol	Carl Roth	99.5 %
Ethyltriethoxysilane	Alfa Aesar	96 %
Glycerol	Carl Roth	99.5 %

Chemical	Supplier	Quality
Hexadecylamine	Merck Millipore	92 %
Hydrogen peroxide	Bernd Kraft	30 %
Hydrochloric acid (conc.)	Carl Roth	25 %
Methyl isobutyl carbinol	Alfa Aesar	99 %
n-Dodecyltriethoxysilane	Alfa Aesar	95 %
n-Octyltriethoxysilane	Alfa Aesar	95 %
Oleic acid	Alfa Aesar	90 %
Silicon dioxide	Quarzwerte GmbH	98 %
Starch (soluble)	Acros Organics	p.a.
Sulphuric acid	Bernd Kraft	96 %
Toluene	Carl Roth	99.5 %
Tween80 <sup>®</sup>	Sigma-Aldrich	100 %

### Software

Material	Supplier
CamExpert	Teledyne Dalsa
ChemDraw Prime v16.0	PerkinElmer
CurveExpert Basic	Hyams Development
DynamicStudio v4.00	Dantec Dynamics
Excel 2013	Microsoft
Fusion 360	Autodesk
Illustrator CS6 v16.0.3 x64	Adobe
ImageJ v1.50i	GPL (open source)
iSpeed viewer	Olympus
KNIME analytics platform v3.4.2	GPL (open source)
MATLAB R2014a	Mathworks
Mintab v18.1.0.0	Minitab Inc.
Origin v8.5	OriginLab
Photoshop CS6 v13.0.1 x64	Adobe
SCA 20	DataPhysics Instruments GmbH
Tecplot 360 EX 2016 R1	Tecplot, Inc.
Vieworks Camera Control Tool	Vieworks
Visio 2013	Microsoft

The single bubble flotation column presented in chapter 3.1.1.1 is made from a special UV-permeable PMMA. The transmission spectrum of this PMMA is given in Fig. 9-1.

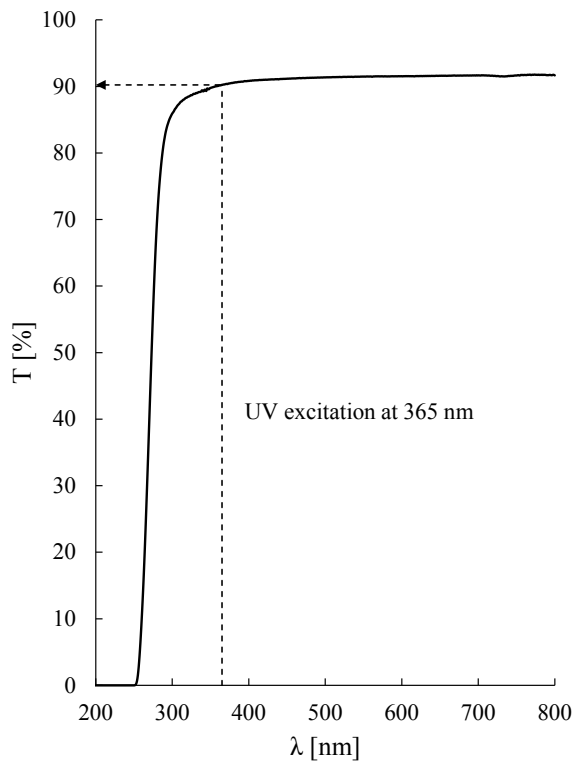


**Fig. 9-1.** Transmission T vs. wavelength  $\lambda$  for the special UV-permeable poly(methyl methacrylate) used for the design of the single bubble flotation column (cf. chapter 3.1.1.1).

### 9.1.2 Supporting information for two-phase investigations

In the following diagrams, the corresponding results to the measurements in MIBC solutions obtained for measurements in HDA solutions are presented (cf. chapter 4.2).

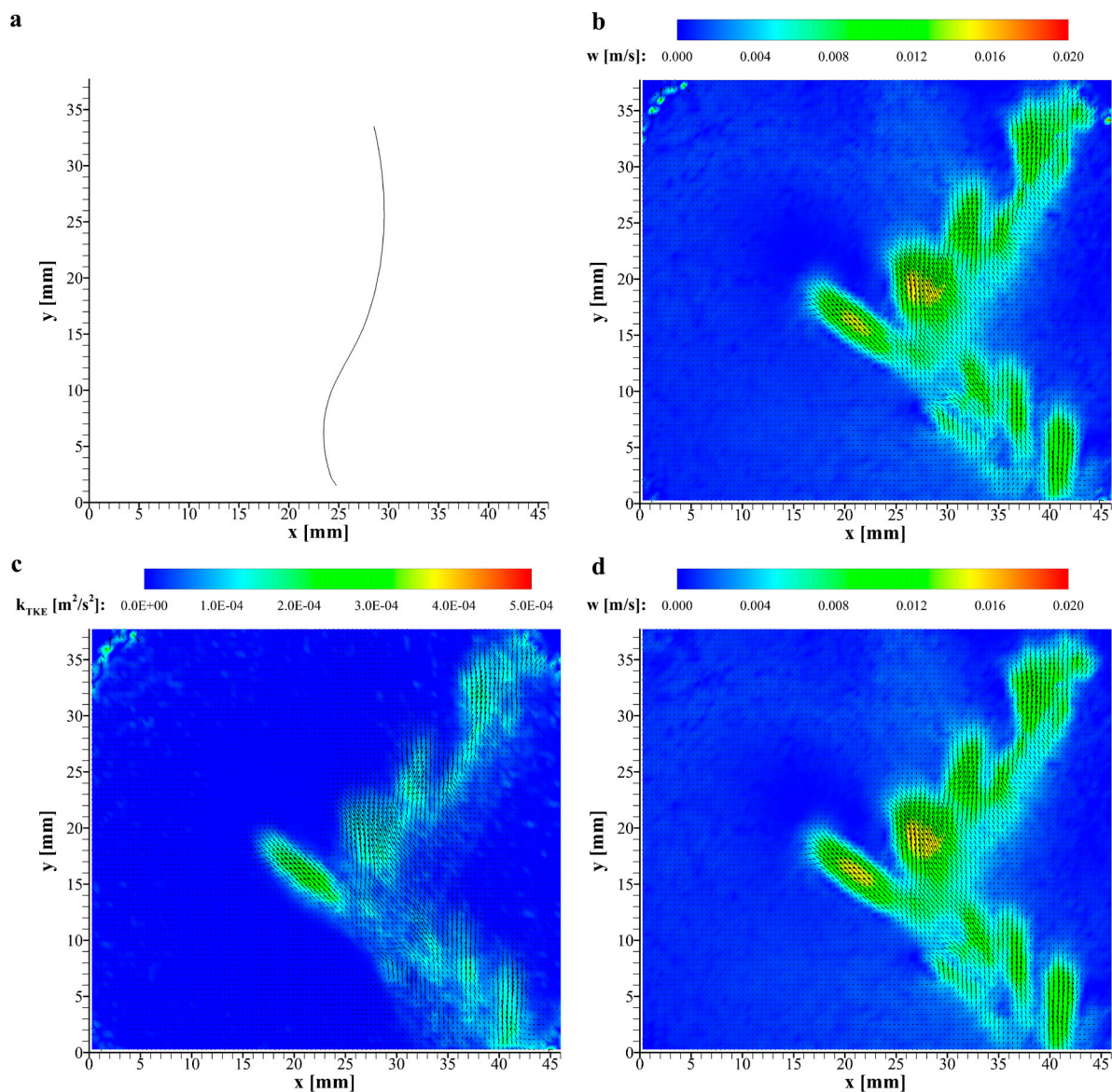


**Fig. 9-2.** Bubble trajectory (a), mean liquid velocity vector field (b), mean vector field as indicator for turbulent kinetic energy  $k_{\text{TKE}}$  (c), and reconstructed mean liquid velocity vector field using POD mode 0 coefficient (d) all for 1.7  $\mu\text{mol/L}$  hexadecylamine (blank spots indicate values larger than scale) [230].

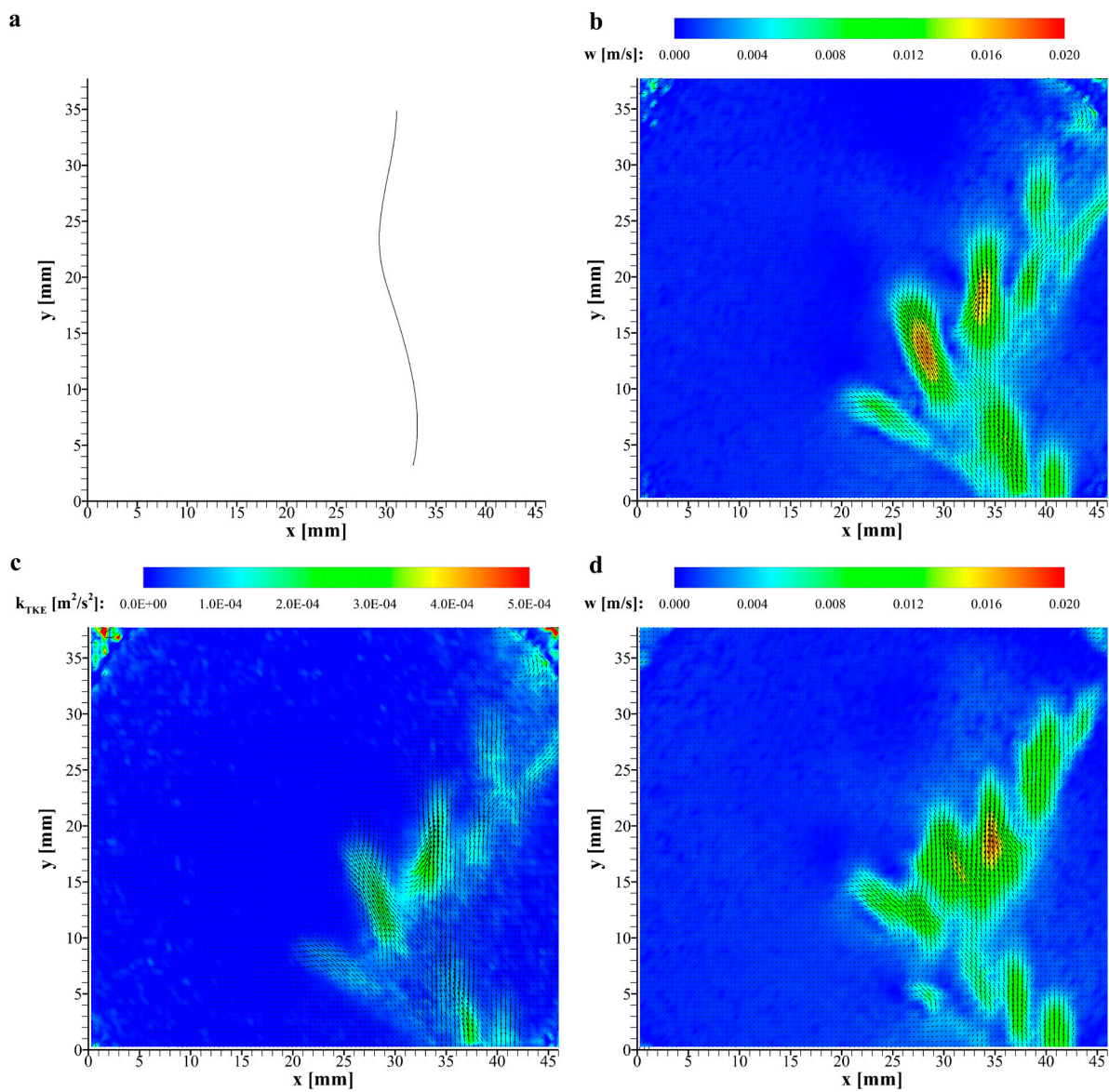


**Fig. 9-3.** Bubble trajectory (a), mean liquid velocity vector field (b), mean vector field as indicator for turbulent kinetic energy  $k_{TKE}$  (c), and reconstructed mean liquid velocity vector field using POD mode 0 coefficient (d) all for 5.2  $\mu\text{mol/L}$  hexadecylamine (blank spots indicate values larger than scale) [230].

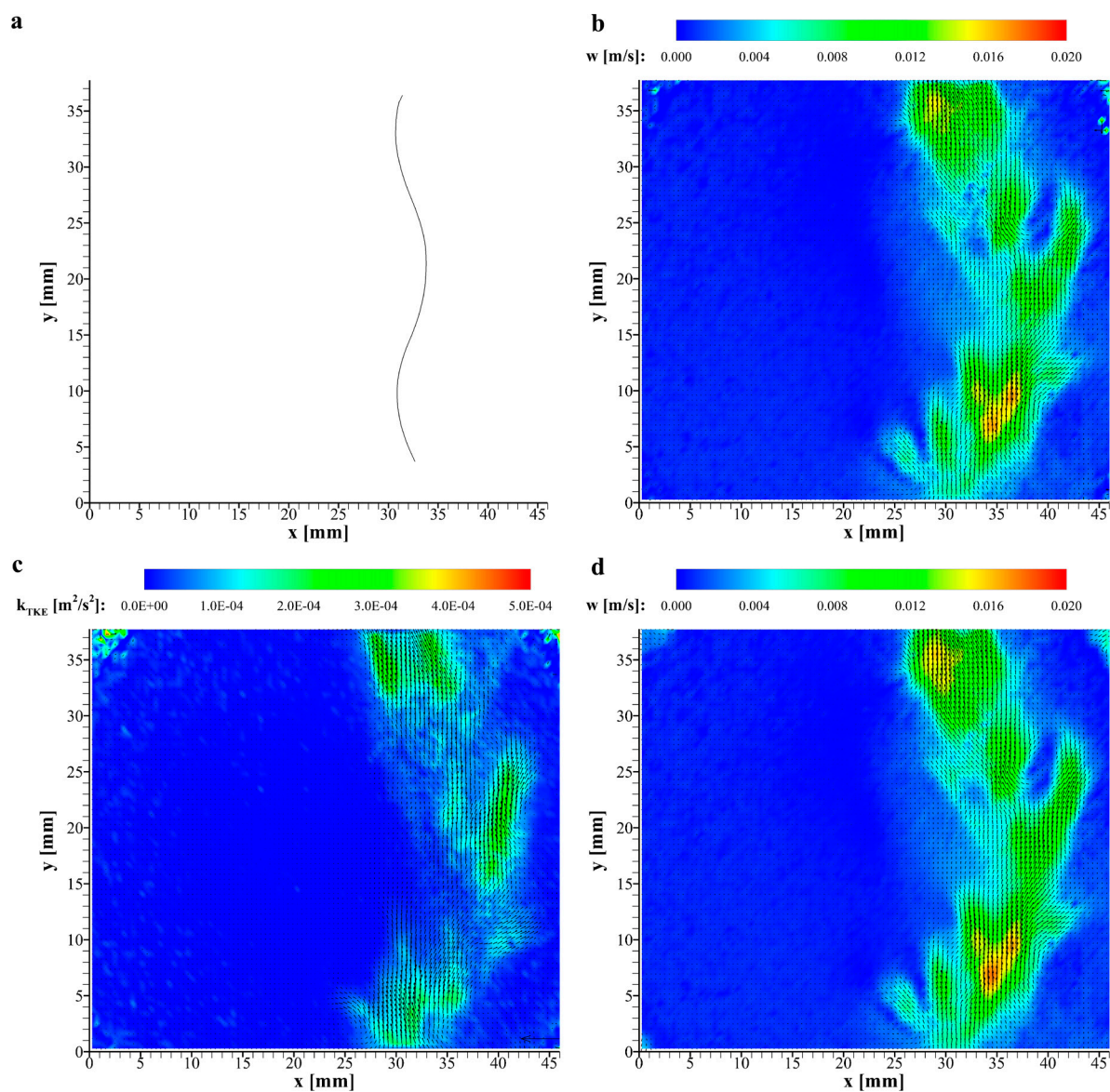


**Fig. 9-4.** Bubble trajectory (a), mean liquid velocity vector field (b), mean vector field as indicator for turbulent kinetic energy  $k_{\text{TKE}}$  (c), and reconstructed mean liquid velocity vector field using POD mode 0 coefficient (d) all for 24.2  $\mu\text{mol/L}$  hexadecylamine (blank spots indicate values larger than scale) [230].

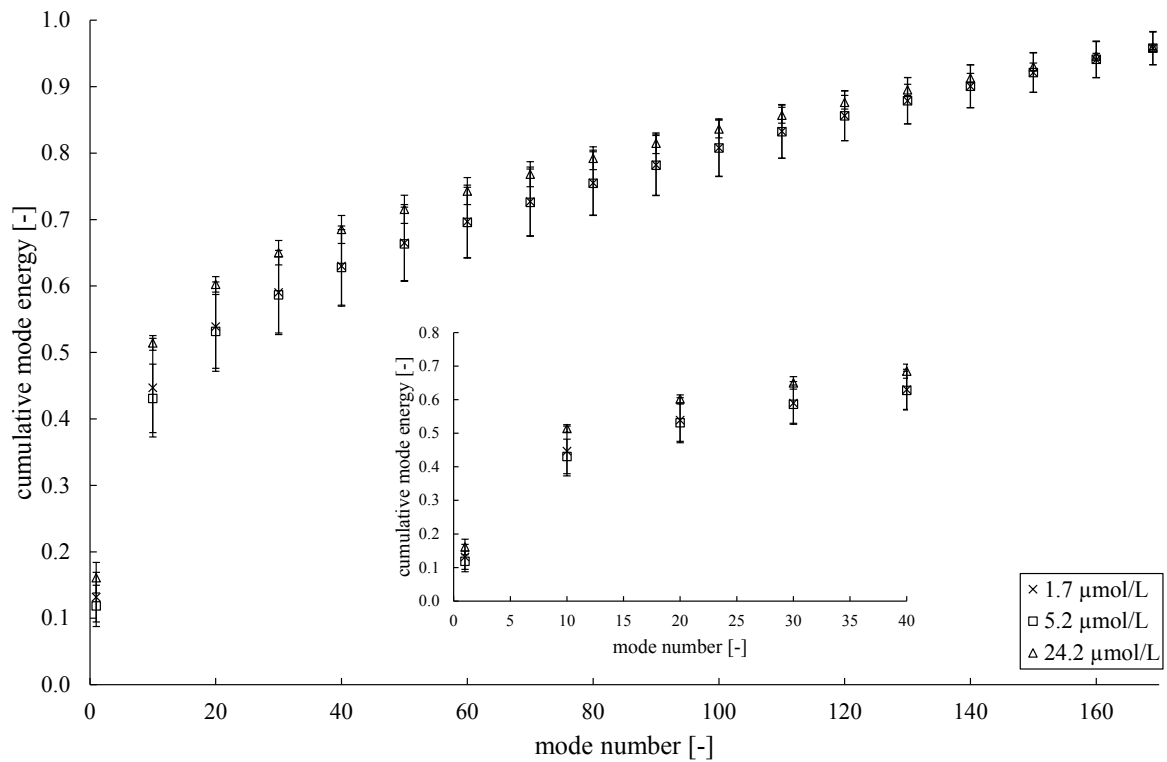


**Fig. 9-5.** Eigenvalues of modes shown as cumulative percentage sum of the turbulent kinetic energy of the fluctuating velocity field for POD analysis of varying hexadecylamine concentrations (only every 10<sup>th</sup> value shown) [230].

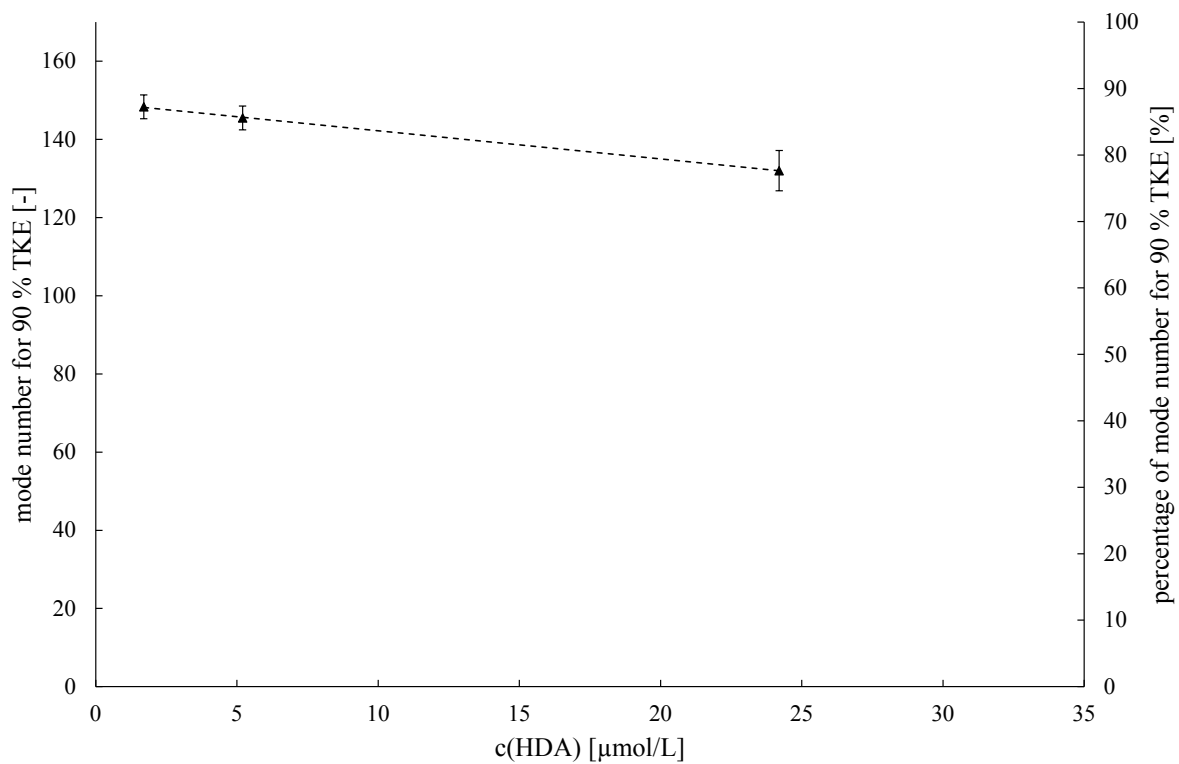


**Fig. 9-6.** Mode number and corresponding percentage necessary to represent 90 % of turbulent kinetic energy (TKE) depending on hexadecylamine concentration [230].

### 9.1.3 Supporting information for single bubble flotation experiments

#### 9.1.3.1 Liquid surface tension of ethanol-water solutions

The relationship between liquid surface tension  $\sigma$  of aqueous ethanol solutions and weight fraction of ethanol  $w_{\text{EtOH}}$ , which has been used for the determination of the critical surface tension of wettability  $\bar{\gamma}_c$  via film flotation experiments, e.g. of the glass particles (cf. chapter 5.1.2), is presented in Fig. 9-7. The data has been taken from literature [300].

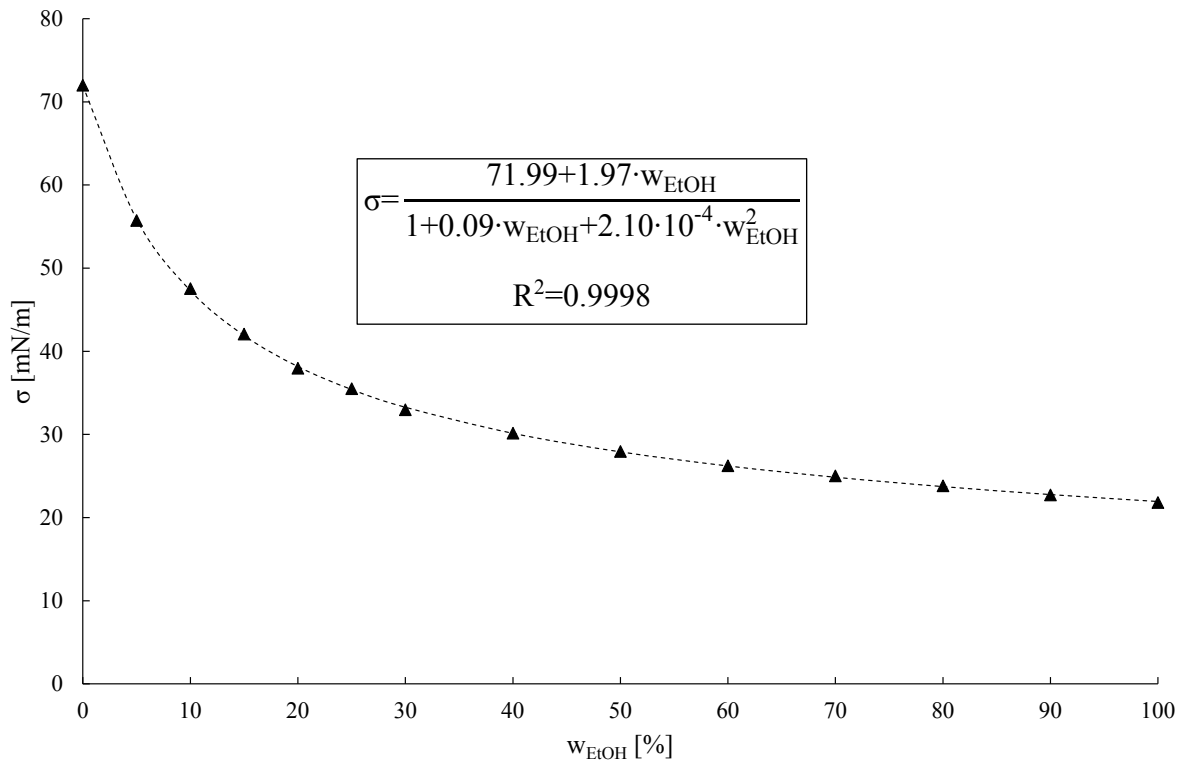


**Fig. 9-7.** Liquid surface tension  $\sigma$  of ethanol-water solutions with varying weight fractions of ethanol  $w_{\text{EtOH}}$  [300]. Dashed line indicates trend as represented by the rational model equation stated in the figure.

#### 9.1.3.2 Calculation of the circulating pump frequencies

As a premise for the particles to be suspended in the dispersion cell, the velocity of the liquid entering the dispersion cell has to be equal to that of the settling velocity of the particles  $w_s$ :

$$w_s = \sqrt{\frac{4}{3} \cdot \frac{(\rho_p - \rho_l) \cdot g \cdot d_p}{\rho_l \cdot c_D}} \quad (3-4)$$

The drag coefficient  $c_D$  in Eq. (3-4) is calculated using Kaskas equation (cf. chapter 3.2.1.2).

Thus,  $w_s(d_{50,3^*} = 86 \mu\text{m}) = 4.7 \cdot 10^{-3} \text{ m/s}$  and  $w_s(d_{50,3^*} = 56 \mu\text{m}) = 2.9 \cdot 10^{-2} \text{ m/s}$ .

The volumetric liquid flow rate  $\dot{V}$  of the pump is calculated via Eq. (9-1) with a cross-sectional area  $A$ :

$$\dot{V} = A \cdot w_s \quad (9-1)$$

The dispersion cell has a conical form, which is why a mean cross-sectional area is calculated. The mean area estimated for the calculation of  $\dot{V}$  is  $640 \text{ mm}^2$ . Thus,  $\dot{V}(d_{50,3^*}=86 \text{ }\mu\text{m})=0.18 \text{ L/min}$  and  $\dot{V}(d_{50,3^*}=256 \text{ }\mu\text{m})=1.14 \text{ L/min}$ .

From calibration experiments a linear relationship between  $\dot{V}$  and the adjusted frequency of the pump  $f$  is found (see Fig. 9-8). Thus, the frequency of the circulating pump can be calculated using this linear relationship.

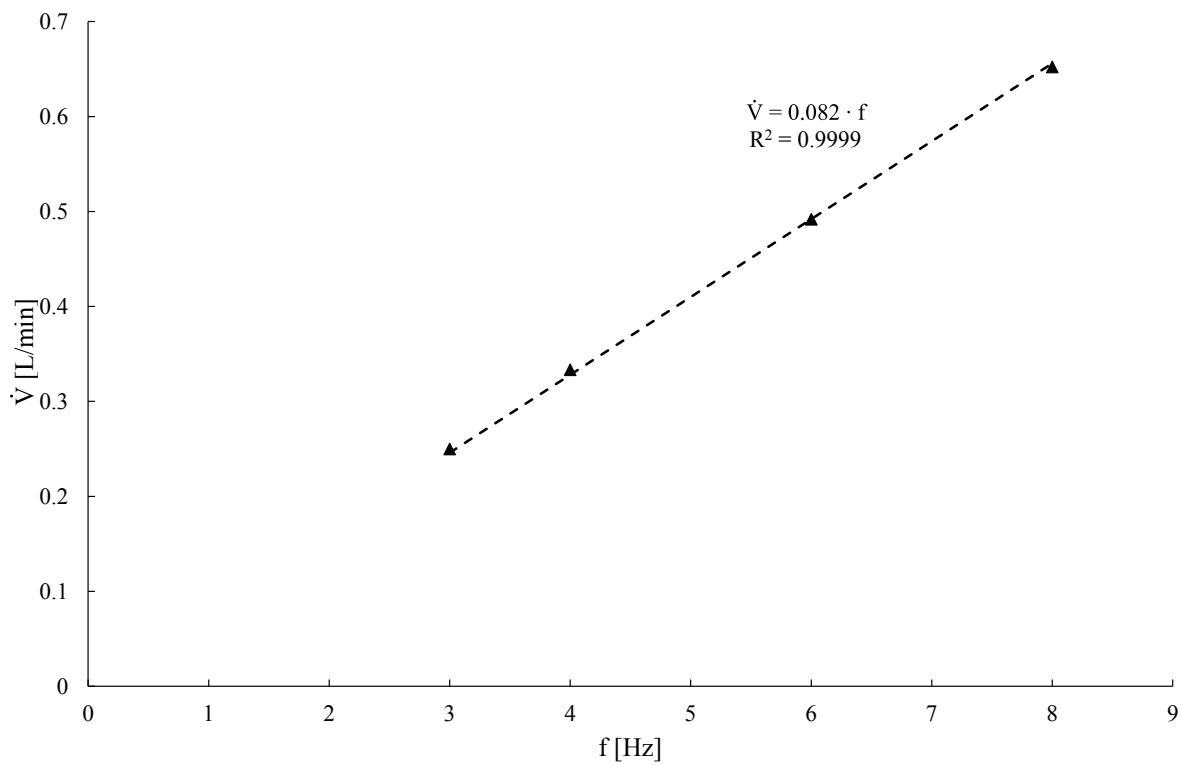


**Fig. 9-8.** Relationship between volumetric liquid flow rate  $\dot{V}$  and pump frequency  $f$ .

### 9.1.4 Supporting information for fluorescent fluorite mineral

The fluorescence spectra of an aqueous suspension of fluorescent fluorite particles is shown in Fig. 9-9. In Fig. 9-9a the emission is held constant at 420 nm, which refers to the colour blue. In Fig. 9-9b the excitation is held constant at 365 nm.

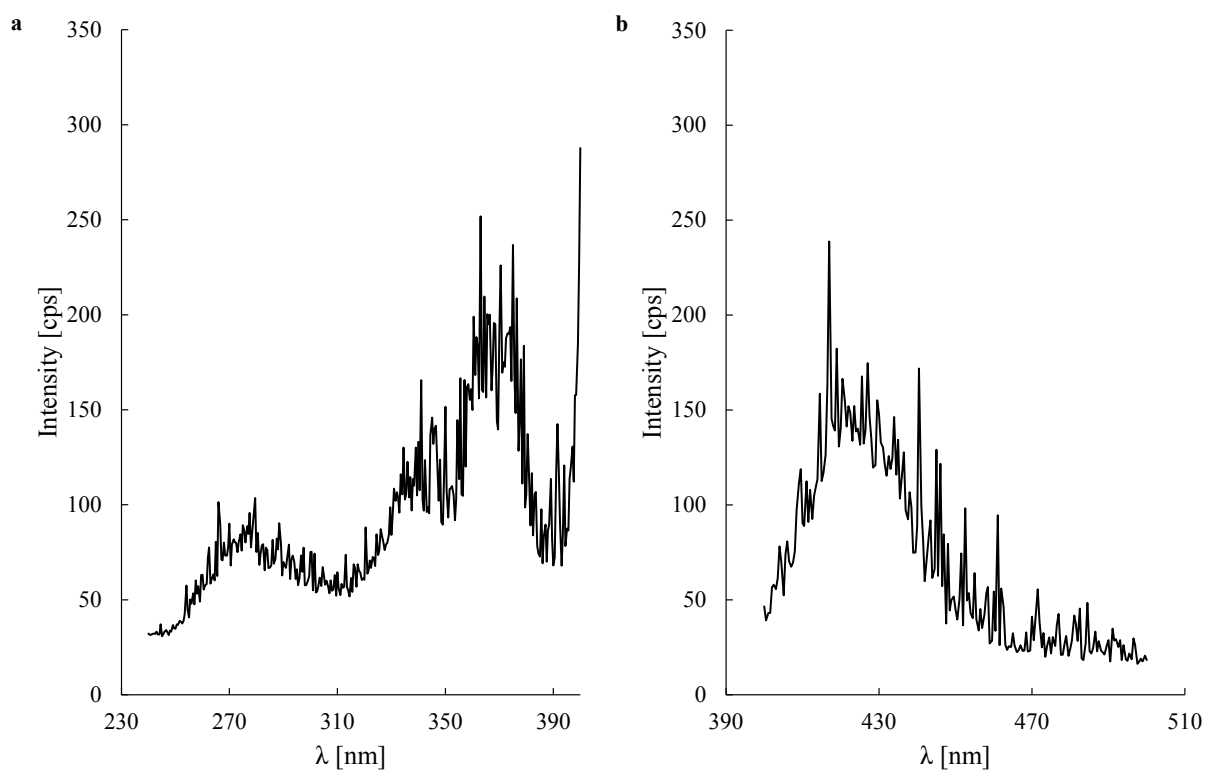


**Fig. 9-9.** Fluorescence spectra of an aqueous suspension of fluorescent fluorite mineral particles: measurement at a constant emission of 420 nm (a) and measurement at a constant excitation of 365 nm (b).

## 9.2 List of publications

### Publications

#### Peer Reviewed

- 03/2019 Lewandowski, B., Ben Said, B., Ulbricht, M., Krekel, G.: “Application of Raman spectroscopy to the flotation process of fluorite”, *Minerals Engineering* **135** (2019), p. 129-138, DOI: 10.1016/j.mineng.2019.02.038
- 03/2019 Lewandowski, B., Fertig, M., Krekel, G., Ulbricht, M.: “Analysis of wake structures in bubbly flows using Particle Image Velocimetry (PIV)”, *Chemical & Process Engineering* **40** (2019), p.49-55, DOI: 10.24425/cpe.2018.124996
- 01/2019 Lewandowski, B., Fertig, M., Ulbricht, M., Krekel, G.: “Relationship between bubble characteristics and hydrodynamic parameters for single bubbles in presence of surface active agents”, *Chemical Engineering Science* **199** (2019), p. 179-198, DOI: 10.1016/j.ces.2019.01.026
- 05/2018 Lewandowski, B., Ulbricht, M., Krekel, G.: “An automated image analysing routine for estimation of equivalent diameter in high-speed image sequences with high accuracy and its validation”, *Experimental Thermal and Fluid Science* **98** (2018), p. 158-169, DOI: 10.1016/j.expthermflusci.2018.05.016

#### Conference Proceedings

- 09/2018 Lewandowski, B., Nielsen, C.; Fertig, M., Schippers, C., Serdarevic, S., Ix, A., Kuhl, I., Schröder, S., Ulbricht, M., Krekel, G.: “Anwendung fortgeschrittener optischer Methoden zur Charakterisierung komplexer Mehrphasenströmungen”, *Chemie Ingenieur Technik*, **90** (2018), p. 1317-1318, DOI: 10.1002/cite.201855401
- 04/2018 Lewandowski, B., Fertig, M., Krekel, G., Ulbricht, M.: “Analysis of wake structures in bubbly flows using Particle Image Velocimetry (PIV)”, 7<sup>th</sup> EYEC monograph, 2018, p. 367-375, ISBN: 978-83-936575-5-1
- 04/2018 Lewandowski, B., Nielsen, C., Krekel, G., Ulbricht, M.: “Investigation of formation and characteristics of heterocoagulates in flotation processes with Shadowgraphy”, p. 205-214, 7<sup>th</sup> EYEC monograph, 2018, ISBN: 978-83-936575-5-1

**Presentations / Talks**

- 03/2019 6<sup>th</sup> Promovendentag Niederrhein University of Applied Sciences, Mönchengladbach  
„Anwendung optischer Methoden zur Untersuchung und Charakterisierung komplexer Mehrphasenströmungen in Zweiphasen- und Dreiphasensystemen“
- 11/2018 Process Mineralogy '18, Cape Town, South Africa  
„Application of Raman spectroscopy to the flotation process of fluorite“
- 09/2018 Annual ProcessNet conference and 33rd annual DECHEMA Biotechnology conference, Aachen  
„Anwendung fortgeschrittener optischer Methoden zur Charakterisierung komplexer Mehrphasenströmungen“
- 04/2018 7<sup>th</sup> European Young Engineers Conference, Warsaw, Poland  
“Analysis of *wake* structures in bubbly flows using *Particle Image Velocimetry* (PIV)” and  
“Investigation of formation and characteristics of heterocoagulates in flotation processes with *Shadowgraphy*”
- 02/2018 5<sup>th</sup> Promovendentag Niederrhein University of Applied Sciences, Krefeld  
„Untersuchung komplexer Mehrphasenströmungen mittels optischer Methoden am Beispiel des Flotationsprozesses“
- 10/2016 7<sup>th</sup> Young Chemists' Symposium “Ruhr”, Dortmund  
„Investigation of the flotation process of fluorite by optical methods“

**Posters**

- 03/2018 Annual Symposium ProcessNet Subject Division “Multiphase flows”, Bremen  
„Analyse des durch aufsteigende Luftblasen induzierten Strömungsfeldes mittels *Particle Image Velocimetry* (PIV)“
- 03/2017 Annual Symposium ProcessNet Subject Division “Multiphase flows”, Dresden  
„Untersuchung frei aufsteigender Blasen in einer modularen Flotationskolonne mittels optischer Methoden“
- 01/2017 4<sup>th</sup> Promovendentag University of Applied Sciences Niederrhein, Krefeld  
„Aufbau und Inbetriebnahme einer modularen Versuchsapparatur zur Beobachtung frei aufsteigender Einzelblasen mittels optischer Methoden“
- 09/2016 Annual ProcessNet conference und 32nd annual DECHEMA Biotechnology conference, Aachen  
„Untersuchung der Flotation von Flussspat (CaF<sub>2</sub>) mittels optischer Methoden“

### **9.3 Curriculum Vitae**

Der Lebenslauf ist in der Online-Version aus Gründen des Datenschutzes nicht enthalten.